

Semi-Analytical Tools for the Analysis of Laminated Composite Cylindrical and Conical Imperfect Shells under Various Loading and Boundary Conditions

Doctoral Thesis

Saullo Giovanni Pereira Castro

Semi-Analytical Tools for the Analysis of Laminated Composite Cylindrical and Conical Imperfect Shells under Various Loading and Boundary Conditions

Doctoral Thesis

(Dissertation)

to be awarded the degree

Doctor of Engineering (Dr.-Ing.)

submitted by

Saullo Giovanni Pereira Castro

from Lorena-SP, Brazil

approved by the Faculty of Natural and Material Science,

Clausthal University of Technology,

Date of oral examination

9th of December, 2014

Dean

Prof. Dr. rer. nat. Winfried Daum

Chairperson of the Board of Examiners

Prof. Dr.-Ing. Heinz Palkowski

Supervising tutor

Prof. Dr.-Ing. Gerhard Ziegmann

Reviewers

Prof. Dr.-Ing. Richard Degenhardt

PD Dr.-Ing. habil. Christian Mittelstedt

To my mother Ana Rita

To my father Enio

To my sister Carolina

To my brothers Bruno and Rodrigo

To my wife Kelly Cristine

To my family

To my uncle Jaime Prudente

To the friends who are always close to us

Contents

Contents	i
Abstract	i
Zusammenfassung	iii
Aknowledgements	v
Preface	ix
1 Deterministic Approaches for the Design of Imperfection Sensitive Shells	1
1.1 The NASA SP-8007	4
1.2 The SPLA	7
1.2.1 Definition of P1	7
1.2.2 The Constancy of the Buckling Load after P1	10
1.2.3 Multiple Perturbation Load Approach (MPLA)	10
1.2.4 Advanced Single Perturbation Load Approach (α -SPLA)	11
1.3 Reduced Energy Method and other Imperfection Patterns	13
1.4 Comparing Geometric Imperfections and Lower-Bound Methods	15
1.5 Effect of Load Asymmetries	19
1.6 Closure Remarks	23
2 Constitutive and Kinematic Equations for Cylindrical and Conical Shells	25
2.1 Constitutive Equations	26
2.1.1 Stress-Strain Relations for Anisotropic Materials	26
2.1.2 Stress-Strain Relations for Monoclinic Materials	28
2.1.3 Stress-Strain Relations for Orthotropic Materials	28
2.1.4 Laminate Equations	31
2.2 Kinematics Equations for Conical and Cylindrical Shells	36
2.2.1 Plane-Stress Relations for Orthotropic Materials	36
2.2.2 Strain-Displacement Relations for Cones and Cylinders	37
2.2.3 Kinematic Equations for Laminates	41
2.2.4 Kinematic Equations for the FSDT	44
2.2.5 Kinematic Equations for the CLPT	47
2.2.6 Matrix Form of the Kinematic Equations	49
2.3 Shear Correction Factors	54
2.4 Constitutive equations for the FSDT and CLPT	56
3 Non-Linear and Linear Buckling Formulation using the Ritz Method	59
3.1 General Non-Linear Formulation	60

3.2	Non-Linear Formulation for Conical and Cylindrical Shells	64
3.2.1	Definition of the Model	64
3.2.2	Obtaining the Structural Matrices.....	66
3.2.3	Geometric Stiffness Matrix.....	68
3.3	Initial Imperfections.....	70
3.4	Linear Buckling Formulation.....	71
3.4.1	Combined Load Cases	73
3.5	Elastic Boundary Conditions	74
3.6	Approximation Functions	76
3.7	External Force Vector	81
3.7.1	Defining the Components of the External Force Vector.....	81
3.7.2	Calculating the Components of the External Force Vector	82
3.8	Integration of the Stiffness Matrices	85
3.8.1	Sub-Division of the Stiffness Matrices	85
3.8.2	Analytical Integration of $[K_0]$, $[K_{G0}]$ and $[K_e]$	87
3.8.3	Analytical integration for Cones.....	89
3.8.4	Numerical Integration of $[K_{0L}]$, $[K_{LL}]$, $[K_G]$ and $\{F_{int}\}$	89
3.9	Non-Linear Algorithms.....	93
3.9.1	Full-Newton-Raphson	93
3.9.2	Modified Newton-Raphson	93
3.9.3	Line Search Algorithms.....	93
3.9.4	Riks (Arc-Length) Method	95
3.9.5	Convergence and Divergence Criteria and Other Non-Linear Parameters	97
4	Verification of the Proposed Models.....	99
4.1	Convergence of the Analytical Integration for Cones.....	100
4.2	Convergence of Linear Buckling Responses	105
4.3	Convergence of Linear Static Responses	110
4.3.1	Displacement Field	110
4.3.2	Stress Field	113
4.4	Convergence of the Numerical Integration	115
4.5	Convergence of Non-Linear Static Responses.....	116
4.6	Studies with Linear Buckling Responses	117
4.6.1	Axial Compression	118
4.6.2	Torsion.....	124
4.6.3	Pressure.....	124
4.7	Comparison with Shadmehri.....	129
4.8	Test Results from Meyer-Piening	132
4.9	Non-Linear Analysis using the SPLA.....	135
4.10	Representation of Measured Imperfection Fields	138
4.11	Non-Linear Analyses using Initial Imperfections	143
4.12	Non-Uniform Axial Load.....	146

5	Conclusion	149
Appendix A	Material and Geometric Data for Cones and Cylinders	151
Appendix B	Implementing Differential Operators	153
Appendix C	Some Routines Used in the Studies	159
Appendix D	Hardware and Software Configuration Used Along this Thesis	161
	References	163
	List of Symbols	169
	List of Figures	173
	List of Equations	175

Abstract

The non-linear buckling of unstiffened laminated composite cones and cylinders will be investigated and new semi-analytical models capable to predict the static and the instability response of these shells under various loads and boundary conditions will be proposed. An introduction is given to the reader in order to present and discuss some of the main deterministic approaches currently used for the design of imperfection sensitive structures. From this introduction it will become clear the need for non-linear tools that are able to take into account both geometric and load imperfections, which are recognized to be among the main factors affecting the load carrying capacity of the shells under discussion.

The complete non-linear strain equations are derived using two Equivalent Single-Layer Theories: the Classical Laminated Plate Theory and the First-order Shear Deformation Theory. The non-linear terms will be identified corresponding to Donnell's, Sanders' and Timoshenko and Gere' assumptions, but the discussion will focus on Donnell's and Sanders' equations. The resulting strain-displacement equations will then be applied to the stationary conditions of the total potential energy in order to obtain the non-linear static equations and the eigenvalue problem that can be used to predict the instability behavior, the latter using the neutral equilibrium criterion.

The Ritz method is selected to solve the non-linear set of equations and a new set of appropriate approximation functions for the displacement field is proposed, in order to simulate axial compression, torsion, pressure, load asymmetry, any arbitrary surface or concentrated loads; and any load case combining these loads. Elastic constraints are used to produce a wide range of boundary conditions, covering the four types of boundary conditions commonly used in the literature.

Two methods to solve the non-linear static equations are discussed: Newton-Raphson with line search and Riks; both presented in the full form, where the tangent stiffness matrix is calculated at every iteration; and in the modified form, where the tangent stiffness matrix is updated at the beginning of each load increment (or arc-length increment) and kept constant along the iterations.

An analytical integration scheme is proposed for the linear stiffness matrices and a numerical integration scheme proposed for the non-linear stiffness matrices. The analytical integration schemes assume constant laminate properties over the whole conical/cylindrical surface. For conical shells a novel approximation is proposed in order to efficiently perform the analytical integration of the linear stiffness matrices.

Detailed convergence analyses are presented and the proposed models are verified with finite element results, models available from the literature and test results from the literature. All the developed tools and algorithms are presented in detail and made available to the reader online.

Keywords:

Ritz method, Linear, Non-Linear, Static, Buckling, Composite, Cone, Cylinder, Pressure, Torsion, Axial Load, Axial Compression, Donnell, Sanders, Imperfection

Zusammenfassung

Das nichtlineare Beulen unversteifter Faserverbundzylinder und -konen wird untersucht, sowie neue semi-analytische Modelle, welche in der Lage sind sowohl die statische Reaktion, als auch das Instabilitätsverhalten dieser Schalen unter verschiedenen Lasten und Randbedingungen vorherzusagen werden vorgeschlagen. In der Einleitung werden die wichtigsten deterministischen Ansätze dargestellt, die derzeit zur Auslegung imperfektionsempfindlicher Strukturen Verwendung finden. Die Einführung verdeutlicht die Notwendigkeit nichtlinearer Lösungsverfahren, welche sowohl geometrische, als auch Lastimperfektionen berücksichtigen können. Es sind genau diese Imperfektionen, die einen Hauptteil der Reduktion der Tragfähigkeit der Schalen ausmachen.

Die gesamten nichtlinearen Dehnungsgleichungen sind aus zwei Äquivalenten Einzelschicht-Theorien abgeleitet: Die klassische Laminattheorie und Schubdeformationstheorie 1.Ordnung. Die nichtlinearen Terme werden entsprechend den Gleichungen von Donnell's-, von Sanders- und von Timoshenko und Gere's identifiziert, aber im Weiteren werden nur die Gleichungen von Donnell und Sanders betrachtet. Die daraus resultierenden Spannungs-Dehnung-Beziehungen werden dann auf die stationären Bedingungen der potentiellen Gesamtenergie angewendet, um die nichtlinearen statischen Gleichungen und das Eigenwertproblem zu erhalten, welches zum Lösen des Instabilitätsverhalten mittels des Gleichgewichtskriteriums verwendet werden kann.

Das Ritz-Verfahren wird zum Lösen der nichtlinearen Gleichungen verwendet, wobei ein neuer Satz an geeigneten Ansatzfunktionen für das Verschiebungsfeld vorgeschlagen wird, um axiale Stauchung, Torsion, Druck oder Ungleichförmigkeit der Lasteinleitung zu simulieren. Desweiteren ist es möglich jede beliebige Lastfunktion, Einzellast oder eine Kombination verschiedener Lastfälle zu berücksichtigen. Elastische Federn werden verwendet, um eine Vielzahl an Randbedingungen zu erzeugen und somit die vier am häufigsten in der Literatur verwendeten Randbedingungsarten abzudecken.

Um die nichtlinearen statischen Gleichungen zu lösen wurden zwei Methoden diskutiert: Newton-Raphson mit dem Zeilen-Such-Algorithmus und Riks. Beide werden in ihrer Gesamtform dargestellt, wobei die Tangentensteifigkeitsmatrix bei jeder Iteration berechnet wird. Ebenso wird sie in der modifizierten Form, in der die Tangentensteifigkeitsmatrix zu Beginn jeder Laststufe (oder Bogenlänge Inkrement) nur einmal berechnet wird, dargelegt und konstant gehalten für alle folgende Iterationen.

Für die linearen Steifigkeitsmatrizen ist ein analytisches Integrationsschema ratsam und für die nichtlinearen Steifigkeitsmatrizen wird ein numerisches Integrationsschema vorgeschlagen. Die analytischen Integrationsverfahren setzen konstante Lamineigenschaften über die gesamte konische / zylindrische Oberfläche voraus. Für die konischen Schalen wird eine neuartige Approximation vorgeschlagen, um die analytische Integration der linearen Steifigkeitsmatrix effizient durchzuführen.

Eine detaillierte Konvergenzanalyse wurde durchgeführt und die vorgeschlagenen Modelle sind mit Finiten-Elementen-Ergebnissen, sowie mit Modellen und Testergebnissen aus Fachliteratur verifiziert. Alle entwickelten Werkzeuge und Algorithmen sind im Detail dargelegt und dem Leser online zur Verfügung gestellt.

Acknowledgements

This thesis is totally dedicated to:

My parents (Ana Rita and Enio) who have always supported and believed on me, to my sister Carolina and my brothers Bruno and Rodrigo for being such good friends since they were born.

My wife Kelly who has greatly supported me during the PhD and has made my life full of colors wherever we are.

My great family who has always helped me. My uncle Jaime Prudente who helped me to find out who I am.

All the Professors I had during my fundamental education and high school. Despite I cannot remember all of them, they were all very important and Prof. Ângela, Prof. Ribas and Prof. Sônia really managed to project their personalities and advices inside my mind. All the Professors I had during my Informatics Technician course between February of 1999 and December of 2000, who gave me the first contact with programming logic and some programming languages (CLIPPER, Pascal and Visual Basic).

All the Professors I had during the Material Engineering course between March of 2001 and December of 2005 at the EEL-USP (old FAENQUIL), specially to Prof. Antonio Jefferson S. Machado, Prof. Carlos Alberto M. dos Santos (Susto), Prof. Carlos A. Nunes (Jacaré), Prof. Carlos Antonio Baptista, Prof. Carlos Shigue, Prof. Daltro Pinatti, Prof. Gilberto C. Coelho, Prof. Hugo Sandim, Prof. Maurício, Prof. Miguel Barboza, Prof. Rosa Ana Conte.

My friend Alex Diego A. Coelho, who I had the pleasure to study together during the Material Engineering course, and for whom I am eternally grateful for being such a good example and also for being by best man in my wedding.

My first advisor Prof. Fernando Vernilli Jr. who showed me for the first time how research could be conceived and focused in order to solve problems that are practical for the industry. This contact with applied research was essential to develop my interest on research.

All the teachers and lecturers of the EMBRAER Engineering Specialization Program, which I took part from October 2006 to January 2008.

Prof. José A. Hernandez, my advisor during my Master graduation between 2008 and 2009. I will always be thankful to him for supporting me on the optimization schemes we developed and for continuing on this line of research with new Master students, which I also had the pleasure to co-advise. Prof. Hernandez was also a great motivator for me to go on with the PhD studies abroad.

EMBRAER represented by all the colleagues who greatly helped me since I finished the Engineering Specialization Program in February 2008. Alexandre and Toscano who were my first guiders during my first month, then Vinícius Cunha and Poliana Dias who first taught me in practice how to work with NASTRAN and VBA programming, and shared their experience regarding technical reports. Valdir Rossi, Alexandre Barandier, Andrea Massuda, André Padovani, Eduardo Bandeira, Felipe Vinaud, Marcos Ariseto, Rodrigo Tadeu, Wagner Ponciano and all the other colleagues who always gave me valuable feedbacks during the time I was in the stress analysis

group. Thiago Guimarães who I had the pleasure to co-advise during his Master studies, despite I felt that it was he who was advising me at the end. My special gratitude also to Marco Cecchini, Alexandre Moura, Edgard Souza, Fábio Cunha, Fernanda Ravetti, João Paulo Lirani, José Pontarolli, Leonardo Oliveira, Marcelo Corbani, Maria Fernanda Marson and all the other colleagues of the CAE group, who have taught me much of what I know about programming and have given me chances to take part in challenging projects since I started there.

Prof. Raphael T. Haftka for being so kind during my first attempts looking for PhD proposals, and to Felipe A. C. Viana who gave important tips about how to address the professors in English.

Dr. Fábio Cunha who introduced me to Prof. Richard Degenhardt and guided me through the bureaucratic processes of the PhD and during my adaptation period in Germany.

Prof. Richard Degenhardt who has always been a motivation machine for all his co-workers and advised students, including me. He is the coordinator of the DESICOS Project [1] that supported my PhD and for which I worked between February 2012 and January 2015.

Prof. Gerhard Ziegmann who gave me the chance to enrol in TU Clausthal and super guided me along all the procedures required by the university, giving me valuable feedbacks about all my steps along the PhD and future possibilities.

Dr. Zimmermann who gave the insight that resulted in our first publication (Ref. [2]) and provided valuable advices and reviews to the studies conducted in the first year of the PhD.

Private University of Applied Sciences (PFH – “Private Fachhochschule Göttingen”) which was my employer during the PhD, being one of the partners in the DESICOS project. Special thanks to PFH’s campus in Stade and the co-workers located there, who helped me during this time: Ms. Peggy Repenning, Prof. Wilm F. Unckenbold, Mr. Gero Haschenburger, Ms. Verena Steffens, Mr. Gültekin Ülker, Ms. Bianca Schneppe, Mr. Bjørn-Arne Klaehn, Ms. Julia Schiffbäumer.

Dr. Mariano A. Arbelo who worked on the same topic as me and with whom I had the pleasure to share the office in the period between July of 2012 and June of 2014. Mariano also has my special gratitude for advising me and participating in the many technical discussions we had during this time.

Dr. Ke Liang who finished his PhD during the running period of DESICOS, shared with me his great technical background and was so kind to check some of my equations, giving me valuable feedbacks.

Ms. Regina Khakimova who is also a PhD candidate working on DESICOS and has taken part on our technical discussions.

The students I had the pleasure to co-advise during my PhD time: Ms. Annemarie Herrmann, Mr. Johannes Solaß, Mr. Victor Casado. I will always remember all of you and the great conversations we had during this time.

Mr. Pavel Schor and to Dr. Hailan Xu who stayed with us for a summer internship in the Summer of 2013 and whose technical background greatly contributed to our studies in DESICOS and the PhD time.

Prof. Christian Mittelstedt who gave the insight to find the right set of approximation functions for the displacement fields used along this thesis and has continuously co-authored and provided great reviews about my work.

Prof. Francisco A. C. Monteiro for being such a great advisor regarding non-linear shell theories and non-linear algorithms.

Dr. Mark Hilburger who joined as a co-author in the second publication (Ref. [3]) related to this thesis, providing great feedbacks and collaborating to significantly improve the quality of the manuscript.

Mr. David Degenhardt for helping me out with the German version of the Abstract.

All the DESICOS partners who constantly helped to develop many topics presented in this thesis through the valuable feedbacks given in our meetings.

Stade Toastmasters Club who welcomed me as a new member in 2012 (Birte, Britta, Colin, Daniel, Elke, Heidy, Helga, Henning, Hinrich, Jim, Marian, Meike, Melanie, PF, Regina, Sabine, Sven and Thomas), where I could find an atmosphere to learn English, and develop my public presentation and leadership skills.

Ms. Erika Schulz who was my landlady during February of 2012 and November of 2013 (my first 2 years in Stade) and taught me most of what I know about the German language and culture.

My dance teachers who greatly helped me to become a better and more skilled person: Marinalva Soares, Val Garcia, Rose Reis, Gil, Márcia, Marília, Tamires, Marcos Cabral, Rosana Cabral, Fernando Oliveira, all working in Brazil, and Rose, working in Stade, Germany.

The free software community, which is a vast group formed by those who want to make their developments accessible to others. The tools developed along this thesis are mainly based on Python [4], SymPy [5], NumPy [6], SciPy [7] and Cython [8]. Most of the results are plotted using Matplotlib [9]. The author sincerely thanks all the people contributing to these libraries. The author also tried the Cubature tool for multidimensional numerical integration developed by Prof. Steven G. Johnson from the MIT [10], and a wrapper for Python has been written [11].

The StackOverflow community where many interesting, helpful and important discussions concerning programming are available [12].

Preface

Since 2012 the author worked in the DESICOS project [1] in parallel with the development of this Doctorate thesis, in an overall time of 3 years. In the first year most of the focus was in the development of fast pre- and post- processing tools for the commercial finite element software Abaqus, in order to allow huge parametric studies involving the non-linear buckling analysis of unstiffened cylindrical and conical shells under various loading and boundary conditions, and using different imperfection patterns. These tools are available through the DESICOS web site [1] or from Ref. [13]. At the end of the first year and in the first half of the second year the author was mostly dedicated to the studies that resulted in the publications of Refs. [2] and [3], both discussed in Chapter 1. From the second half of the second year until the second half of the third year, the author has been dedicated to the development of semi-analytical tools, which will be described Chapters 2 and 3, and verified in Chapter 4.

Chapter 1 introduces the reader to the context where the thesis is inserted and states the problem that will be treated on the subsequent chapters. In summary, the design of imperfection sensitive structures such as unstiffened cones and cylinders or skin-dominated stiffened structures usually require the application of knock-down factors in order to calculate the buckling load using classical methods. By classical methods one could refer to the typical linear buckling analysis performed using finite elements or classical formulae, usually keeping the structure in simple supports that restrain the translations but not the rotations. For cylindrical structures, the currently most applied guideline that provides such knock-down factors is the NASA SP-8007, which was empirically built using experimental data from 1930s to 1960s, and therefore the guideline can be considered outdated since it ignores all the developments regarding new manufacturing processes, testing setups and analysis capabilities. In Chapter 1 the limitations of NASA SP-8007 is further discussed and the new developments regarding deterministic methods are presented, where it is shown the important influence of geometric imperfections and load asymmetries on the buckling behavior of cylindrical shells.

From the discussion of Chapter 1 one important conclusion is that non-linear buckling calculations are an indispensable part or any modern guideline applied for the design of imperfection sensitive structures. From the literature one can find many non-linear buckling formulations for isotropic structures, but very few for composite structures. Among the few authors dealing with composite structures, none seem to present a formulation that solves the complete displacement field (similarly to what is performed in a finite element procedure) considering a more general load and boundary condition case. This motivated the development of this thesis focused on semi-analytical methods that are capable of solving the complete displacement and stress field for various loading and boundary conditions.

Chapter 2 presents the constitutive and the kinematic equations for laminated composite cylindrical and conical shells using two Equivalent Single-Layer Theories: the Classical Laminated Plate Theory (CLPT) and the First-order Shear Deformation Theory (FSDT). The full non-linear strain expressions are obtained for both cases and from this complete set of non-linear equations it will be identified the terms that correspond to Donnell's, Sanders' and Timoshenko and Gere's equations. Only the non-linear equations using Donnell's and Sanders' assumptions are implemented

and discussed in the subsequent chapters, and this choice is justified along the discussion. All the formulation is derived and presented in matrix form in order to make the present development easier to implement and easier to apply to other problems using different non-linear theories, kinematic equations, loads or boundary conditions.

Chapter 3 will apply the kinematic and constitutive equations of Chapter 2 into the total potential energy functional in order to obtain the non-linear system of equations that form the non-linear static problem. The non-linear equations will then be solved using two non-linear algorithms: the Newton-Raphson with line search and the Riks (arc-length) method. Instead of deriving the governing differential equations, the Ritz method has been chosen where the displacement field is approximated using a known set of base functions that must respect the geometric boundary conditions. The solution is then directly obtained in a weak form from the stationary conditions of the total potential energy functional. Furthermore, the neutral equilibrium criterion is applied to the total potential energy functional in order to obtain the eigenvalue problem that represents the structural instability condition, from where the linear buckling equations are derived as a special case of the more general, non-linear formulation. Linear buckling equations for axial compression, torsion, pressure and combined cases using these loads are derived. Elastic boundary conditions are included to the formulation in order to increase the range of possible boundary conditions, and the four main types of boundary conditions found in the literature are covered. Chapter 3 also explains the layout of the stiffness matrices, which is the basis for the integration schemes used to obtain the stiffness matrices and the internal force vector.

In Chapter 4 convergence studies are performed in order to gather experience about the behavior of the proposed models for different boundary conditions, loads, different structures, for linear static, non-linear static and linear buckling analysis. The converged models are compared and verified against other models available in the literature, finite element results and test data available in the literature.

The discussion is closed in Chapter 5, summarizing the most relevant observations from the other chapters, discussing the advantages and limitations of the proposed methods and suggesting topics for research in future studies.

Saullo G. P. Castro

Stade, Germany

1 Deterministic Approaches for the Design of Imperfection Sensitive Shells

Since the beginning of 1900s researchers developing formulations for the buckling of thin-walled cylinders, e.g. Southwell (1914) [14], have already observed a discrepancy between theoretical and experimental results, where the buckling loads measured in tests were typically much lower than predicted buckling loads using the available theories, that considered a geometrically perfect cylinder. Southwell found that his theory could not be applied for real cases where geometric imperfections and load asymmetries could take place. Flügge (1932) [15] and Donnell (1934) [16] were the first authors to develop formulations taking into account the effects of initial geometric imperfections, but the proposed non-linear theories failed to predict the experimental buckling loads, requiring to use in the theories geometric imperfections of large-magnitude in order to match the experimental results, which “could scarcely have escaped the notice of the investigators” [17]. Moreover, Flügge’s and Donnell’s theories produce a gradual appearance of buckles accompanied by an increase of the reaction load, whereas in the experiments the buckling is typically characterized by a sudden dynamic buckling event with a reduction of the reaction load. Koiter’s theory (1945, which was translated from Dutch to English in the 1960s by Riks [17]) was the first to accurately predict the imperfection sensitivity trends that were observed experimentally [17]. In 1950 Donnell and Wan [18], independently from the study of Koiter, modified the procedure adopted by Donnell [16] sixteen years earlier and proposed a new method, which was followed by several investigators with some modifications [19]. Arbocz (1992) [20] states that the Koiter’s “General Theory of Elastic Stability” is widely accepted. It is important to mention that Koiter’s theory is valid if the elasticity limit is not exceeded anywhere in the material [21]. In addition, the theory is based on an asymptotic expansion about the bifurcation point and is limited to small-magnitude imperfections and the range of validity is generally unknown. Recent applications of the Koiter’s method for the buckling of thin-walled laminated composite cylinders proposing higher order approximations for the knock-down factor successfully increased the range of applicability of the original method, but the approach is still limited to imperfections up to half of the shell thickness [22].

At the time Koiter proposed his theory the industry already needed guidelines for the design of imperfection sensitive structures. Such guidelines should explain how to take the imperfection sensitivity into account, especially for the calculation of rocket and launcher structures [23]. In 1960, Seide, Weingarten and Morgan (see [24] and [25]) published a collection of experimental results which was one of the main precursors for the well-known NASA SP-8007 guideline, published in 1965 and revised in 1968 to its most popular version [26]. This guideline is still used (in 2014) for the calculation of the design load at the preliminary design phase for many components of satellite launcher structures, which in many cases consist of unstiffened shells. Important advantages of the NASA SP-8007 at the time it was conceived are the simplicity and the reduced computational cost.

In the 1960s the relatively limited computational power limited the use of the non-linear methods available at that time, including the Koiter's theory, and the currently available computational power opened the possibility to apply non-linear analyses considering many variables representing the complex behaviour of imperfection sensitive structures under instability conditions [23]. This possibility aided the development of new approaches, which can be classified in two large groups: stochastic or deterministic.

In a stochastic approach the simulations are performed changing some of the analysis variables within an uncertainty range, which may be related to the geometric imperfection pattern applied, material properties, stacking sequence of the laminates, load imperfections and any other structural parameter that may significantly affect the structural response of interest. The structural response, which may be the buckling load, is obtained for a pre-determined level of reliability, and then presented as a mean value and a standard deviation, for example. Extra factors of safety should be used if the variables not considered in the stochastic simulation have a significant effect on the evaluated response, for example, if the stochastic simulation does not include parameters for load imperfections there should be a factor of safety accounting for that [23]. The uncertainties are determined based on real data, carrying the typical variances for each of the variables involved in the analysis. For measured geometric imperfections, the Caltech group ([27], [28]) and others ([29], [30]) started the first imperfection databases in laboratory scale shells, being followed by large-scale surveys [23]. Degenhardt et al. (2010) [31] applied Monte Carlo simulations in order to predict less conservative KDFs for composite cylinders under axial compression, based on real measured imperfections without varying using general imperfection distributions. Rolfes et al. (2009) [32] created distribution functions that would allow one to apply the imperfections obtained for one shell in the analysis of other shells, but still involving a high computational cost due to the need to compute multiple times the desired response varying the input variables in many levels. Kriegesmann et al. (2011) [33] presented a semi-analytic procedure for fast predictions of stochastic distributions of buckling loads, which is one possibility to reduce the overall computational cost involved with the stochastic analysis.

The deterministic approaches are those in which a reference buckling load is calculated and the design load is obtained multiplying this reference buckling load by a KDF. When using the NASA SP-8007 guideline the reference buckling load can be the one obtained from a linear buckling analysis and the knock-down factor (KDF) is given by Eq. (1.1.1).

New deterministic approaches have been developed and they propose other methods that no longer require empirical lower-bound curves such as the one given by Eq. (1.1.1) in order to obtain the KDF. Hühne et al, 2005 [34] proposed a deterministic approach called the Single Perturbation Load Approach (SPLA) in which a lateral load is applied prior to the axial compression. The applied single perturbation load (SPL) stimulates a single buckle during the subsequent axial compression. In Fig. 1.1.1 it is shown the typical modelling procedure needed for the SPLA. Hühne [35] observed that for very small lateral loads the global instability is the first instability, with the post-buckled pattern usually characterized by two rows of buckles that go around the circumference. The author also verified that if the lateral load is increased a local instability occurs before the global buckling, producing a local dimple which is analogous to the snap-through verified in arch-shaped beams with a transverse load in the middle, also called by Timoshenko & Gere as reversal of deflections [36].

This local instability will be called herein a “local snap-through” (LST). This nomenclature was also used by Haynie & Hilburger (2010) [37].

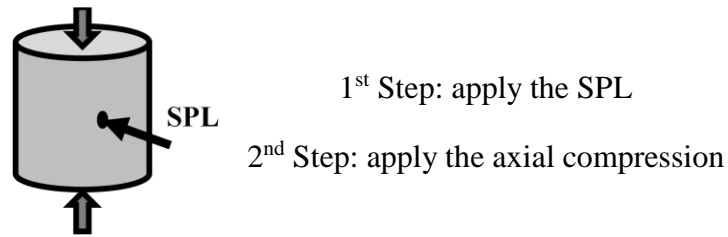


Fig. 1.1.1: The Single Perturbation Load Approach (SPLA)

Winterstetter & Schmidt [38] classified the geometric imperfections as “realistic”, “worst” or “stimulating”. As discussed by Hühne et al. (2008) [35], single buckles are: “realistic”, because they can be verified in real test conditions; “worst case”, as explained by Deml & Wunderlich (1997) [39] using a modified finite element model that was capable of finding the geometric imperfection that gave the minimum buckling load ; and “stimulating” since the buckling process is initiated by single buckles, as demonstrated by Esslinger (1970) [40], using high-speed cameras. Hühne’s main goal when proposing the SPLA was to provide a straightforward and robust method, based on the concept that it stimulates a single buckle, making the SPLA a promising method to estimate realistic knock-down factors to be used at the preliminary design phase of imperfection sensitive structures.

In 1994, Geier et al. [41] investigated the effects of non-uniform loads in the so called “shim tests” where shims are used to create the load asymmetry, verifying the high effect of the shim thickness on the buckling response. In 2002, Hühne et al. [42] applied the shim tests to a deeper investigation, also observing the strong influence of the load asymmetry on the buckling response. Hühne already showed that the SPLA could only be used to represent geometric imperfections and that an extra knock-down factor would be required if load asymmetries should also be taken into account. Wagner and Hühne (2014) [43] proposed the Advanced Single Perturbation Load Approach (α -SPLA) where a load asymmetry is included in the calculation of the knock-down factors by assuming a misalignment angle α of the upper edge, which can be seen as a misalignment of the testing apparatus.

The Reduced Stiffness Method (RSM) developed by Croll (1972) [44], Batista & Croll (1979) [45] and collaborators is another deterministic method for calculating lower-bounds, besides the NASA SP-8007. Croll & Batista (1981) [46] used this concept to find lower-bounds for axially compressed linear-elastic isotropic cylinders. The method has been mostly applied in the civil engineering field [47] and it is based on three postulates summarized as follows [48]: 1) Significant geometric non-linearities appear due to changes in the membrane resistance. For instance, in the buckling of an in-plane loaded plate there is no non-linearity up to the point where some disturbance causes a normal deformation. The normal deformation causes a load eccentricity that creates bending, interacting non-linearly with the reduction of the membrane stiffness, which continuously decreases in the post-buckled regime. In any case where a thin-walled structural member is initially under high compressive stresses with a high membrane component of the strain energy, the displacements are predicted linearly up to the point where the membrane stiffness starts to decrease. 2) For thin-walled structures, the loss of stiffness in the post-buckling regime can only occur when there is membrane resistance at the pre-buckled state, meaning that if the shell does not have any

membrane energy prior to buckling there will be no loss of stiffness after buckling. 3) The lower-bound buckling load for a particular load case will be given by an analysis in which the membrane stiffness is totally removed.

Sosa et al. (2006) [49] showed the equivalence between the Reduced Stiffness Method and the Reduced Energy Method (REM). Along the studies presented in Section 1.3 the REM will be implemented in a general finite element solver following the procedure explained by Sosa et al., in which a reduction factor α is applied to the membrane stiffness components instead of completely eliminating it as originally proposed by Croll [48]. This approach assumes that the shell with degraded membrane stiffness will have non-linear pre- and post-buckled shapes similar to the eigenvector obtained through linear buckling analysis. Sosa & Godoy (2010) [50] compared the REM using this assumption with non-linear post-buckling analysis and showed that this assumption may not be valid in some cases, leading to non-conservative estimatives. In such cases the computation of correction coefficients is required, making the REM less straightforward because of the need for non-linear analyses.

The various methods presented in the discussion above will be detailed in the following sections and at the end of this chapter a brief conclusion will be given.

1.1 The NASA SP-8007

The main curve used when applying the NASA SP-8007 guideline is shown in Fig. 1.1.1, which consists in a collection of experimental results and a lower-bound curve that gives the shell buckling knockdown factor, denoted by γ in Eq. (1.1.1), as a function of the radius over thickness ratio R/t . Calculating γ for isotropic unstiffened cylinders requires only the cylinder radius and the wall thickness, whereas for orthotropic materials it is shown how an equivalent thickness t_{eq} is used. However, despite a correction is given for composite materials, one could note that this approach does not consider all the orthotropic stiffness terms such as those related to the membrane-bending (\bar{B}_{ij}), tension-shear (A_{16} , A_{26}) or the bending-twist (D_{16} , D_{26}) coupling. Such stiffness terms can have a significant influence on the buckling behavior, consequently on the resulting knock-down factors, as demonstrated by Geier et al. (2002) [51] and further detailed in the following.

$$\gamma = 1 - 0.902(1 - e^{-\phi}) \quad (1.1.1)$$

Isotropic:

$$\phi = \frac{1}{16} \sqrt{\frac{R}{t}}$$

Orthotropic:

$$\phi = \frac{1}{16} \sqrt{\frac{R}{t_{eq}}} \quad t_{eq} = 3.4689 \left(\frac{D_{11}D_{22}}{A_{11}A_{22}} \right)^{\frac{1}{4}}$$

where A_{11} , A_{22} , D_{11} and D_{22} are the extensional and bending stiffnesses extracted from the composite ABD matrix.

In the NASA SP-8007 guideline the KDF denoted by γ in Eq. (1.1.1) is called correlation factor, accounting for the disparity between experiments and theory. Theoretical equations for the buckling load for both isotropic and orthotropic cylinders are also provided in NASA SP-8007, where the correlation factor can be applied. However, in modern applications of the guideline the

reference buckling load is calculated using a linear buckling analysis and the design load finally obtained multiplying this reference buckling load by γ as shown in Eq. (1.1.2).

$$F_{design} = F_{theoretical} \cdot \gamma \quad (1.1.2)$$

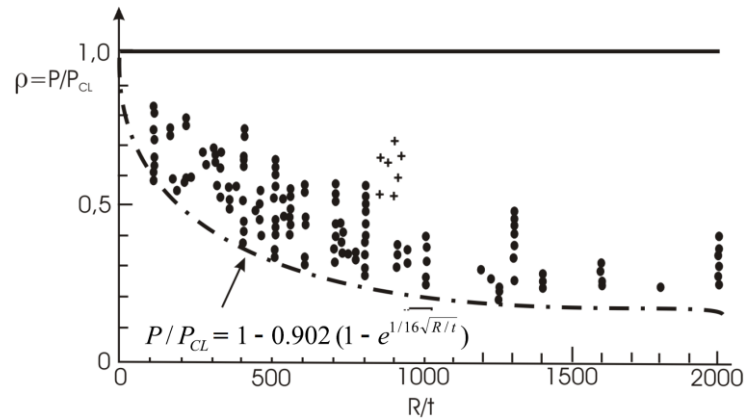


Fig. 1.1.1: Test Data for Isotropic Cylinders under Axial Compression (modified from Arbocz and Starnes Jr. [23])

Many authors have proved that the NASA SP-8007 guideline gives conservative estimations for the buckling load of imperfect shells (see Arbocz & Starnes Jr. [23], Hilburger et al [52], Hühne et al [34] and [35], Degenhardt et al. [53]). The author believes that the main aspect deserving attention when applying the NASA SP-8007 for composite shells is that it does not consider the laminate stacking sequence in the calculations, which usually has a significant influence for non-symmetric thin-walled cylinders and cones. Table 1.1.1 shows the knock-down factors (KDFs) calculated using the NASA guideline and the Single Perturbation Load Approach (SPL) (detailed in the next sections) for two cylinders with the same number of plies and using the same ply orientations, but one having the inverted stacking sequence of the other. These two cylinders were originally designed by Zimmermann (1992) [54]. Note that the NASA SP-8007 gives the same result for both shells, the KDF obtained using the SPLA shows that the buckling load of cylinder Z33 significantly decreases with the increase of the imperfection amplitude created by the lateral load.

Table 1.1.1: KDFs calculated using the NASA SP-8007 and the SPLA

	Z32	Z33
Stacking sequence	IN[$\mp 51 / \mp 45 / \mp 37 / \mp 19 / 0_2$] _{OUT}	IN[$0_2 / \pm 19 / \pm 37 / \pm 45 / \pm 51$] _{OUT}
Height	510 mm	510 mm
Radius	250 mm	250 mm
F_{crit}	98.694 kN	191.667 kN
KDF		
NASA SP-8007	0.477	0.477
KDF		
SPLA (Ref. [2])	0.951	0.627

The discussion presented in Geier et al. (2002) [51] explains in a deeper detail the influence of the stacking sequence on the buckling load, and an overview of this discussion can be given based on Fig. 1.1.2, which shows the membrane and bending forces with their corresponding strains acting in

a shell element. The buckles that arise in the buckling mechanism may produce a local increase or a local decrease of the cylinder radius. For a buckle growing outwards the local radius increases and there will be positive extensional strains in the circumferential direction, defined as ε_{22} , and positive curvatures κ_{11} and κ_{22} . A stabilizing effect would be one that creates internal forces tending to decrease the local radius, which are positive moments M_{11} and M_{22} and membrane forces N_{11} and N_{22} . Referring to Eq. (1.1.3) it can be seen that this is achieved when terms B_{11} , B_{12} and B_{22} are positive. The same reasoning is valid for a buckle growing inwards, for which ε_{22} is negative, and κ_{11} and κ_{22} positives. The stabilizing internal moments will appear as negative M_{11} and M_{22} and the stabilizing membrane stresses would be negative N_{11} and N_{22} , which can also be achieved when B_{11} , B_{12} and B_{22} are positive. For real laminates the author verified that for positives B_{12} and B_{22} , element B_{11} is negative. Therefore, B_{12} and B_{22} seems to play the most important role. For symmetric laminates the angled plies are placed at both sides and their effect is counterbalanced such that all the coupling terms B_{ij} are zero.

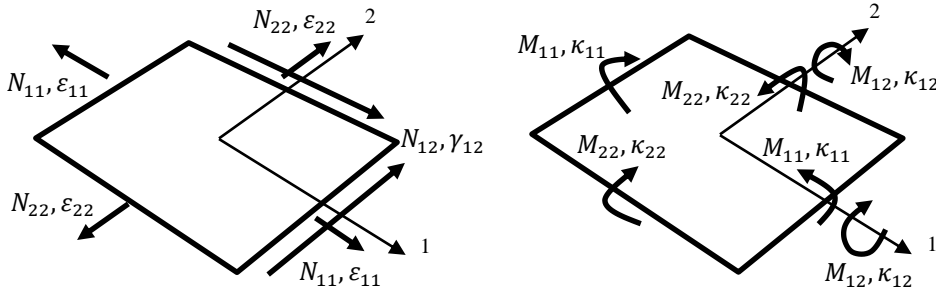


Fig. 1.1.2: Membrane Forces, Moments, Extensional and Rotation Strains acting in a Shell Element

$$\begin{aligned} N_{11} &= B_{11}\kappa_{11} + B_{12}\kappa_{22} + B_{16}\kappa_{12} & M_{11} &= B_{11}\varepsilon_{11} + B_{12}\varepsilon_{22} + B_{16}\gamma_{12} \\ N_{22} &= B_{12}\kappa_{11} + B_{22}\kappa_{22} + B_{26}\kappa_{12} & M_{22} &= B_{12}\varepsilon_{11} + B_{22}\varepsilon_{22} + B_{26}\gamma_{12} \end{aligned} \quad (1.1.3)$$

Cylinders Z32 and Z33 give a good picture of how much the stacking sequence affects the buckling load and the imperfection sensitivity. The coupling stiffness matrices $[B]$ for the two cylinders are shown in Fig. 1.1.3 and the term B_{12} discussed above is depicted. Since Z33 has the stacking sequence stabilizing the appearance of buckles, the perfect shell reaches a higher buckling load and the effect of a geometric imperfection, such as the one created using the SPLA, is more pronounced than for Z32 which already has a destabilizing effect from its stacking sequence.

$$[B]_{Z32} = \begin{bmatrix} 15.7 & -4.2 & 1.8 \\ -4.2 & -7.4 & 1.4 \\ 1.8 & 1.4 & -4.2 \end{bmatrix} \times 10^3 \frac{N}{mm} \quad [B]_{Z33} = \begin{bmatrix} -15.7 & 4.2 & -1.8 \\ 4.2 & 7.4 & -1.4 \\ -1.8 & -1.4 & 4.2 \end{bmatrix} \times 10^3 \frac{N}{mm}$$

Fig. 1.1.3: Coupling Stiffness Matrices for Cylinders Z32 and Z33

1.2 The SPLA

Hühne observed that the buckling load remains nearly constant after a threshold perturbation load named $P1$, as shown in Fig. 1.2.1. After $P1$ the global buckling load is considerably less sensitive to a further increase of the perturbation load magnitude, and for this reason Hühne [35] suggested to use as a design load the corresponding buckling load obtained when $P1$ is applied, called $N1$. It is important to emphasize that in the SPLA only geometric imperfections are taken into account, and other types of imperfection such as load asymmetries are not considered. An important difference of the knock-down curve of Fig. 1.2.1 to the originally proposed by Hühne et al. [35] is that four regions are considered instead of three, as verified by Castro et al. [2]. The additional region is because before $P1$ there is a perturbation load threshold called $PLST$ that will be the perturbation load that creates a local snap-through before the global buckling. Since in all the cases verified by the author up to now the value of $P1$ is very close to $PLST$, the identification of $PLST$ is rather difficult and it is common in the literature to ignore $PLST$ and say that the local snap-through is created for perturbation loads higher than $P1$.

In order to make the SPLA a straightforward method such as the currently applied NASA SP-8007, the $P1$ value must be known beforehand in order to allow the analyst to perform one non-linear buckling simulation that suffices to calculate the KDF and therefore the design load. Some empirical formulas have been proposed (see for example Wang et al. [55]), but they have a limited range of validity for the R/t and furthermore they are applicable only for metallic structures. The SPLA may contribute to fully exploit the potential of composite structures by determining a knock-down factors that depends on the specific laminate chosen by the designer, avoiding unnecessary conservativeness eventually imposed when the NASA SP-8007 is applied. The next sub-sections will present some studies performed by the author in order to obtain more insight about the phenomena connected to the SPLA.

1.2.1 Definition of $P1$

A precise definition of the threshold perturbation load $P1$ is needed in order to pave the way for future developments that aim a fast calculation of $N1$. Castro et al. (2014) [3] present a detailed discussion and some results are herein reproduced. In Fig. 1.2.1 it is shown the knock-down (KD) curve of cylinder Z33 divided in four regions, separated by $PLST$, $P1$ and $P2$, where: 1) $PLST$ is the smallest SPL that creates a local-snap through (LST); and 2) $P2$ is the SPL beyond which the LST is created smoothly, without a sudden drop of the axial reaction load and with the axial stiffness changing gradually. In Fig. 1.2.2 it is shown the LST pattern compared with the global post-buckling pattern. As already mentioned, usually the $PLST$ cannot be clearly identified because it is very close to $P1$, justifying that determining $P1$ is sufficient and one can assume that the local snap-through starts to appear when a perturbation load of value $P1$ is applied.

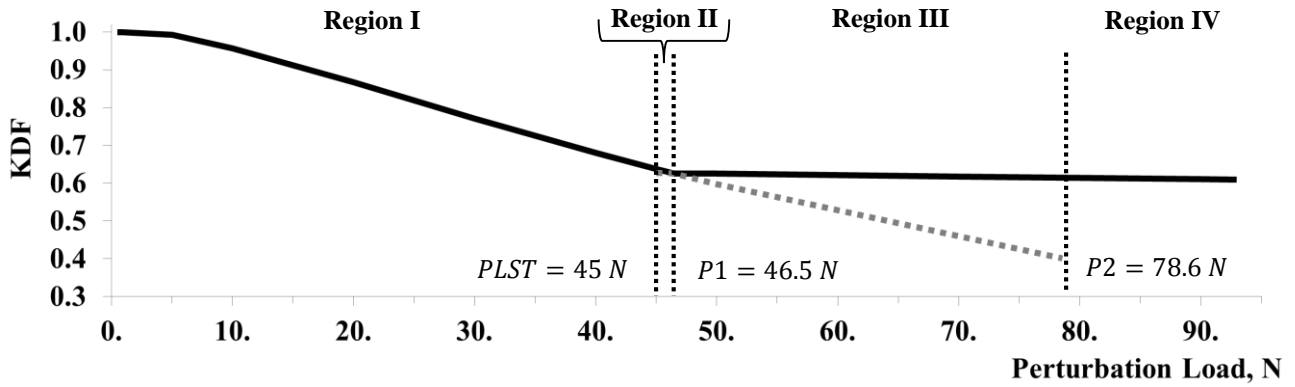


Fig. 1.2.1: Four Regions in the SPLA Knock-Down Curve, modified from Castro et al. [2]

In Fig. 1.2.3 it is shown the load-shortening curves (LS curves) obtained for Z33 for each region presented in Fig. 1.2.1. Note that for $SPL < PLST$ (region I) the LS curve shows a single drop of reaction load, for $PLST \leq SPL < P1$ (region II) there are two drops and the first corresponds to the appearance of a local snap-through (LST), illustrated in Fig. 1.2.2–a, and the second drop to the global buckling, illustrated in Fig. 1.2.2–b. For $P1 \leq SPL < P2$ (region III) the two drops are still present and the first drop is brought to a lower reaction load level with the increase of the initial SPL value. Finally, for $SPL \geq P2$ (region IV) the first drop of reaction load is no longer identified and the LST appearance can be identified in the load shortening curve by the change of axial stiffness that occurs smoothly.



Fig. 1.2.2: Displacement Patterns for the Local Snap-Through and the Global Buckling, modified from Castro et al. [2]

In Fig. 1.2.4 it is shown a KD curve for Z33 similar to the one presented in Fig. 1.2.1, but using perturbation loads between 40N and 50N in order to emphasize the region surrounding $P1$. In Fig. 1.2.4–b before $P1$ the dashed line represents the LST unexpectedly happening at a higher reaction load level than the global buckling; and after $P1$ the dashed line represents the LST happening at a lower reaction load level than the global buckling. From Fig. 1.2.4 it can be seen that $P1$ is the single perturbation load that, when applied, causes a LST to occur at the same reaction load as the global buckling, which is the definition needed for the development of analytical or semi-analytical models aimed to calculate $P1$.

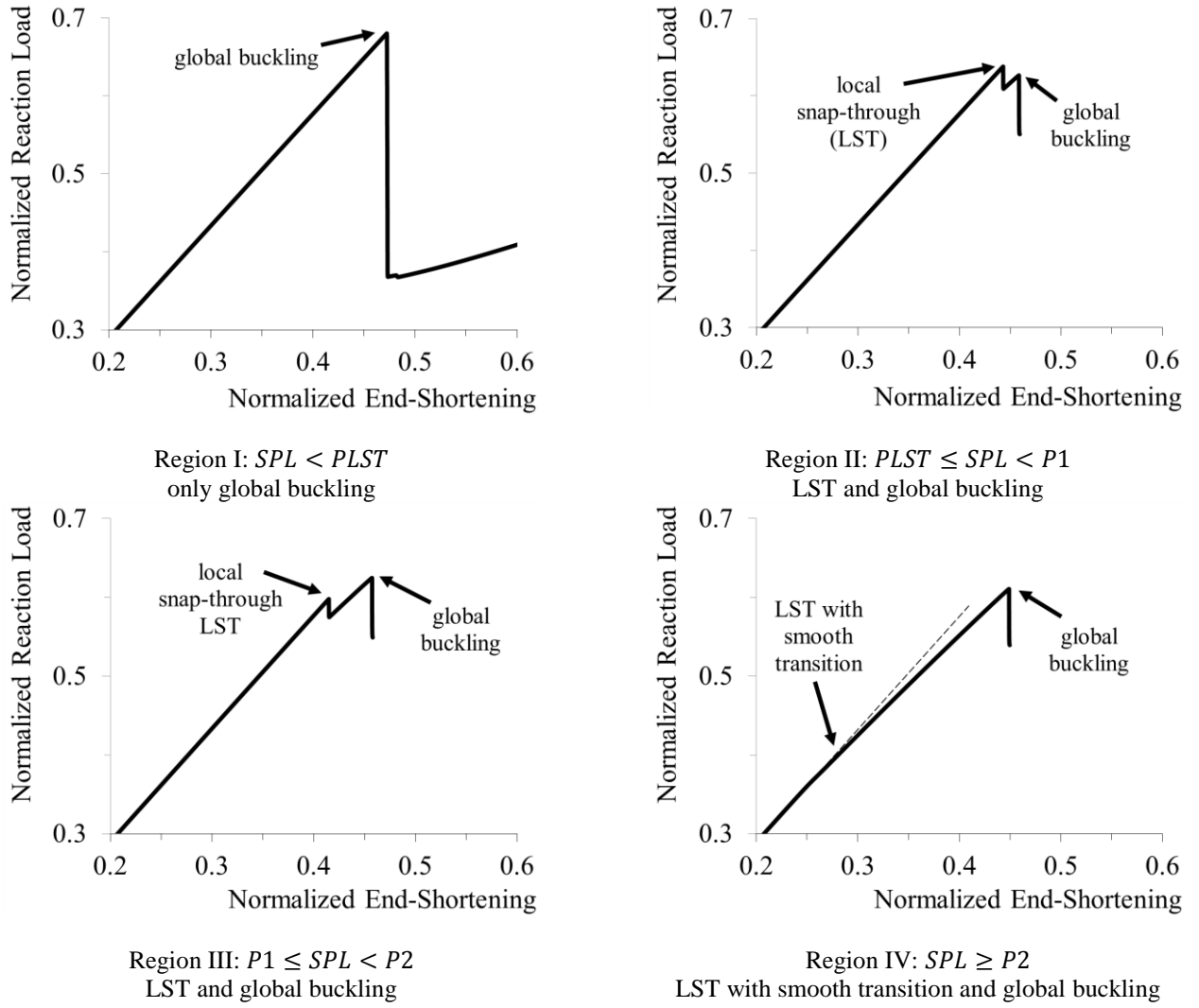
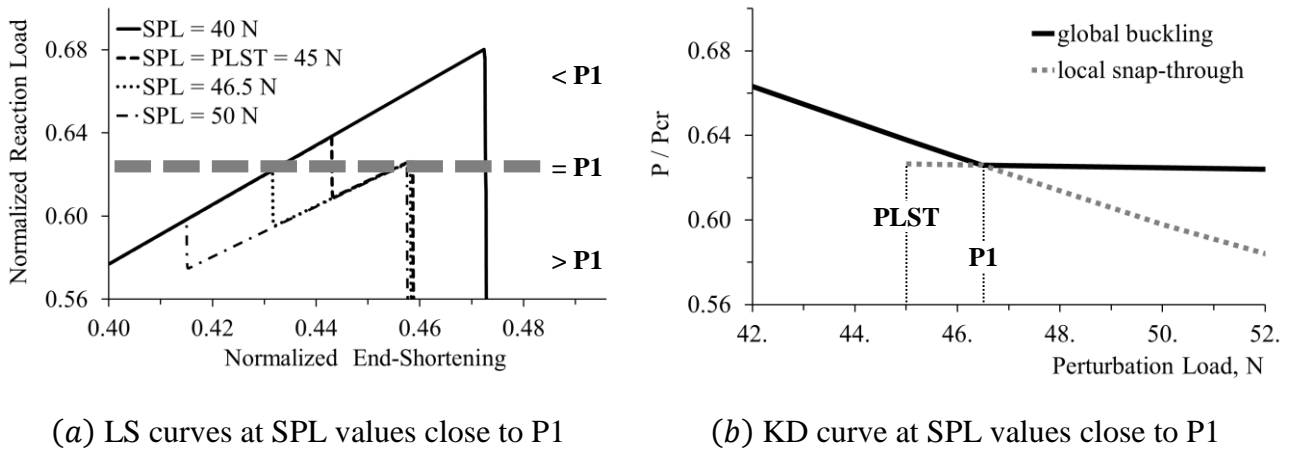


Fig. 1.2.3: LS curves for different perturbation load levels, cylinder Z33, copied from Castro et al. [2]



(a) LS curves at SPL values close to $P1$

(b) KD curve at SPL values close to $P1$

Fig. 1.2.4: Detailed Evaluation of the LS curves and KD curves close to $P1$, Cylinder Z33

1.2.2 The Constancy of the Buckling Load after P1

As described in the previous section the study of Castro et al. (2014) [2] contributed to a new definition of P1. Another contribution presented by the authors, based on the insights given by Dr. Zimmermann (senior researcher at the German Aerospace Center), is the explanation about the constancy of the global buckling load observed after the threshold perturbation load P1, when the Single Perturbation Load Approach (SPLA) is used. This constancy can be seen in Fig. 1.2.1, Fig. 1.2.6 and Fig. 1.4.3, for example. The discussion presented herein is a summary of what is presented in Ref. [2].

When the single perturbation load value SPL is higher than the threshold $PLST$, a local snap-through appears before the global buckling (cf. Fig. 1.2.4). This appearance can be detected by a drop of the reaction load for a displacement controlled axial compression simulation or test. The local snap-through appearance can also be identified monitoring the normal displacement at the perturbation load application point during the axial compression. The local snap-through, illustrated in Fig. 1.2.2, consists on a defect of relatively large proportions when compared to the normal displacement caused by the perturbation load itself, and it was verified that the dimensions of this defect depends more on the axial compression level than on the perturbation load level. It was also verified that in many cases the perturbation load can even be withdrawn after the local snap-through had been created and the defect produced by the local snap-through would remain stable. Since this defect dominates the buckling behavior, higher perturbation loads can be applied and the global buckling load will not significantly change. One would expect the buckling load to remain nearly constant for $SPL \geq PLST$, but since the global buckling load is higher than the local snap-through load, the constancy is verified only for $SPL \geq P1$.

1.2.3 Multiple Perturbation Load Approach (MPLA)

Arbelo et al. (2014) [56] have proposed the multiple perturbation load approach which uses multiple concentrated loads to produce the geometric imperfection that will cause the reduction of the buckling load resistance. The method is an extension of the SPLA using more than one perturbation load. A limitation of the SPLA for stiffened structures is that depending on the stiffener's characteristics the imperfection caused by a single perturbation load will not propagate around the structure, making the predictions obtained through the SPLA non-conservative. Arbelo also verified that for unstiffened structures the use of multiple perturbation loads significantly reduce the design load obtained compared to the SPLA. In Fig. 1.2.5 three configurations of multiple perturbation loads are shown for cylinder Z33 and the results of each one are presented in Fig. 1.2.6. A significant reduction of the $N1$ load can be seen, corresponding to a KDF reduction from 0.617 using the SPLA to 0.489 using the MPLA with 4 loads.

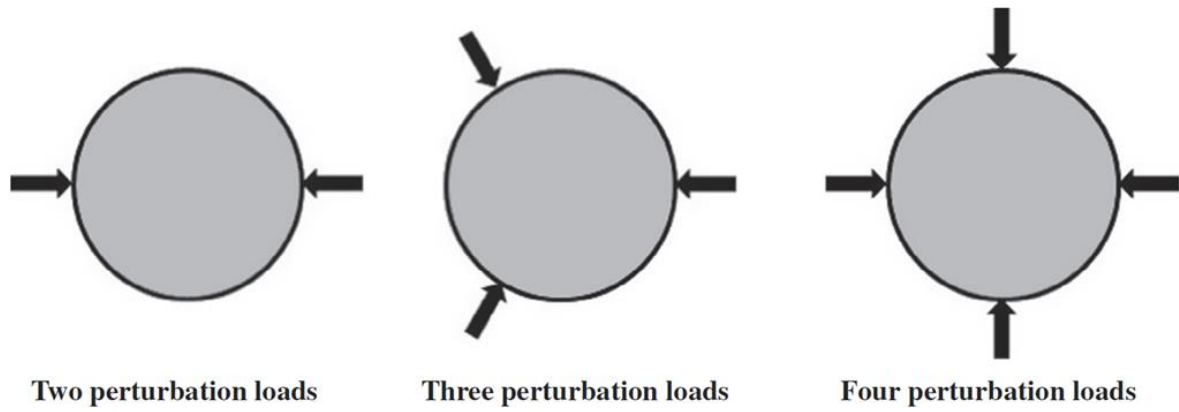


Fig. 1.2.5: Load cases used in the MPLA, copied from Arbelo et al. [56]

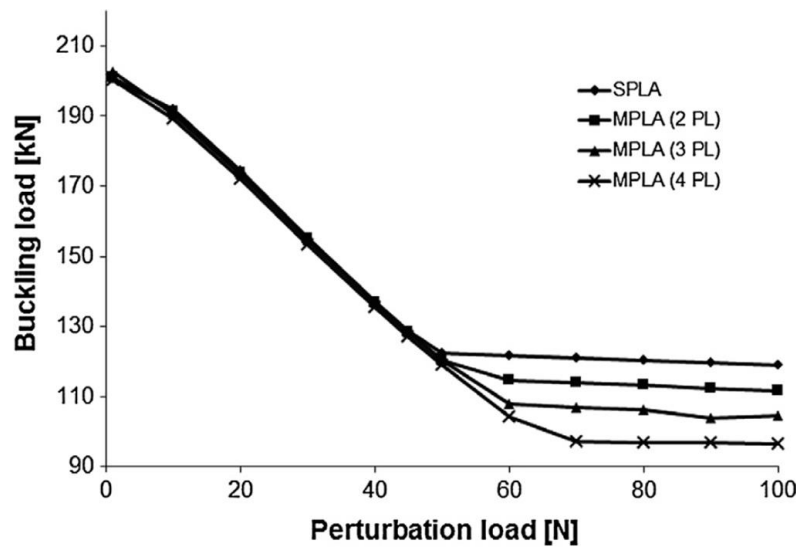


Fig. 1.2.6: MPLA curves for cylinder Z33, copied from Arbelo et al. [56]

1.2.4 Advanced Single Perturbation Load Approach (α -SPLA)

In the Advanced Single Perturbation Load Approach (α -SPLA) a load asymmetry is included in the calculation of the knock-down factor by assuming a misalignment angle α of the upper edge. Due to the convention adopted all over this thesis, the misalignment angle will be called β while α refers to the semi-vertex angle of the conical structures. The relation between the axial displacement close to the single-perturbation load application point is shown in Fig. 1.2.7 and Eq. (1.2.1) [43].

As reported by Kriegesmann et al. (2010) [57], many experiments have been conducted to measure the geometric imperfections of the tested samples, but very few recorded the load asymmetry level present during the tests. Therefore, the authors proposed a method to estimate the load asymmetry of the test setup since this parameter strongly affects the buckling response [42] [43].

Assuming that the two main factors contributing to the knock-down factor of the shell structures are the geometric imperfections and the load asymmetries, the authors applied the measured imperfection pattern to the finite element model by translating the nodal positions and evaluated the influence of β for many different values of ω , resulting in an average buckling load for

each β . The estimated β value of the test setup is the one with the average buckling load that mostly approaches the test results.

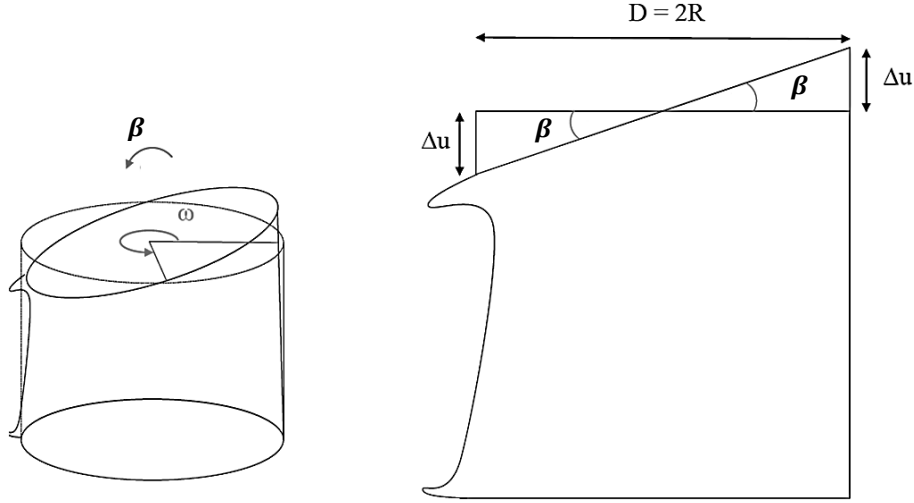


Fig. 1.2.7: Bending angle β in terms of the axial displacement, modified from Wagner and Hühne [43]

$$\Delta u = R \tan(\beta) \quad (1.2.1)$$

Since Wagner and Hühne [43] employed Kriegesmann's method to find β in the α -SPLA, the assumption that the geometric imperfection and the load asymmetry are the two most significant factors affecting the knock-down factor must hold for the α -SPLA. Wagner and Hühne observed that a load asymmetry as small as 0.02° is sufficient to reduce the load carrying capacity by 50% for imperfection sensitive structures such as Z33, while for insensitive structures such as cylinder Z32 the same β will reduce the buckling load by only 17%. Note that the mechanical properties that generate the sensitivity to geometric imperfections also generate the sensitivity to load asymmetries.

Since the α -SPLA can take load asymmetries into account, this method should be preferred over the SPLA when load asymmetries are present. The main problem is that Kriegesmann's method to determine β requires access to measured imperfection data, and therefore the α -SPLA undermines one of the major advantages of the SPLA, i.e. finding a knock-down factor and a design load without any previous knowledge of the structure being designed. To overcome this drawback Wagner and Hühne [43] proposed a method to estimate the Δu value of Eq. (1.2.1) based on SPLA results, but the authors recognize that this method needs further development in order to be applicable.

1.3 Reduced Energy Method and other Imperfection Patterns

Sosa et al. [49] suggested a methodology to apply general purpose finite element solvers to evaluate the knock-down factor of arbitrary shell geometries using the Reduced Energy Method (REM). The authors performed a test to evaluate which element types in Abaqus can be applied with the REM, and in their studies the typical elements used for thin-shell analysis were selected, which can be grouped as linear: S3, S3R, STRI3, S4 and S4R; and parabolic: S8R5, S9R5 and STRI65. The studies showed that only the element STRI3, whose formulation involves an analytical integration to calculate the stiffness matrices, showed a converged value of knock-down factor when diminishing the membrane stiffness. The knock-down factor is evaluated by:

$$KDF = \frac{U^{2b} + \frac{1}{\alpha} U^{2m}}{U^{2b} + U^{2m}} \quad (1.3.1)$$

where α is a reduction factor. In a general purpose solver such as Abaqus it is not possible to compute separately the bending and the membrane contributions to the internal strain energy, so that an indirect approach based on three steps is suggested by the authors [49]:

- i. The eigenmodes are obtained using a classical linear buckling analysis
- ii. The eigenmode (eigenvector) is used as an initial displacement field, working as a load field applied to the finite element model, and a linear static analysis is performed to compute the corresponding strain energy (total strain energy, considering both the membrane and bending contributions)
- iii. The eigenmode is once more applied as an initial displacement field, but now the reduction factor α is applied to “erode” the membrane stiffness and the corresponding strain energy is again computed

The third step is accomplished by removing from the element constitutive matrix the membrane sub-matrix. The constitutive matrix for each element can be obtained from the stress-strain relation:

$$\{N\} = \begin{bmatrix} [A'] & [B] \\ [B] & [D] \end{bmatrix} \{\varepsilon\} \quad (1.3.2)$$

with (cf. Section 2.4):

$$\begin{aligned} \{N\}^T &= \{N_{xx} \quad N_{yy} \quad N_{xy} \quad Q_y \quad Q_x \quad M_{xx} \quad M_{yy} \quad M_{xy} \quad M_{yz} \quad M_{xz}\} \\ \{\varepsilon\}^T &= \{\varepsilon_{xx}^{(0)} \quad \varepsilon_{yy}^{(0)} \quad \gamma_{xy}^{(0)} \quad \gamma_{yz}^{(0)} \quad \gamma_{xz}^{(0)} \quad \varepsilon_{xx}^{(1)} \quad \varepsilon_{yy}^{(1)} \quad \gamma_{xy}^{(1)} \quad \gamma_{yz}^{(1)} \quad \gamma_{xz}^{(1)}\} \end{aligned}$$

where $[A']$ is the membrane stiffness sub-matrix with reduced stiffness, defined as:

$$[A'] = \frac{1}{\alpha} [A] \quad (1.3.3)$$

The studies presented by Castro et al. (2014) [3] applied the procedure described above for the determination of knock-down factors for cylinders Z33 and Z07 (both described in Table A.2), using the first 50 eigenmodes obtained from a linear buckling analysis. From the results of Fig. 1.3.1 it can be seen that only the odd modes are shown (1st, 3rd, 5th ...) since the next even ones (2nd, 4th, 6th ...) have the same eigenvalue with the eigenvector is offset by $\pi/2$. The buckling modes for the two cylinders are shown Fig. 1.3.2 and Fig. 1.3.3. From Fig. 1.3.1 it can be seen that using the REM the worst-case modes are the 33rd and the 25th, while the modes that produce the higher knock-down factors are the 47th and the 49th, respectively for cylinders Z07 and Z33, further discussion is presented in the next section, where the method is compared with non-linear buckling analyses.

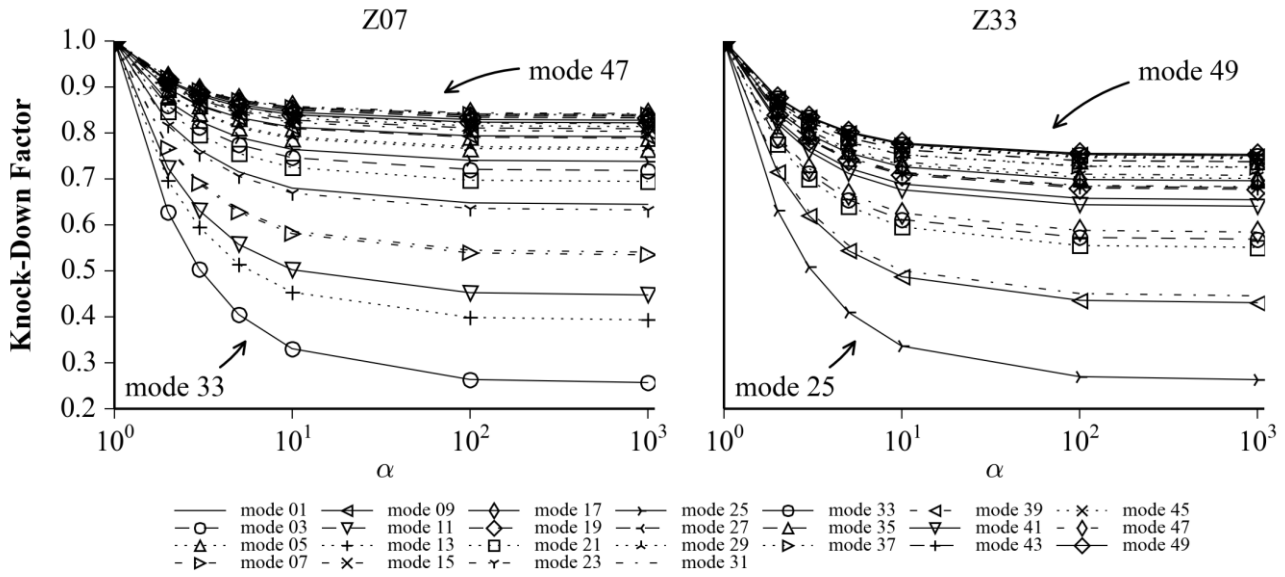


Fig. 1.3.1: KDFs using the Reduced Energy Method (REM), copied from Castro et al. [3]

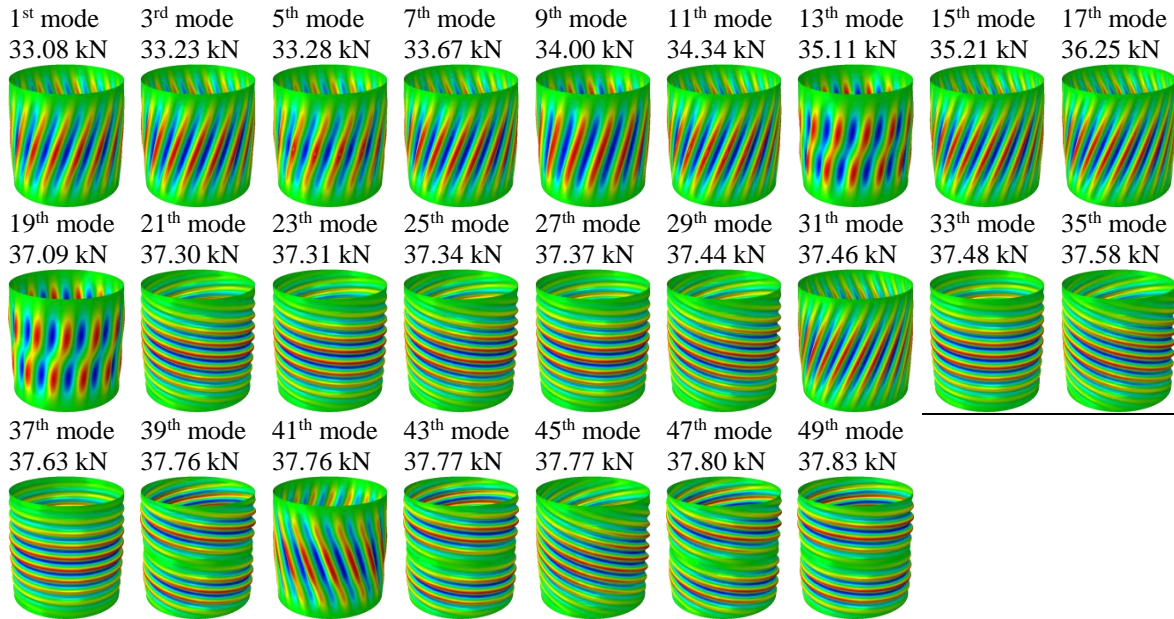
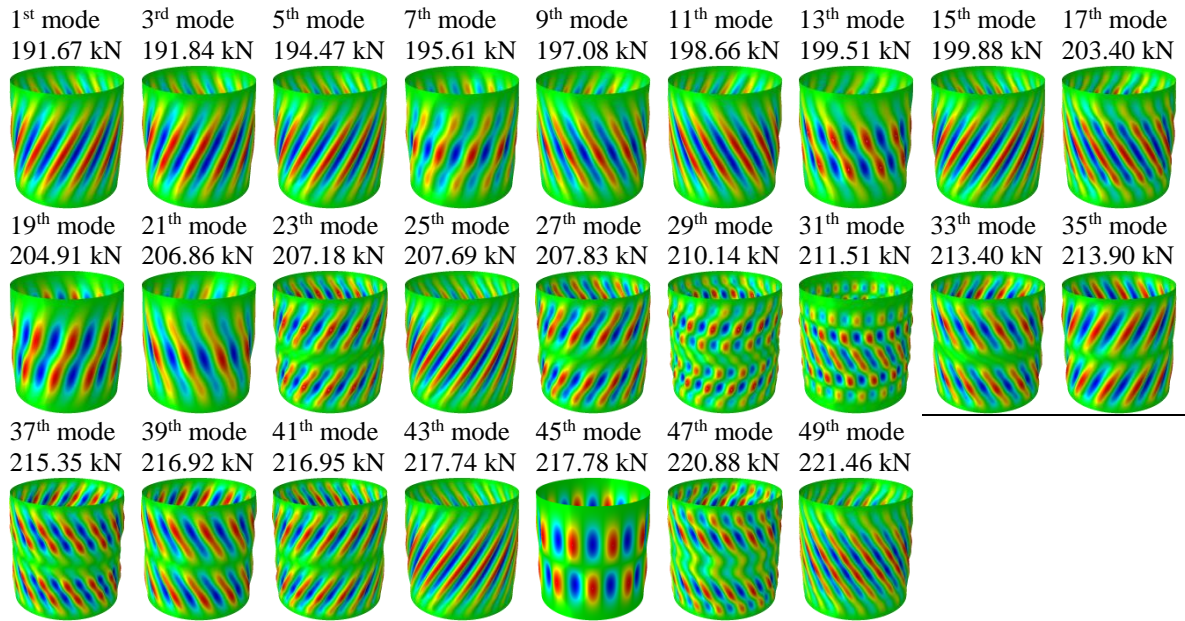


Fig. 1.3.2: First 50th Buckling Modes for Cylinder Z07

Fig. 1.3.3: First 50th Buckling Modes for Cylinder Z33

1.4 Comparing Geometric Imperfections and Lower-Bound Methods

In this section the study presented in Castro et al. (2014) [3] will be discussed in order to give more inside about the effect of different imperfection patterns on the buckling response and the comparison with the lower-bound methods already discussed in the previous sections. The first type of imperfection discussed consists on linear buckling modes of Fig. 1.3.2 and Fig. 1.3.3, referred to as linear buckling mode-shaped imperfections (LBMI). The LBMI is compared with the SPLA, the REM and the NASA SP-8007 for cylinders Z07 and Z33 and the results are shown in Fig. 1.4.3. The REM produced a wide range of KDFs for the two composite cylinders analyzed: from 0.26 to 0.84 for cylinder Z07 and from 0.26 to 0.75 for cylinder Z33. Besides the wide range of variability of the KDFs, the REM does not predict the lower-bound values obtained with non-linear analysis and the LBMI. In addition, the buckling modes causing the lowest KDFs for the REM are not the same buckling modes causing the lowest KDFs in the non-linear computations. From the REM results for cylinder Z07 of Fig. 1.3.1 it can be seen that the 33rd mode gives the lowest KDF, which is in agreement with the non-linear results of Fig. 1.4.3–a, but the REM results also show that the highest KDF is associated with the 47th mode, while the non-linear analysis shows that mode 47 belongs to the group causing the lowest KDFs. Similarly, for Z33 the REM shows that the highest KDF is obtained with the 49th buckling mode, but the non-linear computations of Fig. 1.4.3 show that this buckling mode belongs to the group causing the lowest buckling modes.

Recalling that the Reduced Energy Method implementation proposed by Sosa et al. (2006) [49] is based on the assumption that the linear buckling modes are similar to the non-linear post-buckled shape, the discrepancy described above is most probably due to the fact that for the shells under consideration this similarity does not hold. Sosa & Godoy (2010) [50] already proposed a correction procedure for the REM that should be used when the non-linear pre- and post-buckled shapes do not resemble the linear buckling mode, but no further investigations were performed herein regarding the

REM approach with corrections since the need for non-linear analyses in the correction procedure undermines the advantage of the original proposal of Sosa et al. (2006) [49], which is to use only linear buckling and linear static analyses to estimate the knock-down factor. The corrections would be required if one decided to evaluate the REM applicability as a tool to calculate lower-bound KDFs for composite unstiffened cylinders presented. From the studies herein performed it can be said that the REM with linear buckling analysis cannot be used to predict knock-down factors due to the wide variability depending on which mode is chosen; and to the fact that even if many modes are evaluated there is no guarantee that these predictions are conservative or not.

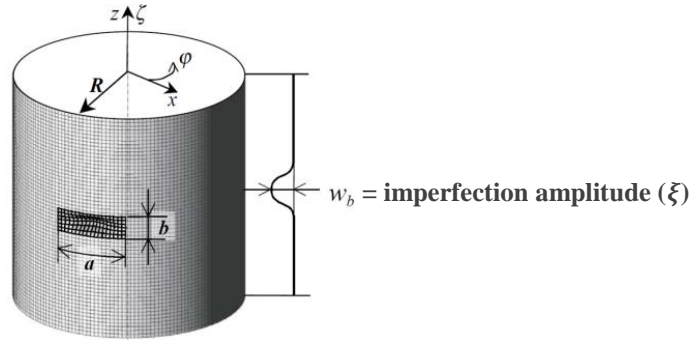


Fig. 1.4.1: Geometric Dimple Imperfection (GDI), modified from Wullschleger [58]

Cylinder Z07 shows two groups of eigenmodes: one axially oriented and another circumferentially oriented (cf. Fig. 1.3.2). These groups correspond to the two distinct response trends shown in Fig. 1.4.3–a. In particular, the results indicate that cylinders with circumferentially oriented eigenmodes exhibit lower KDFs. This is in agreement with the three postulates of the REM, that the circumferentially aligned mode shapes (e.g., axisymmetric or nearly axisymmetric) degrade the membrane stiffness more efficiently than the axially oriented ones. Observations [3] of many load-shortening curves for variable imperfection amplitudes show a pronounced axial stiffness reduction in the load-shortening curve obtained for cylinder Z07, already for relatively small imperfection amplitudes when using the circumferentially oriented LBMs, which is also in agreement with the referred postulates.

In the study of Castro et al. [3] geometric dimple (GDI), axisymmetric and real measured imperfection (MSI) are compared and it has been observed that axisymmetric imperfections should be used if one seeks for the worst-case imperfection pattern, i.e. the imperfection pattern that produces the lowest knock-down factor for a given imperfection amplitude. Although it is important to know the worst-case imperfection that provides a lower-bound reference, the analysts are usually interested on rather realistic imperfection patterns that will produce a buckling response closer to what is observed in a real test or application condition, not on the worst-case that usually results in overly conservative designs. Taking the real measured imperfection as a reference and ignoring any load asymmetries it has been found that the SPLA was able to predict buckling loads which are conservative but still close to the real measured imperfections. The conservativeness was for $(\xi/h) < 4$ and to give more sense to this number, the industry partners of DESICOS [1] have stated that the developed study cases should kept in the range where $(\xi/h) \leq 2$, since imperfections beyond this level are only sporadic in real cases and can easily be identified even with eye inspection procedures.

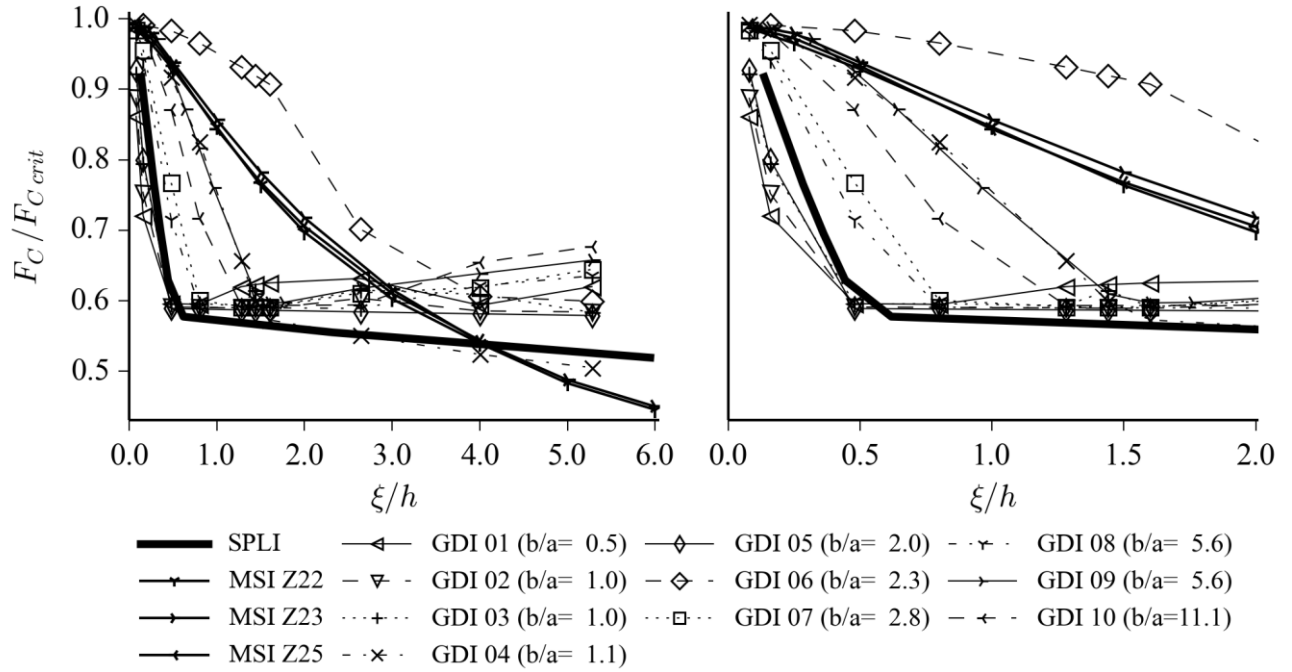


Fig. 1.4.2: Knock-down curves for the MSI, SPLI, and GDIs, for Z07, modified from Castro et al. [3]

Comparing the dimple imperfections (GDI) with the SPLA, the results showed that the dimple imperfection response highly depends on the shape parameters defining the dimple (cf. Fig. 1.4.1) and that the SPLA produced almost a lower-bound for most of the simulations using different dimple configurations, as shown in Fig. 1.4.2. Due to the simplicity of the SPLA, the use of a single perturbation load to produce the geometric imperfection is preferred over the geometric dimple, guaranteeing yet the achievement of a more conservative result for most of the cases. The stiffening effect observed for the GDI for higher (ξ/h) values happens because in the simulations this imperfection was applied translating the finite element nodes without creating any initial stresses (stress-free initial state).

The use of axisymmetric imperfections (ASI) is also studied by Castro et al. [3] and compared to the worst-case buckling modes that showed a circumferentially oriented pattern. The results demonstrated that with the ASI one can obtain the same knock-down factor given by the worst buckling modes without the need to choose the right mode, providing an adequate imperfection pattern suitable to investigate worst-case scenarios, i.e. to establish the lower-bound buckling load values that one can assume for a given imperfection amplitude.

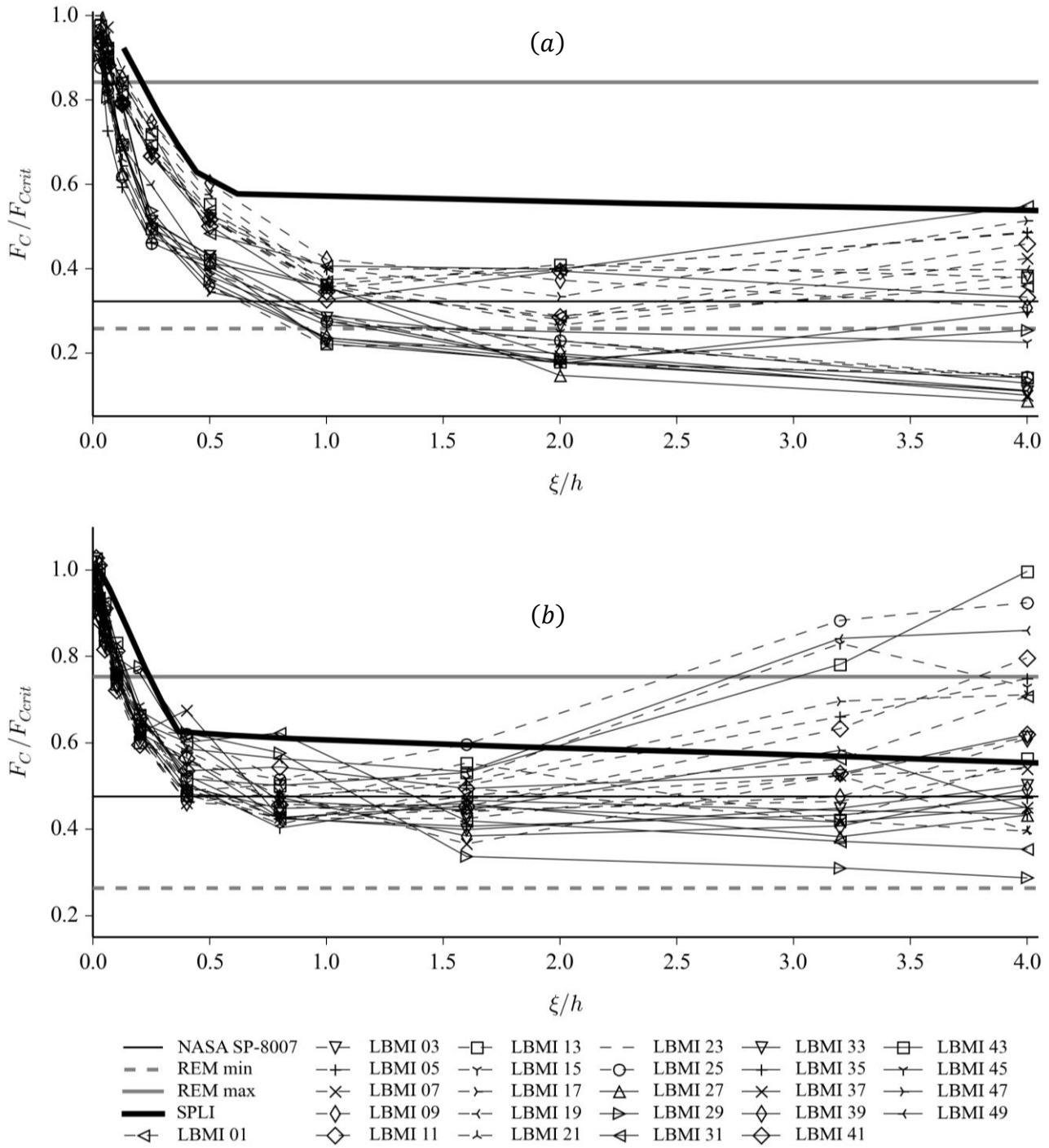


Fig. 1.4.3: Knock-down curves for SPLA, REM, NASA SP-8007 and LBMI, modified from Castro et al. [3]

1.5 Effect of Load Asymmetries

As already mentioned in Section 1.2.4, load asymmetries and geometric imperfections are in most of the cases the two factors that mostly affect the buckling response of thin-walled cylinders and cones, and it has been shown [42] [57] that the shells with a higher sensitivity to geometric imperfections will also be sensitive to load asymmetries. In the study of Hühne et al. (2002) [42], the load asymmetry was created using shims of different thickness in one side of the testing machine, placed between the testing machine top plate and the test specimen, as shown in Fig. 1.5.1. In the next chapters this load asymmetry will be represented as a rigid misalignment of the upper plate β with a circumferential offset angle ω , as shown in Fig. 1.2.7. When shims are applied, the shim thickness t_{shim} can be used to calculate β using Eq. (1.2.1) as $\beta = \text{atan}(t_{shim}/R)$.

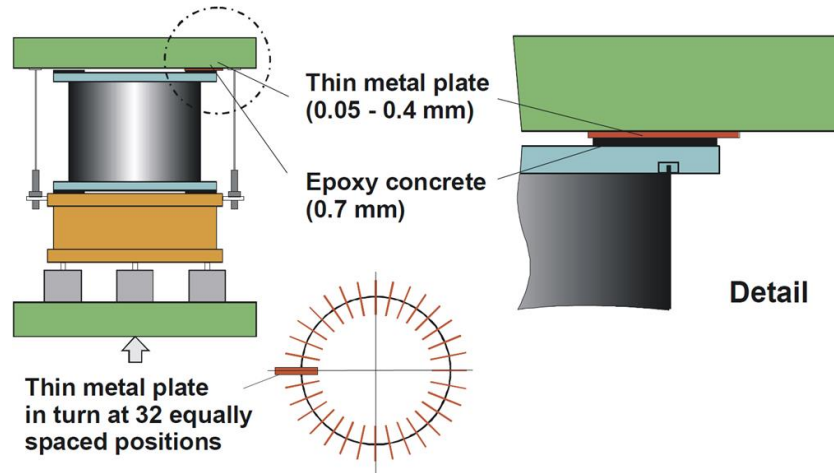


Fig. 1.5.1: Load Asymmetry Created with Shims, copied from Hühne et al. [42]

Finite element analyses were carried out using 4 of the cylinders tested by Hühne et al. [42], and they are shown in Table 1.5.1. The material properties correspond to material “Geier 2002” defined in Table A.1. All the cylinders have a radius of 250mm and are 510mm height. The thickness of each lamina is 0.125mm. The shim thicknesses of Table 1.5.1 were used to compute a set of β values, which are shown in Table 1.5.2. Many values of ω are also shown, which are used in the studies combining the load asymmetry with the geometric imperfection created by a single perturbation load. Angle ω is measured about the single perturbation load and the single perturbation load values chosen for each cylinder are shown in Table 1.5.3.

The finite element model was created using the developed plugin for Abaqus [13] (Version 1) and the code shown in Eq. (C.1). The load asymmetry is created using gap elements with a variable gap width along the top edge. The mesh consists of 180 quadrilateral-linear elements around the circumference with an aspect ratio of 1:1. The non-linear solver chosen was the Newton-Raphson with artificial damping using a constant damping factor of 10^{-7} and a maximum step increment of 0.01. The results are shown in Fig. 1.5.2 and Fig. 1.5.3, where the knock-down factor (KDF) is plotted as a function of the ratio between the imperfection amplitude and the laminate thickness (ξ/h).

The first observation is that cylinders Z22 and Z24, which were designed to have a minimal buckling load, are less sensitive to the imperfection amplitude, and cylinders Z14 and Z23, designed to have a maximized buckling load, are more sensitive to the imperfection amplitude. This behavior is explained by the discussion presented in Section 1.1 about the contrasting behavior of cylinders Z32 and Z33. An interesting observation here is that cylinders Z22 and Z24, with low imperfection sensitivity, are very sensitive to the load asymmetry, while cylinders Z14 and Z23 are sensitive to the geometric imperfection and not very sensitive to the load asymmetry. When the perturbation load is aligned with the load asymmetry, i.e. when $\omega = 0$, the lowest knock-down factors are obtained.

Table 1.5.1: Cylinders and shims used in the load asymmetry studies, modified from Hühne et al. [42]

Cylinder	h_{lam}	Stacking Sequence	t (mm)					
			0.00	0.05	0.10	0.20	0.30	0.40
Z14	0.75	$[\pm 51 / 90_2 / \pm 40]$	■		■	■		■
Z22	0.75	$[\pm 49 / \pm 36 / 0_2]$	■	■	■	■		■
Z23	1.25	$[\pm 60 / 0_2 / \pm 68 / \pm 52 / \pm 37]$	■		■	■	■	■
Z24	1.25	$[\pm 51 / \pm 45 / \pm 37 / \pm 19 / 0_2]$	■			■		■

Table 1.5.2: Values of ω and β used in the load asymmetry studies

ω values	$[0^\circ, 45^\circ, 90^\circ, 135^\circ, 180^\circ]$
β values	$[0^\circ, 0.00573^\circ, 0.01146^\circ, 0.02292^\circ, 0.03438^\circ, 0.04584^\circ, 0.0573^\circ]$

Table 1.5.3: Single perturbation load values used in the load asymmetry studies

Cylinder	Perturbation Loads (N)
Z14	[1, 5, 10, 30, 50, 70, 90, 110, 130]
Z22	[1, 5, 10, 30, 50, 70, 90, 110, 130]
Z23	[1, 2, 3, 4, 5, 6, 10]
Z24	[1, 2, 3, 4, 5, 6, 10]

The aim of the studies presented in this section was only to provide a deeper knowledge about the importance of the load asymmetry for the buckling behavior and to investigate a simple and efficient modelling proposal to create the load asymmetry. The author recommends further studies in this direction, using more refined models and trying to establish the general trends when combining load asymmetry with geometric imperfections. Other types of load asymmetries should also be evaluated, especially those using non-rigid supports, which represent real application cases with a higher fidelity.

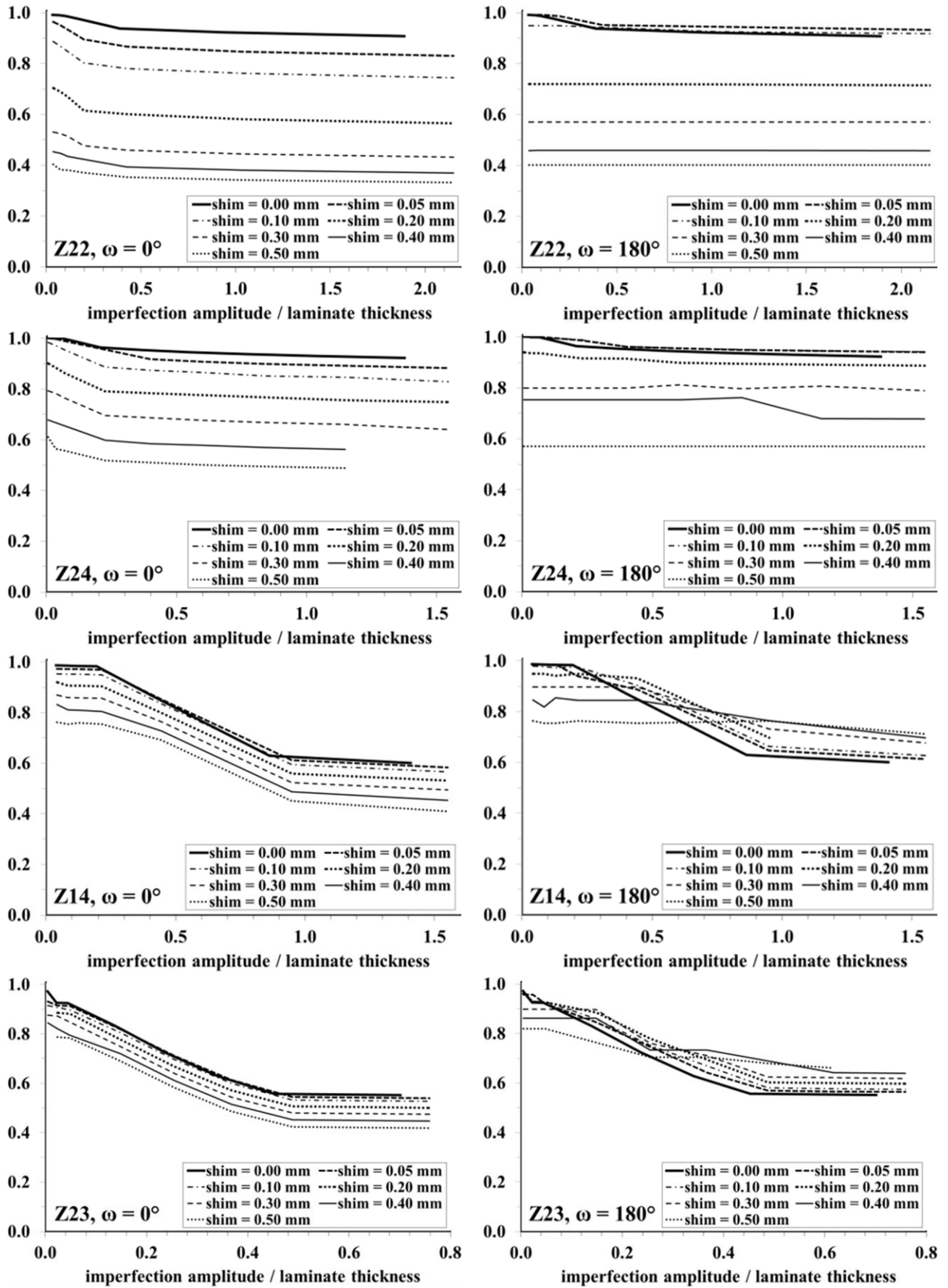
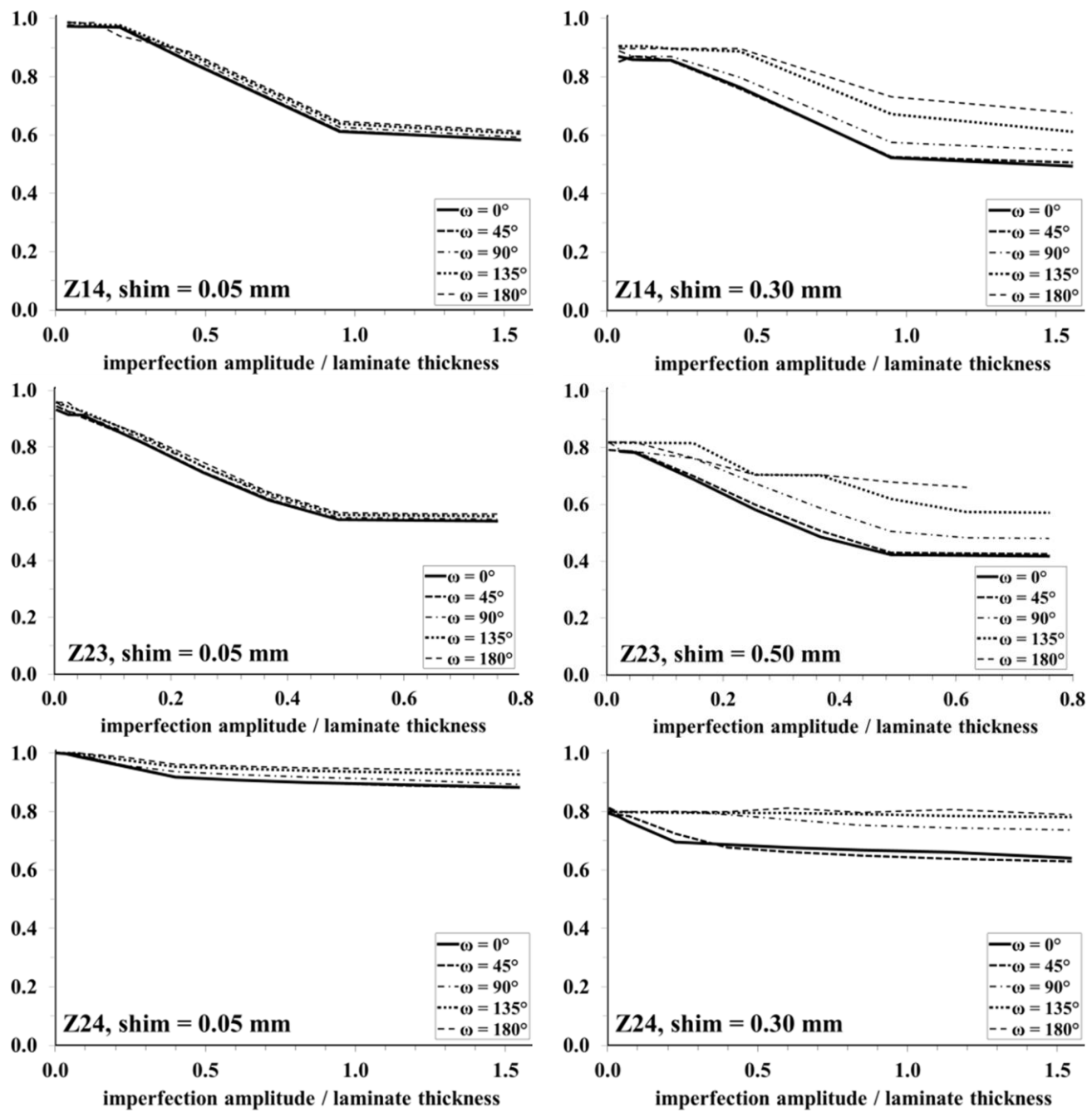


Fig. 1.5.2: Imperfection amplitude effect for different shims thicknesses

Fig. 1.5.3: Imperfection amplitude effect for different ω values

1.6 Closure Remarks

This chapter presented some of the main deterministic methods for the design of imperfection sensitive shells, focusing on unstiffened structures. Some final remarks are given in this section in order to show the author's opinion about the main topics covered along this chapter and to pave the way for the developments presented in the next chapters.

The NASA SP-8007 was developed on the 1960s based on experimental data of isotropic structures manufactured and tested between the 1930s and the 1960s. All the manufacturing development since then has not been taken into account by the guideline. Despite recent studies have demonstrated that this guideline is conservative for the design of composite shells, in the author's perspective the NASA SP-8007 should not be used because it does not take into account the important influence of the stacking sequence of laminated structures, as detailed in the previous sections.

The MPLA showed to produce reduced KDFs when compared to the SPLA, raising the question if the SPLA could overestimate the load carrying capacity of real structures. One should also consider that the results obtained with multiple perturbation loads can lead to knock-down factors that are even more conservative than the NASA SP-8007. Is the MPLA conservative or the SPLA overestimates the load carrying capacity? The choice about how many perturbation loads should be used, their position and their values in order to representatively account for the structural behavior is a choice that demands further development around these two methods.

The Advanced Single Perturbation Load Approach (α -SPLA) includes the important influence of the load asymmetry into the knock-down factor calculated using the SPLA. The main drawback of this method is that it requires previous knowledge about the imperfection pattern of the structure, undermining one of the main advantages of the SPLA, which is the independence of any previous knowledge about the structural real imperfections. New developments are being carried out by Wagner and Hühne [43] in order to provide better estimations for the load asymmetry parameter without the need for experimental data.

The Reduced Energy Method (REM) is based on valuable physical observations on the buckling mechanism, such that understanding this method automatically leads to a better understanding of the buckling phenomenon and shell theories. The developments of Sosa et al. [49] [50] to adapt this method to commercially available finite element procedure are valuable and the authors already demonstrated the limitations of the assumption that the linear buckling modes are representative of the non-linear buckling modes, showing that this is not always the case and that the KDF predictions using the REM must again rely on computationally expensive non-linear analyses in order to apply the correction procedure proposed by the authors. This limitation has also been observed by Castro et al. (2014) [3] in the studies herein discussed.

Regarding the many different types of geometric imperfections available, if one wishes to use a worst-case imperfection pattern the axisymmetric imperfections are the recommended choice [3]. Despite there may be a buckling mode that shows a circumferentially oriented pattern and would result in the same knock-down factor as the axisymmetric imperfections, this buckling mode is not guaranteed and one would have to look for the right buckling mode to be used as initial imperfection.

The study of Castro et al. [3] showed that the SPLA produces a knock-down factor which is more conservative than the real measured imperfections, but yet not as conservative as other imperfections such as the linear buckling modes (LBMI) or the axisymmetric imperfection (ASI). Besides, the SPLA not causes the axial stiffness reduction observed by the LBMI and the ASI. When compared to similar imperfection patterns such as the dimple imperfections, the SPLA requires fewer parameters to be defined and for the cases investigated the buckling response covered most of the dimple configurations. The fact that the geometric dimple is applied translating the nodal positions in the finite element model allows a stiffening effect verified for higher imperfection amplitudes, also observed for the buckling modes that show an axially oriented pattern.

From the studies presented in this chapter it became clear that the methods leading to correct predictions of the knock-down factor are those in which non-linear analyses are employed. Finite element is the most applied method for such analyses, but the search for alternative tools that offer a higher efficiency in the calculations is of great importance, especially for the development of new guidelines aimed to provide less conservative knock-down factors for the design of imperfection sensitive structures. Such guidelines require numerous non-linear analyses which will usually be limited by the number of licenses of a commercially available finite element tool or by the computational power. Therefore, the next chapters are focused on the development of a semi-analytical tool based on the Ritz method.

2 Constitutive and Kinematic Equations for Cylindrical and Conical Shells

The constitutive equations are those describing how much strain and stress is developed inside the material as a reaction to the external loads [59] [60]. The kinematic equations are the strain-displacement relations giving the rate of change of each strain component in the body when subjected to a displacement field. No strain is developed when no relative displacement takes place, such as in rigid body motions [61].

A homogeneous material body is one with the same properties throughout its volume, so that the elastic modulus is independent of the position. Anisotropy appears when the material has different properties in different directions. The isotropic case is when all the material properties are the same in all directions in a given point of the material body. Homogeneity and heterogeneity are properties related to the position inside the material, while isotropy and anisotropy are directional properties [59].

The equations developed throughout this text will deal with ideally elastic materials, which are those that fully recover the original form upon removal of the external forces that caused the deformation under isothermal conditions. Only isothermal conditions will be considered and all the deformations are assumed constant with time, i.e. no creep effects are taken into account. Moreover the material behavior is assumed to be hyperelastic, where the work done by the stresses during a deformation is dependent only of the initial and final states [59].

A laminate is defined as the group of two or more laminas or plies bonded together to act as an integral structural element [60]. For a laminate with plies of different materials stacked on top of each other the heterogeneity exists through the thickness. This chapter defines the elastic constants governing the mechanical behavior of a single ply (or lamina) and then the assembly of these laminas to give the laminate mechanical properties.

Concerning the different non-linear approximations used for the kinematic relations, Simitses et al. (1985) [62] presents a comparison between Donnell's (1934) [16] and Sanders' (1961) [63] non-linear equations for the buckling of axially compressed orthotropic cylinders under axisymmetric imperfections, and the general trend observed by the authors is that the Donnell's equations can overestimate the buckling load, especially for thinner and longer cylinders. Goldfeld et al. (2003) [64] extended the study of Simitses et al. [62] to isotropic conical shells and included in the comparison Timoshenko and Gere's non-linear kinematic equations [36], concluding that Sanders' equations already give an accuracy comparable to Timoshenko and Gere's equations. Goldfeld studies also supported the observation of Simitses that the more accurate non-linear equations give lower buckling load estimatives, though this difference is very small in most of the cases. Geier and Singh (1997) [65] are among the first authors to present a formulation for the linear

buckling loads of laminated composite cylinders and panels, developing the equations for thin and moderately thick shells, where the thick shell formulation is similar to the Sanders' equations. In 2007, Goldfeld [66] used a model with variable thickness for laminated composite cones and also verified that Donnell's equations can overestimate the buckling load and result in higher imperfection sensitivity, while more accurate models result in lower buckling loads and less imperfection sensitivity.

From the literature review described above it can be seen that the Sanders' equations already achieve a reasonable accuracy for the prediction of the imperfection sensitivity of thin-walled structures, and therefore the following discussion will develop non-linear equations using the terms corresponding to the Donnell's and the Sanders' assumptions.

2.1 Constitutive Equations

2.1.1 Stress-Strain Relations for Anisotropic Materials

The linear constitutive model for infinitesimal deformation is referred to as the generalized Hooke's law [59]. Considering an initial state of residual stress σ^0 , an infinitesimal increase in the applied loads will cause strains to develop and the related stresses are described by Eq. (2.1.1) [59].

$$\sigma_{ij} = C_{ijkl}\varepsilon_{kl} + \sigma_{ij}^0 \quad (2.1.1)$$

where σ_{ij}^0 represents the initial stresses, C_{ijkl} one element of the fourth order tensor C containing the material properties and ε_{kl} the corresponding strains. The fourth order tensor C of material properties is usually named stiffness tensor [59]. Assuming that each index i, j, k, ℓ can assume three values (one for each material direction shown in Fig. 2.1.1) mathematically the tensor C contains $3^4 = 81$ different scalars, but the number of independent components of C is considerably less. The symmetry of the stress tensor is necessary for the conservation of angular momentum, making $\sigma_{ij} = \sigma_{ji}$, reducing the number of independent scalars to $3! \times 3^2 = 6 \times 9 = 54$. The strain tensor is symmetric by its definition, making $\varepsilon_{kl} = \varepsilon_{\ell k}$, reducing C to a 6×6 matrix with 36 independent scalars [59].

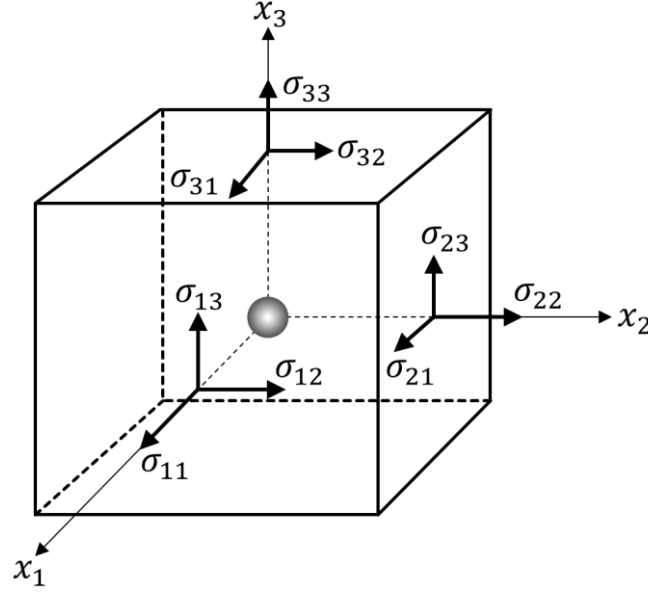


Fig. 2.1.1: Notation used for the stress components in Cartesian rectangular coordinates

Another equation is obtained from the assumption of material hyperelasticity. Equation (2.1.2) shows that $C_{ijkl} = C_{klij}$, reducing the number of independent material stiffness components to 21, as illustrated in the matrix representation of C :

$$\sigma_{ij} = \frac{\partial U_0}{\partial \varepsilon_{ij}} = C_{ijkl} \varepsilon_{kl} + \sigma_{ij}^0$$

$$\frac{\partial^2 U_0}{\partial \varepsilon_{ij} \partial \varepsilon_{kl}} = C_{ijkl} = \frac{\partial^2 U_0}{\partial \varepsilon_{kl} \partial \varepsilon_{ij}} = C_{klij}$$

$$\begin{Bmatrix} \sigma_{11} \\ \sigma_{22} \\ \sigma_{33} \\ \sigma_{23} \\ \sigma_{13} \\ \sigma_{12} \end{Bmatrix} = \begin{bmatrix} C_{1111} & C_{1122} & C_{1133} & C_{1123} & C_{1113} & C_{1112} \\ C_{2211} & C_{2222} & C_{2233} & C_{2223} & C_{2213} & C_{2212} \\ C_{3311} & C_{3322} & C_{3333} & C_{3323} & C_{3313} & C_{3312} \\ C_{2311} & C_{2322} & C_{2333} & C_{2323} & C_{2313} & C_{2312} \\ C_{1311} & C_{1322} & C_{1333} & C_{1323} & C_{1313} & C_{1312} \\ C_{1211} & C_{1222} & C_{1233} & C_{1223} & C_{1213} & C_{1212} \end{bmatrix} \begin{Bmatrix} \varepsilon_{11} \\ \varepsilon_{22} \\ \varepsilon_{33} \\ \varepsilon_{23} \\ \varepsilon_{13} \\ \varepsilon_{12} \end{Bmatrix} + \begin{Bmatrix} \sigma_{11}^0 \\ \sigma_{22}^0 \\ \sigma_{33}^0 \\ \sigma_{23}^0 \\ \sigma_{13}^0 \\ \sigma_{12}^0 \end{Bmatrix} \quad (2.1.2)$$

In Eq. (2.1.2) note the use of the strain energy density function $U_0(\varepsilon_{ij})$ to describe the energy state of the body, and this representation is possible for hyperelastic solids where the work done by the stresses during a deformation depends only on the initial and final states, not being relevant the path between the two states [59].

It is convenient to change the tensor notation to the engineering notation or the Voigt-Kelvin notation [59], which simplifies the indices as shown in Eq. (2.1.3). Along this text the indices 1,2,3 will be frequently called x, y, z , respectively when dealing with Cartesian coordinates and x, θ, z when dealing with Cylindrical coordinates. As emphasized by Reddy (2004) [59] the engineering notation renders the stiffness tensor, the strain tensor and the stress tensor to non-tensor components, which do not transform in the same way as the components of a vector or a tensor.

$$\begin{aligned}
\sigma_{11} &= \sigma_{xx} = \sigma_1 & \sigma_{22} &= \sigma_{yy} = \sigma_2 & \sigma_{33} &= \sigma_{zz} = \sigma_3 \\
\sigma_{23} &= \sigma_{yz} = \sigma_4 & \sigma_{13} &= \sigma_{xz} = \sigma_5 & \sigma_{12} &= \sigma_{xy} = \sigma_6 \\
\varepsilon_{11} &= \varepsilon_{xx} = \varepsilon_1 & \varepsilon_{22} &= \varepsilon_{yy} = \varepsilon_2 & \varepsilon_{33} &= \varepsilon_{zz} = \varepsilon_3 \\
2\varepsilon_{23} &= \gamma_{23} = \gamma_{yz} = \varepsilon_4 & 2\varepsilon_{13} &= \gamma_{13} = \gamma_{xz} = \varepsilon_5 & 2\varepsilon_{12} &= \gamma_{12} = \gamma_{xy} = \varepsilon_6
\end{aligned}$$

$$\begin{Bmatrix} \sigma_1 \\ \sigma_2 \\ \sigma_3 \\ \sigma_4 \\ \sigma_5 \\ \sigma_6 \end{Bmatrix} = \begin{bmatrix} C_{11} & C_{12} & C_{13} & C_{14} & C_{15} & C_{16} \\ C_{12} & C_{22} & C_{23} & C_{24} & C_{25} & C_{26} \\ C_{13} & C_{23} & C_{33} & C_{34} & C_{35} & C_{36} \\ C_{14} & C_{24} & C_{34} & C_{44} & C_{45} & C_{46} \\ C_{15} & C_{25} & C_{35} & C_{45} & C_{55} & C_{56} \\ C_{16} & C_{26} & C_{36} & C_{46} & C_{56} & C_{66} \end{bmatrix} \begin{Bmatrix} \varepsilon_1 \\ \varepsilon_2 \\ \varepsilon_3 \\ \varepsilon_4 \\ \varepsilon_5 \\ \varepsilon_6 \end{Bmatrix} + \begin{Bmatrix} \sigma_1^0 \\ \sigma_2^0 \\ \sigma_3^0 \\ \sigma_4^0 \\ \sigma_5^0 \\ \sigma_6^0 \end{Bmatrix} \quad (2.1.3)$$

because of the conventions for $\varepsilon_4, \varepsilon_5, \varepsilon_6$ it follows that:

$$C_{k\ell[23,13,12]} = 2C_{i[4,5,6]}.$$

2.1.2 Stress-Strain Relations for Monoclinic Materials

Monoclinic materials are those with one plane of symmetry regarding the directional properties and it is important to understand this concept of symmetry for such materials before moving to the discussion about orthotropic materials.

Assuming the plane of symmetry to be $z = 0$ makes the transverse strains ε_4 and ε_5 decoupled with the normal stresses. Also, the shear strain parallel to the plane of symmetry ε_6 will not produce transversal stresses σ_4 and σ_5 . The resulting stiffness matrix is shown in Eq. (2.1.4), where there are 13 independent elastic constants that describe the material behavior.

$$\begin{Bmatrix} \sigma_1 \\ \sigma_2 \\ \sigma_3 \\ \sigma_4 \\ \sigma_5 \\ \sigma_6 \end{Bmatrix} = \begin{bmatrix} C_{11} & C_{12} & C_{13} & 0 & 0 & C_{16} \\ C_{12} & C_{22} & C_{23} & 0 & 0 & C_{26} \\ C_{13} & C_{23} & C_{33} & 0 & 0 & C_{36} \\ 0 & 0 & 0 & C_{44} & C_{45} & 0 \\ 0 & 0 & 0 & C_{45} & C_{55} & 0 \\ C_{16} & C_{26} & C_{36} & 0 & 0 & C_{66} \end{bmatrix} \begin{Bmatrix} \varepsilon_1 \\ \varepsilon_2 \\ \varepsilon_3 \\ \varepsilon_4 \\ \varepsilon_5 \\ \varepsilon_6 \end{Bmatrix} + \begin{Bmatrix} \sigma_1^0 \\ \sigma_2^0 \\ \sigma_3^0 \\ \sigma_4^0 \\ \sigma_5^0 \\ \sigma_6^0 \end{Bmatrix} \quad (2.1.4)$$

2.1.3 Stress-Strain Relations for Orthotropic Materials

Orthotropic materials are those with three mutually orthogonal planes of symmetry, and the reasoning applied for the monoclinic symmetry can be extended here, but in the orthotropic case all the shear strains are decoupled among each other and the normal stresses are only function of the normal strains. The orthotropic matrix is shown in Eq. (2.1.5), with 9 independent elastic constants to be determined.

$$\begin{Bmatrix} \sigma_1 \\ \sigma_2 \\ \sigma_3 \\ \sigma_4 \\ \sigma_5 \\ \sigma_6 \end{Bmatrix} = \begin{bmatrix} C_{11} & C_{12} & C_{13} & 0 & 0 & 0 \\ C_{12} & C_{22} & C_{23} & 0 & 0 & 0 \\ C_{13} & C_{23} & C_{33} & 0 & 0 & 0 \\ 0 & 0 & 0 & C_{44} & 0 & 0 \\ 0 & 0 & 0 & 0 & C_{55} & 0 \\ 0 & 0 & 0 & 0 & 0 & C_{66} \end{bmatrix} \begin{Bmatrix} \varepsilon_1 \\ \varepsilon_2 \\ \varepsilon_3 \\ \varepsilon_4 \\ \varepsilon_5 \\ \varepsilon_6 \end{Bmatrix} + \begin{Bmatrix} \sigma_1^0 \\ \sigma_2^0 \\ \sigma_3^0 \\ \sigma_4^0 \\ \sigma_5^0 \\ \sigma_6^0 \end{Bmatrix} \quad (2.1.5)$$

The three planes of symmetry that characterize an orthotropic material can be verified in a unidirectional or in a cross-ply (or woven) lamina, the latter only when the interwoven fibers are positioned orthogonally to each other. The material properties of a single orthotropic ply are determined in laboratory in terms of engineering constants such as Young's modulus, shear modulus and Poisson's ratios ([59], [60]). The strains can be readily expressed in terms of the stresses as shown in Eq. (2.1.6).

$$\begin{aligned} \varepsilon_1 &= \frac{\sigma_1}{E_1} - \frac{\nu_{21}\sigma_2}{E_2} - \frac{\nu_{31}\sigma_3}{E_3} & \varepsilon_4 &= 2\varepsilon_{23} = \frac{\sigma_{23}}{G_{23}} \\ \varepsilon_2 &= -\frac{\nu_{12}\sigma_1}{E_1} + \frac{\sigma_2}{E_2} - \frac{\nu_{32}\sigma_3}{E_3} & \varepsilon_5 &= 2\varepsilon_{13} = \frac{\sigma_{13}}{G_{13}} \\ \varepsilon_3 &= -\frac{\nu_{13}\sigma_1}{E_1} - \frac{\nu_{23}\sigma_2}{E_2} + \frac{\sigma_3}{E_3} & \varepsilon_6 &= 2\varepsilon_{12} = \frac{\sigma_{12}}{G_{12}} \end{aligned} \quad (2.1.6)$$

The constitutive matrix $[C]$ is assumed to be invertible so that the strains can be expressed in terms of the stresses, giving the compliance matrix $[S]$ ([59], [60]), shown in Eq. (2.1.11) for an orthotropic material. Writing the strain-stress relations in tensor notation gives:

$$\varepsilon_{ij} = S_{ijkl}\sigma_{kl} \quad (2.1.7)$$

or in engineering notation:

$$\varepsilon_i = S_{ij}\sigma_j \quad (2.1.8)$$

or in matrix notation:

$$\{\varepsilon\} = [S]\{\sigma\} \quad (2.1.9)$$

with:

$$\begin{aligned} \{\varepsilon\}^T &= \{\varepsilon_1 \quad \varepsilon_2 \quad \varepsilon_3 \quad \varepsilon_4 \quad \varepsilon_5 \quad \varepsilon_6\} \\ \{\sigma\}^T &= \{\sigma_1 \quad \sigma_2 \quad \sigma_3 \quad \sigma_{23} \quad \sigma_{13} \quad \sigma_{12}\} \end{aligned} \quad (2.1.10)$$

The matrix form of Eq. (2.1.9) will be adopted and the compliance matrix $[S]$ becomes:

$$[S] = \begin{bmatrix} S_{11} & S_{12} & S_{13} & 0 & 0 & 0 \\ S_{12} & S_{22} & S_{23} & 0 & 0 & 0 \\ S_{13} & S_{23} & S_{33} & 0 & 0 & 0 \\ 0 & 0 & 0 & S_{44} & 0 & 0 \\ 0 & 0 & 0 & 0 & S_{55} & 0 \\ 0 & 0 & 0 & 0 & 0 & S_{66} \end{bmatrix} = \begin{bmatrix} \frac{1}{E_1} & -\frac{\nu_{21}}{E_2} & -\frac{\nu_{31}}{E_3} & 0 & 0 & 0 \\ -\frac{\nu_{12}}{E_1} & \frac{1}{E_2} & -\frac{\nu_{32}}{E_3} & 0 & 0 & 0 \\ -\frac{\nu_{13}}{E_1} & -\frac{\nu_{23}}{E_2} & \frac{1}{E_3} & 0 & 0 & 0 \\ 0 & 0 & 0 & \frac{1}{G_{23}} & 0 & 0 \\ 0 & 0 & 0 & 0 & \frac{1}{G_{13}} & 0 \\ 0 & 0 & 0 & 0 & 0 & \frac{1}{G_{12}} \end{bmatrix} \quad (2.1.11)$$

From the symmetry of $[S]$ the following relations among the Poisson's ratios are obtained:

$$\frac{\nu_{12}}{E_1} = \frac{\nu_{21}}{E_2}; \quad \frac{\nu_{13}}{E_1} = \frac{\nu_{31}}{E_3}; \quad \frac{\nu_{23}}{E_2} = \frac{\nu_{32}}{E_3} \quad (2.1.12)$$

From Eq. (2.1.11) and Eq. (2.1.12) it can be seen that 9 independent engineering constants are sufficient to describe the behavior of an orthotropic lamina, which is in accordance with the number of independent terms in the stiffness matrix for the same type of material, as shown in Eq. (2.1.5). These terms can be related to the engineering constants by making $[C] = [S]^{-1}$, giving the relations shown in Eq. (2.1.13) ([59], [60]).

$$\begin{aligned} C_{11} &= \frac{S_{22}S_{33} - S_{23}^2}{S} = \frac{1 - \nu_{23}\nu_{32}}{E_2E_3\Delta} \\ C_{22} &= \frac{S_{33}S_{11} - S_{13}^2}{S} = \frac{1 - \nu_{13}\nu_{31}}{E_1E_3\Delta} \\ C_{33} &= \frac{S_{11}S_{22} - S_{12}^2}{S} = \frac{1 - \nu_{12}\nu_{21}}{E_1E_2\Delta} \\ C_{44} &= \frac{1}{S_{44}} = G_{23}; \quad C_{55} = \frac{1}{S_{55}} = G_{13}; \quad C_{66} = \frac{1}{S_{66}} = G_{12} \\ C_{12} &= \frac{S_{13}S_{23} - S_{12}S_{33}}{S} = \frac{\nu_{21} + \nu_{31}\nu_{23}}{E_2E_3\Delta} = \frac{\nu_{12} + \nu_{32}\nu_{13}}{E_1E_3\Delta} \\ C_{13} &= \frac{S_{12}S_{23} - S_{13}S_{22}}{S} = \frac{\nu_{31} + \nu_{21}\nu_{32}}{E_2E_3\Delta} = \frac{\nu_{13} + \nu_{12}\nu_{23}}{E_1E_2\Delta} \\ C_{23} &= \frac{S_{12}S_{13} - S_{23}S_{11}}{S} = \frac{\nu_{32} + \nu_{12}\nu_{31}}{E_1E_3\Delta} = \frac{\nu_{23} + \nu_{21}\nu_{13}}{E_1E_2\Delta} \end{aligned} \quad (2.1.13)$$

Jones [60] discusses further simplifications of the elastic constants for unidirectionally reinforced laminas based on the physical symmetry of the fibers and the matrix, enabling one to treat the 3rd direction as being equivalent to the 2nd direction, and vice-versa, based on the observation that both are transverse to the fibers. Such simplifications are shown in Eq. (2.1.12).

$$\begin{aligned} E_3 &= E_2 \\ \nu_{31} &= \nu_{21} \\ G_{13} &= G_{12} \end{aligned} \quad (2.1.14)$$

In the assumption of Eq. (2.1.12) note that plane 23 becomes an isotropic plane, either for a regular or a random fiber-distribution in the lamina. In practice there will be a slight difference between the material properties along directions 2 and 3 after curing, because the lamina is compacted in the 3rd direction in most of the manufacturing processes, but this effect has a minor influence on the mechanical properties and therefore it is generally neglected due to the great simplification obtained.

2.1.4 Laminate Equations

When the laminas are stacked upon each other they do not necessarily keep their 1st direction aligned with the laminate 1st direction. As a convention, the laminate 1,2,3 directions will be called x, y, z , while the 1,2,3 directions of a given layer will be called x_1, x_2 and x_3 . The corresponding basis vectors of each coordinate system are $\hat{e}_x, \hat{e}_y, \hat{e}_z$ for the laminate and $\hat{e}_1, \hat{e}_2, \hat{e}_3$ for the lamina. This convention is based on Reddy (2004) [59]. It is assumed that the z directions are always parallel throughout this discussion.

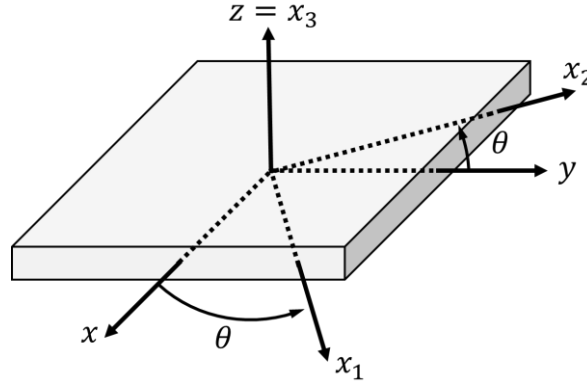


Fig. 2.1.2: Ply and laminate coordinate systems

In Fig. 2.1.2 it is shown how the ply coordinate system is positioned about the laminate coordinate system, from where the following relations can be obtained:

$$\begin{aligned} \begin{Bmatrix} x_1 \\ x_2 \\ x_3 \end{Bmatrix} &= \begin{bmatrix} \cos \theta & \sin \theta & 0 \\ -\sin \theta & \cos \theta & 0 \\ 0 & 0 & 1 \end{bmatrix} \begin{Bmatrix} x \\ y \\ z \end{Bmatrix} = [L] \begin{Bmatrix} x \\ y \\ z \end{Bmatrix} \\ \begin{Bmatrix} \hat{e}_1 \\ \hat{e}_2 \\ \hat{e}_3 \end{Bmatrix} &= [L] \begin{Bmatrix} \hat{e}_x \\ \hat{e}_y \\ \hat{e}_z \end{Bmatrix}; \quad \begin{Bmatrix} \hat{e}_x \\ \hat{e}_y \\ \hat{e}_z \end{Bmatrix} = [L]^T \begin{Bmatrix} \hat{e}_1 \\ \hat{e}_2 \\ \hat{e}_3 \end{Bmatrix} \end{aligned} \quad (2.1.15)$$

with:

$$[L]^T = [L]^{-1}$$

The transformation shown in Eq. (2.1.15) is a vector transformation, or a first order tensor transformation, where the stress transformation from one coordinate system to another can be performed using the second-order tensor transformation shown in Eq. (2.1.16). Note that the Einstein summation convention is applied for the repeated indices. The subscript “lam” stands for laminate.

$$(\sigma_{kq})_{ply} = \ell_{ki} \ell_{qj} (\sigma_{ij})_{lam}; \quad (\sigma_{kq})_{lam} = \ell_{ik} \ell_{jq} (\sigma_{ij})_{ply} \quad (2.1.16)$$

As already commented, the use of non-tensor components when adopting the engineering notation do not allow a tensor transformations such as the one shown in Eq. (2.1.16) [59]. The interchangeability of indices ℓ_{ki} to ℓ_{ik} and ℓ_{qj} to ℓ_{jq} when passing from one coordinate system to another is valid because $[L]^T = [L]^{-1}$. Expanding Eq. (2.1.16) for one stress component to illustrate how the second-order tensor operates gives:

$$\begin{aligned} (\sigma_{kq})_{laminar} &= \ell_{ik} \ell_{jq} (\sigma_{ij})_{ply} \\ (\sigma_{11})_{laminar} &= \ell_{11} \ell_{11} (\sigma_{11})_{ply} + \ell_{11} \ell_{21} (\sigma_{12})_{ply} + \ell_{21} \ell_{11} (\sigma_{21})_{ply} + \ell_{21} \ell_{21} (\sigma_{22})_{ply} \\ (\sigma_{11})_{laminar} &= \cos^2 \theta (\sigma_{11})_{ply} - \cos \theta \sin \theta (\sigma_{12})_{ply} - \sin \theta \cos \theta (\sigma_{21})_{ply} + \sin^2 \theta (\sigma_{22})_{ply} \\ (\sigma_{11})_{laminar} &= \cos^2 \theta (\sigma_{11})_{ply} - \sin 2\theta (\sigma_{12})_{ply} + \sin^2 \theta (\sigma_{22})_{ply} \end{aligned} \quad (2.1.17)$$

Applying the same procedure shown in Eq. (2.1.17) for all the stress components will results in the following transformation matrices:

$$\begin{aligned} \begin{Bmatrix} \sigma_{xx} \\ \sigma_{yy} \\ \sigma_{zz} \\ \sigma_{yz} \\ \sigma_{xz} \\ \sigma_{xy} \end{Bmatrix}_{lam} &= \begin{bmatrix} \cos^2 \theta & \sin^2 \theta & 0 & 0 & 0 & -\sin 2\theta \\ \sin^2 \theta & \cos^2 \theta & 0 & 0 & 0 & \sin 2\theta \\ 0 & 0 & 1 & 0 & 0 & 0 \\ 0 & 0 & 0 & \cos \theta & \sin \theta & 0 \\ 0 & 0 & 0 & -\sin \theta & \cos \theta & 0 \\ \sin \theta \cos \theta & -\sin \theta \cos \theta & 0 & 0 & 0 & \cos^2 \theta - \sin^2 \theta \end{bmatrix} \begin{Bmatrix} \sigma_{11} \\ \sigma_{22} \\ \sigma_{33} \\ \sigma_{23} \\ \sigma_{13} \\ \sigma_{12} \end{Bmatrix}_{ply} \\ \begin{Bmatrix} \sigma_{11} \\ \sigma_{22} \\ \sigma_{33} \\ \sigma_{23} \\ \sigma_{13} \\ \sigma_{12} \end{Bmatrix}_{ply} &= \begin{bmatrix} \cos^2 \theta & \sin^2 \theta & 0 & 0 & 0 & \sin 2\theta \\ \sin^2 \theta & \cos^2 \theta & 0 & 0 & 0 & -\sin 2\theta \\ 0 & 0 & 1 & 0 & 0 & 0 \\ 0 & 0 & 0 & \cos \theta & -\sin \theta & 0 \\ 0 & 0 & 0 & \sin \theta & \cos \theta & 0 \\ -\sin \theta \cos \theta & \sin \theta \cos \theta & 0 & 0 & 0 & \cos^2 \theta - \sin^2 \theta \end{bmatrix} \begin{Bmatrix} \sigma_{xx} \\ \sigma_{yy} \\ \sigma_{zz} \\ \sigma_{yz} \\ \sigma_{xz} \\ \sigma_{xy} \end{Bmatrix}_{lam} \\ \{\sigma\}_{lam} &= [T] \{\sigma\}_{ply} \\ \{\sigma\}_{ply} &= [T]^{-1} \{\sigma\}_{lam} = [R] \{\sigma\}_{lam} \end{aligned} \quad (2.1.18)$$

Since the strains are also second-order tensors, a similar transformation derived for stresses can be used for strains. However, the original strain vector has been changed when adopting the engineering notation:

$$2\varepsilon_{23} = \gamma_{23} = \gamma_{yz} = \varepsilon_4; \quad 2\varepsilon_{13} = \gamma_{13} = \gamma_{xz} = \varepsilon_5; \quad 2\varepsilon_{12} = \gamma_{12} = \gamma_{xy} = \varepsilon_6 \quad (2.1.19)$$

making necessary some changes in the transformation matrices of Eq. (2.1.18) to be applicable for strains [59]. The transformation matrices for strains are given below. It can be seen their relation with the stress transformation matrices.

$$\begin{aligned}
\begin{Bmatrix} \varepsilon_{xx} \\ \varepsilon_{yy} \\ \varepsilon_{zz} \\ 2\varepsilon_{yz} \\ 2\varepsilon_{xz} \\ 2\varepsilon_{xy} \end{Bmatrix}_{lam} &= \begin{bmatrix} \cos^2 \theta & \sin^2 \theta & 0 & 0 & 0 & -\sin \theta \cos \theta \\ \sin^2 \theta & \cos^2 \theta & 0 & 0 & 0 & \sin \theta \cos \theta \\ 0 & 0 & 1 & 0 & 0 & 0 \\ 0 & 0 & 0 & \cos \theta & \sin \theta & 0 \\ 0 & 0 & 0 & -\sin \theta & \cos \theta & 0 \\ \sin 2\theta & -\sin 2\theta & 0 & 0 & 0 & \cos^2 \theta - \sin^2 \theta \end{bmatrix} \begin{Bmatrix} \varepsilon_{11} \\ \varepsilon_{22} \\ \varepsilon_{33} \\ \varepsilon_{23} \\ \varepsilon_{13} \\ \varepsilon_{12} \end{Bmatrix}_{ply} \\
\begin{Bmatrix} \varepsilon_{11} \\ \varepsilon_{22} \\ \varepsilon_{33} \\ \varepsilon_{23} \\ \varepsilon_{13} \\ \varepsilon_{12} \end{Bmatrix}_{ply} &= \begin{bmatrix} \cos^2 \theta & \sin^2 \theta & 0 & 0 & 0 & \sin \theta \cos \theta \\ \sin^2 \theta & \cos^2 \theta & 0 & 0 & 0 & -\sin \theta \cos \theta \\ 0 & 0 & 1 & 0 & 0 & 0 \\ 0 & 0 & 0 & \cos \theta & -\sin \theta & 0 \\ 0 & 0 & 0 & \sin \theta & \cos \theta & 0 \\ -\sin 2\theta & \sin 2\theta & 0 & 0 & 0 & \cos^2 \theta - \sin^2 \theta \end{bmatrix} \begin{Bmatrix} \varepsilon_{xx} \\ \varepsilon_{yy} \\ \varepsilon_{zz} \\ 2\varepsilon_{yz} \\ 2\varepsilon_{xz} \\ 2\varepsilon_{xy} \end{Bmatrix}_{lam} \\
\{\varepsilon\}_{lam} &= [R]^T \{\varepsilon\}_{ply} \\
\{\varepsilon\}_{ply} &= [T]^T \{\varepsilon\}_{lam}
\end{aligned} \tag{2.1.20}$$

Writing the stresses as a function of the strains in matrix form makes it clear how to obtain the coordinate transformation $ply \leftrightarrow lam$ for the stiffness tensor:

$$\begin{aligned}
\{\sigma\}_{lam} &= [C]_{lam} \{\varepsilon\}_{lam} & \{\sigma\}_{ply} &= [C]_{ply} \{\varepsilon\}_{ply} \\
[T] \{\sigma\}_{ply} &= [C]_{lam} [R]^T \{\varepsilon\}_{ply} & [R] \{\sigma\}_{lam} &= [C]_{ply} [T]^T \{\varepsilon\}_{lam} \\
\{\sigma\}_{ply} &= [R] [C]_{lam} [R]^T \{\varepsilon\}_{ply} & \{\sigma\}_{lam} &= [T] [C]_{ply} [T]^T \{\varepsilon\}_{lam} \\
\text{but:} & & \text{but:} & \\
\{\sigma\}_{ply} &= [C]_{ply} \{\varepsilon\}_{ply} & \{\sigma\}_{lam} &= [C]_{lam} \{\varepsilon\}_{lam} \\
\text{giving:} & & \text{giving:} & \\
[C]_{ply} &= [R] [C]_{lam} [R]^T & [C]_{lam} &= [T] [C]_{ply} [T]^T \\
[C] &= [R] [\bar{C}] [R]^T & [\bar{C}] &= [C]_{lam}
\end{aligned} \tag{2.1.21}$$

The same transformation scheme is applicable to the plane stress-reduced stiffnesses Q_{ij} . The original $[T]$ and $[R]$ matrices must be changed to account for the plane-stress state, removing the 3rd row and the 3rd column, and moving the original 4th and 5th rows and columns to the last positions, in order to cope with the definition of $[Q]$ of Eq. (2.2.4), and the resulting transformation matrices are:

$$\begin{aligned}
T_Q &= \begin{bmatrix} \cos^2 \theta & \sin^2 \theta & -\sin 2\theta & 0 & 0 \\ \sin^2 \theta & \cos^2 \theta & \sin 2\theta & 0 & 0 \\ \sin \theta \cos \theta & -\sin \theta \cos \theta & \cos^2 \theta - \sin^2 \theta & 0 & 0 \\ 0 & 0 & 0 & \cos \theta & \sin \theta \\ 0 & 0 & 0 & -\sin \theta & \cos \theta \end{bmatrix} \\
R_Q &= \begin{bmatrix} \cos^2 \theta & \sin^2 \theta & \sin 2\theta & 0 & 0 \\ \sin^2 \theta & \cos^2 \theta & -\sin 2\theta & 0 & 0 \\ -\sin \theta \cos \theta & \sin \theta \cos \theta & \cos^2 \theta - \sin^2 \theta & 0 & 0 \\ 0 & 0 & 0 & \cos \theta & -\sin \theta \\ 0 & 0 & 0 & \sin \theta & \cos \theta \end{bmatrix} \quad (2.1.22) \\
[Q]_{ply} &= [R_Q][Q]_{lam}[R_Q]^T & [Q]_{lam} &= [T_Q][Q]_{ply}[T_Q]^T \\
[Q] &= [R_Q][\bar{Q}][R_Q]^T & [\bar{Q}] &= [T_Q][Q][T_Q]^T
\end{aligned}$$

The modified transformation matrices $[T_Q]$ and $[R_Q]$ of Eq. (2.1.22) can be directly used to for the plane-stress case. The calculated \bar{Q}_{ij} terms are [59]:

$$\begin{aligned}
\bar{Q}_{11} &= Q_{11} \cos^4 \theta + 2(Q_{12} + 2Q_{66}) \sin^2 \theta \cos^2 \theta + Q_{22} \sin^4 \theta \\
\bar{Q}_{12} &= (Q_{11} + Q_{22} - 4Q_{66}) \sin^2 \theta \cos^2 \theta + Q_{12}(\sin^4 \theta + \cos^4 \theta) \\
\bar{Q}_{22} &= Q_{11} \sin^4 \theta + 2(Q_{12} + 2Q_{66}) \sin^2 \theta \cos^2 \theta + Q_{22} \cos^4 \theta \\
\bar{Q}_{16} &= (Q_{11} - Q_{12} - 2Q_{66}) \sin \theta \cos^3 \theta + (Q_{12} - Q_{22} + 2Q_{66}) \sin^3 \theta \cos \theta \\
\bar{Q}_{26} &= (Q_{11} - Q_{12} - 2Q_{66}) \sin^3 \theta \cos \theta + (Q_{12} - Q_{22} + 2Q_{66}) \sin \theta \cos^3 \theta \\
\bar{Q}_{66} &= (Q_{11} + Q_{22} - 2Q_{12} - 2Q_{66}) \sin^2 \theta \cos^2 \theta + Q_{66}(\sin^4 \theta + \cos^4 \theta) \\
\bar{Q}_{44} &= Q_{44} \cos^2 \theta + Q_{55} \sin^2 \theta \\
\bar{Q}_{45} &= (Q_{55} - Q_{44}) \cos \theta \sin \theta \\
\bar{Q}_{55} &= Q_{55} \cos^2 \theta + Q_{44} \sin^2 \theta
\end{aligned} \quad (2.1.23)$$

The force and moment resultants acting on an infinitesimal part of the laminate under plane-stress conditions are illustrated in Fig. 2.1.3. The quantities $N_{xx}, N_{yy}, N_{xy}, Q_x, Q_y$ are measured as force per unit length (e.g. N/m), while the quantities M_{xx}, M_{yy}, M_{xy} are measured as force times unit length per unit length (e.g. $N \cdot m/m$).

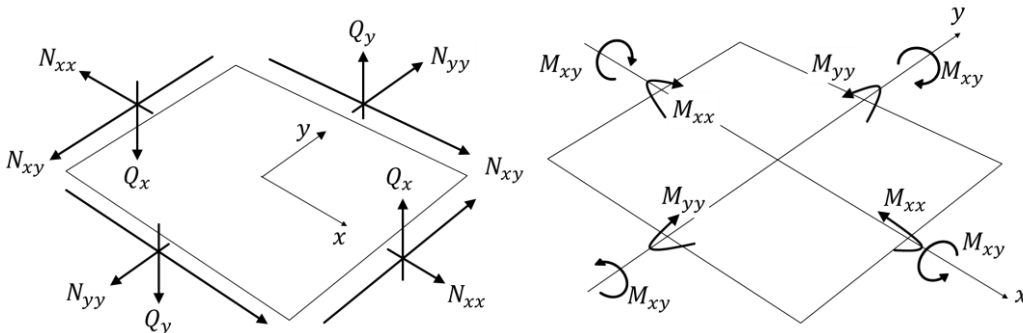


Fig. 2.1.3: Force and moment resultants on a plate element

The distributed forces and moments are directly related to the stresses acting on the plate element, and also on the shell element assuming that the Donnell's assumption of *radius* \gg *thickness* is valid, as explained in Eq. (2.2.17), leading to following integrals ([59], [60]):

$$\begin{aligned}
 N_{xx} &= \int_{-\frac{t}{2}}^{\frac{t}{2}} \sigma_{xx} dz; & N_{yy} &= \int_{-\frac{t}{2}}^{\frac{t}{2}} \sigma_{yy} dz; & N_{xy} &= \int_{-\frac{t}{2}}^{\frac{t}{2}} \sigma_{xy} dz \\
 Q_y &= \int_{-\frac{t}{2}}^{\frac{t}{2}} \sigma_{yz} dz; & Q_x &= \int_{-\frac{t}{2}}^{\frac{t}{2}} \sigma_{xz} dz \\
 M_{xx} &= \int_{-\frac{t}{2}}^{\frac{t}{2}} \sigma_{xx} z dz; & M_{yy} &= \int_{-\frac{t}{2}}^{\frac{t}{2}} \sigma_{yy} z dz; & M_{xy} &= \int_{-\frac{t}{2}}^{\frac{t}{2}} \sigma_{xy} z dz \\
 M_{yz} &= \int_{-\frac{t}{2}}^{\frac{t}{2}} \sigma_{yz} z dz; & M_{xz} &= \int_{-\frac{t}{2}}^{\frac{t}{2}} \sigma_{xz} z dz
 \end{aligned} \tag{2.1.24}$$

The integration is significantly simplified by assuming a constant stiffness through each ply, which is true unless the ply has temperature-dependent or moisture-dependent properties and a temperature or a moisture gradient exists across the ply [60]. In the present study no hygrothermal effects are being considered, such that this assumption holds true. Rewriting the integrals in Eq. (2.1.24) in terms of the strains using Eq. (2.2.4) and then transforming the plane-stress stiffness terms to the laminate coordinate system using Eq. (2.1.22) or Eq. (2.1.23) the following relations are obtained:

$$\begin{Bmatrix} N_{xx} \\ N_{yy} \\ N_{xy} \\ Q_y \\ Q_x \end{Bmatrix} = \sum_{k=1}^N \begin{bmatrix} \bar{Q}_{11} & \bar{Q}_{12} & \bar{Q}_{16} & 0 & 0 \\ \bar{Q}_{12} & \bar{Q}_{22} & \bar{Q}_{26} & 0 & 0 \\ \bar{Q}_{16} & \bar{Q}_{26} & \bar{Q}_{66} & 0 & 0 \\ 0 & 0 & 0 & \bar{Q}_{44} & \bar{Q}_{45} \\ 0 & 0 & 0 & \bar{Q}_{45} & \bar{Q}_{55} \end{bmatrix}^{(k)} \int_{z_k}^{z_{k+1}} \begin{Bmatrix} \varepsilon_{xx} \\ \varepsilon_{yy} \\ \varepsilon_{xy} \\ \varepsilon_{yz} \\ \varepsilon_{xz} \end{Bmatrix}^{(k)} dz \tag{2.1.25}$$

$$\begin{Bmatrix} M_{xx} \\ M_{yy} \\ M_{xy} \\ M_{yz} \\ M_{xz} \end{Bmatrix} = \sum_{k=1}^N \begin{bmatrix} \bar{Q}_{11} & \bar{Q}_{12} & \bar{Q}_{16} & 0 & 0 \\ \bar{Q}_{12} & \bar{Q}_{22} & \bar{Q}_{26} & 0 & 0 \\ \bar{Q}_{16} & \bar{Q}_{26} & \bar{Q}_{66} & 0 & 0 \\ 0 & 0 & 0 & \bar{Q}_{44} & \bar{Q}_{45} \\ 0 & 0 & 0 & \bar{Q}_{45} & \bar{Q}_{55} \end{bmatrix}^{(k)} \int_{z_k}^{z_{k+1}} z \begin{Bmatrix} \varepsilon_{xx} \\ \varepsilon_{yy} \\ \varepsilon_{xy} \\ \varepsilon_{yz} \\ \varepsilon_{xz} \end{Bmatrix}^{(k)} dz \tag{2.1.26}$$

where z_k and z_{k+1} are the position at the z coordinate of at bottom and at the top of each ply, respectively. Note that if the stiffness cannot be assumed constant within the ply, the $[\bar{Q}]$ matrix cannot be moved outside the integral.

2.2 Kinematics Equations for Conical and Cylindrical Shells

The kinematic equations are those describing how the strains develop in a material body under a given displacement field caused by a set of applied loads. Along this section the general Green-Lagrange strain tensor and the non-linear strain equations are presented and used to derive the conical equations, which contain the cylindrical equations as a particular case. An overview about kinematic equations for composite laminates using different theories will be given, some of the most important Equivalent Single Layer Theories used to impose approximations concerning the displacements and rotations will be discussed: the Classical Laminated Plate Theory (CLPT) and the First-order Shear Deformation Theory (FSDT); formulated in details and used to achieve the non-linear kinematic equations. First the FSDT equations will be obtained, and then used to obtain the CLPT equations as a special case. The non-linear terms belonging to the Donnell's and Sanders' equations will be identified and the kinematic equations for these two non-linear theories will be further developed in matrix form in order to be used along the subsequent chapters.

2.2.1 Plane-Stress Relations for Orthotropic Materials

The analysis of unidirectionally reinforced laminas or woven fabrics with orthogonal weaving direction is simplified by assuming a plane-stress state, which can be expressed as:

$$\sigma_3 = \sigma_{33} = 0; \quad \sigma_4 = \sigma_{23} = 0; \quad \sigma_5 = \sigma_{13} = 0 \quad (2.2.1)$$

As explained by Jones [60] this simplification is a reasonable assumption since most laminates are designed to carry loads that lie in the direction of the reinforcing fibers and in most applications normal stresses such as σ_3 are unnatural conditions that are not efficiently withstood by the materials usually applied as laminas. The following relations are obtained:

$$\varepsilon_3 = -\frac{\nu_{13}\sigma_1}{E_1} - \frac{\nu_{23}\sigma_2}{E_2}; \quad \gamma_{23} = 0; \quad \gamma_{13} = 0 \quad (2.2.2)$$

making simpler the strain-stress relations of Eq. (2.1.11):

$$\begin{aligned} \begin{Bmatrix} \varepsilon_1 \\ \varepsilon_2 \\ \varepsilon_6 \end{Bmatrix} &= \begin{bmatrix} S_{11} & S_{12} & 0 \\ S_{12} & S_{22} & 0 \\ 0 & 0 & S_{66} \end{bmatrix} \begin{Bmatrix} \sigma_1 \\ \sigma_2 \\ \sigma_6 \end{Bmatrix} \\ S_{11} &= \frac{1}{E_1}; \quad S_{12} = -\frac{\nu_{12}}{E_1} = -\frac{\nu_{21}}{E_2}; \quad S_{22} = \frac{1}{E_2}; \quad S_{66} = \frac{1}{G_{12}} \end{aligned} \quad (2.2.3)$$

In Equations (2.2.1), (2.2.2) and (2.2.3) a full state of plane-stress is assumed where the transverse shear quantities σ_{23} and σ_{13} are ignored. This assumption holds, for example, when the Classical Laminated Plate Theory (CLPT) is adopted, as discussed in Section 2.2.3. Since the First-order Shear Deformation Theory (FSDT) will also be used along this thesis, where this pure state of plane-stress does not hold, the kinematic equations will be developed for the more general case considering the transverse shear components $\sigma_{23}, \sigma_{13}, \gamma_{23}$ and γ_{13} . For an orthotropic lamina, the stress-strain relations for the plane-stress case with transverse shear included are obtained by

inverting the following strain-stress relations. The Q_{ij} values are called plane stress-reduced stiffnesses [59].

$$\begin{aligned}
 \begin{Bmatrix} \sigma_1 \\ \sigma_2 \\ \sigma_6 \\ \sigma_4 \\ \sigma_5 \end{Bmatrix} &= \begin{bmatrix} Q_{11} & Q_{12} & 0 & 0 & 0 \\ Q_{12} & Q_{22} & 0 & 0 & 0 \\ 0 & 0 & Q_{66} & 0 & 0 \\ 0 & 0 & 0 & Q_{44} & 0 \\ 0 & 0 & 0 & 0 & Q_{55} \end{bmatrix} \begin{Bmatrix} \varepsilon_1 \\ \varepsilon_2 \\ \varepsilon_6 \\ \varepsilon_4 \\ \varepsilon_5 \end{Bmatrix} & \quad \begin{aligned} Q_{11} &= \frac{E_1}{1 - \nu_{12}\nu_{21}} \\ Q_{12} &= \frac{\nu_{12}E_2}{1 - \nu_{12}\nu_{21}} \\ Q_{22} &= \frac{E_2}{1 - \nu_{12}\nu_{21}} \\ Q_{66} &= G_{12} \\ Q_{44} &= G_{23} \\ Q_{55} &= G_{13} \end{aligned} \\
 \begin{Bmatrix} \sigma_1 \\ \sigma_2 \\ \sigma_6 \\ \sigma_4 \\ \sigma_5 \end{Bmatrix} &= [Q] \begin{Bmatrix} \varepsilon_1 \\ \varepsilon_2 \\ \varepsilon_6 \\ \varepsilon_4 \\ \varepsilon_5 \end{Bmatrix}; \quad \text{or} \quad \begin{Bmatrix} \sigma_{xx} \\ \sigma_{yy} \\ \sigma_{xy} \\ \sigma_{yz} \\ \sigma_{xz} \end{Bmatrix} = [Q] \begin{Bmatrix} \varepsilon_{xx} \\ \varepsilon_{yy} \\ \varepsilon_{xy} \\ \varepsilon_{yz} \\ \varepsilon_{xz} \end{Bmatrix} & \quad (2.2.4)
 \end{aligned}$$

The stress and strain vectors were rearranged to keep the terms related to transverse shear easier to separate during the analyses where the transverse shear is ignored. This convenience will become clearer in the discussion presented in Section 2.2.3 about the Classical Laminated Plate Theory and the Shear Deformation Theories.

2.2.2 Strain-Displacement Relations for Cones and Cylinders

Zhang (1993) [67] presents a throughout review about the many different shell theories. Hadi and Ameen 2011 [68] present a complete set of non-linear equations for shells with double curvature. According to the three-dimensional elasticity theory [69], the strain components referred to an arbitrary orthogonal coordinate system $(\alpha_1, \alpha_2, \alpha_3)$ can be written as (modified from Zhang, 1993 [67]):

$$\begin{aligned}
 \epsilon_{11} &= \frac{1}{2 \left(\left(\frac{e_{13}}{2} - \omega_2 \right)^2 + \left(\frac{e_{12}}{2} + \omega_3 \right)^2 + e_{11}^2 \right)} + e_{11} \\
 \epsilon_{22} &= \frac{1}{2} \left(\left(\frac{e_{23}}{2} + \omega_1 \right)^2 + \left(\frac{e_{12}}{2} - \omega_3 \right)^2 + e_{22}^2 \right) + e_{22} \\
 \epsilon_{33} &= \frac{1}{2} \left(\left(\frac{e_{23}}{2} - \omega_1 \right)^2 + \left(\frac{e_{13}}{2} + \omega_2 \right)^2 + e_{33}^2 \right) + e_{33} \\
 \epsilon_{12} &= \left(\frac{e_{23}}{2} + \omega_1 \right) \left(\frac{e_{13}}{2} - \omega_2 \right) + e_{11} \left(\frac{e_{12}}{2} - \omega_3 \right) + e_{22} \left(\frac{e_{12}}{2} + \omega_3 \right) + e_{12} \\
 \epsilon_{13} &= e_{33} \left(\frac{e_{13}}{2} - \omega_2 \right) + e_{11} \left(\frac{e_{13}}{2} + \omega_2 \right) + \left(\frac{e_{23}}{2} - \omega_1 \right) \left(\frac{e_{12}}{2} + \omega_3 \right) + e_{13} \\
 \epsilon_{23} &= e_{22} \left(\frac{e_{23}}{2} - \omega_1 \right) + e_{33} \left(\frac{e_{23}}{2} + \omega_1 \right) + \left(\frac{e_{13}}{2} + \omega_2 \right) \left(\frac{e_{12}}{2} - \omega_3 \right) + e_{23}
 \end{aligned} \quad (2.2.5)$$

where the parameters e_{ij} and ω_i are (the conventional notation for partial derivatives $\partial/\partial x$ is used here for the sake of clarity):

$$\begin{aligned}
e_{11} &:= \frac{\partial u}{\partial x_1} + \frac{v}{H_1 H_2} \frac{\partial H_1}{\partial x_2} + \frac{w}{H_1 H_3} \frac{\partial H_1}{\partial x_3} & \omega_1 &:= \frac{\frac{\partial(H_3 w)}{\partial x_2} - \frac{\partial(H_2 v)}{\partial x_3}}{2(H_2 H_3)} \\
e_{22} &:= \frac{u}{H_1 H_2} \frac{\partial H_2}{\partial x_1} + \frac{\partial v}{\partial x_2} + \frac{w}{H_2 H_3} \frac{\partial H_2}{\partial x_3} & \omega_2 &:= \frac{\frac{\partial(H_1 u)}{\partial x_3} - \frac{\partial(H_3 w)}{\partial x_1}}{2(H_1 H_3)} \\
e_{33} &:= \frac{u}{H_1 H_3} \frac{\partial H_3}{\partial x_1} + \frac{v}{H_2 H_3} \frac{\partial H_3}{\partial x_2} + \frac{\partial w}{\partial x_3} & \omega_3 &:= \frac{\frac{\partial(H_2 v)}{\partial x_1} - \frac{\partial(H_1 u)}{\partial x_2}}{2(H_1 H_2)} \\
e_{12} &:= \frac{H_1}{H_2} \frac{\partial}{\partial x_2} \left(\frac{u}{H_1} \right) + \frac{H_2}{H_1} \frac{\partial}{\partial x_1} \left(\frac{v}{H_2} \right) \\
e_{13} &:= \frac{H_1}{H_3} \frac{\partial}{\partial x_3} \left(\frac{u}{H_1} \right) + \frac{H_3}{H_1} \frac{\partial}{\partial x_1} \left(\frac{w}{H_3} \right) \\
e_{23} &:= \frac{H_2}{H_3} \frac{\partial}{\partial x_3} \left(\frac{v}{H_2} \right) + \frac{H_3}{H_2} \frac{\partial}{\partial x_2} \left(\frac{w}{H_3} \right)
\end{aligned} \tag{2.2.6}$$

with u, v, w being the displacements along directions $\alpha_1, \alpha_2, \alpha_3$, respectively; and H_1, H_2, H_3 are the Lamé coefficients, defined as:

$$\begin{aligned}
H_1 &= \sqrt{(X_{1,x_1})^2 + (X_{2,x_1})^2 + (X_{3,x_1})^2} \\
H_2 &= \sqrt{(X_{1,x_2})^2 + (X_{2,x_2})^2 + (X_{3,x_2})^2} \\
H_3 &= \sqrt{(X_{1,x_3})^2 + (X_{2,x_3})^2 + (X_{3,x_3})^2}
\end{aligned} \tag{2.2.7}$$

The kinematic equations given by Eqs. (2.2.5)–(2.2.7) are general for any orthogonal curvilinear coordinate system and therefore they can be used to obtain the conical /cylindrical shell equations. Functions $X_1, X_2, X_3 = f(x_1, x_2, x_3)$ can be determined from Fig. 2.2.1, where the adopted coordinate system is a modified version of Shadmehri (2012) ([70], [71]), such that the origin of the x axis starts at the top radius instead of at the cone vertex, allowing an easier change to the cylindrical case, where $\alpha = 0$. This convention is close to the one adopted by Barbero & Reddy (1990) [72] for cylindrical shells. Another convention for conical shells may be found in Tong & Wang (1992) [73]. The coordinate transformations are defined in Eq. (2.2.8).

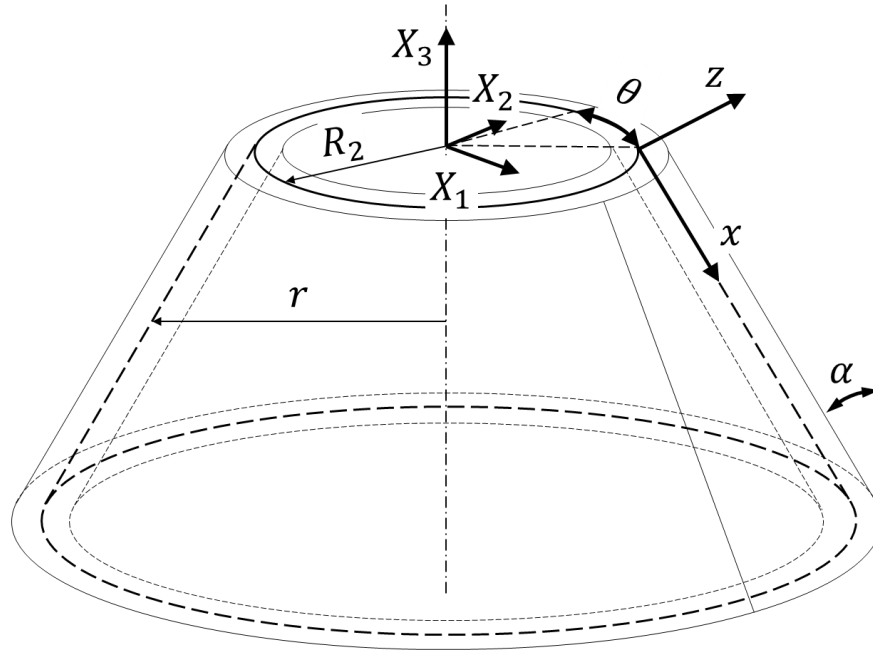


Fig. 2.2.1: Coordinate system used for the derivation of the shell equations

$$\begin{aligned}
 x_1 &= x & X_1 &= R(x, z) \cos \theta \\
 x_2 &= \theta & X_2 &= R(x, z) \sin \theta \\
 x_3 &= z & X_3 &= z \sin \alpha - x \cos \alpha \\
 R(x, z) &= R_2 + x \sin \alpha + z \cos \alpha
 \end{aligned} \tag{2.2.8}$$

Defining:

$$\begin{aligned}
 \varepsilon_{xx} &= \epsilon_{11} & 2\varepsilon_{x\theta} &= \epsilon_{12} \\
 \varepsilon_{\theta\theta} &= \epsilon_{22} & 2\varepsilon_{xz} &= \epsilon_{13} \\
 \varepsilon_{zz} &= \epsilon_{33} & 2\varepsilon_{\theta z} &= \epsilon_{23}
 \end{aligned} \tag{2.2.9}$$

the non-linear kinematic relations for conical /cylindrical shells can be calculated, giving:

$$\begin{aligned}
\varepsilon_{xx} &= u_{,x} + \frac{NL}{2}(u_{,x}^2 + v_{,x}^2 + w_{,x}^2) \\
\varepsilon_{\theta\theta} &= \frac{v_{,\theta}}{R(x,z)} + \frac{u \sin \alpha + w \cos \alpha}{r} \\
&\quad + \frac{NL}{2R(x,z)^2} [(-u_{,\theta} + v \sin \alpha)^2 + (u \sin \alpha + v_{,\theta} + w \cos \alpha)^2 + (v \cos \alpha - w_{,\theta})^2] \\
\varepsilon_{zz} &= w_{,z} + \frac{NL}{2}(u_{,z}^2 + v_{,z}^2 + w_{,z}^2) \\
\gamma_{x\theta} = 2\varepsilon_{x\theta} &= v_{,x} - \frac{v \sin \alpha}{R(x,z)} + \frac{u_{,\theta}}{R(x,z)} \\
&\quad + \frac{NL}{R(x,z)} [u_{,x}(u_{,\theta} - v \sin \alpha) + v_{,x}(u \sin \alpha + v_{,\theta} + w \cos \alpha) + w_{,x}(-v \cos \alpha + w_{,\theta})] \\
\gamma_{\theta z} = 2\varepsilon_{\theta z} &= v_{,z} - \frac{v \cos \alpha}{R(x,z)} + \frac{w_{,\theta}}{R(x,z)} \\
&\quad + \frac{NL}{R(x,z)} [u_{,z}(u_{,\theta} - v \sin \alpha) + v_{,z}(u \sin \alpha + v_{,\theta} + w \cos \alpha) + w_{,z}(-v \cos \alpha + w_{,\theta})] \\
\gamma_{xz} = 2\varepsilon_{xz} &= u_{,z} + w_{,x} + NL(u_{,x}u_{,z} + v_{,x}v_{,z} + w_{,x}w_{,z})
\end{aligned} \tag{2.2.10}$$

It will become convenient to assume a constant radius along the thickness by applying the shallow shell assumption that $r \gg z$, such that $r + z \approx r$:

$$\begin{aligned}
r &= R_2 + x \sin \alpha \\
R(x,z) &= r + z \cos \alpha
\end{aligned} \tag{2.2.11}$$

Using the simplification of Eq. (2.2.11) and assuming a cylinder, where $\alpha = 0$, the relations of Eq. (2.2.10) are further simplified resulting in Eq. (2.2.12).

$$\begin{aligned}
r &= R_1 = R_2 \\
\varepsilon_{xx} &= u_{,x} + \frac{NL}{2}(u_{,x}^2 + v_{,x}^2 + w_{,x}^2) \\
\varepsilon_{\theta\theta} &= \frac{v_{,\theta}}{r} + \frac{w}{r} + \frac{NL}{2r^2} [(-u_{,\theta})^2 + (v_{,\theta} + w)^2 + (v - w_{,\theta})^2] \\
\varepsilon_{zz} &= w_{,z} + \frac{NL}{2}(u_{,z}^2 + v_{,z}^2 + w_{,z}^2) \\
\gamma_{x\theta} = 2\varepsilon_{x\theta} &= v_{,x} + \frac{u_{,\theta}}{r} + \frac{NL}{r} [u_{,x}(u_{,\theta}) + v_{,x}(v_{,\theta} + w) + w_{,x}(-v + w_{,\theta})] \\
\gamma_{\theta z} = 2\varepsilon_{\theta z} &= v_{,z} - \frac{v}{r} + \frac{w_{,\theta}}{r} + \frac{NL}{r} [u_{,z}(u_{,\theta}) + v_{,z}(v_{,\theta} + w) + w_{,z}(-v + w_{,\theta})] \\
\gamma_{xz} = 2\varepsilon_{xz} &= u_{,z} + w_{,x} + NL(u_{,x}u_{,z} + v_{,x}v_{,z} + w_{,x}w_{,z})
\end{aligned} \tag{2.2.12}$$

2.2.3 Kinematic Equations for Laminates

Most of the analyses performed on composite plates have been based on one of the following approaches (copied from Reddy, 2004 [59]):

- i. Equivalent single-layer (ESL) theories (2-D)
 - a. Classical laminated plate theory
 - b. Shear deformation laminated plate theories
- ii. Three-dimensional elasticity theory (3-D)
 - a. Traditional 3-D elasticity formulations
 - b. Layer-wise theories

The ESL theories are simpler and computationally cheaper than the three-dimensional theories, providing sufficient accuracy for global responses such as gross deflections, critical buckling loads and fundamental vibration frequencies of thin and moderately thick laminates [59]. The ESL models may give low-accurate results for thick laminates and for strain and stresses at the ply level near geometric and material discontinuities or near regions of intense loading – where precise stress predictions are required; and therefore for such cases the 3-D theories are recommended [59]. Reddy states that among the ESL theories the First-order Shear Deformation Theory (FSDT) including transverse extensibility ($\varepsilon_{zz} \neq 0$) seems to provide the best compromise solution between accuracy, economy and simplicity [59], and at this point it is important to mention that the FSDT developed along this thesis will not consider this transverse extensibility.

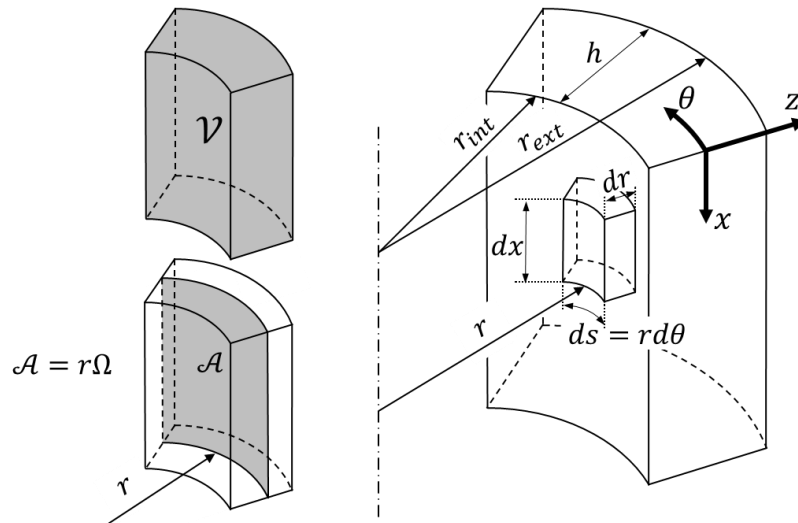


Fig. 2.2.2: Scheme to show the shallow shell assumption $r \gg h$

Since the models developed along this thesis are aimed to predict buckling loads (a global response) the ESL theories will be adopted and the corresponding approximations for displacement field presented in the following discussion. The kinematics of deformation for thin-walled structures allows the development of some assumptions that reduce the 3-D problem to a 2-D problem [72], [59]. This reduction is possible because the approximated displacement field for the 2-D case is expressed in terms of the thickness coordinate z as shown in Eqs. (2.2.19)–(2.2.22). The reduction from the 3-D space to the 2-D space is illustrated for a cylindrical coordinate system in Fig. 2.2.2.

Given a function $f(x, \theta, z)$, its integral over the 3-D domain \mathcal{V} can be expressed as:

$$\int_{\mathcal{V}} f(x, \theta, z) d\mathcal{V} = \int_{r_{int}}^{r_{ext}} \int_{\Omega} f(x, \theta, z) R(x, z) d\Omega dr \quad (2.2.13)$$

using the following substitutions based on Fig. 2.2.2:

$$d\Omega = d\theta dz; \quad dA = r d\Omega; \quad R(x, z) = r + z; \quad dr = dz \quad (2.2.14)$$

the integral of Eq. (2.2.13) becomes:

$$\int_{\mathcal{V}} f(x, \theta, z) d\mathcal{V} = \int_{-\frac{h}{2}}^{\frac{h}{2}} \int_A f(x, \theta, z) (r + z) \frac{dA}{R(x, z)} dz = \int_{-\frac{h}{2}}^{\frac{h}{2}} \int_A f(x, \theta, z) \left(1 + \frac{z}{r}\right) dA dz \quad (2.2.15)$$

Applying the shallow shell theory assumption that $r \gg z$, will result in:

$$\begin{aligned} \left(1 + \frac{z}{r}\right) &\approx 1 \\ (r + z) &\approx r \end{aligned} \quad (2.2.16)$$

leading Eq. (2.2.15) to:

$$\int_{\mathcal{V}} f(x, \theta, z) d\mathcal{V} = \int_{-\frac{h}{2}}^{\frac{h}{2}} \int_{\mathcal{A}} f(x, \theta, z) d\mathcal{A} dz = \int_{z=-\frac{h}{2}}^{z=\frac{h}{2}} \int_{s=0}^{s=2\pi r} \int_{x=0}^{x=L} f(x, \theta, z) dx ds dz \quad (2.2.17)$$

or in terms of θ :

$$\int_{\mathcal{V}} f(x, \theta, z) d\mathcal{V} = \int_{-\frac{h}{2}}^{\frac{h}{2}} \int_{\Omega} f(x, \theta, z) r d\Omega dz = \int_{z=-\frac{h}{2}}^{z=\frac{h}{2}} \int_{\theta=0}^{\theta=2\pi} \int_{x=0}^{x=L} f(x, \theta, z) r dx d\theta dz \quad (2.2.18)$$

Equation (2.2.18) will be the basis for the reduction from the 3-D domain to the 2-D domain when using the ESL theories. The simplest of the ESL theories is the Classical Laminated Plate Theory (CLPT) which is an extension of the Classical Plate Theory to composite laminates [59], where the Kirchhoff hypotheses hold [59]:

- i. Transverse normals remain straight after deformation;
- ii. Transverse normals do not experience elongation ($\varepsilon_{zz} = 0$);
- iii. The transverse normals rotate so that they remain perpendicular to the mid-surface after deformation (no transverse shear takes place, i.e. $\gamma_{yz} = \gamma_{xz} = 0$).

If there is no normal elongation and the normal remains straight (first two assumptions) then the normal displacement is constant along the thickness ($w = w_0$ and $\varepsilon_{zz} = 0$) [59]. The third hypothesis makes the mid-surface rotations connected to the normal displacement field, as given in Eq. (2.2.19) and illustrated in Fig. 2.2.3. In Eq. (2.2.19) the quantities u_0, v_0, w_0 represent the mid-surface displacement field, which are used with the rotations $\phi_x = -w_{,x}$ and $\phi_\theta = -w_{,\theta}/r$ to calculate the complete displacement field at any point in the shell.

Applying the CLPT to problems where the surface dimension-to-thickness ratio is large usually provides enough accuracy for isotropic problems. However, its application for layered composite shells can lead to as much as 30% error in the prediction of deflections, stresses and natural frequencies [72]. And for this reason it may be necessary to apply kinematic theories that take transverse shears into account, relaxing the third Kirchhoff hypothesis by relaxing the connection between the normal displacement field and the mid-surface rotations, such that transverse shear strains may develop ($\gamma_{yz} \neq \gamma_{xz} \neq 0$) [59]. The First-order Shear Deformation Theory (FSDT) assumes a constant shear strain along the thickness coordinate, which is a gross approximation of the real strain distribution which is at least quadratic along the thickness [59], [74]. The connection of the rotation with the normal displacement also results in stiffer models when compared to any model that allows transverse shear strains to develop, meaning that a given structure simulated using the CLPT will show a stiffer behavior than if simulated using the FSDT. Equation (2.2.20) shows the displacement field of the CLPT and three other shear deformation theories, and Fig. 2.2.3 illustrates the kinematics of the CLPT compared to the FSDT.

$$\begin{aligned} u(x, \theta, z, t) &= u_0(x, \theta, t) - zw_{,x} \\ v(x, \theta, z, t) &= v_0(x, \theta, t) - z \frac{1}{r} w_{,\theta} \\ w(x, \theta, z, t) &= w_0(x, \theta, t) \end{aligned} \quad \begin{array}{l} \text{Classical Laminated} \\ \text{Plate Theory (CLPT)} \end{array} \quad (2.2.19)$$

$$\begin{aligned} u(x, \theta, z, t) &= u_0(x, \theta, t) + z\phi_x(x, \theta, t) \\ v(x, \theta, z, t) &= v_0(x, \theta, t) + z\phi_\theta(x, \theta, t) \\ w(x, \theta, z, t) &= w_0(x, \theta, t) \end{aligned} \quad \begin{array}{l} \text{First-order Shear} \\ \text{Deformation Theory} \\ \text{(FSDT)} \end{array} \quad (2.2.20)$$

$$\begin{aligned} u(x, \theta, z, t) &= u_0(x, \theta, t) + z\phi_x(x, \theta, t) + z^2\psi_x(x, \theta, t) \\ v(x, \theta, z, t) &= v_0(x, \theta, t) + z\phi_\theta(x, \theta, t) + z^2\psi_\theta(x, \theta, t) \\ w(x, \theta, z, t) &= w_0(x, \theta, t) \end{aligned} \quad \begin{array}{l} \text{Second-order Shear} \\ \text{Deformation Theory} \end{array} \quad (2.2.21)$$

$$\begin{aligned} u(x, \theta, z, t) &= u_0(x, \theta, t) + z\phi_x(x, \theta, t) + z^2\psi_x(x, \theta, t) + z^3\lambda_x(x, \theta, t) \\ v(x, \theta, z, t) &= v_0(x, \theta, t) + z\phi_\theta(x, \theta, t) + z^2\psi_\theta(x, \theta, t) + z^3\lambda_\theta(x, \theta, t) \\ w(x, \theta, z, t) &= w_0(x, \theta, t) \end{aligned} \quad \begin{array}{l} \text{Third-order Shear} \\ \text{Deformation Theory} \end{array} \quad (2.2.22)$$

To simplify the notation, the mid-surface displacements u_0, v_0, w_0 will be written as u, v, w along the next sections of this thesis.

Higher order shear deformation theories are shown in Eq. (2.2.21) and (2.2.22). The use of higher polynomials introduces additional unknowns in the displacement fields that are difficult to give a physical interpretation [59]. Reddy [75], [76] developed a third-order laminated plate theory that accommodates quadratic variation of strains along the thickness and the proper vanishing of the transverse shear strains at the shell bottom and top surfaces, dispensing the use of shear correction factors since the shear strain energy obtained is already coherent. Models dispensing shear correction factors may be handy when validating FSDT correction factors or finite element results since in most of the commercial finite element codes the FSDT is used to derive the shell element's equations. In Chapter 4 studies with linear buckling will show a strong influence of the correction factors in some cases, even for thin-walled shells.

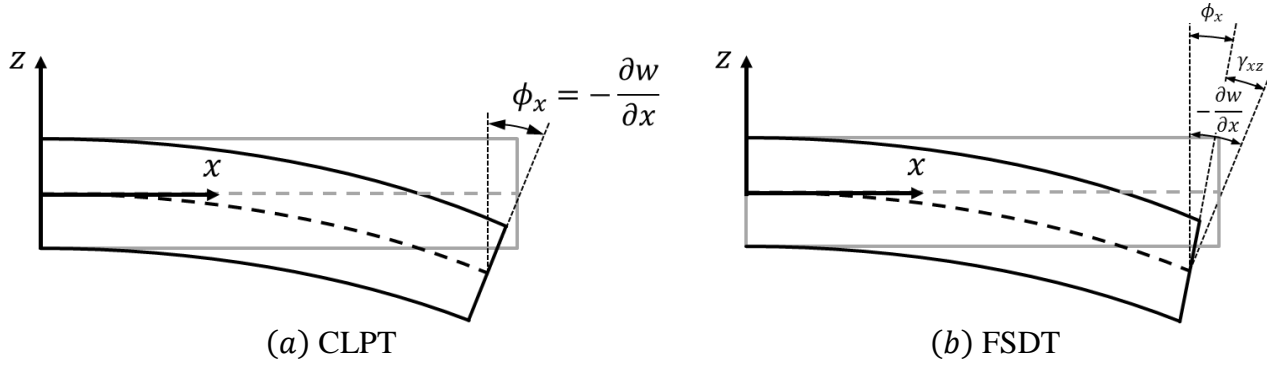


Fig. 2.2.3: Kinematics of a Shell Plate for the CLPT and the FSDT

2.2.4 Kinematic Equations for the FSDT

The general equations of motion for conical structures after applying the assumption that $r \gg z$, so that $R(x, z) = r + z \cos(\alpha) \approx r$, will be used in this section. The FSDT displacement field is given in Eq. (2.2.20) and is applied in Eq. (2.2.10) to obtain the corresponding kinematic equations. The mid-surface displacements are u, v, w , and the rotations ϕ_x and ϕ_θ . Writing the strains in the form of Eq. (2.2.23) and making the necessary manipulations will result in Eq. (2.2.24).

$$\{\varepsilon\} = \begin{Bmatrix} \varepsilon_1 \\ \varepsilon_2 \\ \varepsilon_3 \\ \varepsilon_4 \end{Bmatrix} = \begin{Bmatrix} \varepsilon_{xx} \\ \varepsilon_{\theta\theta} \\ \gamma_{x\theta} \\ \gamma_{\theta z} \\ \gamma_{xz} \end{Bmatrix} = \begin{Bmatrix} \varepsilon_{xx}^{(0)} \\ \varepsilon_{\theta\theta}^{(0)} \\ \gamma_{x\theta}^{(0)} \\ \gamma_{\theta z}^{(0)} \\ \gamma_{xz}^{(0)} \end{Bmatrix} + z \begin{Bmatrix} \varepsilon_{xx}^{(1)} \\ \varepsilon_{\theta\theta}^{(1)} \\ \gamma_{x\theta}^{(1)} \\ \gamma_{\theta z}^{(1)} \\ \gamma_{xz}^{(1)} \end{Bmatrix} + z^2 \begin{Bmatrix} \varepsilon_{xx}^{(2)} \\ \varepsilon_{\theta\theta}^{(2)} \\ \gamma_{x\theta}^{(2)} \\ \gamma_{\theta z}^{(2)} \\ \gamma_{xz}^{(2)} \end{Bmatrix} \quad (2.2.23)$$

Note in Eq. (2.2.24) that the non-linear terms of the kinematic equations were separated in those corresponding to the equations of Donnell's [16], Sanders' [63], Timoshenko and Gere's and other non-linear terms not used in any of these three non-linear theories. The Donnell terms are included by default. When the Sanders' equations are used $\delta_1 = 1$, $\delta_2 = 0$ and $\delta_3 = 0$. When Timoshenko and Gere's equations are used $\delta_1 = 1$, $\delta_2 = 1$ and $\delta_3 = 0$. The case with $\delta_1 = \delta_2 = \delta_3 = 1$ will not be investigated along this thesis and it would result in the full kinematic relations for the FSDT. Equation (2.2.24) is in agreement with Simites et al. (1985) [77] [62], Tong & Wang (1992) [73], Goldfeld et al. (2003) [64], Goldfeld (2007) [66] and Shadmehri et al. (2012) [70].

$$\begin{aligned}
\varepsilon_{xx}^{(0)} &= u_{,x} + \frac{w_{,x}^2}{2} + \delta_2 \frac{v_{,x}^2}{2} + \delta_3 \frac{u_{,x}^2}{2} \\
\varepsilon_{xx}^{(1)} &= \phi_{x,x} + \delta_3 (u_{,x} \phi_{x,x} + v_{,x} \phi_{\theta,x}) \\
\varepsilon_{xx}^{(2)} &= \frac{\delta_3}{2} (\phi_{x,x}^2 + \phi_{\theta,x}^2) \\
\varepsilon_{\theta\theta}^{(0)} &= \frac{1}{r} (u \sin \alpha + v_{,\theta} + w \cos \alpha) + \frac{w_{,\theta}^2}{2r^2} + \delta_1 \frac{\cos \alpha}{r} v \left(\frac{1}{2r} \cos \alpha v - \frac{1}{r} w_{,\theta} \right) + \delta_2 \frac{1}{2r^2} (v_{,\theta} + \cos \alpha w)^2 \\
&\quad + \delta_3 \frac{1}{2r^2} [\sin(\alpha)^2 u^2 - 2 \sin \alpha v u_{,\theta} + 2 \sin \alpha u (\cos \alpha w + v_{,\theta}) + u_{,\theta}^2] \\
\varepsilon_{\theta\theta}^{(1)} &= \frac{1}{r} (\phi_x \sin \alpha + \phi_{\theta,\theta}) \\
&\quad + \frac{\delta_3}{2r^2} [v \phi_{\theta} - \cos \alpha \phi_{\theta} w_{,\theta} + u_{,\theta} \phi_{x,\theta} - \sin \alpha (\phi_{\theta} u_{,\theta} - \phi_x v_{,\theta} + v \phi_{x,\theta}) + v_{,\theta} \phi_{\theta,\theta} \\
&\quad + (\sin \alpha u + \cos \alpha w) (\sin \alpha \phi_x + \phi_{\theta,\theta})] \\
\varepsilon_{\theta\theta}^{(2)} &= \frac{\delta_3}{2r^2} [(-\phi_{x,\theta} + \phi_{\theta} \sin \alpha)^2 + (\phi_{x,\theta} + \phi_{\theta} \sin \alpha)^2 + (\phi_{\theta} \cos \alpha)^2] \\
\gamma_{x\theta}^{(0)} &= v_{,x} + \frac{1}{r} (u_{,\theta} - v \sin \alpha) + \frac{1}{r} w_{,x} w_{,\theta} - \delta_1 \frac{\cos \alpha}{r} v w_{,x} + \delta_2 \frac{1}{r} v_{,x} v_{,\theta} \\
&\quad + \frac{\delta_3}{r} [u_{,x} (u_{,\theta} - \sin \alpha v) + v_{,x} (\sin \alpha u + \cos \alpha w)] \\
\gamma_{x\theta}^{(1)} &= \left(\frac{\phi_{x,\theta}}{r} + \phi_{\theta,x} - \frac{\phi_{\theta} \sin \alpha}{r} \right) \\
&\quad + \frac{\delta_3}{r} [-\phi_{\theta} (\sin \alpha u_{,x} + \cos \alpha w_{,x}) + \sin \alpha \phi_x v_{,x} + (-\sin \alpha v + u_{,\theta}) \phi_{x,x} + u_{,x} \phi_{x,\theta} \\
&\quad + (\sin \alpha u + v_{,\theta}) \phi_{\theta,x} + v_{,x} \phi_{\theta,\theta} + \cos \alpha w \phi_{\theta,x}] \\
\gamma_{x\theta}^{(2)} &= \frac{\delta_3}{r} [-\sin \alpha \phi_{\theta} \phi_{x,x} + \phi_{x,x} \phi_{x,\theta} + \phi_{\theta,x} (\sin \alpha \phi_x + \phi_{\theta,\theta})] \\
\gamma_{\theta z}^{(0)} &= \phi_{\theta} + \frac{1}{r} w_{,\theta} - \frac{1}{r} v \cos \alpha + \frac{\delta_3}{r} [-\sin \alpha v \phi_x + \phi_x u_{,\theta} + \phi_{\theta} (\sin \alpha u + \cos \alpha w + v_{,\theta})] \\
\gamma_{\theta z}^{(1)} &= -\frac{1}{r} \phi_{\theta} \cos \alpha + \frac{\delta_3}{r} [\phi_x \phi_{x,\theta} + \phi_{\theta} \phi_{\theta,\theta}] \\
\gamma_{\theta z}^{(2)} &= 0 \\
\gamma_{xz}^{(0)} &= w_{,x} + \phi_x + \delta_3 (u_{,x} \phi_x + v_{,x} \phi_{\theta}) \\
\gamma_{xz}^{(1)} &= \delta_3 (\phi_{x,x} \phi_x + \phi_{\theta,x} \phi_{\theta}) \\
\gamma_{xz}^{(2)} &= 0
\end{aligned} \tag{2.2.24}$$

The next step is to separate the terms that are relevant for this thesis making $\delta_2 = \delta_3 = 0$, and adding the presence of an initial imperfection field represented by w_0 as presented by Simites et al. (1985) [62], Arbocz (1992) [20], Yeh et al. (1994) [78], Almroth (1966) [79] and Yamada et al. (2008) [80]. The partial derivatives related to the imperfection field $w_{0,x}$ and $w_{0,\theta}$ added to the terms corresponding to Sanders' equations were taken from Simites [62]. The following equations for the strain field are obtained.

$$\begin{aligned}
 \varepsilon_{xx}^{(0)} &= u_{,x} + \frac{w_{,x}^2}{2} + w_{0,x} w_{,x} \\
 \varepsilon_{\theta\theta}^{(0)} &= \frac{1}{r} (\sin \alpha u + v_{,\theta} + \cos \alpha w) + \frac{1}{2r^2} w_{,\theta}^2 + \frac{1}{r^2} w_{0,\theta} w_{,\theta} + \delta_1 \frac{\cos \alpha}{r} v \left(\frac{\cos \alpha}{2r} v - \frac{1}{r} (w_{,\theta} + w_{0,\theta}) \right) \\
 \gamma_{x\theta}^{(0)} &= v_{,x} + \frac{1}{r} (u_{,\theta} - \sin \alpha v) + \frac{1}{r} w_{,x} w_{,\theta} + \frac{1}{r} w_{0,x} w_{,\theta} + \frac{1}{r} w_{0,\theta} w_{,x} - \delta_1 \frac{\cos \alpha}{r} v (w_{,x} + w_{0,x}) \\
 \varepsilon_{xx}^{(1)} &= \phi_{x,x} \\
 \varepsilon_{\theta\theta}^{(1)} &= \frac{1}{r} (\sin \alpha \phi_x + \phi_{\theta,\theta}) \\
 \gamma_{x\theta}^{(1)} &= \left(\frac{\phi_{x,\theta}}{r} + \phi_{\theta,x} - \frac{\sin \alpha}{r} \phi_\theta \right) \\
 \gamma_{\theta z}^{(0)} &= \phi_\theta + \frac{1}{r} w_{,\theta} - \cos \alpha \frac{1}{r} v \\
 \gamma_{xz}^{(0)} &= w_{,x} + \phi_x
 \end{aligned} \tag{2.2.25}$$

The variation of the strain vector $\{\delta\varepsilon\}$ can be written as:

$$\begin{aligned}
 \delta\varepsilon_{xx}^{(0)} &= \delta u_{,x} + w_{,x} \delta w_{,x} + w_{0,x} \delta w_{,x} \\
 \delta\varepsilon_{\theta\theta}^{(0)} &= \frac{1}{r} (\sin \alpha \delta u + \delta v_{,\theta} + \cos \alpha \delta w) + \frac{1}{r^2} w_{,\theta} \delta w_{,\theta} + \frac{1}{r^2} w_{0,\theta} \delta w_{,\theta} \\
 &\quad + \delta_1 \frac{\cos \alpha}{r^2} (\cos \alpha v \delta v - v \delta w_{,\theta} - w_{,\theta} \delta v - w_{0,\theta} \delta v) \\
 \delta\gamma_{x\theta}^{(0)} &= \delta v_{,x} + \frac{1}{r} (\delta u_{,\theta} - \sin \alpha \delta v) + \frac{1}{r} w_{,x} \delta w_{,\theta} + \frac{1}{r} w_{,\theta} \delta w_{,x} + \frac{1}{r} w_{0,x} \delta w_{,\theta} + \frac{1}{r} w_{0,\theta} \delta w_{,x} \\
 &\quad - \delta_1 \frac{\cos \alpha}{r} (v \delta w_{,x} + w_{,x} \delta v + w_{0,x} \delta v) \\
 \delta\varepsilon_{xx}^{(1)} &= \delta\phi_{x,x} \\
 \delta\varepsilon_{\theta\theta}^{(1)} &= \frac{1}{r} (\sin \alpha \delta\phi_x + \delta\phi_{\theta,\theta}) \\
 \delta\gamma_{x\theta}^{(1)} &= \left(\frac{\delta\phi_{x,\theta}}{r} + \delta\phi_{\theta,x} - \frac{\sin \alpha}{r} \delta\phi_\theta \right) \\
 \delta\gamma_{\theta z}^{(0)} &= \delta\phi_\theta + \frac{1}{r} \delta w_{,\theta} - \frac{\cos \alpha}{r} \delta v \\
 \delta\gamma_{xz}^{(0)} &= \delta w_{,x} + \delta\phi_x
 \end{aligned} \tag{2.2.26}$$

2.2.5 Kinematic Equations for the CLPT

The kinematic relations for the Classical Laminated Plate Theory (CLPT) can be obtained substituting the displacement approximation of Eq. (2.2.19) into Eq. (2.2.10), but here these relations will be directly obtained from the FSDT equations by making the following substitutions:

$$\begin{aligned}\phi_x &= -w_{,x} \\ \phi_\theta &= -\frac{1}{r}w_{,\theta} + \delta_1 \frac{v}{r} \cos \alpha \\ \gamma_{\theta z} &= \gamma_{xz} = 0\end{aligned}\tag{2.2.27}$$

In Eq. (2.2.27) note that when the Sanders's equations are used ($\delta_1 = 1$) the rotation ϕ_θ is corrected with an additional term, according to Ref. [63]. The strains can be written in the form:

$$\{\varepsilon\} = \begin{Bmatrix} \varepsilon_1 \\ \varepsilon_2 \\ \varepsilon_6 \end{Bmatrix} = \begin{Bmatrix} \varepsilon_{xx} \\ \varepsilon_{\theta\theta} \\ \gamma_{x\theta} \end{Bmatrix} = \begin{Bmatrix} \varepsilon_{xx}^{(0)} \\ \varepsilon_{\theta\theta}^{(0)} \\ \gamma_{x\theta}^{(0)} \end{Bmatrix} + z \begin{Bmatrix} \varepsilon_{xx}^{(1)} \\ \varepsilon_{\theta\theta}^{(1)} \\ \gamma_{x\theta}^{(1)} \end{Bmatrix} + z^2 \begin{Bmatrix} \varepsilon_{xx}^{(2)} \\ \varepsilon_{\theta\theta}^{(2)} \\ \gamma_{x\theta}^{(2)} \end{Bmatrix}\tag{2.2.28}$$

Applying the substitutions of Eq. (2.2.27) into Eq. (2.2.24) will result in Eq. (2.2.29).

$$\begin{aligned}
\varepsilon_{xx}^{(0)} &= u_{,x} + \frac{w_{,x}^2}{2} + \delta_2 \frac{v_{,x}^2}{2} + \delta_3 \frac{u_{,x}^2}{2} \\
\varepsilon_{xx}^{(1)} &= -w_{,xx} + \delta_3 \left(-u_{,x} w_{,xx} - \frac{1}{r} v_{,x} w_{,\theta x} + \frac{v_{,x}^2}{r} \right) \\
\varepsilon_{xx}^{(2)} &= \frac{\delta_3}{2} \left(w_{,xx}^2 + \frac{1}{r^2} w_{,\theta x}^2 \right) \\
\varepsilon_{\theta\theta}^{(0)} &= \frac{1}{r} (u \sin \alpha + v_{,\theta} + w \cos \alpha) + \frac{w_{,\theta}^2}{2r^2} + \delta_1 \frac{\cos \alpha}{r} v \left(\frac{1}{2r} \cos \alpha v - \frac{1}{r} w_{,\theta} \right) + \delta_2 \frac{1}{2r^2} (v_{,\theta} + \cos \alpha w)^2 \\
&\quad + \delta_3 \frac{1}{2r^2} [\sin(\alpha)^2 u^2 - 2 \sin \alpha v u_{,\theta} + 2 \sin \alpha u (\cos \alpha w + v_{,\theta}) + u_{,\theta}^2] \\
\varepsilon_{\theta\theta}^{(1)} &= -\frac{1}{r} \left(w_{,x} \sin \alpha + \frac{1}{r} w_{,\theta\theta} \right) + \delta_1 \frac{\cos \alpha}{r^2} v_{,\theta} \\
&\quad + \frac{\delta_3}{2r^2} \left[\frac{v^2}{r} - \frac{1}{r} v w_{,\theta} - \frac{1}{r} \cos \alpha v w_{,\theta} + \frac{1}{r} \cos \alpha w_{,\theta}^2 - u_{,\theta} w_{,x\theta} \right. \\
&\quad + \sin \alpha \left(\frac{1}{r} w_{,\theta} u_{,\theta} - \frac{1}{r} v u_{,\theta} - w_{,x} v_{,\theta} + w_{,x\theta} v \right) - \frac{1}{r} v_{,\theta} w_{,\theta\theta} + \frac{1}{r} v_{,\theta}^2 \\
&\quad \left. - (\sin \alpha u + \cos \alpha w) \left(\sin \alpha w_{,x} + \frac{1}{r} w_{,\theta\theta} - \frac{1}{r} v_{,\theta} \right) \right] \\
\varepsilon_{\theta\theta}^{(2)} &= \frac{\delta_3}{2r^2} \left[\left(w_{,x\theta} - \frac{1}{r} w_{,\theta} \sin \alpha \right)^2 + \left(-w_{,x\theta} - \frac{1}{r} w_{,\theta} \sin \alpha \right)^2 + \left(-\frac{1}{r} w_{,\theta} \cos \alpha \right)^2 \right] \\
\gamma_{x\theta}^{(0)} &= v_{,x} + \frac{1}{r} (u_{,\theta} - v \sin \alpha) + \frac{1}{r} w_{,x} w_{,\theta} - \delta_1 \frac{\cos \alpha}{r} v w_{,x} + \delta_2 \frac{1}{r} v_{,x} v_{,\theta} \\
&\quad + \frac{\delta_3}{r} [u_{,x} (u_{,\theta} - \sin \alpha v) + v_{,x} (\sin \alpha u + \cos \alpha w)] \\
\gamma_{x\theta}^{(1)} &= -\frac{1}{r} \left(2w_{,x\theta} - \frac{\sin \alpha}{r} w_{,\theta} \right) + \delta_1 \frac{\cos \alpha}{r} \left(v_{,x} - \frac{\sin \alpha}{r} v \right) \\
&\quad + \frac{\delta_3}{r} \left[\frac{1}{r} (w_{,\theta} - v) (\sin \alpha u_{,x} + \cos \alpha w_{,x}) - \sin \alpha w_{,x} v_{,x} + (\sin \alpha v - u_{,\theta}) w_{,xx} \right. \\
&\quad - u_{,x} w_{,x\theta} - \frac{1}{r} (\sin \alpha u + v_{,\theta}) (w_{,x\theta} - v_{,x}) - \frac{1}{r} v_{,x} (w_{,\theta\theta} - v_{,\theta}) \\
&\quad \left. - \frac{1}{r} \cos \alpha w (w_{,x\theta} - v_{,x}) \right] \\
\gamma_{x\theta}^{(2)} &= \frac{\delta_3}{r} \left[-\sin \alpha \frac{1}{r} w_{,\theta} w_{,xx} + w_{,xx} w_{,x\theta} + \frac{1}{r} w_{,\theta x} \left(\sin \alpha w_{,x} + \frac{1}{r} w_{,\theta\theta} \right) \right]
\end{aligned} \tag{2.2.29}$$

Similarly to what has been done for the FSDT, Eq. (2.2.29) will be rewritten considering only the terms that are relevant for this thesis and including the initial imperfection field w_0 , giving:

$$\begin{aligned}
\varepsilon_{xx}^{(0)} &= u_{,x} + \frac{1}{2} w_{,x}^2 + w_{0,x} w_{,x} \\
\varepsilon_{\theta\theta}^{(0)} &= \frac{1}{r} (\sin \alpha u + v_{,\theta} + \cos \alpha w) + \frac{1}{2r^2} w_{,\theta}^2 + \frac{1}{r^2} w_{0,\theta} w_{,\theta} + \delta_1 \frac{\cos \alpha}{r} v \left(\frac{\cos \alpha}{2r} v - \frac{1}{r} (w_{,\theta} + w_{0,\theta}) \right) \\
\gamma_{x\theta}^{(0)} &= v_{,x} + \frac{1}{r} (u_{,\theta} - \sin \alpha v) + \frac{1}{r} w_{,x} w_{,\theta} + \frac{1}{r} w_{0,x} w_{,\theta} + \frac{1}{r} w_{0,\theta} w_{,x} - \delta_1 \frac{\cos \alpha}{r} v (w_{,x} + w_{0,x}) \\
\varepsilon_{xx}^{(1)} &= -w_{,xx} \\
\varepsilon_{\theta\theta}^{(1)} &= -\frac{1}{r} \left(\sin \alpha w_{,x} + \frac{1}{r} w_{,\theta\theta} \right) + \delta_1 \frac{\cos \alpha}{r^2} v_{,\theta} \\
\gamma_{x\theta}^{(1)} &= -\frac{1}{r} \left(2 w_{,x\theta} - \frac{\sin \alpha}{r} w_{,\theta} \right) + \delta_1 \frac{\cos \alpha}{r} \left(v_{,x} - \frac{\sin \alpha}{r} v \right)
\end{aligned} \tag{2.2.30}$$

The variation of the strain vector $\{\delta \varepsilon\}$ can be written as:

$$\begin{aligned}
\delta \varepsilon_{xx}^{(0)} &= \delta u_{,x} + w_{,x} \delta w_{,x} + w_{0,x} \delta w_{,x} \\
\delta \varepsilon_{\theta\theta}^{(0)} &= \frac{1}{r} (\sin \alpha \delta u + \delta v_{,\theta} + \cos \alpha \delta w) + \frac{1}{r^2} w_{,\theta} \delta w_{,\theta} + \frac{1}{r^2} w_{0,\theta} \delta w_{,\theta} \\
&\quad + \delta_1 \frac{\cos \alpha}{r^2} (\cos \alpha v \delta v - v \delta w_{,\theta} - w_{,\theta} \delta v - w_{0,\theta} \delta v) \\
\delta \gamma_{x\theta}^{(0)} &= \delta v_{,x} + \frac{1}{r} (\delta u_{,\theta} - \sin \alpha \delta v) + \frac{1}{r} w_{,x} \delta w_{,\theta} + \frac{1}{r} w_{,\theta} \delta w_{,x} + \frac{1}{r} w_{0,x} \delta w_{,\theta} + \frac{1}{r} w_{0,\theta} \delta w_{,x} \\
&\quad - \delta_1 \frac{\cos \alpha}{r} (v \delta w_{,x} + w_{,x} \delta v + w_{0,x} \delta v) \\
\delta \varepsilon_{xx}^{(1)} &= -\delta w_{,xx} \\
\delta \varepsilon_{\theta\theta}^{(1)} &= -\frac{1}{r} \left(\sin \alpha \delta w_{,x} + \frac{1}{r} \delta w_{,\theta\theta} \right) + \delta_1 \frac{\cos \alpha}{r^2} \delta v_{,\theta} \\
\delta \gamma_{x\theta}^{(1)} &= -\frac{1}{r} \left(2 \delta w_{,x\theta} - \frac{\sin \alpha}{r} \delta w_{,\theta} \right) + \delta_1 \frac{\cos \alpha}{r} \left(\delta v_{,x} - \frac{\sin \alpha}{r} \delta v \right)
\end{aligned} \tag{2.2.31}$$

2.2.6 Matrix Form of the Kinematic Equations

Considering the relevant strain components given in Eqs. (2.2.25) and (2.2.30), the strain vector $\{\varepsilon\}$ and the displacement vector $\{u\}$ for the CLPT and the FSDT will be represented as:

$$\begin{aligned}
\{\varepsilon\}_{CLPT}^T &= \{\varepsilon_{xx}^{(0)} \quad \varepsilon_{\theta\theta}^{(0)} \quad \gamma_{x\theta}^{(0)} \quad \varepsilon_{xx}^{(1)} \quad \varepsilon_{\theta\theta}^{(1)} \quad \gamma_{x\theta}^{(1)}\} \\
\{\varepsilon\}_{FSDT}^T &= \{\varepsilon_{xx}^{(0)} \quad \varepsilon_{\theta\theta}^{(0)} \quad \gamma_{x\theta}^{(0)} \quad \varepsilon_{xx}^{(1)} \quad \varepsilon_{\theta\theta}^{(1)} \quad \gamma_{x\theta}^{(1)} \quad \gamma_{\theta z}^{(0)} \quad \gamma_{xz}^{(0)}\} \\
\{u\}_{CLPT}^T &= \{u \quad v \quad w\} \\
\{u\}_{FSDT}^T &= \{u \quad v \quad w \quad \phi_x \quad \phi_\theta\}
\end{aligned} \tag{2.2.32}$$

Chapter 3 shows in details how the Ritz method can be used to solve non-linear static and linear buckling problems, where the displacement field can be approximated using the general matrix form:

$$\{u\} = [g]\{c\} \tag{2.2.33}$$

where $[g]$ contains the known base functions and $\{c\}$ the corresponding unknown amplitudes. The solution consists on finding $\{c\}$, i.e. the Ritz constants, as detailed in Chapter 3. Using this approximation, the strain vector can assume the general form [81]:

$$\begin{aligned}
\{\varepsilon\} &= \{\varepsilon_0\} + \{\varepsilon_L\} + \{\varepsilon_{L_0}\} \\
\{\varepsilon_0\} &= [B_0]\{c\} \\
\{\varepsilon_L\} &= \frac{1}{2} [B_L]\{c\} \\
\{\varepsilon_{L_0}\} &= [B_{L_0}]\{c\}
\end{aligned} \tag{2.2.34}$$

where $\{\varepsilon_0\}$ and $\{\varepsilon_L\}$ contains the linear and the non-linear strain terms due to large deflections and $\{\varepsilon_{L_0}\}$ contains the non-linear strain terms due to the presence of an initial imperfection field w_0 . The matrices $[B_0]$ and $[B_L]$ contain the linear and non-linear kinematic terms, respectively, and $[B_{L_0}]$ contains the non-linear kinematic terms due to the initial imperfection field w_0 ; all defined in the following discussion.

The matrix $[B_0]$ can be represented as a function of the approximation base functions $[g]$ as:

$$[B_0] = [d_0][g] \quad (2.2.35)$$

where $[d_0]$ contains the differential operators that render the base functions $[g]$ to the proper kinematic relations. From Eqs. (2.2.25) and (2.2.30) matrix $[d_0]$ can be built for the CLPT and the FSDT and the result is shown in Eq. (2.2.36), which is in accordance with Shadmehri et al. (2012) [70]. Note the terms corresponding to Sanders' equations, activated when $\delta_1 = 1$, for the CLPT case.

$$[d_0]_{CLPT} = \begin{bmatrix} \frac{\partial}{\partial x} & 0 & 0 \\ \frac{\sin \alpha}{r} & \frac{1}{r} \frac{\partial}{\partial \theta} & \frac{\cos \alpha}{r} \\ \frac{1}{r} \frac{\partial}{\partial \theta} & \frac{\partial}{\partial x} - \frac{\sin \alpha}{r} & 0 \\ 0 & 0 & -\frac{\partial^2}{\partial x^2} \\ 0 & \delta_1 \frac{\cos \alpha}{r^2} \frac{\partial}{\partial \theta} & -\frac{1}{r} \left(\sin \alpha \frac{\partial}{\partial x} + \frac{1}{r} \frac{\partial^2}{\partial \theta^2} \right) \\ 0 & \delta_1 \frac{\cos \alpha}{r} \left(\frac{\partial}{\partial x} - \frac{\sin \alpha}{r} \right) & -\frac{1}{r} \left(2 \frac{\partial^2}{\partial x \partial \theta} - \frac{\sin \alpha}{r} \frac{\partial}{\partial \theta} \right) \end{bmatrix}$$

$$[d_0]_{FSDT} = \begin{bmatrix} \frac{\partial}{\partial x} & 0 & 0 & 0 & 0 \\ \frac{\sin \alpha}{r} & \frac{1}{r} \frac{\partial}{\partial \theta} & \frac{\cos \alpha}{r} & 0 & 0 \\ \frac{1}{r} \frac{\partial}{\partial \theta} & \frac{\partial}{\partial x} - \frac{\sin \alpha}{r} & 0 & 0 & 0 \\ 0 & 0 & 0 & \frac{\partial}{\partial x} & 0 \\ 0 & 0 & 0 & \frac{\sin \alpha}{r} & \frac{1}{r} \frac{\partial}{\partial \theta} \\ 0 & 0 & 0 & \frac{1}{r} \frac{\partial}{\partial \theta} & \frac{\partial}{\partial x} - \frac{\sin \alpha}{r} \\ 0 & -\frac{\cos \alpha}{r} & \frac{1}{r} \frac{\partial}{\partial \theta} & 0 & 1 \\ 0 & 0 & \frac{\partial}{\partial x} & 1 & 0 \end{bmatrix} \quad (2.2.36)$$

For the non-linear kinematic relations Eqs. (2.2.25) and (2.2.30) show that the non-linear terms for the CLPT and the FSDT are similar, making it possible to treat both kinematic assumptions in the same discussion. Considering first the Donnell's equations, (with $\delta_1 = \delta_2 = \delta_3 = 0$). The non-linear part of the strain vector can be written as (the matrices for the CLPT can be obtained by removing the last two rows of $[A]$ and $[A_0]$):

$$\{\varepsilon_L\}_{Donnell}^{FSDT} = \frac{1}{2} \begin{bmatrix} w_{,x} & 0 \\ 0 & \frac{1}{r} w_{,\theta} \\ \frac{1}{r} w_{,\theta} & w_{,x} \\ 0 & 0 \\ 0 & 0 \\ 0 & 0 \\ 0 & 0 \end{bmatrix} \begin{bmatrix} w_{,x} \\ \frac{1}{r} w_{,\theta} \end{bmatrix} \quad \{\varepsilon_{L_0}\}_{Donnell}^{FSDT} = \begin{bmatrix} w_{0,x} & 0 \\ 0 & \frac{1}{r} w_{0,\theta} \\ \frac{1}{r} w_{0,\theta} & w_{0,x} \\ 0 & 0 \\ 0 & 0 \\ 0 & 0 \\ 0 & 0 \end{bmatrix} \begin{bmatrix} w_{,x} \\ \frac{1}{r} w_{,\theta} \end{bmatrix} \quad (2.2.37)$$

which can be rearranged as:

$$\begin{aligned} \{\varepsilon_L\}_{Donnell} &= \frac{1}{2} [B_L] \{c\} & \{\varepsilon_{L_0}\}_{Donnell} &= [B_{L_0}] \{c\} \\ [B_L] &= [A][G] & [B_{L_0}] &= [A_0][G] \\ [A]_{Donnell}^{FSDT} &= \begin{bmatrix} w_{,x} & 0 \\ 0 & \frac{1}{r} w_{,\theta} \\ \frac{1}{r} w_{,\theta} & w_{,x} \\ 0 & 0 \\ 0 & 0 \\ 0 & 0 \\ 0 & 0 \end{bmatrix} & [A_0]_{Donnell}^{FSDT} &= \begin{bmatrix} w_{0,x} & 0 \\ 0 & \frac{1}{r} w_{0,\theta} \\ \frac{1}{r} w_{0,\theta} & w_{0,x} \\ 0 & 0 \\ 0 & 0 \\ 0 & 0 \\ 0 & 0 \end{bmatrix} \\ [G] &= [G_d][g] & & \\ [G_d]_{Donnell}^{CLPT} &= \begin{bmatrix} 0 & 0 & \frac{\partial}{\partial x} \\ 0 & 0 & \frac{1}{r} \frac{\partial}{\partial \theta} \end{bmatrix} & & \\ [G_d]_{Donnell}^{FSDT} &= \begin{bmatrix} 0 & 0 & \frac{\partial}{\partial x} & 0 & 0 \\ 0 & 0 & \frac{1}{r} \frac{\partial}{\partial \theta} & 0 & 0 \end{bmatrix} \end{aligned} \quad (2.2.38)$$

For the Sanders's equations, obtained from Eq. (2.2.25) or Eq. (2.2.30) when $\delta_1 = 1$ and $\delta_2 = \delta_3 = 0$, the non-linear part of the strain vector can be written as (the matrices for the FSDT can be obtained by adding two rows at the end of $[A]$ and $[A_0]$):

$$\{\varepsilon_L\}_{Sanders}^{CLPT} = \frac{1}{2} \begin{bmatrix} w_{,x} & 0 & 0 \\ 0 & \frac{1}{r} w_{,\theta} - \frac{\cos \alpha}{r} v & -\frac{1}{r} w_{,\theta} + \frac{\cos \alpha}{r} v \\ \frac{1}{r} w_{,\theta} - \frac{\cos \alpha}{r} v & w_{,x} & -w_{,x} \\ 0 & 0 & 0 \\ 0 & 0 & 0 \\ 0 & 0 & 0 \end{bmatrix} \begin{bmatrix} w_{,x} \\ \frac{1}{r} w_{,\theta} \\ \frac{\cos \alpha}{r} v \end{bmatrix} \quad (2.2.39)$$

$$\{\varepsilon_{L_0}\}_{\substack{\text{Sanders} \\ \text{CLPT}}} = \begin{bmatrix} w_{0,x} & 0 & 0 \\ 0 & \frac{1}{r}w_{0,\theta} & -\frac{1}{r}w_{0,\theta} \\ \frac{1}{r}w_{0,\theta} & w_{0,x} & -w_{0,x} \\ 0 & 0 & 0 \\ 0 & 0 & 0 \\ 0 & 0 & 0 \end{bmatrix} \begin{bmatrix} w_{,x} \\ \frac{1}{r}w_{,\theta} \\ \frac{\cos \alpha}{r}v \end{bmatrix}$$

and writing in the form of Eq. (2.2.38), the matrices $[A]$, $[A_0]$ and $[G_d]$ for the Sanders' equations can be defined as:

$$[A]_{\substack{\text{Sanders} \\ \text{CLPT}}} = \begin{bmatrix} w_{,x} & 0 & 0 \\ 0 & \frac{1}{r}w_{,\theta} - \frac{\cos \alpha}{r}v & -\frac{1}{r}w_{,\theta} + \frac{\cos \alpha}{r}v \\ \frac{1}{r}w_{,\theta} - \frac{\cos \alpha}{r}v & w_{,x} & -w_{,x} \\ 0 & 0 & 0 \\ 0 & 0 & 0 \\ 0 & 0 & 0 \end{bmatrix}$$

$$[A_0]_{\substack{\text{Sanders} \\ \text{CLPT}}} = \begin{bmatrix} w_{0,x} & 0 & 0 \\ 0 & \frac{1}{r}w_{0,\theta} & -\frac{1}{r}w_{0,\theta} \\ \frac{1}{r}w_{0,\theta} & w_{0,x} & -w_{0,x} \\ 0 & 0 & 0 \\ 0 & 0 & 0 \\ 0 & 0 & 0 \end{bmatrix} \quad (2.2.40)$$

$$[G_d]_{\substack{\text{Sanders} \\ \text{CLPT}}} = \begin{bmatrix} 0 & 0 & \frac{\partial}{\partial x} \\ 0 & 0 & \frac{1}{r} \frac{\partial}{\partial \theta} \\ 0 & \frac{\cos \alpha}{r} & 0 \end{bmatrix} \quad [G_d]_{\substack{\text{Sanders} \\ \text{FSDT}}} = \begin{bmatrix} 0 & 0 & \frac{\partial}{\partial x} & 0 & 0 \\ 0 & 0 & \frac{1}{r} \frac{\partial}{\partial \theta} & 0 & 0 \\ 0 & \frac{\cos \alpha}{r} & 0 & 0 & 0 \end{bmatrix}$$

The variation of the strain vector $\{\delta\varepsilon\}$ can also be represented in matrix form as:

$$\begin{aligned} \{\delta\varepsilon\} &= \{\delta\varepsilon_0\} + \{\delta\varepsilon_L\} + \{\delta\varepsilon_{L_0}\} \\ \{\delta\varepsilon\} &= [\bar{B}]\{\delta c\} \end{aligned} \quad (2.2.41)$$

The non-linear part of the variation of the strain vector $\{\delta\varepsilon\}$ can be written as:

$$\begin{aligned}
\{\delta\varepsilon_L\}_{Donnell} &= \begin{bmatrix} w_{,x} & 0 \\ 0 & \frac{1}{r}w_{,\theta} \\ \frac{1}{r}w_{,\theta} & w_{,x} \\ 0 & 0 \\ 0 & 0 \\ 0 & 0 \\ 0 & 0 \end{bmatrix} [G]\{\delta c\} & \{\delta\varepsilon_{L_0}\}_{Donnell} &= \begin{bmatrix} w_{0,x} & 0 \\ 0 & \frac{1}{r}w_{0,\theta} \\ \frac{1}{r}w_{0,\theta} & w_{0,x} \\ 0 & 0 \\ 0 & 0 \\ 0 & 0 \\ 0 & 0 \end{bmatrix} [G]\{\delta c\} \\
\{\delta\varepsilon_L\}_{Donnell} &= [A][G]\{\delta c\} & \{\delta\varepsilon_{L_0}\}_{Donnell} &= [A_0][G]\{\delta c\} \\
&= [B_L]\{\delta c\} & &= [B_{L_0}]\{\delta c\}
\end{aligned} \tag{2.2.42}$$

Comparing Eq. (2.2.37) with Eq. (2.2.42) and the linear terms between Eqs. (2.2.25) and (2.2.26) for the FSDT, and between Eqs. (2.2.30) and (2.2.31) for the CLPT, it can be seen that:

$$\begin{aligned}
\{\delta\varepsilon_0\} &= [B_0]\{\delta c\} \\
\{\delta\varepsilon_L\} &= [B_L]\{\delta c\} \\
\{\delta\varepsilon_{L_0}\} &= [B_{L_0}]\{\delta c\} \\
\therefore [\bar{B}] &= [B_0] + [B_L] + [B_{L_0}]
\end{aligned} \tag{2.2.43}$$

The relations of Eqs. (2.2.35) and (2.2.43) and the definitions of $[B_0]$, $[B_L]$ and $[B_{L_0}]$ will be extensively applied along the next sections, and are applicable for both Donnell's and Sanders' equations.

The matrices $[d_0]$ of Eq. (2.2.36) and matrices $[G_d]$ of Eqs. (2.2.38) and (2.2.40) are matrices of differential operators that can be implemented in convenient ways, as detailed in Appendix B.

2.3 Shear Correction Factors

In the First-order Shear Deformation Theory (FSDT) for both composite and isotropic cases the shear strains and stresses are constant along the thickness. It is known from the elementary theory of homogeneous beams that the transverse shear stress varies parabolically along the beam thickness [74], while for composite laminate beams and plates the transverse shear stresses vary at least quadratically through the thickness [59]. This discrepancy between the actual and the approximated stress distribution will result in shear strain energies that are incorrect. The usual practice is to compute the transverse shear force resultants Q_x, Q_y multiplying the shear stiffness by a shear correction factor K . In other words, the shear correction factor is needed to force that the approximated shear strain state will render the same strain energy as the real shear strain state. Bathe (1996) [82] presents the shear correction factor as being the ratio between an equivalent and the real cross-sectional area, $K = A_s/A$, where the equivalent area A_s is calculated such as the average shear stress will produce the same strain energy as the real shear stress. In this thesis the equivalent area will not be used and K will be defined as the ratio between the shear strain energy obtained with the approximated and the real strain energy states. For an isotropic plate with rectangular cross-section the actual shear strain due to an applied shear force Q_y is [59]:

$$\gamma_{yz_actual} = \frac{3Q_y}{2Gwh} \left[1 - \left(\frac{2z}{h} \right)^2 \right]; -\frac{h}{2} \leq z \leq \frac{h}{2} \quad (2.3.1)$$

The strain energies corresponding to the actual strain U_{actual} and to the approximated strain U_{approx} can be written as [59]:

$$\begin{aligned} U_{actual} &= \frac{G}{2} \int_A \gamma_{yz_actual}^2 dA = \frac{3Q_y^2}{5Gwh} \\ U_{approx} &= \frac{G}{2} \int_A \gamma_{yz_approx}^2 dA = \frac{Q_y^2}{2Gwh} \end{aligned} \quad (2.3.2)$$

And the shear correction factor is defined by:

$$K = \frac{U_{approx}}{U_{actual}} = \frac{5}{6} \quad (2.3.3)$$

General purpose finite element solvers also implement shear corrections for the many different element types and cross-section shapes. In Abaqus [83] the shear correction for beam elements is given by the following formula:

$$\bar{K}_{\alpha 3} = f_p^\alpha K_{\alpha 3} \quad f_p^\alpha = \frac{1}{\left(1 + \xi \cdot SCF \frac{L^2 A}{12 I_{\alpha\alpha}}\right)}$$

$$\xi = \begin{cases} 1.0 & \text{for first order elements} \\ 10^{-4} & \text{for second order elements} \end{cases} \quad SCF = \text{slenderness compensation factor} \quad (0.25 \text{ by default}) \quad (2.3.4)$$

$$L = \text{length of the element} \quad A = \text{cross-sectional area}$$

$$I_{\alpha\alpha} = \text{inertia in the } \alpha\text{-direction}$$

where $\bar{K}_{\alpha 3}$ is the section shear stiffness in the α -direction (which can be 1 or 2, i.e. the local directions of the cross-section), f_p^α is a dimensionless factor used to prevent the shear stiffness from becoming too large in slender beam elements, $K_{\alpha 3}$ is the actual shear stiffness of the section, in force units. The actual shear stiffness of the section is defined by:

$$K_{\alpha 3} = kGA \quad (2.3.5)$$

where G is the elastic shear modulus and k a shear factor which depends on the section type. Cowper (1996) [84] provides shear factors for many cross sections, as shown in Table 2.3.1 (copied from the Abaqus Analysis User's Manual [83]).

The definitions presented herein will be used along the next chapters in order to compare the results from the developed semi-analytical models with finite elements' results.

Table 2.3.1: Shear factors for many cross sections defined by Cowper (1996) [84]

Section type	Shear factor, k	Section type	Shear factor
Arbitrary	1.0	L	1.0
Box	0.44	Meshed	1.0
Circular	0.89	Non-linear generalized	1.0
Elbow	0.85	Pipe	0.53
Generalized	1.0	Rectangular	0.85
Hexagonal	0.53	Trapezoidal	0.822
I (and T)	0.44		

2.4 Constitutive equations for the FSDT and CLPT

The constitutive equations for a laminate under a plane stress state and including the transverse shear components are given in Eqs. (2.1.25) and (2.1.26) for the membrane and bending components, respectively. Taking the relevant strain vector components from Eq. (2.2.23) based on Eq. (2.2.26) for the FSDT will result in the constitutive equations for the FSDT, from where the CLPT constitutive equations can be obtained as a special case. The membrane terms become:

$$\begin{Bmatrix} N_{xx} \\ N_{\theta\theta} \\ N_{x\theta} \\ Q_\theta \\ Q_x \end{Bmatrix} = \sum_{k=1}^N \begin{bmatrix} \bar{Q}_{11} & \bar{Q}_{12} & \bar{Q}_{16} & 0 & 0 \\ \bar{Q}_{12} & \bar{Q}_{22} & \bar{Q}_{26} & 0 & 0 \\ \bar{Q}_{16} & \bar{Q}_{26} & \bar{Q}_{66} & 0 & 0 \\ 0 & 0 & 0 & \bar{Q}_{44} & \bar{Q}_{45} \\ 0 & 0 & 0 & \bar{Q}_{45} & \bar{Q}_{55} \end{bmatrix}^{(k)} \int_{z_k}^{z_{k+1}} \begin{Bmatrix} \varepsilon_{xx}^{(0)} \\ \varepsilon_{\theta\theta}^{(0)} \\ \gamma_{x\theta}^{(0)} \\ \gamma_{\theta z}^{(0)} \\ \gamma_{xz}^{(0)} \end{Bmatrix} + z \begin{Bmatrix} \varepsilon_{xx}^{(1)} \\ \varepsilon_{\theta\theta}^{(1)} \\ \gamma_{x\theta}^{(1)} \\ 0 \\ 0 \end{Bmatrix} dz \quad (2.4.1)$$

where the null terms in $[\bar{Q}]^{(k)}$ allow separation of the force vector as follows:

$$\begin{Bmatrix} N_{xx} \\ N_{\theta\theta} \\ N_{x\theta} \end{Bmatrix} = \sum_{k=1}^N \begin{bmatrix} \bar{Q}_{11} & \bar{Q}_{12} & \bar{Q}_{16} \\ \bar{Q}_{12} & \bar{Q}_{22} & \bar{Q}_{26} \\ \bar{Q}_{16} & \bar{Q}_{26} & \bar{Q}_{66} \end{bmatrix}^{(k)} \left[\begin{Bmatrix} \varepsilon_{xx}^{(0)} \\ \varepsilon_{\theta\theta}^{(0)} \\ \gamma_{x\theta}^{(0)} \end{Bmatrix} \int_{z_k}^{z_{k+1}} dz + \begin{Bmatrix} \varepsilon_{xx}^{(1)} \\ \varepsilon_{\theta\theta}^{(1)} \\ \gamma_{x\theta}^{(1)} \end{Bmatrix} \int_{z_k}^{z_{k+1}} z dz \right] \quad (2.4.2)$$

$$\begin{Bmatrix} Q_\theta \\ Q_x \end{Bmatrix} = \sum_{k=1}^N \begin{bmatrix} \bar{Q}_{44} & \bar{Q}_{45} \\ \bar{Q}_{45} & \bar{Q}_{55} \end{bmatrix}^{(k)} \left[\begin{Bmatrix} \gamma_{\theta z}^{(0)} \\ \gamma_{xz}^{(0)} \end{Bmatrix} \int_{z_k}^{z_{k+1}} dz \right]$$

and integrating for z gives:

$$\begin{Bmatrix} N_{xx} \\ N_{\theta\theta} \\ N_{x\theta} \end{Bmatrix} = \sum_{k=1}^N \begin{bmatrix} \bar{Q}_{11} & \bar{Q}_{12} & \bar{Q}_{16} \\ \bar{Q}_{12} & \bar{Q}_{22} & \bar{Q}_{26} \\ \bar{Q}_{16} & \bar{Q}_{26} & \bar{Q}_{66} \end{bmatrix}^{(k)} \left[\begin{Bmatrix} \varepsilon_{xx}^{(0)} \\ \varepsilon_{\theta\theta}^{(0)} \\ \gamma_{x\theta}^{(0)} \end{Bmatrix} (z_{k+1} - z_k) + \begin{Bmatrix} \varepsilon_{xx}^{(1)} \\ \varepsilon_{\theta\theta}^{(1)} \\ \gamma_{x\theta}^{(1)} \end{Bmatrix} \frac{1}{2} (z_{k+1}^2 - z_k^2) \right] \quad (2.4.3)$$

$$\begin{Bmatrix} Q_\theta \\ Q_x \end{Bmatrix} = \sum_{k=1}^N \begin{bmatrix} \bar{Q}_{44} & \bar{Q}_{45} \\ \bar{Q}_{45} & \bar{Q}_{55} \end{bmatrix}^{(k)} \left[\begin{Bmatrix} \gamma_{\theta z}^{(0)} \\ \gamma_{xz}^{(0)} \end{Bmatrix} (z_{k+1} - z_k) \right]$$

Defining the matrices $[A]$, $[B]$, $[D]$ such that:

$$\begin{aligned} A_{ij} &= \sum_{k=1}^N \bar{Q}_{ij}^{(k)} (z_{k+1} - z_k) \\ B_{ij} &= \frac{1}{2} \sum_{k=1}^N \bar{Q}_{ij}^{(k)} (z_{k+1}^2 - z_k^2) \\ D_{ij} &= \frac{1}{3} \sum_{k=1}^N \bar{Q}_{ij}^{(k)} (z_{k+1}^3 - z_k^3) \end{aligned} \quad (2.4.4)$$

allows rewriting Eq. (2.4.3) as:

$$\begin{Bmatrix} N_{xx} \\ N_{\theta\theta} \\ N_{x\theta} \end{Bmatrix} = \begin{bmatrix} A_{11} & A_{12} & A_{16} \\ A_{12} & A_{22} & A_{26} \\ A_{16} & A_{26} & A_{66} \end{bmatrix} \begin{Bmatrix} \varepsilon_{xx}^{(0)} \\ \varepsilon_{\theta\theta}^{(0)} \\ \gamma_{x\theta}^{(0)} \end{Bmatrix} + \begin{bmatrix} B_{11} & B_{12} & B_{16} \\ B_{12} & B_{22} & B_{26} \\ B_{16} & B_{26} & B_{66} \end{bmatrix} \begin{Bmatrix} \varepsilon_{xx}^{(1)} \\ \varepsilon_{\theta\theta}^{(1)} \\ \gamma_{x\theta}^{(1)} \end{Bmatrix} \quad (2.4.5)$$

$$\begin{Bmatrix} Q_{\theta} \\ Q_x \end{Bmatrix} = \begin{bmatrix} A_{44} & A_{45} \\ A_{45} & A_{55} \end{bmatrix} \begin{Bmatrix} \gamma_{\theta z}^{(0)} \\ \gamma_{xz}^{(0)} \end{Bmatrix}$$

The same integration procedure can be applied to the bending terms of Eq. (2.1.26), separating the moment vector due to the null terms in the $[\bar{Q}]$ matrix, as follows:

$$\begin{Bmatrix} M_{xx} \\ M_{\theta\theta} \\ M_{x\theta} \end{Bmatrix} = \sum_{k=1}^N \begin{bmatrix} \bar{Q}_{11} & \bar{Q}_{12} & \bar{Q}_{16} \\ \bar{Q}_{12} & \bar{Q}_{22} & \bar{Q}_{26} \\ \bar{Q}_{16} & \bar{Q}_{26} & \bar{Q}_{66} \end{bmatrix}^{(k)} \left[\begin{Bmatrix} \varepsilon_{xx}^{(0)} \\ \varepsilon_{\theta\theta}^{(0)} \\ \gamma_{x\theta}^{(0)} \end{Bmatrix} \int_{z_k}^{z_{k+1}} z dz + \begin{Bmatrix} \varepsilon_{xx}^{(1)} \\ \varepsilon_{\theta\theta}^{(1)} \\ \gamma_{x\theta}^{(1)} \end{Bmatrix} \int_{z_k}^{z_{k+1}} z^2 dz \right] \quad (2.4.6)$$

$$\begin{Bmatrix} M_{\theta z} \\ M_{xz} \end{Bmatrix} = \sum_{k=1}^N \begin{bmatrix} \bar{Q}_{44} & \bar{Q}_{45} \\ \bar{Q}_{45} & \bar{Q}_{55} \end{bmatrix}^{(k)} \left[\begin{Bmatrix} \gamma_{\theta z}^{(0)} \\ \gamma_{xz}^{(0)} \end{Bmatrix} \int_{z_k}^{z_{k+1}} z dz \right]$$

Note that moments $M_{\theta z}$ and M_{xz} are present but they are not considered in the CLPT or the FSDT. The integration along z gives:

$$\begin{Bmatrix} M_{xx} \\ M_{\theta\theta} \\ M_{x\theta} \end{Bmatrix} = \sum_{k=1}^N \begin{bmatrix} \bar{Q}_{11} & \bar{Q}_{12} & \bar{Q}_{16} \\ \bar{Q}_{12} & \bar{Q}_{22} & \bar{Q}_{26} \\ \bar{Q}_{16} & \bar{Q}_{26} & \bar{Q}_{66} \end{bmatrix}^{(k)} \left[\begin{Bmatrix} \varepsilon_{xx}^{(0)} \\ \varepsilon_{\theta\theta}^{(0)} \\ \gamma_{x\theta}^{(0)} \end{Bmatrix} \frac{1}{2} (z_{k+1}^2 - z_k^2) + \begin{Bmatrix} \varepsilon_{xx}^{(1)} \\ \varepsilon_{\theta\theta}^{(1)} \\ \gamma_{x\theta}^{(1)} \end{Bmatrix} \frac{1}{3} (z_{k+1}^3 - z_k^3) \right] \quad (2.4.7)$$

Using the definitions of $[A]$, $[B]$, $[D]$ from Eq. (2.4.4):

$$\begin{Bmatrix} M_{xx} \\ M_{\theta\theta} \\ M_{x\theta} \end{Bmatrix} = \begin{bmatrix} B_{11} & B_{12} & B_{16} \\ B_{12} & B_{22} & B_{26} \\ B_{16} & B_{26} & B_{66} \end{bmatrix} \begin{Bmatrix} \varepsilon_{xx}^{(0)} \\ \varepsilon_{\theta\theta}^{(0)} \\ \gamma_{x\theta}^{(0)} \end{Bmatrix} + \begin{bmatrix} D_{11} & D_{12} & D_{16} \\ D_{12} & D_{22} & D_{26} \\ D_{16} & D_{26} & D_{66} \end{bmatrix} \begin{Bmatrix} \varepsilon_{xx}^{(1)} \\ \varepsilon_{\theta\theta}^{(1)} \\ \gamma_{x\theta}^{(1)} \end{Bmatrix} \quad (2.4.8)$$

The strain vectors for the FSDT and the CLPT can be arranged as shown in Eq. (2.2.32), repeated here for convenience:

$$\begin{aligned} \{\varepsilon\}_{CLPT}^T &= \{\varepsilon_{xx}^{(0)} \quad \varepsilon_{\theta\theta}^{(0)} \quad \gamma_{x\theta}^{(0)} \quad \varepsilon_{xx}^{(1)} \quad \varepsilon_{\theta\theta}^{(1)} \quad \gamma_{x\theta}^{(1)}\} \\ \{\varepsilon\}_{FSDT}^T &= \{\varepsilon_{xx}^{(0)} \quad \varepsilon_{\theta\theta}^{(0)} \quad \gamma_{x\theta}^{(0)} \quad \varepsilon_{xx}^{(1)} \quad \varepsilon_{\theta\theta}^{(1)} \quad \gamma_{x\theta}^{(1)} \quad \gamma_{\theta z}^{(0)} \quad \gamma_{xz}^{(0)}\} \end{aligned} \quad (2.4.9)$$

such that the constitutive matrices can be rearranged as shown in Eq. (2.4.10). Note that the shear correction factor K is included in the FSDT terms.

$$\begin{aligned}
[F]_{FSDT} &= \begin{bmatrix} A_{11} & A_{12} & A_{16} & B_{11} & B_{12} & B_{16} & 0 & 0 \\ A_{12} & A_{22} & A_{26} & B_{12} & B_{22} & B_{26} & 0 & 0 \\ A_{16} & A_{26} & A_{66} & B_{16} & B_{26} & B_{66} & 0 & 0 \\ B_{11} & B_{12} & B_{16} & D_{11} & D_{12} & D_{16} & 0 & 0 \\ B_{12} & B_{22} & B_{26} & D_{12} & D_{22} & D_{26} & 0 & 0 \\ B_{16} & B_{26} & B_{66} & D_{16} & D_{26} & D_{66} & 0 & 0 \\ 0 & 0 & 0 & 0 & 0 & 0 & KA_{44} & KA_{45} \\ 0 & 0 & 0 & 0 & 0 & 0 & KA_{45} & KA_{55} \end{bmatrix} \\
[F]_{CLPT} &= \begin{bmatrix} A_{11} & A_{12} & A_{16} & B_{11} & B_{12} & B_{16} \\ A_{12} & A_{22} & A_{26} & B_{12} & B_{22} & B_{26} \\ A_{16} & A_{26} & A_{66} & B_{16} & B_{26} & B_{66} \\ B_{11} & B_{12} & B_{16} & D_{11} & D_{12} & D_{16} \\ B_{12} & B_{22} & B_{26} & D_{12} & D_{22} & D_{26} \\ B_{16} & B_{26} & B_{66} & D_{16} & D_{26} & D_{66} \end{bmatrix}
\end{aligned} \tag{2.4.10}$$

For isotropic materials the constitutive matrix terms are calculated based on the expressions of Eq. (2.4.11).

$$\begin{aligned}
A_{11} &= Q_{11}h = \frac{Eh}{1-\nu^2} & D_{11} &= Q_{11}\frac{h^3}{12} = \frac{Eh^3}{12(1-\nu^2)} \\
A_{12} &= Q_{12}h = \frac{\nu Eh}{1-\nu^2} & D_{12} &= Q_{12}\frac{h^3}{12} = \frac{\nu Eh^3}{12(1-\nu^2)} \\
A_{22} &= Q_{22}h = \frac{Eh}{1-\nu^2} & D_{22} &= Q_{22}\frac{h^3}{12} = \frac{Eh^3}{12(1-\nu^2)} \\
A_{66} &= Q_{66}h = Gh & D_{66} &= Q_{66}\frac{h^3}{12} = \frac{Gh^3}{12} \\
A_{44} &= KG_{23}h & & \\
A_{55} &= KG_{13}h & &
\end{aligned} \tag{2.4.11}$$

In the current implementation [85] convenient functions to obtain the laminate constitutive matrix $[F]$ have been implemented and the reader should refer to the documentation for more details, under “compmech/composite”.

3 Non-Linear and Linear Buckling Formulation using the Ritz Method

The differential equations governing the mechanical behavior of conical shells can be obtained by a direct evaluation Newton's second law applied to a representative infinitesimal element [59] such as the one shown in Fig. 2.1.3. Most of the equations derived by Timoshenko ([74], [86], [61] [87]) are based on this type of analytical evaluation, requiring one to identify and mathematically describe the dependency of all the variables interacting in the representative element, which for complicated systems becomes a cumbersome and intractable task [59]. Moreover, some boundary conditions are not clearly determined only by analytical inspection [59], making it difficult to establish the whole set of equations required to solve complex systems. Based on this it is a common practice to obtain the governing equations of a given system from the total potential energy functional Π , by making it stationary with respect to the unknown field variables and integrating by parts in order to isolate the variation of these variables. Such approach will lead to the so called Euler-Lagrange equations.

The so called direct methods do not require the determination of the differential equations and neither the boundary conditions [88]. The Ritz method belongs to this class and its application to obtain the non-linear system of equations that solve the field variables related to the conical and cylindrical shells under discussion is presented along this chapter. A matrix notation is adopted where one can readily see the similarities between the Ritz and the Finite Element Method (FEM) [89], with the basic difference that for the Ritz method the unknown variables (called Ritz constants) correspond to the amplitudes of each term in the approximation functions while in the FEM the unknown variables (called degrees of freedom) correspond to the displacements and rotations of the elements' nodes. Besides the non-linear equations, the linear buckling equations will be obtained from a general non-linear eigenvalue problem.

Obtaining the proper set of approximation functions required for the Ritz method is one of the most important steps for a successful implementation, and the boundary conditions usually dictate the approximation functions to be selected. In this chapter a large set of boundary conditions will be covered through the application of elastic boundary conditions.

The detailed formulation of all the linear and non-linear matrices and vectors involved in the analysis' steps is presented and the integration schemes used to calculate them are explained. The solution schemes using such matrices are derived and the implementation of some algorithms used to solve these systems are detailed (Newton-Raphson with line search and Riks).

3.1 General Non-Linear Formulation

The total potential energy of a solid system can be expressed as:

$$\Pi = U + V \quad (3.1.1)$$

where U is the internal energy and V the external energy. The stationary condition of the total potential energy Π can be expressed as [59] [88]:

$$\delta\Pi = \delta U + \delta V = 0 \quad (3.1.2)$$

Note that in a non-linear incremental analysis Eq. (3.1.2) is usually not fulfilled at any arbitrary iteration due to the unbalance between the internal and external forces, and the resulting inequality can be represented by a residual force vector $\{R\}$:

$$\delta\Pi = \delta U + \delta V = \{\delta c\}^T \{R\} \quad (3.1.3)$$

where $\{\delta c\}$ is the variation of the Ritz constants vector. The definition of the residual force vector for a given iteration $(k - 1)$ is:

$$\{R\}^{(k-1)} = \{F_{int}\}^{(k-1)} - (\{F_{ext_0}\} + \lambda^{(k-1)}\{F_{ext_\lambda}\}) \quad (3.1.4)$$

with λ being a scalar load multiplier for the variable part of the external force vector $\{F_{ext_\lambda}\}$; vector $\{F_{ext_0}\}$ contains the external forces not subjected to the load multiplier and $\{F_{int}\}$ is internal force vector. For load controlled iterative methods, such as those belonging to the Newton-Raphson family, the multiplier λ is set constant ($\lambda^{(k-1)} = \lambda$) for a given load increment, while when using the Riks (arc-length) method the multiplier λ is variable within the load increment [82] [90]. In a first approach the formulation will be developed for the Newton-Raphson method since it will lead to the same structural matrices required for the other methods presented in the next sections.

The equilibrium is approached when $\{R\} \rightarrow \{0\}$ such that there will be a given iteration k where the equilibrium is finally achieved and $\{R\}^{(k)} = \{0\}$. Using a Taylor expansion at $\{R\}^{(k-1)}$ to find $\{R\}^{(k)}$ in terms of $\{R\}^{(k-1)}$, the following expression is obtained:

$$\{R\}^{(k)} = \{R\}^{(k-1)} + \left. \frac{\partial \{R\}}{\partial \{c\}} \right|_{(k-1)} \{\delta c\}^{(k)} + O(2) = \{0\} \quad (3.1.5)$$

Ignoring the 2nd and higher order terms, Eq. (3.1.5) becomes:

$$\{R\}^{(k)} = \{R\}^{(k-1)} + \{\delta R\}^{(k)} = \{0\} \quad (3.1.6)$$

In Eq. (3.1.5) the term $\left. \frac{\partial \{R\}}{\partial \{c\}} \right|_{(k-1)}$ corresponds to the structural tangent stiffness matrix $[K_T]$ at iteration $k - 1$, such that:

$$\begin{aligned} [K_T^{(k-1)}] &= \left. \frac{\partial \{R\}}{\partial \{c\}} \right|_{(k-1)} \\ \therefore \{\delta R\}^{(k)} &= [K_T^{(k-1)}] \{\delta c\} \end{aligned} \quad (3.1.7)$$

and using the definition of Eq. (3.1.7) into Eq. (3.1.5) leads to:

$$\{R\}^{(k-1)} + [K_T^{(k-1)}]\{\delta c\}^{(k)} = \{0\} \quad (3.1.8)$$

which can be solved for $\{\delta c\}$:

$$\{\delta c\}^{(k)} = -[K_T^{(k-1)}]^{-1}\{R\}^{(k-1)} \quad (3.1.9)$$

The set of Ritz constants is then updated with:

$$\{c\}^{(k)} = \{c\}^{(k-1)} + \{\delta c\}^{(k)} \quad (3.1.10)$$

To solve the non-linear problem the tangent stiffness matrix $[K_T]$ and the residual force vector $\{R\}$ must be calculated for every iteration in the full Newton-Raphson method and the vector of Ritz constants $\{c\}^{(k)}$ is updated for each iteration until the convergence is achieved, following a given criterion (cf. Section 3.9.5). In other non-linear algorithms discussed in the next sections the calculation of $[K_T]$ at each iteration is avoided since it is usually computationally expensive. Based on the definition of $\{R\}$ from Eq. (3.1.3) it can be seen that the energy functionals must be known. The internal energy can be represented for a general solid by the following integral:

$$U = \frac{1}{2} \int_{\mathcal{V}} \{\sigma\}^T \{\varepsilon\} d\mathcal{V} \quad (3.1.11)$$

and its variation renders:

$$\delta U = \frac{1}{2} \int_{\mathcal{V}} (\{\sigma\}^T \{\delta \varepsilon\} + \{\delta \sigma\}^T \{\varepsilon\}) d\mathcal{V} \quad (3.1.12)$$

In Section 2.1 it was shown that the stress vector $\{\sigma\}$ can be expressed in terms of the strain vector using the constitutive matrix $[C]$ as $\{\sigma\} = [C]\{\varepsilon\}$, such that:

$$\delta U = \frac{1}{2} \int_{\mathcal{V}} (\{\varepsilon\}^T [C] \{\delta \varepsilon\} + \{\delta \varepsilon\}^T [C] \{\varepsilon\}) d\mathcal{V} \quad (3.1.13)$$

Due to the symmetry of $[C]$ it comes that $\{\varepsilon\}^T [C] \{\delta \varepsilon\} = \{\delta \varepsilon\}^T [C] \{\varepsilon\}$, and:

$$\begin{aligned} \delta U &= \int_{\mathcal{V}} \{\delta \varepsilon\}^T [C] \{\varepsilon\} d\mathcal{V} \\ &= \int_{\mathcal{V}} \{\delta \varepsilon\}^T \{\sigma\} d\mathcal{V} \end{aligned} \quad (3.1.14)$$

The variation of the external energy δV when only conservative forces are present (i.e. forces not depending on the displacement field) can be represented by the general expression:

$$\delta V = -\{\delta c\}^T (\{F_{ext0}\} + \lambda \{F_{ext\lambda}\}) \quad (3.1.15)$$

As mentioned in Section 2.2.6, in the Ritz method the unknown displacement field $\{u\}$ is approximated, and the general expression can be used to represent this approximation:

$$\{u\} = [g]\{c\} \quad (3.1.16)$$

where the elements of $\{c\}$ is the vector containing the unknown set of Ritz constants. In Section 2.2.6 it is also shown that the strain vector $\{\varepsilon\}$ and its variation $\{\delta\varepsilon\}$ can be represented by the general form:

$$\begin{aligned} \{\varepsilon\} &= \{\varepsilon_0\} + \{\varepsilon_L\} + \{\varepsilon_{L_0}\} \\ \{\delta\varepsilon\} &= \{\delta\varepsilon_0\} + \{\delta\varepsilon_L\} + \{\delta\varepsilon_{L_0}\} \end{aligned} \quad (3.1.17)$$

where:

$$\begin{aligned} \{\varepsilon_0\} &= [B_0]\{c\} & \{\delta\varepsilon\} &= [\bar{B}]\{\delta c\} \\ \{\varepsilon_L\} &= \frac{1}{2}[B_L]\{c\} & \{\delta\varepsilon_0\} &= [B_0]\{\delta c\} \\ \{\varepsilon_{L_0}\} &= [B_{L_0}]\{c\} & \{\delta\varepsilon_L\} &= [B_L]\{\delta c\} \\ & & \{\delta\varepsilon_{L_0}\} &= [B_{L_0}]\{\delta c\} \\ & & \therefore [\bar{B}] &= [B_0] + [B_L] + [B_{L_0}] \end{aligned} \quad (3.1.18)$$

Substituting the strain definitions of Eqs. (3.1.15)–(3.1.18) into Eq. (3.1.3) gives the following expression for the residual force vector $\{R\}$:

$$\begin{aligned} \{\delta c\}^T \{R\} &= \delta U + \delta V \\ &= \{\delta c\}^T \int_{\mathcal{V}} [\bar{B}]^T \{\sigma\} d\mathcal{V} - \{\delta c\}^T (\{F_{ext_0}\} + \lambda \{F_{ext_\lambda}\}) \end{aligned} \quad (3.1.19)$$

which can be rearranged to obtain the expression for $\{R\}$:

$$\{R\} = \int_{\mathcal{V}} [\bar{B}]^T \{\sigma\} d\mathcal{V} - (\{F_{ext_0}\} + \lambda \{F_{ext_\lambda}\}) \quad (3.1.20)$$

Comparing to the definition of Eq. (3.1.4) it comes that:

$$\{F_{int}\} = \int_{\mathcal{V}} [\bar{B}]^T \{\sigma\} d\mathcal{V} \quad (3.1.21)$$

which is in accordance with the definition found in the literature [90]. The tangent stiffness matrix $[K_T]$ can be calculated using the definition of Eq. (3.1.7), where the variation $\{\delta R\}$ can be calculated from Eq. (3.1.20), giving:

$$\{\delta R\} = [K_T]\{\delta c\} = \delta \left(\int_{\mathcal{V}} [\bar{B}]^T \{\sigma\} d\mathcal{V} \right) - \delta (\{F_{ext_0}\} + \lambda \{F_{ext_\lambda}\}) \quad (3.1.22)$$

Considering only conservative external forces, i.e. no contacts or forces depending on the displacement field such as follower forces, Eq. (3.1.22) becomes:

$$[K_T]\{\delta c\} = \delta \left(\int_{\mathcal{V}} [\bar{B}]^T \{\sigma\} d\mathcal{V} \right) \quad (3.1.23)$$

$$= \int_{\mathcal{V}} [\delta \bar{B}]^T \{\sigma\} d\mathcal{V} + \int_{\mathcal{V}} [\bar{B}]^T \{\delta \sigma\} d\mathcal{V}$$

The left-hand integral, as shown in the next sections, can be written as:

$$\int_{\mathcal{V}} [\delta \bar{B}]^T \{\sigma\} d\mathcal{V} = [K_G] \{\delta c\} \quad (3.1.24)$$

where $[K_G]$ is the geometric stiffness matrix. The right-hand integral can be written as:

$$\begin{aligned} \int_{\mathcal{V}} [\bar{B}]^T \{\delta \sigma\} d\mathcal{V} &= \int_{\mathcal{V}} [\bar{B}]^T [C] \{\delta \varepsilon\} d\mathcal{V} = [K_L] \{\delta c\} \\ [K_L] &= \int_{\mathcal{V}} [\bar{B}]^T [C] [\bar{B}] d\mathcal{V} \end{aligned} \quad (3.1.25)$$

where $[K_L]$ is the constitutive matrix including large displacements. Expanding $[K_L]$'s integral will lead to the definition of other structural matrices:

$$\begin{aligned} [K_L] &= \int_{\mathcal{V}} [\bar{B}]^T [C] [\bar{B}] d\mathcal{V} \\ &= \int_{\mathcal{V}} ([B_0] + [B_L] + [B_{L_0}])^T [C] ([B_0] + [B_L] + [B_{L_0}]) d\mathcal{V} \\ &= [K_0] + [K_{0L}] + [K_{L0}] + [K_{LL}] \end{aligned} \quad (3.1.26)$$

with:

$$\begin{aligned} [K_0] &= \int_{\mathcal{V}} [B_0]^T [C] [B_0] d\mathcal{V} \\ [K_{0L}] &= \int_{\mathcal{V}} [B_0]^T [C] ([B_L] + [B_{L_0}]) d\mathcal{V} \\ [K_{L0}] &= \int_{\mathcal{V}} ([B_L] + [B_{L_0}])^T [C] [B_0] d\mathcal{V} = [K_{0L}]^T \\ [K_{LL}] &= \int_{\mathcal{V}} ([B_L] + [B_{L_0}])^T [C] ([B_L] + [B_{L_0}]) d\mathcal{V} \end{aligned} \quad (3.1.27)$$

The definitions derived along this section allow building the complete non-linear problem. The calculation of the tangent stiffness matrix $[K_T]$ resumes itself into the calculation of the four matrices: $[K_0]$, $[K_{0L}]$, $[K_{LL}]$ and $[K_G]$. Note that the relation $[K_{L0}] = [K_{0L}]^T$ is used to avoid a duplicated calculation of the corresponding integrals. The author verified that matrix $[K_{L0}]$ is the most time consuming to calculate, such that the use of this relation leads to about 40% of reduction in the computational time for the iterations where the tangent stiffness matrix $[K_T]$ must be calculated. The formulation given in this section is applicable to any structural problem where the external forces are conservative, i.e. do not depend on the displacement field (no follower forces or

contacts, for example). The next section will apply this formulation to the cylindrical and conical shells herein investigated.

3.2 Non-Linear Formulation for Conical and Cylindrical Shells

3.2.1 Definition of the Model

In Fig. 3.2.1 it is shown the conical model with the coordinate system adopted. A pressure load P is shown in Fig. 3.2.1–a, defined as positive in the direction of the z axis. A torsion load T and a compressive load F_C applied at the top edge are shown. Many perturbation loads F_{PLi} can be applied and one is schematically shown in Fig. 3.2.1–a. As shown in Fig. 3.2.1–b, the axial load F_C may be misaligned about the conical axis by ξ_{LA} , creating a bending moment M_{LA} , and the azimuth angle of this load asymmetry is given by ω .

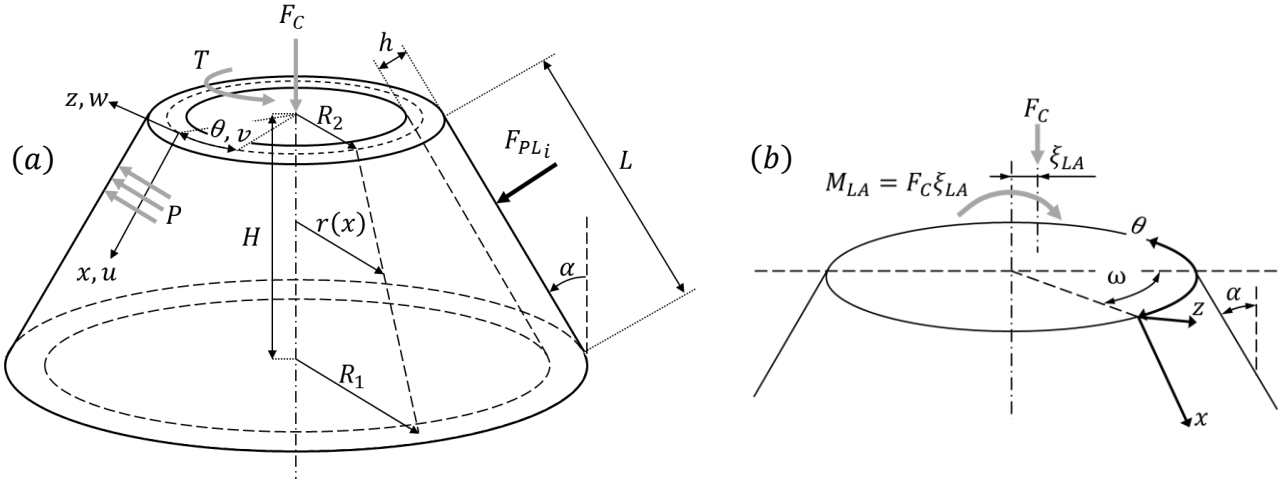


Fig. 3.2.1: Cone / Cylinder Model

It is convenient to define a general equation for the axial load distribution at the top edge in order to simulate cases with load asymmetries. In Fig. 3.2.2 it is illustrated such a general load distribution, which can be represented by the Fourier Series:

$$N_{xx_{top}} = N_{xx_0} + \sum_{\ell_2=1}^{n_2} \left(N_{xx_{\ell_2 a}} \sin(\ell_2(\theta - \omega)) + N_{xx_{\ell_2 b}} \cos(\ell_2(\theta - \omega)) \right) \quad (3.2.1)$$

the reader may note that the same indices used for the approximation functions presented in Section 3.6 are also used in Eq. (3.2.1).

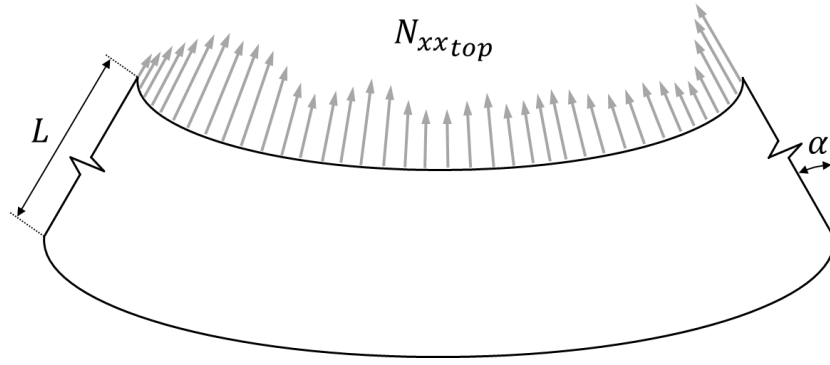


Fig. 3.2.2: Load Distribution at the Top Edge

Using the general load distribution of Fig. 3.2.2 makes the load case using F_C and M_{LA} illustrated in Fig. 3.2.1–*b* a special case, for which it is convenient to determine the values for the terms of Eq. (3.2.1) that will result on the equivalent load.

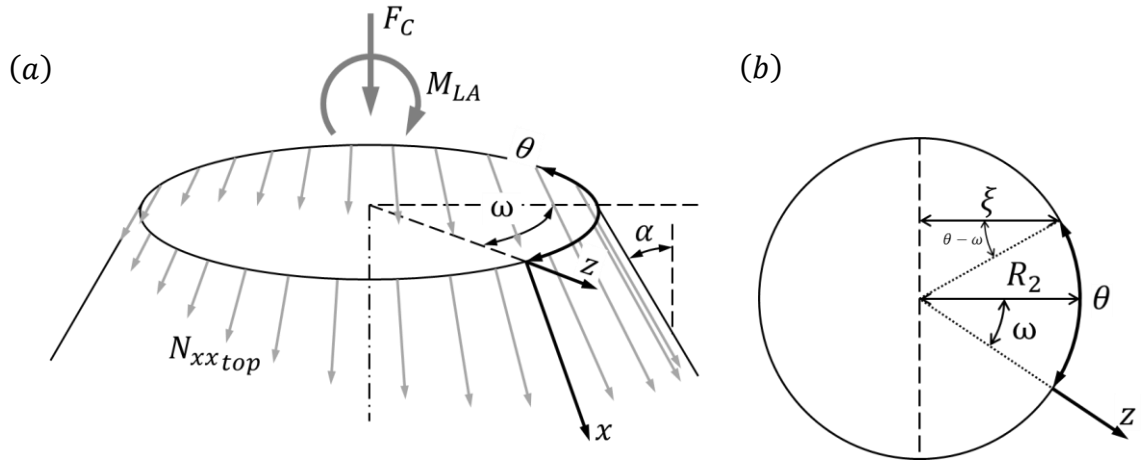


Fig. 3.2.3: Load Distribution due to Axial Load + Bending Moment

Consider Fig. 3.2.3, where it is shown F_C and M_{LA} with their equivalent load distribution $N_{xx_{top}}$. The relation between the axial load F_C (cf. Fig. 3.2.1) and the distributed load $N_{xx_{top}}$ is given by:

$$F_C = \cos \alpha \oint N_{xx_{top}} R_2 d\theta \quad (3.2.2)$$

which can be integrated to give:

$$N_{xx_0} = \frac{F_C}{2\pi R_2 \cos \alpha} \quad (3.2.3)$$

The following equation correlates the bending moment M_{LA} and the distributed load $N_{xx_{top}}$:

$$\begin{aligned} \xi &= R_2 \cos(\theta - \omega) \\ M_{LA} &= \cos \alpha \oint N_{xx_{top}} \xi R_2 d\theta \end{aligned} \quad (3.2.4)$$

which can be integrated to give:

$$N_{xx1b} = \frac{M_{LA}}{\pi(R_2)^2 \cos \alpha} \quad (3.2.5)$$

where N_{xx1b} is the term $N_{xx\ell_2b}$ for $\ell_2 = 1$. Equations (3.2.3) and (3.2.5) are valid no matter how many terms are chosen for the Fourier Series of Eq. (3.2.1).

3.2.2 Obtaining the Structural Matrices

Using the Equivalent Single-Layer (ESL) assumptions presented in Chapter 2, the three-dimensional integrations of Section 3.1 can be approximated by two-dimensional integrations. The plane stress state assumed for the First-order Shear Deformation Theory (FSDT), which includes the transverse stresses and the corresponding strains, can be written as:

$$\begin{aligned} \{\sigma\}^T &= \{\sigma_{xx} \quad \sigma_{\theta\theta} \quad \sigma_{x\theta} \quad \sigma_{\theta z} \quad \sigma_{xz}\} \\ \{\varepsilon\}^T &= \{\varepsilon_{xx} \quad \varepsilon_{\theta\theta} \quad \gamma_{x\theta} \quad \gamma_{\theta z} \quad \gamma_{xz}\} \end{aligned} \quad (3.2.6)$$

From the kinematic equations obtained for the FSDT and the CLPT in Sections 2.2.4 and 2.2.5, it can be seen that the strains are represented as:

$$\{\varepsilon\} = \{\varepsilon^{(0)}\} + z\{\varepsilon^{(1)}\} \quad (3.2.7)$$

where vector $\{\varepsilon^{(0)}\}$ contains the in-plane strains and vector $\{\varepsilon^{(1)}\}$ the rotational strains. Substituting Eqs. (3.2.6) and (3.2.7) into Eq. (3.1.11), taking only the relevant terms based on the results of Eqs. (2.2.25) and (2.2.30); and considering the integral of Eq. (2.2.18):

$$\begin{aligned} U &= \frac{1}{2} \int_V (\sigma_{xx} \varepsilon_{xx} + \sigma_{\theta\theta} \varepsilon_{\theta\theta} + \sigma_{x\theta} \gamma_{x\theta} + \sigma_{\theta z} \gamma_{\theta z} + \sigma_{xz} \gamma_{xz}) dV \\ U &= \frac{1}{2} \int_{z=-\frac{h}{2}}^{z=\frac{h}{2}} \int_{\theta=0}^{\theta=2\pi} \int_{x=0}^{x=L} \left(\sigma_{xx} \varepsilon_{xx}^{(0)} + z \sigma_{xx} \varepsilon_{xx}^{(1)} + \sigma_{\theta\theta} \varepsilon_{\theta\theta}^{(0)} + z \sigma_{\theta\theta} \varepsilon_{\theta\theta}^{(1)} + \sigma_{x\theta} \gamma_{x\theta}^{(0)} \right. \\ &\quad \left. + z \sigma_{x\theta} \gamma_{x\theta}^{(1)} + \sigma_{\theta z} \gamma_{\theta z}^{(0)} + \sigma_{xz} \gamma_{xz}^{(0)} \right) r dx d\theta dz \end{aligned} \quad (3.2.8)$$

applying the definitions of Eq. (2.1.24) and substituting the “y” variable by “ $r \cdot \theta$ ”:

$$\begin{aligned} U &= \frac{1}{2} \int_{\theta=0}^{\theta=2\pi} \int_{x=0}^{x=L} \left(N_{xx} \varepsilon_{xx}^{(0)} + M_{xx} \varepsilon_{xx}^{(1)} + N_{\theta\theta} \varepsilon_{\theta\theta}^{(0)} + M_{\theta\theta} \varepsilon_{\theta\theta}^{(1)} + N_{x\theta} \gamma_{x\theta}^{(0)} + M_{x\theta} \gamma_{x\theta}^{(1)} \right. \\ &\quad \left. + Q_{\theta} \gamma_{\theta z}^{(0)} + Q_x \gamma_{xz}^{(0)} \right) r dx d\theta \end{aligned} \quad (3.2.9)$$

Recalling that for the FSDT:

$$\begin{aligned}\{N\}_{FSDT}^T &= \{N_{xx} \quad N_{\theta\theta} \quad N_{x\theta} \quad M_{xx} \quad M_{\theta\theta} \quad M_{x\theta} \quad Q_\theta \quad Q_x\} \\ \{\varepsilon\}_{FSDT}^T &= \{\varepsilon_{xx}^{(0)} \quad \varepsilon_{\theta\theta}^{(0)} \quad \gamma_{x\theta}^{(0)} \quad \varepsilon_{xx}^{(1)} \quad \varepsilon_{\theta\theta}^{(1)} \quad \gamma_{x\theta}^{(1)} \quad \gamma_{\theta z}^{(0)} \quad \gamma_{xz}^{(0)}\}\end{aligned}\quad (3.2.10)$$

and for the CLPT:

$$\begin{aligned}\{N\}_{CLPT}^T &= \{N_{xx} \quad N_{\theta\theta} \quad N_{x\theta} \quad M_{xx} \quad M_{\theta\theta} \quad M_{x\theta}\} \\ \{\varepsilon\}_{CLPT}^T &= \{\varepsilon_{xx}^{(0)} \quad \varepsilon_{\theta\theta}^{(0)} \quad \gamma_{x\theta}^{(0)} \quad \varepsilon_{xx}^{(1)} \quad \varepsilon_{\theta\theta}^{(1)} \quad \gamma_{x\theta}^{(1)}\}\end{aligned}\quad (3.2.11)$$

it comes that Eq. (3.2.9) can be rewritten for both the FSDT and the CLPT as:

$$U = \frac{1}{2} \int_{\theta=0}^{\theta=2\pi} \int_{x=0}^{x=L} \{\varepsilon\}^T \{N\} r dx d\theta \quad (3.2.12)$$

and its variation becomes:

$$\delta U = \int_{\theta=0}^{\theta=2\pi} \int_{x=0}^{x=L} \{\delta\varepsilon\}^T \{N\} r dx d\theta \quad (3.2.13)$$

Using the definition of the variation of the external energy functional δV given in Eq. (3.1.15), the residual force vector $\{R\}$ defined in Eq. (3.1.3) becomes:

$$\begin{aligned}\{\delta c\}^T \{R\} &= \delta U + \delta V \\ &= \int_{\theta=0}^{\theta=2\pi} \int_{x=0}^{x=L} \{\delta\varepsilon\}^T \{N\} r dx d\theta - \{\delta c\}^T (\{F_{ext0}\} + \lambda \{F_{ext\lambda}\}) \\ &= \{\delta c\}^T \int_{\theta=0}^{\theta=2\pi} \int_{x=0}^{x=L} [\bar{B}]^T \{N\} r dx d\theta - \{\delta c\}^T (\{F_{ext0}\} + \lambda \{F_{ext\lambda}\})\end{aligned}\quad (3.2.14)$$

and rearranging gives:

$$\{R\} = \int_{\theta=0}^{\theta=2\pi} \int_{x=0}^{x=L} [\bar{B}]^T \{N\} r dx d\theta - (\{F_{ext0}\} + \lambda \{F_{ext\lambda}\}) \quad (3.2.15)$$

Comparing to the definition of Eq. (3.1.4) it comes that:

$$\{F_{int}\} = \int_{\theta=0}^{\theta=2\pi} \int_{x=0}^{x=L} [\bar{B}]^T \{N\} r dx d\theta \quad (3.2.16)$$

The tangent stiffness matrix $[K_T]$ can be calculated using the definition of Eq. (3.1.7), where the variation $\{\delta R\}$ can be calculated from Eq. (3.2.15), giving:

$$\{\delta R\} = [K_T] \{\delta c\} = \delta \left(\int_{\theta=0}^{\theta=2\pi} \int_{x=0}^{x=L} [\bar{B}]^T \{N\} r dx d\theta \right) - \delta (\{F_{ext0}\} + \lambda \{F_{ext\lambda}\}) \quad (3.2.17)$$

Considering only conservative forces ($\delta\{F_{ext}\} = \{0\}$):

$$\begin{aligned} [K_T]\{\delta c\} &= \delta \left(\int_{\theta=0}^{\theta=2\pi} \int_{x=0}^{x=L} [\bar{B}]^T \{N\} r dx d\theta \right) \\ &= \int_{\theta=0}^{\theta=2\pi} \int_{x=0}^{x=L} [\delta \bar{B}]^T \{N\} r dx d\theta + \int_{\theta=0}^{\theta=2\pi} \int_{x=0}^{x=L} [\bar{B}]^T \{\delta N\} r dx d\theta \end{aligned} \quad (3.2.18)$$

Based on Eqs. (3.1.25) – (3.1.27), the right-hand integral of Eq. (3.2.18) will result in:

$$\begin{aligned} [K_0] &= \int_{\theta=0}^{\theta=2\pi} \int_{x=0}^{x=L} [B_0]^T [F] [B_0] r dx d\theta \\ [K_{0L}] &= \int_{\theta=0}^{\theta=2\pi} \int_{x=0}^{x=L} [B_0]^T [F] ([B_L] + [B_{L_0}]) r dx d\theta \\ [K_{L0}] &= \int_{\theta=0}^{\theta=2\pi} \int_{x=0}^{x=L} ([B_L] + [B_{L_0}])^T [F] [B_0] r dx d\theta = [K_{0L}]^T \\ [K_{LL}] &= \int_{\theta=0}^{\theta=2\pi} \int_{x=0}^{x=L} ([B_L] + [B_{L_0}])^T [F] ([B_L] + [B_{L_0}]) r dx d\theta \end{aligned} \quad (3.2.19)$$

The next section will detail the solution of the left-hand integral of Eq. (3.2.18), related to the geometric stiffness matrix $[K_G]$.

3.2.3 Geometric Stiffness Matrix

The left-hand integral of Eq. (3.2.18) is related to the geometric stiffness matrix $[K_G]$ as:

$$[K_G]\{\delta c\} = \int_{\theta=0}^{\theta=2\pi} \int_{x=0}^{x=L} [\delta \bar{B}]^T \{N\} r dx d\theta \quad (3.2.20)$$

From the definition of $[\bar{B}]$ given in Section 2.2.6 in Eq. (2.2.43), the Eq. (3.2.20) becomes:

$$[\delta \bar{B}] = [\delta B_0] + [\delta B_L] + [\delta B_{L_0}] \quad (3.2.21)$$

Inspecting the elements of $[B_0]$, $[B_L]$ and $[B_{L_0}]$ given in Eqs. (2.2.36) and (2.2.42), it comes that (for both Donnell's and Sanders' equations):

$$[\delta \bar{B}] = [\delta B_L] = [\delta A][G] \quad (3.2.22)$$

Using Eq. (3.2.22) into Eq. (3.2.20) and expanding using the Donnell's equations given in Eq. (2.2.38):

$$[K_G]\{\delta c\} = \int_{\theta=0}^{\theta=2\pi} \int_{x=0}^{x=L} [G]^T \begin{bmatrix} \delta w_{,x} N_{xx} + \frac{1}{r} \delta w_{,\theta} N_{x\theta} \\ \frac{1}{r} \delta w_{,\theta} N_{\theta\theta} + \delta w_{,x} N_{x\theta} \end{bmatrix} r dx d\theta \quad (3.2.23)$$

which can be rearranged as:

$$[K_G]\{\delta c\} = \int_{\theta=0}^{\theta=2\pi} \int_{x=0}^{x=L} [G]^T [N_{K_G}] \begin{bmatrix} \delta w_{,x} \\ \frac{1}{r} \delta w_{,\theta} \end{bmatrix} r dx d\theta \quad (3.2.24)$$

$$[N_{K_G}]_{Donnell} = \begin{bmatrix} N_{xx} & N_{x\theta} \\ N_{x\theta} & N_{\theta\theta} \end{bmatrix}$$

using the definition of matrix $[G]$ given in Eqs. (2.2.37) and (2.2.38):

$$[K_G]\{\delta c\} = \left(\int_{\theta=0}^{\theta=2\pi} \int_{x=0}^{x=L} [G]^T [N_{K_G}] [G] r dx d\theta \right) \{\delta c\} \quad (3.2.25)$$

$$\therefore [K_G]_{Donnell} = \int_{\theta=0}^{\theta=2\pi} \int_{x=0}^{x=L} [G]^T [N_{K_G}] [G] r dx d\theta$$

Expanding Eq. (3.2.20) using Sanders' equations given in Eq. (2.2.40) renders:

$$[K_G]\{\delta c\} = \int_{\theta=0}^{\theta=2\pi} \int_{x=0}^{x=L} [G]^T \begin{bmatrix} \delta w_{,x} N_{xx} + \left(\frac{1}{r} \delta w_{,\theta} - \frac{\cos \alpha}{r} \delta v \right) N_{x\theta} \\ \left(\frac{1}{r} \delta w_{,\theta} - \frac{\cos \alpha}{r} \delta v \right) N_{\theta\theta} + \delta w_{,x} N_{x\theta} \\ \left(-\frac{1}{r} \delta w_{,\theta} + \frac{\cos \alpha}{r} \delta v \right) N_{\theta\theta} - \delta w_{,x} N_{x\theta} \end{bmatrix} r dx d\theta \quad (3.2.26)$$

which can be rearranged as:

$$[K_G]\{\delta c\} = \int_{\theta=0}^{\theta=2\pi} \int_{x=0}^{x=L} [G]^T [N_{K_G}] \begin{bmatrix} \delta w_{,x} \\ \frac{1}{r} \delta w_{,\theta} \\ \frac{\cos \alpha}{r} \delta v \end{bmatrix} r dx d\theta \quad (3.2.27)$$

$$[N_{K_G}]_{Sanders} = \begin{bmatrix} N_{xx} & N_{x\theta} & -N_{x\theta} \\ N_{x\theta} & N_{\theta\theta} & -N_{\theta\theta} \\ -N_{x\theta} & -N_{\theta\theta} & N_{\theta\theta} \end{bmatrix}$$

using the definition of matrix $[G]$ given in Eqs. (2.2.39) and (2.2.40) will result in:

$$[K_G]_{Sanders} = \int_{\theta=0}^{\theta=2\pi} \int_{x=0}^{x=L} [G]^T [N_{K_G}] [G] r dx d\theta \quad (3.2.28)$$

As expected, Eqs. (3.2.25) and (3.2.28) have the same format but one should keep in mind that matrices $[G]$ and $[N_{K_G}]$ will depend on the kinematic equations and on the non-linear theory chosen.

3.3 Initial Imperfections

The non-linear equations discussed in Section 2.2.6 can take into account an initial imperfection field w_0 that will directly influence the non-linear strains grouped in the vector component $\{\varepsilon_{L_0}\}$. Arbocz [91] proposed in 1969 the half-cosine function for the imperfection field, which can be written as:

$$w_0 = \sum_{j=0}^{n_0} \sum_{i=0}^{m_0} \cos\left(\frac{i\pi x}{L}\right) (A_{ij} \cos(j\theta) + B_{ij} \sin(j\theta)) \quad (3.3.1)$$

where A_{ij} and B_{ij} are the amplitudes of each corresponding base function. The derivatives $w_{0,x}$ and $w_{0,\theta}$ used in the non-linear kinematic equations are:

$$\begin{aligned} w_{0,x} &= \sum_{j=0}^{n_0} \sum_{i=0}^{m_0} -\frac{i\pi}{L} \sin\left(\frac{i\pi x}{L}\right) (A_{ij} \cos(j\theta) + B_{ij} \sin(j\theta)) \\ w_{0,\theta} &= \sum_{j=0}^{n_0} \sum_{i=0}^{m_0} \cos\left(\frac{i\pi x}{L}\right) j (-A_{ij} \sin(j\theta) + B_{ij} \cos(j\theta)) \end{aligned} \quad (3.3.2)$$

The coefficients A_{ij} and B_{ij} are calculated in the implemented routines [85] using the least-squares method of NumPy [6], and one implementation using pure Python/NumPy is given in Eq. (C.2). The three dimensional points corresponding to the geometric imperfections used in this thesis are obtained using the ATOS imperfection measurement system [92], when not otherwise specified. In the current implementation [85] Eq. (3.3.1) is represented in matrix form as:

$$\begin{aligned} w_0 &= \{a\}^T \{c_0\} \\ \{a\} &= \{f_{x_0} \sin(0\theta) \quad f_{x_0} \cos(0\theta) \quad f_{x_1} \sin(0\theta) \quad f_{x_1} \cos(0\theta) \quad \cdots \quad f_{x_{m_0}} \sin(0\theta) \quad f_{x_{m_0}} \cos(0\theta) \\ &\quad \cdots \quad f_{x_i} \sin(j\theta) \quad f_{x_i} \cos(j\theta) \quad \cdots \quad f_{x_{m_0}} \sin(n_0\theta) \quad f_{x_{m_0}} \cos(n_0\theta)\} \\ f_{x_i} &= \cos\left(\frac{i\pi x}{L}\right) \end{aligned} \quad (3.3.3)$$

where $\{c_0\}$ contains the coefficients A_{ij} and B_{ij} arranged in vector form. Analogously, the functions $w_{0,x}(x, \theta)$ and $w_{0,\theta}(x, \theta)$ are also implemented in the matrix form of Eq. (3.3.3), as shown in Eq. (3.3.4).

$$w_{0,x} = \left(\frac{\partial \{a\}}{\partial x}\right)^T \{c_0\} \quad w_{0,\theta} = \left(\frac{\partial \{a\}}{\partial \theta}\right)^T \{c_0\} \quad (3.3.4)$$

3.4 Linear Buckling Formulation

The linear buckling behavior can be calculated applying the neutral equilibrium criterion [71] [93]:

$$\delta^2 \Pi = \delta(\delta U + \delta V) = 0 \quad (3.4.1)$$

Using the definition of δU from Eq. (3.1.14) and the definition of δV from Eq. (3.1.15):

$$\delta \left(\{\delta c\}^T \int_V [\bar{B}]^T \{\sigma\} dV \right) - \delta \left(\{\delta c\}^T (\{F_{ext0}\} + \lambda \{F_{ext\lambda}\}) \right) = 0 \quad (3.4.2)$$

When only conservative forces are used:

$$\{\delta c\}^T \left(\int_V [\delta \bar{B}]^T \{\sigma\} dV + \int_V [\bar{B}]^T \{\delta \sigma\} dV \right) = 0 \quad (3.4.3)$$

which has the integrals analogous to Eq. (3.1.23), whose solution is known, leading to:

$$\{\delta c\}^T ([K_G] + [K_L]) \{\delta c\} = 0 \quad (3.4.4)$$

Since Eq. (3.4.4) must hold for any variation $\{\delta c\}$, it comes that at the buckling point:

$$\det([K_G] + [K_L]) = 0 \quad (3.4.5)$$

Evaluating the elements of the constitutive stiffness matrix $[K_L]$ it can be seen that only positive terms are possible, and therefore $[K_L]$ is positive definite. On the other hand $[K_G]$ may contain negative terms when compressive stresses are present. Assuming that all the stresses are linearly adjusted by an unknown load multiplier λ , Eq. (3.4.5) can be rewritten as a generalized eigenvalue problem [94], giving:

$$[K_L]\{\Phi\} = -\lambda[K_G]\{\Phi\} \quad (3.4.6)$$

where $\{\Phi\}$ is an eigenvector that corresponds to the eigenvalue λ . Since $[K_L]$ is not a singular matrix the eigenvalue problem can also be written as a standard eigenvalue problem [94]:

$$[K_L]^{-1}[K_G]\{\Phi\} = \frac{1}{-\lambda}[I]\{\Phi\} \quad (3.4.7)$$

where $[I]$ is an identity matrix. The use of Eq. (3.4.7) with the sparse matrix solvers of SciPy ([6] [7]) allow a high performance calculation of a desired number of eigenvalue/eigenvector pairs. The author observed that some numerical adjusts may considerably speed up the solver; and in the implementation adopted for this thesis [85] a much higher convergence was achieved by changing the sign of the right-hand side of Eq. (3.4.7), using an initial guess of 1 for the eigenvalue and then correcting the sign of the obtained eigenvalues.

The linear buckling equations can be directly obtained from Eqs. (3.4.6) or (3.4.7) by using the linear stiffness matrix and initial stress state, which from Fig. 3.2.1 can be calculated with the following expressions:

$$N_{xx_0} = \frac{-F_c}{2\pi r \cos \alpha} + \frac{P r}{2 \cos \alpha}; \quad N_{\theta\theta_0} = \frac{P r}{\cos \alpha}; \quad N_{x\theta_0} = \frac{-T}{2\pi r^2} \quad (3.4.8)$$

Replacing the quantities of Eq. (3.4.8) to calculate $[N_{K_G}]$ using Eqs. (3.2.24) or (3.2.27) for the Donnell's or Sanders' equations will result in the geometric stiffness matrix due to the initial stress state, called $[K_{G_0}]$. Using $[K_{G_0}]$ and the linear stiffness matrix $[K_0]$ into Eq. (3.4.6) will give the linear buckling equations in its generalized form:

$$[K_0]\{\Phi\} = -\lambda[K_{G_0}]\{\Phi\} \quad (3.4.9)$$

Similarly, Eq. (3.4.7) could be used to obtain the linear buckling equations in its standard form.

3.4.1 Combined Load Cases

Considering Fig. 3.2.1 it can be seen that a compressive load F_C , a torsion load T and a pressure load P are applied simultaneously such that in order to evaluate the linear buckling load of an axially compressed structure the torque and the pressure loads should be set to zero, such that in Eq. (3.4.9) the load multiplier λ will give the amplitude of the compressive load that causes the structural instability.

However, if in the example above one has to calculate the maximum compressive load of a pressurized shell or the maximum torque load of a pre-axially compressed shell, the use of Eq. (3.4.9) no longer gives the correct results, since the load multiplier acts on the whole initial stress state. Separating matrix $[K_{G_0}]$ according to each load component:

$$[K_{G_0}] = [K_{G_0}]_{F_C} + [K_{G_0}]_T + [K_{G_0}]_P \quad (3.4.10)$$

makes it possible to rewrite the eigenvalue problem according to the desired combined load case, and four combined load cases are enumerated below:

- i. find the critical axial load for a fixed torsion load and without pressure

$$([K_0] + [K_{G_0}]_T)\{\Phi\} = -\lambda[K_{G_0}]_{F_C}\{\Phi\} \quad (3.4.11)$$

- ii. find the critical axial load for a fixed pressure load and without torsion

$$([K_0] + [K_{G_0}]_P)\{\Phi\} = -\lambda[K_{G_0}]_{F_C}\{\Phi\} \quad (3.4.12)$$

- iii. find the critical torsion load for a fixed axial load and without pressure

$$([K_0] + [K_{G_0}]_{F_C})\{\Phi\} = -\lambda[K_{G_0}]_T\{\Phi\} \quad (3.4.13)$$

- iv. find the critical axial load for a fixed torsion and a fixed pressure

$$([K_0] + [K_{G_0}]_T + [K_{G_0}]_P)\{\Phi\} = -\lambda[K_{G_0}]_{F_C}\{\Phi\} \quad (3.4.14)$$

Note in Eqs. (3.4.11)–(3.4.14) that the fixed load components go in the left-hand side of the equations, while the load components multiplying λ go in the right-hand side. Other combined load cases are possible and the reader will find it straightforward to build new eigenvalue equations based on the examples given.

3.5 Elastic Boundary Conditions

Elastic boundary conditions are added to the formulation using one approach which is an extended version of what Som and Deb [95] recently published for isotropic cylinders. The distributed elastic stiffnesses for the bottom and top edges are schematically shown in Fig. 3.5.1.

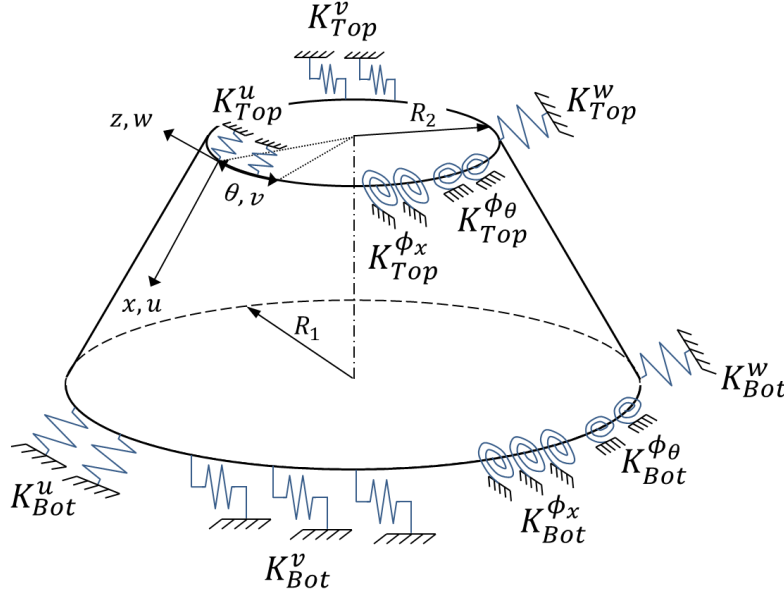


Fig. 3.5.1: Elastic Boundary Conditions

The strain energy associated with the elastic constraints can be written as:

$$U_e = \frac{1}{2} \oint \left(K_{u_{Bot}} u^2|_{x=L} + K_{v_{Bot}} v^2|_{x=L} + K_{w_{Bot}} w^2|_{x=L} + K_{\phi_{x_{Bot}}} \phi_x^2|_{x=L} + K_{\phi_{\theta_{Bot}}} \phi_\theta^2|_{x=L} \right) R_1 d\theta + \frac{1}{2} \oint \left(K_{u_{Top}} u^2|_{x=0} + K_{v_{Top}} v^2|_{x=0} + K_{w_{Top}} w^2|_{x=0} + K_{\phi_{x_{Top}}} \phi_x^2|_{x=0} + K_{\phi_{\theta_{Top}}} \phi_\theta^2|_{x=0} \right) R_2 d\theta \quad (3.5.1)$$

Writing in matrix form and calculating the first variation:

$$\delta U_e = \{c\} [K_e] \{\delta c\} \quad (3.5.2)$$

$$[K_e] = \oint \left(R_1 [g|_{x=L}]^T [K_{Bot}] [g|_{x=L}] + R_2 [g|_{x=0}]^T [K_{Top}] [g|_{x=0}] \right) d\theta$$

with:

$$[K_{Bot}] = \begin{bmatrix} K_{Bot}^u & & & & \\ & K_{Bot}^v & & & \\ & & K_{Bot}^w & & \\ & & & K_{Bot}^{\phi_x} & \\ & & & & K_{Bot}^{\phi_\theta} \end{bmatrix} \quad [K_{Top}] = \begin{bmatrix} K_{Top}^u & & & & \\ & K_{Top}^v & & & \\ & & K_{Top}^w & & \\ & & & K_{Top}^{\phi_x} & \\ & & & & K_{Top}^{\phi_\theta} \end{bmatrix} \quad (3.5.3)$$

In the next sections the elastic stiffnesses of Eq. (3.5.3) will be referred to as $K^u, K^v, \dots, K^{\phi_\theta}$, omitting the subscripts “Bot” and “Top” when applicable to both edges. Assuming a linear stiffness behavior for all the elastic constraints, their contributions of $[K_{Bot}]$ and $[K_{Top}]$ to the structural

stiffness can be considered into the linear stiffness matrix $[K_0]$, and the new linear stiffness matrix considering the elastic boundary conditions becomes:

$$[K_{0e}] = [K_0] + [K_e] \quad (3.5.4)$$

For the FSDT the matrix of containing the base function $[g]$ has five lines:

$$[g]_{FSDT}^T = [[g^u] \quad [g^v] \quad [g^w] \quad [g^{\phi_x}] \quad [g^{\phi_\theta}]] \quad (3.5.5)$$

which is already compatible to the format required in Eq. (3.5.2). On the other hand, for the CLPT matrix $[g]$ has by definition only three lines:

$$[g]_{CLPT}^T = [[g^u] \quad [g^v] \quad [g^w]] \quad (3.5.6)$$

such that the rotations ϕ_x and ϕ_θ have to be calculated and included as additional rows:

$$\begin{aligned} [g^{\phi_x}] &= -\frac{\partial [g^w]}{\partial x} \\ [g^{\phi_\theta}] &= -\frac{1}{r} \frac{\partial [g^w]}{\partial \theta} \end{aligned} \quad (3.5.7)$$

$$[g]_{CLPT \text{ extended}}^T = [[g^u] \quad [g^v] \quad [g^w] \quad [g^{\phi_x}] \quad [g^{\phi_\theta}]]$$

Equations (3.5.1)–(3.5.4) are general for any distribution of elastic stiffness, and for this thesis all the stiffnesses will be assumed constant. Using the elastic boundary condition formulation presented and the proper set of approximation functions for $u, v, w, \phi_x, \phi_\theta$ it is possible to obtain many boundary conditions by setting the right values for each elastic constant. Table 3.5.1 shows the values that should be adopted for the constants in order to obtain the 4 most common types of boundary conditions usually found in the literature and that will be investigated in more detail along this thesis. Note that an infinite value (∞) is actually implemented using a very high number (10^8 when not otherwise specified) and that any behavior between SS and CC can be achieved by changing the K^{ϕ_x} constants. In the current implementation it is possible to use different boundary conditions between the bottom and top edges [85].

Table 3.5.1: Elastic Constants for each Boundary Condition

Simply Supported		Clamped	
SS1: $u = v = w = 0$	$K^u = K^v = K^w = \infty$ $K^{\phi_x} = K^{\phi_\theta} = 0$	CC1: $u = v = w = w_{,x} = 0$	$K^u = K^v = K^w = K^{\phi_x} = \infty$ $K^{\phi_\theta} = 0$
SS2: $v = w = 0$	$K^v = K^w = \infty$ $K^u = K^{\phi_x} = K^{\phi_\theta} = 0$	CC2: $v = w = w_{,x} = 0$	$K^v = K^w = K^{\phi_x} = \infty$ $K^u = K^{\phi_\theta} = 0$
SS3: $u = w = 0$	$K^u = K^w = \infty$ $K^v = K^{\phi_x} = K^{\phi_\theta} = 0$	CC3: $u = w = w_{,x} = 0$	$K^u = K^w = K^{\phi_x} = \infty$ $K^v = K^{\phi_\theta} = 0$
SS4: $w = 0$	$K^w = \infty$ $K^u = K^v = K^{\phi_x} = K^{\phi_\theta} = 0$	CC4: $w = w_{,x} = 0$	$K^w = K^{\phi_x} = \infty$ $K^u = K^v = K^{\phi_\theta} = 0$

3.6 Approximation Functions

One of the limitations of the Ritz method is the difficulty to find a correct set of approximation functions for a given problem ([59], [88]). Some considerations are important when seeking for the right of approximation functions and Reddy (2002) [88] presents a detailed description of two properties that these functions should have:

- i. Convergence: the error should decrease up to a required tolerance when the number of terms is increased
- ii. Completeness: the increment in the number of terms must be so that it will pass through the required order of the real solution. In a polynomial approximation, for example, if the real solution is $u(x) = ax^2 + bx^3 + cx^5$, one sequence of approximations of the form $u_{approx_m}(x) = c_m x^{2m+1}, m = 0, 1, 2, \dots$ is not complete and will never achieve the true solution when m is increased

The fact that the rotations are connected to the normal displacements in the CLPT makes it harder to find approximation functions that satisfy the clamped boundary conditions since the first derivate must also fulfill the boundary conditions where $w = 0$ and $\phi_x = 0$. For the FSDT, since w and ϕ_x have independent approximation functions, it is usually simpler to cope with the boundary conditions and therefore it is simpler to find the right set of approximation functions. However, the inclusion of elastic restraints as explained in Section 3.5 allowed approximation functions of the same complexity for both the CLPT and the FSDT, revealing an additional benefit of this approach.

In the Ritz method the approximation function is composed of a base function g_i and a Ritz constant c_i that gives the amplitude of the function. It is crucial for the base functions g_i to:

- i. satisfy the essential boundary conditions of the problem
- ii. be contiguous along the domain, in order to be used in the variational statement
- iii. be independent from any other base function g_j

A complete Fourier Series [96] can be used to approximate a given field variable in the 2-D domain of the structural model shown in Fig. 3.2.1, giving:

$$f(x, \theta, \{c\}) = \sum_{i=0}^m \sum_{j=0}^n c_{ij_a} \sin\left(i\pi \frac{x}{L}\right) \sin(j\theta) + c_{ij_b} \sin\left(i\pi \frac{x}{L}\right) \cos(j\theta) + c_{ij_c} \cos\left(i\pi \frac{x}{L}\right) \sin(j\theta) + c_{ij_d} \cos\left(i\pi \frac{x}{L}\right) \cos(j\theta) \quad (3.6.1)$$

where c_{ij} represents the Ritz constants contained in $\{c\}$. Note that for a complete series the indices must start at zero. When $j = 0$ the expressions reduce to:

$$f(x, \{c\}) = \sum_{i=0}^m c_{i0_b} \sin\left(i\pi \frac{x}{L}\right) + c_{i0_d} \cos\left(i\pi \frac{x}{L}\right) \quad (3.6.2)$$

which is a function of x only. Considering this observation, Eq. (3.6.1) can be rewritten as:

$$f(x, \theta, \{c\}) = \sum_{i_1=0}^{m_1} (c_{i_1 a} g_{i_1 a} + c_{i_1 b} g_{i_1 b}) + \sum_{i_2=0}^{m_2} \sum_{j_2=1}^{n_2} (c_{i_2 j_2 a} g_{i_2 j_2 a} + c_{i_2 j_2 b} g_{i_2 j_2 b} + c_{i_2 j_2 c} g_{i_2 j_2 c} + c_{i_2 j_2 d} g_{i_2 j_2 d}) \quad (3.6.3)$$

with:

$$\begin{aligned} g_{i_1 a} &= \sin\left(i_1 \pi \frac{x}{L}\right) \\ g_{i_1 b} &= \cos\left(i_1 \pi \frac{x}{L}\right) \\ g_{i_2 j_2 a} &= \sin\left(i_2 \pi \frac{x}{L}\right) \sin(j_2 \theta) \\ g_{i_2 j_2 b} &= \sin\left(i_2 \pi \frac{x}{L}\right) \cos(j_2 \theta) \\ g_{i_2 j_2 c} &= \cos\left(i_2 \pi \frac{x}{L}\right) \sin(j_2 \theta) \\ g_{i_2 j_2 d} &= \cos\left(i_2 \pi \frac{x}{L}\right) \cos(j_2 \theta) \end{aligned} \quad (3.6.4)$$

which can be written in matrix form as:

$$f(x, \theta, \{c\}) = [g_1^f] \{c_1^f\} + [g_2^f] \{c_2^f\} \quad (3.6.5)$$

where $\{c_1^f\}$ and $\{c_2^f\}$ contains the Ritz constants for the field variable f : $c_{i_1 a}$, $c_{i_1 b}$, ... and $c_{i_2 j_2 a}$, $c_{i_2 j_2 b}$, ..., respectively; matrices $[g_1^f]$ and $[g_2^f]$ are the corresponding base functions. The format of Eqs. (3.6.3) and (3.6.5) is preferred over the format of Eq. (3.6.1) because it allows the use of a different number of terms for the functions depending only on x (axisymmetric) by setting $m_1 \neq m_2$. Bürmann et al (2006) used a similar separation for approximation functions applied to stiffened panels [97]. Additional functions will be required and added to Eq. (3.6.3) in order account for the two non-homogeneous boundary conditions of the proposed model (cf. Fig. 3.2.1), i.e. the axial shortening caused by the axial compression and the torsion, both discussed in the present section. The non-homogeneous boundary conditions will be included in a third set of base functions $[g_0^f]$ and Ritz constants $\{c_0^f\}$, such that the field variable f can be approximated as:

$$f(x, \theta, \{c\}) = [g_0^f] \{c_0^f\} + [g_1^f] \{c_1^f\} + [g_2^f] \{c_2^f\} \quad (3.6.6)$$

From Fig. 3.2.1 it can be seen that the field variables being approximated for the conical and cylindrical shells are those contained in the displacement vector $\{u\}^T = \{u \quad v \quad w \quad \phi_x \quad \phi_\theta\}$ for the FSDT and $\{u\}^T = \{u \quad v \quad w\}$ for the CLPT. A proper choice of which terms of Eq. (3.6.3) will be selected for each field variable must be done considering the boundary conditions. In this thesis approximation functions that cover all the boundary condition shown in Table 3.5.1 will be developed and they will result in four different models as detailed in the proceeding discussion.

The base functions can be arranged in order to include all the field variables in a single matrix, such that, for the CLPT:

$$\begin{aligned}
[g_0]_{CLPT}^T &= [[g_0^u] \quad [g_0^v] \quad [g_0^w]] \\
[g_1]_{CLPT}^T &= [[g_1^u] \quad [g_1^v] \quad [g_1^w]] \\
[g_2]_{CLPT}^T &= [[g_2^u] \quad [g_2^v] \quad [g_2^w]]
\end{aligned} \tag{3.6.7}$$

and for the FSDT:

$$\begin{aligned}
[g_0]_{FSDT}^T &= [[g_0^u] \quad [g_0^v] \quad [g_0^w] \quad [g_0^{\phi_x}] \quad [g_0^{\phi_\theta}]] \\
[g_1]_{FSDT}^T &= [[g_1^u] \quad [g_1^v] \quad [g_1^w] \quad [g_1^{\phi_x}] \quad [g_1^{\phi_\theta}]] \\
[g_2]_{FSDT}^T &= [[g_2^u] \quad [g_2^v] \quad [g_2^w] \quad [g_2^{\phi_x}] \quad [g_2^{\phi_\theta}]]
\end{aligned} \tag{3.6.8}$$

Using the base functions presented in the forms of Eq. (3.6.7) or Eq. (3.6.8), the displacement vector $\{u\}$ can be written as:

$$\{u\} = \begin{Bmatrix} u \\ v \\ w \end{Bmatrix} = [g_0]\{c_0\} + [g_1]\{c_1\} + [g_2]\{c_2\} = [[g_0] \quad [g_1] \quad [g_2]] \begin{Bmatrix} \{c_0\} \\ \{c_1\} \\ \{c_2\} \end{Bmatrix} = [g]\{c\} \tag{3.6.9}$$

The non-homogeneous boundary condition terms that form matrix $[g_0]$ are shown in Eq. (3.6.10), which for the model of Fig. 3.2.1 are the top axial displacement of the “testing machine” u_{TM} and the top angular displacement θ_T . Note how the functions contained in $[g_0]$ will allow a linear shortening and a linear torsion. An important observation is that u_{TM} is not measured along the x axis, but along the axial direction (which coincide for cylindrical shells), allowing a convenient correlation between u_{TM} and the applied axial load F_C , as detailed in Sections 3.2.1 and 3.7.

$$\{c_0\}^T = \{u_{TM} \quad \theta_T\}$$

$$[g_0]_{CLPT} = \begin{bmatrix} \frac{(L-x)}{L \cos \alpha} & 0 \\ 0 & \frac{(L-x)R_2}{L} \\ 0 & 0 \end{bmatrix} \quad [g_0]_{FSDT} = \begin{bmatrix} \frac{(L-x)}{L \cos \alpha} & 0 \\ 0 & \frac{(L-x)R_2}{L} \\ 0 & 0 \\ 0 & 0 \\ 0 & 0 \end{bmatrix} \tag{3.6.10}$$

Equation (3.6.11) shows a sub-matrix of the base functions contained in $[g_1]$. It starts at column q and the calculation of the column index is also given for both the CLPT and the FSDT.

$$\begin{aligned}
[g_1]_{CLPT} &= \begin{bmatrix} & g_{1q}^u & & 0 & & \\ \cdots & & g_{1q}^v & & & \\ & 0 & & g_{1q}^w & & \\ & & & & & \cdots \end{bmatrix} & [g_1]_{FSDT} &= \begin{bmatrix} & g_{1q}^u & & & & \\ & & g_{1q}^v & & 0 & \\ & & & g_{1q}^w & & \\ 0 & & & & g_{1q}^{\phi_x} & \\ & & & & & g_{1q}^{\phi_\theta} \\ & & & & & & \cdots \end{bmatrix} \quad (3.6.11) \\
p_{CLPT} &= 3 i_1 + 1 & p_{FSDT} &= 5 i_1 + 1 \\
q_{CLPT} &= 3 k_1 + 1 & q_{FSDT} &= 5 k_1 + 1
\end{aligned}$$

The base functions for $[g_1]$ must be evaluated according to the boundary conditions of Table 3.5.1 and using the proposed field variable function of Eq. (3.6.3). In the proposed model all the edges are restrained to expand and there is no rigid body motion along x and θ , the rotation ϕ_x is zero for clamped boundary conditions and non-zero for simply-supported boundary conditions. Since the elastic constraints presented in Section 3.5 will be applied, a model which allows the development of the rotation ϕ_x can be used and this will also serve to simulate clamped boundary conditions when the corresponding elastic stiffness is properly set according to Table 3.5.1. Based on this discussion, the final proposal for the base functions of $[g_1]$ can be defined as shown in Eq. (3.6.12).

$$\begin{aligned}
g_{1q}^u &= g_{1q}^v = g_{1q}^w = g_{1q}^{\phi_\theta} = \sin\left(k_1 \pi \frac{x}{L}\right) \\
g_{1q}^{\phi_x} &= \cos\left(k_1 \pi \frac{x}{L}\right)
\end{aligned} \quad (3.6.12)$$

Note that more terms of Eq. (3.6.3) could have been kept without negatively affecting the predicted displacements since the elastic constraints will enforce the desired boundary conditions, but using a minimum number of terms to produce the right response is preferred due to the reduced computational cost and to avoid numerical errors that often arise when using high values for the elastic constraints (using double precision the author found such numerical instabilities when $K^{u,v,w,\phi_x,\phi_\theta} > 10^8$).

Equation (3.6.13) shows a sub-matrix of the base functions contained in $[g_2]$ with the corresponding functions for both the CLPT and the FSDT. The formula for the index q where this sub-matrix starts is also given.

$$\begin{aligned}
[g_2]_{CLPT} &= \begin{bmatrix} g_{2q_a}^u & g_{2q_b}^u & & 0 & & \\ \cdots & & g_{2q_a}^v & g_{2q_b}^v & & \cdots \\ & 0 & & g_{2q_a}^w & g_{2q_b}^w & \\ & & & & & \end{bmatrix} \\
p_{CLPT} &= 6[m_2(j_2 - 1) + i_2] + 1 \\
q_{CLPT} &= 6[m_2(\ell_2 - 1) + k_2] + 1 \\
[g_2]_{FSDT} &= \begin{bmatrix} g_{2q_a}^u & g_{2q_b}^u & & & & \\ & g_{2q_a}^v & g_{2q_b}^v & & 0 & \\ & & g_{2q_a}^w & g_{2q_b}^w & & \cdots \\ & 0 & & g_{2q_a}^{\phi_x} & g_{2q_b}^{\phi_x} & \\ & & & & g_{2q_a}^{\phi_\theta} & g_{2q_b}^{\phi_\theta} \end{bmatrix} \quad (3.6.13) \\
p_{FSDT} &= 10[m_2(j_2 - 1) + i_2] + 1 \\
q_{FSDT} &= 10[m_2(\ell_2 - 1) + k_2] + 1
\end{aligned}$$

Recalling Eq. (3.6.3), the author verified that for all the boundary conditions only two terms: $g_{i_2 j_2 a}$ and $g_{i_2 j_2 b}$, or $g_{i_2 j_2 c}$ and $g_{i_2 j_2 d}$; are required to achieve a proper representation of the displacement fields. Writing all the base functions of Eq. (3.6.13) in the form:

$$\begin{aligned}
g_{2q_a}^{u,v,w,\phi_x,\phi_\theta} &= f(x)^{u,v,w,\phi_x,\phi_\theta} \sin(\ell_2 \theta) \\
g_{2q_b}^{u,v,w,\phi_x,\phi_\theta} &= f(x)^{u,v,w,\phi_x,\phi_\theta} \cos(\ell_2 \theta)
\end{aligned} \quad (3.6.14)$$

where functions $f(x)^w$, $f(x)^{\phi_x}$ and $f(x)^{\phi_\theta}$ can use a single expression for all the boundary conditions based on the same arguments given for $[g_1]$:

$$\begin{aligned}
f(x)^w &= \sin(b_x) \\
f(x)^{\phi_x} &= \cos(b_x) \\
f(x)^{\phi_\theta} &= \sin(b_x)
\end{aligned} \quad (3.6.15)$$

with:

$$b_x = k_2 \pi \frac{x}{L}$$

and the expressions for $f(x)^u$ and $f(x)^v$ depend on the boundary condition type, as shown in Table 3.6.1. In the subsequent sections the suffixes BC1, BC2, BC3 and BC4 will be used to identify the models of Table 3.6.1.

Table 3.6.1: Base Functions for $[g_2]$ for many Boundary Conditions

Boundary Condition	$f(x)^u$	$f(x)^v$
BC1	$\sin(b_x)$	$\sin(b_x)$
BC2	$\cos(b_x)$	$\sin(b_x)$
BC3	$\sin(b_x)$	$\cos(b_x)$
BC4	$\cos(b_x)$	$\cos(b_x)$

3.7 External Force Vector

3.7.1 Defining the Components of the External Force Vector

The external force vector $\{F_{ext}\}$ will be composed based on the external load components F_C, T, P, F_{PL_i} of Fig. 3.2.1, such that:

$$\{F_{ext}\} = \{F_{ext_{F_C}}\} + \{F_{ext_T}\} + \{F_{ext_P}\} + \sum_{i=1}^{n_{PL}} \{F_{ext_{F_{PL_i}}}\} \quad (3.7.1)$$

where n_{PL} is the number of perturbation loads. From the general non-linear formulation presented in Section 3.1 it is implicit in Eq. (3.1.4) that $\{F_{ext}\}$ is defined as:

$$\{F_{ext}\} = \{F_{ext_0}\} + \lambda^{(k-1)} \{F_{ext_\lambda}\} \quad (3.7.2)$$

Based on this observation it is clear that one should know which type of non-linear analysis will be performed in order to judge which components of Eq. (3.7.1) should be included in $\{F_{ext_0}\}$ and which should be included in $\{F_{ext_\lambda}\}$, or in other words, which should be kept constant during the non-linear analysis and which should vary according to the load multiplier λ . In the following discussion it is shown how to group the external load components into $\{F_{ext_0}\}$ and $\{F_{ext_\lambda}\}$ for three cases usually found in the literature:

- i. find the critical axial load

$$\begin{aligned} \{F_{ext_\lambda}\} &= \{F_{ext_{F_C}}\} \\ \{F_{ext_0}\} &= \{F_{ext_T}\} + \{F_{ext_P}\} + \sum_i^{n_{PL}} \{F_{ext_{F_{PL_i}}}\} \end{aligned} \quad (3.7.3)$$

- ii. find the critical torsion load

$$\begin{aligned} \{F_{ext_\lambda}\} &= \{F_{ext_T}\} \\ \{F_{ext_0}\} &= \{F_{ext_{F_C}}\} + \{F_{ext_P}\} + \sum_i^{n_{PL}} \{F_{ext_{F_{PL_i}}}\} \end{aligned} \quad (3.7.4)$$

- iii. find the critical pressure load

$$\begin{aligned} \{F_{ext_\lambda}\} &= \{F_{ext_P}\} \\ \{F_{ext_0}\} &= \{F_{ext_{F_C}}\} + \{F_{ext_T}\} + \sum_i^{n_{PL}} \{F_{ext_{F_{PL_i}}}\} \end{aligned} \quad (3.7.5)$$

3.7.2 Calculating the Components of the External Force Vector

Once it is defined how to build the external load vector for a given non-linear analysis purpose, the next step is to define how to calculate each of its components: $\{F_{ext_{F_C}}\}$, $\{F_{ext_T}\}$, $\{F_{ext_P}\}$ and $\{F_{ext_{F_{PLi}}}\}$.

3.7.2.1 Axial Compression and Load Asymmetry

Based on Fig. 3.2.1 the following relation for $\{F_{ext_{F_C}}\}$ can be derived:

$$\{F_{ext_{F_C}}\} = \oint N_{xx_{top}} [g^u|_{x=0}]^T R_2 d\theta \quad (3.7.6)$$

where $[g^u|_{x=0}]$ is a matrix containing the base functions for u at the top edge, which can be written as:

$$[g^u|_{x=0}] = [[g_0^u|_{x=0}] \quad [g_1^u|_{x=0}] \quad [g_2^u|_{x=0}]] \quad (3.7.7)$$

with:

$$\begin{aligned} [g_0^u|_{x=0}] &= [\frac{1}{\cos \alpha} \quad 0] \\ [g_1^u|_{x=0}] &= [0] \end{aligned} \quad (3.7.8)$$

From the approximation functions presented in Section 3.6 (cf. Table 3.6.1) the equation for $[g_2^u|_{x=0}]$ can be written for each of the proposed models as:

$$\begin{aligned} \text{BC1:} \quad [g_2^u|_{x=0}] &= [\cdots \quad \sin(b_x) \sin(\ell_2 \theta) \quad \sin(b_x) \cos(\ell_2 \theta) \quad 0 \quad 0 \quad 0 \quad 0 \quad \cdots] \\ \text{BC2:} \quad [g_2^u|_{x=0}] &= [\cdots \quad \cos(b_x) \sin(\ell_2 \theta) \quad \cos(b_x) \cos(\ell_2 \theta) \quad 0 \quad 0 \quad 0 \quad 0 \quad \cdots] \\ \text{BC3:} \quad [g_2^u|_{x=0}] &= [\cdots \quad \sin(b_x) \sin(\ell_2 \theta) \quad \sin(b_x) \cos(\ell_2 \theta) \quad 0 \quad 0 \quad 0 \quad 0 \quad \cdots] \\ \text{BC4:} \quad [g_2^u|_{x=0}] &= [\cdots \quad \cos(b_x) \sin(\ell_2 \theta) \quad \cos(b_x) \cos(\ell_2 \theta) \quad 0 \quad 0 \quad 0 \quad 0 \quad \cdots] \end{aligned} \quad (3.7.9)$$

Replacing the expressions for $[g^u|_{x=0}]$ into Eq. (3.7.6) and performing the integration will result in the following expressions for $\{F_{ext_{F_C}}\}$:

$$\begin{aligned} \text{BC1:} \quad \{F_{ext_{F_C}}\}^T &= \{F_0 \quad 0 \quad \cdots\} \\ \text{BC2:} \quad \{F_{ext_{F_C}}\}^T &= \{F_0 \quad 0 \quad \cdots \quad f_{k_2 \ell_2 a}^u \quad f_{k_2 \ell_2 b}^u \quad 0 \quad 0 \quad 0 \quad 0 \quad \cdots\} \\ \text{BC3:} \quad \{F_{ext_{F_C}}\}^T &= \{F_0 \quad 0 \quad \cdots\} \\ \text{BC4:} \quad \{F_{ext_{F_C}}\}^T &= \{F_0 \quad 0 \quad \cdots \quad f_{k_2 \ell_2 a}^u \quad f_{k_2 \ell_2 b}^u \quad 0 \quad 0 \quad 0 \quad 0 \quad \cdots\} \end{aligned} \quad (3.7.10)$$

with:

$$\begin{aligned}
f_{k_2 \ell_2 a}^u &= \pi R_2 \left(N_{xx \ell_2 a} \cos(\ell_2 \omega) + N_{xx \ell_2 b} \sin(\ell_2 \omega) \right) \\
f_{k_2 \ell_2 b}^u &= \pi R_2 \left(-N_{xx \ell_2 a} \sin(\ell_2 \omega) + N_{xx \ell_2 b} \cos(\ell_2 \omega) \right) \\
F_0 &= \frac{1}{\cos \alpha} 2\pi R_2 N_{xx_0}
\end{aligned} \tag{3.7.11}$$

From Eq. (3.7.10) it is clear that boundary conditions BC2 and BC4 allow values that are different than zero for $u|_{x=0}$ along θ , and therefore one can apply these models to evaluate a more general case of the axial load distribution which considers any load non-uniformities.

3.7.2.2 Torsion

As shown in Fig. 3.2.1 a constant torsion can be applied at the top edge of the proposed model and the corresponding components of the external force vector can be calculated with:

$$\{F_{ext_T}\} = \oint N_{x\theta_{top}} [g^v|_{x=0}]^T R_2 d\theta \tag{3.7.12}$$

where:

$$N_{x\theta_{top}} = \frac{T}{2\pi R_2} \tag{3.7.13}$$

and $[g^v|_{x=0}]$ can be written as:

$$[g^v|_{x=0}] = [[g_0^v|_{x=0}] \quad [g_1^v|_{x=0}] \quad [g_2^v|_{x=0}]] \tag{3.7.14}$$

with:

$$\begin{aligned}
[g_0^v|_{x=0}] &= [0 \quad R_2] \\
[g_1^v|_{x=0}] &= [0] \\
[g_2^v|_{x=0}] &= [0]
\end{aligned} \tag{3.7.15}$$

Applying the definitions of $[g^v|_{x=0}]$ into Eq. (3.7.12) and performing the integration will result in:

$$\{F_{ext_T}\}^T = \{0 \quad \frac{T}{2\pi R_2} \quad \dots\} \tag{3.7.16}$$

3.7.2.3 Pressure

The external force vector due to the pressure load P illustrated in Fig. 3.2.1 is defined as:

$$\{F_{ext_P}\} = \iint_{x\theta} P [g^w]^T r d\theta dx \quad (3.7.17)$$

From Table 3.6.1 it can be seen that the shape functions for the w displacement are the same for all the boundary conditions, such that $[g^w]$ can be written as:

$$[g^w] = [[g_0^w] \quad [g_1^w] \quad [g_2^w]] \quad (3.7.18)$$

with:

$$\begin{aligned} [g_0^w] &= [0] \\ [g_1^w] &= [\cdots \quad 0 \quad 0 \quad \sin(k_1\pi\frac{x}{L}) \quad \cdots] \\ [g_2^w] &= [\cdots \quad 0 \quad 0 \quad 0 \quad 0 \quad \sin(b_x)\sin(\ell_2\theta) \quad \sin(b_x)\cos(\ell_2\theta) \quad \cdots] \end{aligned} \quad (3.7.19)$$

Substituting the definitions of $[g^w]$ into Eq. (3.7.17) and performing the integration gives:

$$\{F_{ext_P}\}^T = \{0 \quad 0 \quad \cdots \quad 0 \quad 0 \quad \frac{2P}{k_1}(R_2 - (-1)^{k_1}(R_2 + L \sin \alpha)) \quad \cdots\} \quad (3.7.20)$$

3.7.2.4 Perturbation Loads

The perturbation loads $\{F_{PL_i}\}$ are applied punctually and therefore the calculation of their contribution to the external force vector does not require any integration. Given the coordinates x_i, θ_i of a given perturbation load PL_i , the following expression can be obtained for the corresponding external load vector:

$$\{F_{ext_{F_{PL_i}}}\} = [g|_{x_i, \theta_i}]^T \{F_{PL_i}\} \quad (3.7.21)$$

where $[g|_{x_i, \theta_i}]$ is the matrix containing the base functions evaluated at x_i, θ_i and $\{F_{PL_i}\}^T$ the perturbation load vector containing the u, v, w components when the CLPT is used, or the $u, v, w, \phi_x, \phi_\theta$ components when the FSDT is used.

3.8 Integration of the Stiffness Matrices

Section 3.1 shows how to derive the system of equations that solves the non-linear problem iteratively (cf. Eq. (3.1.9)) and Section 3.4 shows how to derive the system that solves the linear buckling problem (cf. Eq. (3.4.9)). Solving these systems of equations is the main step that should be carried out by the analyst in order to obtain the desired structural responses and field variables. Nevertheless, experience has shown that the efficient calculation of the structural matrices that are used in these systems of equations represents a true challenge [89]. The author's experience is that the integration of the linear matrices: $[K_0]$, $[K_e]$ and $[K_{G_0}]$; and the non-linear matrices: $[K_{0L}]$, $[K_{LL}]$ and $[K_G]$; must be efficient. Otherwise, the computational cost to calculate these matrices will be higher than the computational cost associated with the solution of the system of equations.

The present section shows how the linear matrices $[K_0]$, $[K_e]$ and $[K_{G_0}]$ can be efficiently calculated through analytical integration. For conical structures the proposed approximation eliminates all non-integrable terms. It will also be discussed the numerical integration of the non-linear matrices: $[K_{0L}]$, $[K_{LL}]$ and $[K_G]$; and the numerical integration of the internal force vector $\{F_{int}\}$.

All the matrices will be sub-divided according to the approximation functions, creating sub-matrices that depend on the indices i_1 , i_2 and j_2 and will be called smallest repeatable sub-matrices. In this way, the integrands will be formed based on these smallest repeatable sub-matrices, making it convenient to derive expressions that can be integrated analytically or numerically.

3.8.1 Sub-Division of the Stiffness Matrices

For both the analytical and numerical integrations carried out, the structural matrices were subdivided according to the approximation functions discussed in Section 3.6, resulting in nine sub-matrices $[K_{ab}]$, with a and b assuming 0, 1 or 2, as shown in Eq. (3.8.1).

$$[K] = \begin{bmatrix} [K_{00}] & [K_{01}] & [K_{02}] \\ [K_{10}] & [K_{11}] & [K_{12}] \\ [K_{20}] & [K_{21}] & [K_{22}] \end{bmatrix} \quad (3.8.1)$$

From the definitions of $[K_0]$, $[K_{0L}]$ and $[K_{LL}]$ given in Eq. (3.2.19), the definition of $[K_G]$ given in Eqs. (3.2.27) and (3.2.28), and the definition of $[K_e]$ given in Eq.(3.5.2), it can be seen that the only asymmetric matrix is $[K_{0L}]$, being the only one that required the calculation of the sub-matrices 10, 20 and 21. Additionally, only the upper triangular part of the sub-matrices 00, 11 and 22 have to be calculated for $[K_0]$, $[K_{LL}]$, $[K_G]$ and $[K_e]$. Recalling from Eq. (2.2.38) that $[B_L] = [A][G]$, $[B_{L_0}] = [A_0][G]$ and $[G] = [G_d][g]$ the general form of each calculated stiffness sub-matrix can be written as:

$$\begin{aligned}
[K_{0ab}] &= \iint_{x\theta} [g_a]^T [d_0]^T [F] [d_0] [g_b] r d\theta dx \\
[K_{0Lab}] &= \iint_{x\theta} [g_a]^T [d_0]^T [F] ([A] + [A_0]) [G_d] [g_b] r d\theta dx \\
[K_{LLab}] &= \iint_{x\theta} [g_a]^T [G_d]^T ([A] + [A_0])^T [F] ([A] + [A_0]) [G_d] [g_b] r d\theta dx \\
[K_{Gab}] &= \iint_{x\theta} [g_a]^T [G_d]^T [N_{KG}] [G_d] [g_b] r d\theta dx \\
[K_{eab}] &= \oint (R_1 [g_a|_{x=L}]^T [K_{Bot}] [g_b|_{x=L}] + R_2 [g_a|_{x=0}]^T [K_{Top}] [g_b|_{x=0}]) d\theta
\end{aligned} \tag{3.8.2}$$

The sub-matrices $[K_{ab}]$ of Eq. (3.8.2) can be further sub-divided in order to find the smallest repeatable sub-matrices that are required to perform the integrations. The following general format can be used for the sub-matrices of Eq. (3.8.2) without loss of generality:

$$[K_{ab}] = \iint_{x\theta} [g_a]^T [H] [g_b] r d\theta dx \tag{3.8.3}$$

Expanding the integrand $[g_a]^T [H] [g_b]$ according to the matrix form of the base functions, given in Eqs. (3.6.10), (3.6.11) and (3.6.13):

$$[K_{ab}] = \iint_{x\theta} [g_a]^T [H] [g_b] r d\theta dx = \iint_{x\theta} \begin{bmatrix} [g_{a_1}] \\ [g_{a_2}] \\ \vdots \\ [g_{a_p}] \\ \vdots \\ [g_{a_m}] \end{bmatrix}^T [H] \begin{bmatrix} [g_{b_1}] & [g_{b_2}] & \cdots & [g_{b_q}] & \cdots & [g_{b_n}] \end{bmatrix} r d\theta dx \tag{3.8.4}$$

where the formulas of p and q are given in Eqs. (3.6.11) and (3.6.13). Note that for the base functions on the right-hand side the indices i_1 , i_2 and j_2 are replaced by k_1 , k_2 and ℓ_2 . The multiplications of Eq. (3.8.4) can be represented in a rearranged matrix form as:

$$[K_{ab}] = \begin{bmatrix} [K_{ab_{1,1}}] & \cdots & [K_{ab_{1,q}}] & \cdots & [K_{ab_{1,n}}] \\ \vdots & & \vdots & & \vdots \\ [K_{ab_{p,1}}] & \cdots & [K_{ab_{p,q}}] & \cdots & [K_{ab_{p,n}}] \\ \vdots & & \vdots & & \vdots \\ [K_{ab_{m,1}}] & \cdots & [K_{ab_{m,q}}] & \cdots & [K_{ab_{m,n}}] \end{bmatrix} \tag{3.8.5}$$

with the smallest repeatable sub-matrix $[K_{ab_{p,q}}]$ defined as:

$$[K_{ab_{p,q}}] = \iint_{x\theta} [g_{a_p}]^T [H] [g_{b_q}] r d\theta dx \tag{3.8.6}$$

Applying Eq. (3.8.6) to the definitions of Eq. (3.8.2) will render the smallest repeatable sub-matrix for $[K_0]$, $[K_{0L}]$, $[K_{LL}]$ and $[K_G]$, shown in Eq. (3.8.7). Both the analytical and numerical integrations are performed using these smallest repeatable sub-matrices, with $[g_{a_p}]$ calculated with the indices i_1, i_2, j_2 and $[g_{b_q}]$ with the indices k_1, k_2, ℓ_2 in the approximation functions. After the repeatable sub-matrix is calculated, the complete stiffness matrices are obtained varying i_1, i_2, j_2 to populate row-wise and k_1, k_2, ℓ_2 to populate column-wise.

$$\begin{aligned}
[K_{0abp,q}] &= \iint_{x\theta} [g_{a_p}]^T [d_0]^T [F] [d_0] [g_{b_q}] r d\theta dx \\
[K_{0Labp,q}] &= \iint_{x\theta} [g_{a_p}]^T [d_0]^T [F] ([A] + [A_0]) [G_d] [g_{b_q}] r d\theta dx \\
[K_{LLabp,q}] &= \iint_{x\theta} [g_{a_p}]^T [G_d]^T ([A] + [A_0])^T [F] ([A] + [A_0]) [G_d] [g_{b_q}] r d\theta dx \\
[K_{Gabp,q}] &= \iint_{x\theta} [g_{a_p}]^T [G_d]^T [N_{K_G}] [G_d] [g_{b_q}] r d\theta dx \\
[K_{eabp,q}] &= \oint \left(R_1 [g_{a_p}|_{x=L}]^T [K_{Bot}] [g_{b_q}|_{x=L}] + R_2 [g_{a_p}|_{x=0}]^T [K_{Top}] [g_{b_q}|_{x=0}] \right) d\theta
\end{aligned} \tag{3.8.7}$$

3.8.2 Analytical Integration of $[K_0]$, $[K_{G_0}]$ and $[K_e]$

Due to the interrelationship between indices i_1, i_2, j_2 of $[g_{a_p}]$ and indices k_1, k_2, ℓ_2 of $[g_{b_q}]$ many integration conditions must be considered in order to avoid terms with null denominator. For the sub-matrix 11 ($a = 1$ and $b = 1$) it was verified that the analytical integration of $[K_0]$ and $[K_{G_0}]$ led to three conditions:

- i. $(k_1 = i_1)$ ii. $(k_1 \neq i_1)$ iii. $(k_1 = i_1 = 0)$

For the sub-matrix 22 ($a = 2$ and $b = 2$) five conditions were verified:

- i. $(k_2 = i_2) \cup (\ell_2 = j_2)$ iv. $(k_2 = i_2) \cup (\ell_2 \neq j_2)$
- ii. $(k_2 \neq i_2) \cup (\ell_2 = j_2)$ v. $(k_2 = i_2 = 0) \cup (\ell_2 = j_2)$
- iii. $(k_2 \neq i_2) \cup (\ell_2 \neq j_2)$

The author verified that for cylindrical and conical structures with a constant $[F]$ all over the domain the conditions iii and iv led to null sub-matrices, resulting in highly sparse matrices. For example, for $m_2 = n_2 = 20$ and $m_2 = n_2 = 100$ the sub-matrix $[K_{0_{22}}]$ contains only 5% and 1% of non-zero values, respectively, justifying the use of a sparse matrix-based implementation. The current implementation [85] uses the sparse matrix package provided in SciPy [6].

The symbolic commercial software Mathematica [98] was used to perform all the differential operations and the analytical integrations of $[K_0]$, $[K_{G_0}]$ and $[K_e]$. The developed routines and the integrated terms are too extensive to be included in this thesis, but the reader can find them in the freely distributed software that has been developed [85]. After downloading the package, the subroutines can be found in the paths given in Table 3.8.1.

Table 3.8.1: Mathematica subroutines used to obtain $[K_0]$, $[K_{G_0}]$ and $[K_e]$

Model	Path
CLPT-Donnell-BC1	compmech\theory\conecyl\clpt\clpt_donnell_bc1\clpt_donnell_bc1_linear.nb
CLPT-Donnell-BC2	compmech\theory\conecyl\clpt\clpt_donnell_bc2\clpt_donnell_bc2_linear.nb
CLPT-Donnell-BC3	compmech\theory\conecyl\clpt\clpt_donnell_bc3\clpt_donnell_bc3_linear.nb
CLPT-Donnell-BC4	compmech\theory\conecyl\clpt\clpt_donnell_bc4\clpt_donnell_bc4_linear.nb
CLPT-Sanders-BC1	compmech\theory\conecyl\clpt\clpt_sanders_bc1\clpt_sanders_bc1_linear.nb
CLPT-Sanders-BC2	compmech\theory\conecyl\clpt\clpt_sanders_bc2\clpt_sanders_bc2_linear.nb
CLPT-Sanders-BC3	compmech\theory\conecyl\clpt\clpt_sanders_bc3\clpt_sanders_bc3_linear.nb
CLPT-Sanders-BC4	compmech\theory\conecyl\clpt\clpt_sanders_bc4\clpt_sanders_bc4_linear.nb
FSDT-Donnell-BC1	compmech\theory\conecyl\fsdt\fsdt_donnell_bc1\fsdt_donnell_bc1_linear.nb
FSDT-Donnell-BC2	compmech\theory\conecyl\fsdt\fsdt_donnell_bc2\fsdt_donnell_bc2_linear.nb
FSDT-Donnell-BC3	compmech\theory\conecyl\fsdt\fsdt_donnell_bc3\fsdt_donnell_bc3_linear.nb
FSDT-Donnell-BC4	compmech\theory\conecyl\fsdt\fsdt_donnell_bc4\fsdt_donnell_bc4_linear.nb

The results of the subroutines given in Table 3.8.1 are placed in a folder “linear_mathematica”, and a Python subroutine “print_linear_sparse.py” is used to transform it to a sparse format stored in “linear_sparse”. This format is easy to copy-and-paste to the Cython code that will finally be compiled and called from Python. The corresponding Cython subroutines are listed in Table 3.8.2.

Table 3.8.2: Cython subroutines used to obtain $[K_0]$, $[K_{G_0}]$ and $[K_e]$

Model	Path
CLPT-Donnell-BC1	compmech\compmech\conecyl\clpt\clpt_donnell_bc1_linear.pyx
CLPT-Donnell-BC2	compmech\compmech\conecyl\clpt\clpt_donnell_bc2_linear.pyx
CLPT-Donnell-BC3	compmech\compmech\conecyl\clpt\clpt_donnell_bc3_linear.pyx
CLPT-Donnell-BC4	compmech\compmech\conecyl\clpt\clpt_donnell_bc4_linear.pyx
CLPT-Sanders-BC1	compmech\compmech\conecyl\clpt\clpt_sanders_bc1_linear.pyx
CLPT-Sanders-BC2	compmech\compmech\conecyl\clpt\clpt_sanders_bc2_linear.pyx
CLPT-Sanders-BC3	compmech\compmech\conecyl\clpt\clpt_sanders_bc3_linear.pyx
CLPT-Sanders-BC4	compmech\compmech\conecyl\clpt\clpt_sanders_bc4_linear.pyx
FSDT-Donnell-BC1	compmech\compmech\conecyl\fsdt\fsdt_donnell_bc1_linear.pyx
FSDT-Donnell-BC2	compmech\compmech\conecyl\fsdt\fsdt_donnell_bc2_linear.pyx
FSDT-Donnell-BC3	compmech\compmech\conecyl\fsdt\fsdt_donnell_bc3_linear.pyx
FSDT-Donnell-BC4	compmech\compmech\conecyl\fsdt\fsdt_donnell_bc4_linear.pyx

3.8.3 Analytical integration for Cones

For the conical structures the integration of matrices $[K_0]$ and $[K_{G_0}]$ cannot be performed analytically because of the non-constant term $1/r$ that creates non-integrable expressions [99] such as the one shown in Eq. (3.8.8):

$$\int_0^L \frac{1}{r(x)} \cos\left(\pi \frac{x}{L}\right)^2 dx = \int_0^L \frac{1}{R_2 + \sin \alpha x} \cos\left(\pi \frac{x}{L}\right)^2 dx \quad (3.8.8)$$

In this thesis it is proposed to divide the cone in cross-sectional slices of constant radius, as mathematically described in Eq. (3.8.9):

$$\oint \int_0^L \frac{1}{r(x)} f(x, \theta, \alpha) dx d\theta = \oint \sum_{i=1}^s \int_{x_i}^{x_{i+1}} \frac{1}{r_i} f(x, \theta, \alpha) dx d\theta \quad (3.8.9)$$

where each i^{th} slice is delimited by x_i and x_{i+1} , and the constant radius r_i is measured at the cross-section corresponding to $(x_i + x_{i+1})/2$. The procedure of Eq. (3.8.9) is illustrated in Fig. 3.8.1, where it is important to emphasize that the values of $\sin \alpha$ and $\cos \alpha$ that appear in the integrands are still those corresponding to the conical structure, otherwise the correct structural behavior of a cone could not be represented. The computational cost to integrate $[K_0]$ and $[K_{G_0}]$ using this approximation increases linearly with the number of sections.

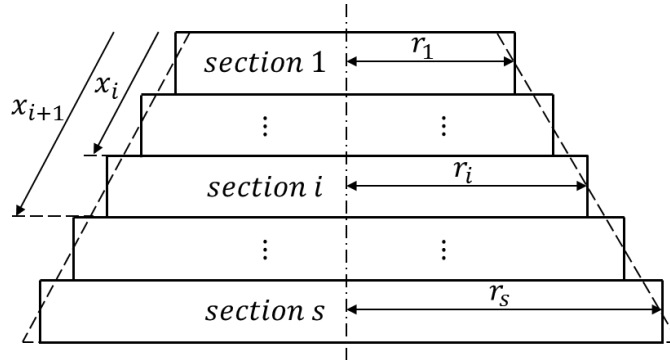


Fig. 3.8.1: Cross-sectional slices of a conical structure for analytical integration.

3.8.4 Numerical Integration of $[K_{0L}]$, $[K_{LL}]$, $[K_G]$ and $\{F_{int}\}$

The matrices $[K_{0L}]$, $[K_G]$ and $[K_{LL}]$ and the internal force vector $\{F_{int}\}$ contain the terms: $w_{,x}$ and $w_{,\theta}$ for Donnell's equations; and v , $w_{,x}$ and $w_{,\theta}$ for Sanders' equations; that are functions of the Ritz constants vector $\{c\}$ and therefore cannot be integrated analytically in a straightforward way. Additionally, when initial imperfections are present the integrands will also contain the field variables $w_{0,x}$ and $w_{0,\theta}$. The author investigated many possibilities to integrate such non-linear integrands and none of them was successful, especially because of the many integration conditions that arise due to the different combinations of indices that will lead to null denominator conditions. For example, it was shown in Section 3.8.2 that 4 conditions were required in the analytical integration of $[K_{0_{22}}]$, but for the analytical integration of $[K_{0L_{22}}]$ hundreds of conditions were

identified, and even though there must be even more unidentified conditions since the results were incorrect. Considering this limitation in the implementation process, the author had to recur to numerical integration algorithms.

A single valued function is one that returns a single value for a given set of input parameters. On the other hand, integrands such as the ones corresponding to matrices $[K_{0L}]$, $[K_G]$ and $[K_{LL}]$ or vector $\{F_{int}\}$ fall into the class of the so called vector valued functions, which are functions that return a matrix or a vector instead of returning a single value, for a given set of input parameters. Therefore, efficient integration algorithms capable of handling vector valued functions are required to obtain the non-linear structural matrices and the internal force vector, allowing a single call for each integration point in order to obtain the whole array, otherwise for a $m \times n$ matrix the integration algorithms would have to execute $m \times n$ more function calls.

The first integration algorithm evaluated by the author was an implementation of the Cubature [100] algorithm written by Prof. Steven G. Johnson from the Massachusetts Institute of Technology (MIT) [10]. This has been wrapped to a Python-callable version by the author [11]. The p-adaptive (where the order of the integration functions is increased) algorithm has shown a better performance than the h-adaptive (where more integration points are added), but this implementation of the cubature algorithm requires a considerably large amount of memory since many integration points are kept in memory in order to be reused during the adaptive integration, and each integration point carries the data corresponding to a full stiffness matrix.

In a second attempt, the 2-D Trapezoidal and the 2-D Simpson's rule [101] have been investigated, where both showed to be applicable to the required tasks and the Trapezoidal rule demonstrated to be more stable and therefore it was set as the default choice in the implemented package [85], despite both options are available. In the 2-D Trapezoidal rule the domain is subdivided into n_x sub-intervals for x and n_θ sub-intervals for θ . Given the integration interval for x being (x_a, x_b) and for θ being (θ_a, θ_b) , each sub-interval for x will have a constant width $h = (x_b - x_a)/m$, and for θ a constant width $k = (\theta_b - \theta_a)/n$. The values for x in each sub-interval are calculated with $x_{i_x} = x_0 + i_x h$ and for θ with $\theta_{i_\theta} = \theta_0 + i_\theta k$. The integral is then approximated as:

$$\iint_{x\theta} f(x, \theta) d\theta dx \approx \frac{1}{4} h k \left\{ f(x_a, \theta_a) + f(x_b, \theta_a) + f(x_a, \theta_b) + f(x_b, \theta_b) + 2 \sum_{i_x=1}^{n_x-1} f(x_{i_x}, \theta_a) \right. \\ \left. + 2 \sum_{i_x=1}^{n_x-1} f(x_{i_x}, \theta_b) + 2 \sum_{i_\theta=1}^{n_\theta-1} f(x_a, \theta_{i_\theta}) + 2 \sum_{i_\theta=1}^{n_\theta-1} f(x_b, \theta_{i_\theta}) + 4 \sum_{i_\theta=1}^{n_\theta-1} \sum_{i_x=1}^{n_x-1} f(x_{i_x}, \theta_{i_\theta}) \right\} \quad (3.8.10)$$

An efficient implementation for the numerical integration of $[K_{0L}]$, $[K_{LL}]$ and $[K_G]$ was achieved decomposing the smallest sub-matrix $[K_{abp,q}]$ defined in Eq. (3.8.7) in a left- and a right-hand side denominated $[K_a]$ and $[K_b]$, respectively. Equation (3.8.11) illustrates this decomposition, Table 3.8.3 shows the definitions of $[K_a]$ and $[K_b]$ for $[K_{0L}]$, $[K_{LL}]$ and $[K_G]$, and Table 3.8.4 the path to the corresponding subroutines, available in the package of Ref. [85]. After running the referred Mathematica subroutines the results are placed in a folder named "nonlinear_mathematica" and the Python script "print_nonlinear_sparse.py" is used to print the output to a folder named "nonlinear_sparse", in a format which is ready to

copy-and-paste to the Cython subroutines listed in Table 3.8.5. The strain functions are also printed and post-processed using the Python scripts “print_fint_0L_L0_LL.py” and “print_strainFunc.py”. When checking the implemented code, note that the terms inside the deepest *for* loops are highly optimized, replacing expressions similar to “ x^2 ” by “ $x \cdot x$ ” in order to avoid function calls, and using buffers to avoid repeated calculations of commonly required expressions.

$$[K_{abp,q}] = [K_a][K_b]$$

$$= \begin{bmatrix} p_{11} & p_{12} & p_{13} & \cdots \\ p_{21} & p_{22} & p_{23} & \\ p_{31} & p_{32} & p_{33} & \\ \vdots & & & \ddots \end{bmatrix} \begin{bmatrix} q_{11} & q_{12} & q_{13} & \cdots \\ q_{21} & q_{22} & q_{23} & \\ q_{31} & q_{32} & q_{33} & \\ \vdots & & & \ddots \end{bmatrix} \quad (3.8.11)$$

Table 3.8.3: Definition of $[K_a]$ and $[K_b]$ for $[K_{0L}]$, $[K_G]$ and $[K_{LL}]$

$[K_{0L}]$	$[K_G]$	$[K_{LL}]$
$[K_a] = r[g_a]^T[d_0]^T[F]$	$[K_a] = r[g_a]^T[G_d]^T[N_{K_G}]$	$[K_a] = r[g_a]^T[G_d]^T([A] + [A_0])^T[F]$
$[K_b] = ([A] + [A_0])[G_d][g_b]$	$[K_b] = [G_d][g_b]$	$[K_b] = ([A] + [A_0])[G_d][g_b]$

Table 3.8.4: Mathematica subroutines used to obtain $[K_a]$ and $[K_b]$ for $[K_{0L}]$, $[K_G]$ and $[K_{LL}]$

Model	Path
CLPT-Donnell-BC1	compmech\theory\conecyl\clpt\clpt_donnell_bc1\clpt_donnell_bc1_nonlinear.nb
CLPT-Donnell-BC2	compmech\theory\conecyl\clpt\clpt_donnell_bc2\clpt_donnell_bc2_nonlinear.nb
CLPT-Donnell-BC3	compmech\theory\conecyl\clpt\clpt_donnell_bc3\clpt_donnell_bc3_nonlinear.nb
CLPT-Donnell-BC4	compmech\theory\conecyl\clpt\clpt_donnell_bc4\clpt_donnell_bc4_nonlinear.nb
CLPT-Sanders-BC1	compmech\theory\conecyl\clpt\clpt_sanders_bc1\clpt_sanders_bc1_nonlinear.nb
CLPT-Sanders-BC2	compmech\theory\conecyl\clpt\clpt_sanders_bc2\clpt_sanders_bc2_nonlinear.nb
CLPT-Sanders-BC3	compmech\theory\conecyl\clpt\clpt_sanders_bc3\clpt_sanders_bc3_nonlinear.nb
CLPT-Sanders-BC4	compmech\theory\conecyl\clpt\clpt_sanders_bc4\clpt_sanders_bc4_nonlinear.nb
FSDT-Donnell-BC1	compmech\theory\conecyl\fsdt\fsdt_donnell_bc1\fsdt_donnell_bc1_nonlinear.nb
FSDT-Donnell-BC2	compmech\theory\conecyl\fsdt\fsdt_donnell_bc2\fsdt_donnell_bc2_nonlinear.nb
FSDT-Donnell-BC3	compmech\theory\conecyl\fsdt\fsdt_donnell_bc3\fsdt_donnell_bc3_nonlinear.nb
FSDT-Donnell-BC4	compmech\theory\conecyl\fsdt\fsdt_donnell_bc4\fsdt_donnell_bc4_nonlinear.nb

Table 3.8.5: Cython subroutines used to obtain $[K_{0L}]$, $[K_G]$ and $[K_{LL}]$

Model	Path
CLPT-Donnell-BC1	compmech\compmech\conecyl\clpt\clpt_donnell_bc1_nonlinear.pyx
CLPT-Donnell-BC2	compmech\compmech\conecyl\clpt\clpt_donnell_bc2_nonlinear.pyx
CLPT-Donnell-BC3	compmech\compmech\conecyl\clpt\clpt_donnell_bc3_nonlinear.pyx
CLPT-Donnell-BC4	compmech\compmech\conecyl\clpt\clpt_donnell_bc4_nonlinear.pyx
CLPT-Sanders-BC1	compmech\compmech\conecyl\clpt\clpt_sanders_bc1_nonlinear.pyx
CLPT-Sanders-BC2	compmech\compmech\conecyl\clpt\clpt_sanders_bc2_nonlinear.pyx
CLPT-Sanders-BC3	compmech\compmech\conecyl\clpt\clpt_sanders_bc3_nonlinear.pyx
CLPT-Sanders-BC4	compmech\compmech\conecyl\clpt\clpt_sanders_bc4_nonlinear.pyx
FSDT-Donnell-BC1	compmech\compmech\conecyl\fsdt\fsdt_donnell_bc1_nonlinear.pyx
FSDT-Donnell-BC2	compmech\compmech\conecyl\fsdt\fsdt_donnell_bc2_nonlinear.pyx
FSDT-Donnell-BC3	compmech\compmech\conecyl\fsdt\fsdt_donnell_bc3_nonlinear.pyx
FSDT-Donnell-BC4	compmech\compmech\conecyl\fsdt\fsdt_donnell_bc4_nonlinear.pyx

In spite the fact that the numerical integration of the non-linear matrices is costly because it involves nested *for* loops up to four levels, the numerical integration of the internal force vector $\{F_{int}\}$ is significantly cheap since it involves *for* loops up to only two levels. Rewriting Eq. (3.2.16) and separating the linear and the non-linear components gives:

$$\{F_{int}\} = \int_{\theta=0}^{\theta=2\pi} \int_{x=0}^{x=L} ([B_0] + [B_L] + [B_{L_0}])^T (\{N_0\} + \{N_L\}) r dx d\theta \quad (3.8.12)$$

where the stress vector has been split in a linear $\{N_0\}$ and a non-linear part $\{N_L\}$, defined as:

$$\{N_0\} = [F]\{\varepsilon_0\} \quad \{N_L\} = [F](\{\varepsilon_L\} + \{\varepsilon_{L_0}\}) \quad (3.8.13)$$

such that:

$$\begin{aligned} \{F_{int}\} &= \{F_{int_{00}}\} + \{F_{int_{0L}}\} + \{F_{int_{L0}}\} + \{F_{int_{LL}}\} \\ \{F_{int_{00}}\} &= \int_{\theta=0}^{\theta=2\pi} \int_{x=0}^{x=L} [B_0]^T \{N_0\} r dx d\theta = [K_0]\{c\} \\ \{F_{int_{0L}}\} &= \int_{\theta=0}^{\theta=2\pi} \int_{x=0}^{x=L} [B_0]^T \{N_L\} r dx d\theta \\ \{F_{int_{L0}}\} &= \int_{\theta=0}^{\theta=2\pi} \int_{x=0}^{x=L} ([B_L] + [B_{L_0}])^T \{N_0\} r dx d\theta \\ \{F_{int_{LL}}\} &= \int_{\theta=0}^{\theta=2\pi} \int_{x=0}^{x=L} ([B_L] + [B_{L_0}])^T \{N_L\} r dx d\theta \end{aligned} \quad (3.8.14)$$

Note in Eq. (3.8.14) that only the non-linear part of $\{F_{int}\}$ has to be integrated numerically, since the linear part is obtained through $[K_0]\{c\}$. The strain function is obtained with the same Mathematica subroutines used to obtain the integrands for the non-linear matrices, given in Table 3.8.4. The post processing is done using the Python scripts “`print_fint_0L_L0_LL.py`” and “`print_strainFunc.py`”, where the first will result in the internal force vector components $\{F_{int_{0L}}\}$, $\{F_{int_{L0}}\}$ and $\{F_{int_{LL}}\}$ of Eq. (3.8.14) and the second script is used to obtain the complete strain functions, that are included in the Cython subroutines named “`*common*.pyx`”.

3.9 Non-Linear Algorithms

This section gives more details about the iterative algorithms used to solve the non-linear systems of equations discussed in Sections 3.1 and 3.2. All the algorithms herein presented fall in the category of the so called incremental algorithms where the load is not applied at once, being divided in load increments with the first load increment determined by the parameter *initialInc* of the developed subroutines, and the next load increment adjusted using many empirically determined formulas, as detailed in the following sub-sections. For a given load increment many iterations are executed until the convergence criteria are fulfilled, or until a divergent behavior is identified. In case of convergence the algorithm moves to the next load increment, while in case of divergence the load increment is reduced and the current incremental step is restarted. Following this general scheme, the next sub-sections will detail many different ways to solve each load increment and present the convergence and divergence criteria adopted for this thesis.

3.9.1 Full-Newton-Raphson

Equation (3.1.10) shows how the Ritz constants vector $\{c\}$ is updated at each iteration up to the convergence. Note that at each iteration the increment $\{\delta c\}$ is calculated using the tangent stiffness matrix $[K_T]$, using Eq. (3.1.9). In the full Newton-Raphson method $[K_T]$ is updated at every iteration, presenting a quadratic convergence rate and a high cost for each iteration since the computation of the tangent stiffness matrix is usually time consuming [90].

3.9.2 Modified Newton-Raphson

In the modified Newton-Raphson method the tangent stiffness matrix $[K_T]$ is calculated at the beginning of each load increment and updated at every n iterations [90]. Although $[K_T]$ is updated only at some iterations, the internal force vector $\{F_{int}\}$ is updated at every iteration, which only slightly increases the computational cost since the numerical integration of $\{F_{int}\}$ is considerably cheaper than the numerical integration of $[K_T]$. Despite the convergence is slower than in the full Newton-Raphson, the computational cost of each iteration is drastically reduced, usually compensating the need for more iterations. The tests performed for this thesis showed that using the modified Newton-Raphson results in a faster non-linear algorithm, especially when the line search algorithm described in Section 3.9.3 is applied in conjunction. The author verified a high dependency of the computational cost with the maximum number of iterations n between each $[K_T]$ update, where $n = 1$ will result in the full Newton-Raphson method and a high value for n will result in a poor convergence behavior, requiring smaller load increments. The value $n = 6$ was adopted and for all the cases a good convergence behavior was obtained for increment sizes up to 0.2.

3.9.3 Line Search Algorithms

The use of line search algorithms is mainly intended to prevent divergence during the iterations, increasing the robustness of the non-linear algorithm [82]. As mentioned in Section 3.9.2 a high number of iterations for an update in $[K_T]$ may result in a poor convergence, but the author verified that this effect is attenuated when using the line search.

The line search technique is an important feature of most numerical techniques applied in unconstrained optimization problems and can be used with a wide range of iterative solution procedures [90]. For the application in the non-linear problem under discussion, let's consider the update of the Ritz constants vector based on Eq. (3.1.10), rewriting it as:

$$\{c\}^{(k)} = \{c\}^{(k-1)} + \eta\{\delta c\}^{(k)} \quad (3.9.1)$$

where η is a scalar set to unity in case no line search is desired. When using line searches η becomes another parameter to be determined in order to minimize the total potential energy functional Π . Assuming that inside the iteration Π becomes only a function of η :

$$\begin{aligned} \Pi(\eta + \delta\eta) &= \Pi(\eta) + \frac{\partial \Pi}{\partial \eta} \delta\eta + \dots \\ &= \Pi(\eta) + \frac{\partial \Pi}{\partial \{c\}} \frac{\partial \{c\}}{\partial \eta} \delta\eta + \dots \\ &= \Pi(\eta) + \{R(\eta)\}^T \{\delta c\} \delta\eta + \dots \end{aligned} \quad (3.9.2)$$

For the solution at η to be stationary:

$$f(\eta) = \frac{\partial \Pi}{\partial \eta} = \{\delta c\}^T \{R(\eta)\} = 0 \quad (3.9.3)$$

Note in Eqs. (3.9.2) and (3.9.3) that the residual force vector $\{R\}$ is written as a function of η , which holds true since the internal force vector $\{F_{int}\}$ is calculated with the updated $\{c\}$ according to Eq. (3.9.1). The system of Eq. (3.9.3) is non-linear and can be solved using the iterative scheme shown in Eq. (3.9.4), taken from Ref. [90], which consists of subsequent linear interpolations that calculate the value for $\eta^{(i)}$ that renders $f(\eta)$ to be zero.

$$\eta^{(i)} = (\eta^{(i-1)} - \eta^{(i-2)}) \left(\frac{-f(\eta^{(i-2)})}{f(\eta^{(i-1)}) - f(\eta^{(i-2)})} \right) \quad (3.9.4)$$

In the current implementation [85] the starting values for the iterative scheme are $\eta^{(0)} = 0$ and $\eta^{(1)} = 1$ and the stopping criterion is:

$$abs(\eta^{(i)} - \eta^{(i-1)}) < 0.01 \quad (3.9.5)$$

giving satisfactory results.

3.9.4 Riks (Arc-Length) Method

Along the incremental solution in a non-linear analysis there may be load steps which would require the applied load to be decreased in order to achieve the equilibrium. Such situations are encountered for example in snap-through problems, for instance the one discussed in Sections 1.2.1 and 1.2.2. The Newton-Raphson methods discussed in the previous sections assume that the external loads are fixed for a given load increment by using a constant load multiplier λ , such that the Taylor expansion of the residual force vector $\{R\}$ is calculated using Eq. (3.1.5). Due to the constancy of λ the Newton-Raphson algorithm fails to achieve the equilibrium in situations where the equilibrium requires the applied load to decrease along the iterative process.

The basic difference of the Riks method is that the load multiplier λ becomes a new unknown variable that will be calculated along the iterative process. This section shows how to develop the non-linear equations based on Eq. (3.1.4) removing the simplification that $\lambda^{(k-1)} = \lambda = \text{constant}$ applied in Section 3.1. Repeating Eq. (3.1.4) for convenience:

$$\{R\}^{(k-1)} = \{F_{int}\}^{(k-1)} - (\{F_{ext_0}\} + \lambda^{(k-1)}\{F_{ext_\lambda}\}) \quad (3.9.6)$$

Assuming that the equilibrium is achieved at iteration k , the Taylor expansion of $\{R\}$ keeping only the linear terms gives:

$$\begin{aligned} \{R\}^{(k)} &= \{R\}^{(k-1)} + \{\delta R\}^{(k)} = \{0\} \\ \{\delta R\}^{(k)} &= \left. \frac{\partial \{R\}}{\partial \{c\}} \right|_{(k-1)} \{\delta c\}^{(k)} + \left. \frac{\partial \{R\}}{\partial \lambda} \right|_{k-1} \delta \lambda^{(k)} \end{aligned} \quad (3.9.7)$$

From the definition of $\{R\}$ given in Eq. (3.1.4), it comes that:

$$\begin{aligned} \left. \frac{\partial \{R\}}{\partial \{c\}} \right|_{(k-1)} &= \left. \frac{\partial \{F_{int}\}}{\partial \{c\}} \right|_{k-1} = [K_T^{(k-1)}] \\ \left. \frac{\partial \{R\}}{\partial \lambda} \right|_{(k-1)} &= -\{F_{ext_\lambda}\} \end{aligned} \quad (3.9.8)$$

where $[K_T^{(k-1)}]$ is the tangent stiffness matrix calculated with data of the last iteration. Substituting Eq. (3.9.8) and Eq. (3.9.6) into Eq. (3.9.7):

$$\{F_{int}\}^{(k-1)} - (\{F_{ext_0}\} + \lambda^{(k-1)}\{F_{ext_\lambda}\}) + [K_T^{(k-1)}]\{\delta c\}^{(k)} - \{F_{ext_\lambda}\}\delta \lambda^{(k)} = 0 \quad (3.9.9)$$

which can be rearranged as suggested by Bathe (1996) [82]:

$$\{\delta c\}^{(k)} = \delta \lambda^{(k)} \{\delta \bar{c}\}^{(k-1)} + \{\delta \bar{c}\}^{(k-1)} \quad (3.9.10)$$

where:

$$\{\delta \bar{c}\}^{(k-1)} = [K_T^{(k-1)}]^{-1} (\{F_{ext_0}\} + \lambda^{(k-1)}\{F_{ext_\lambda}\} - \{F_{int}\}^{(k-1)}) \quad (3.9.11)$$

and:

$$\{\delta \bar{c}\}^{(k-1)} = [K_T^{(k-1)}]^{-1} \{F_{ext\lambda}\} \quad (3.9.12)$$

such that:

$$\begin{aligned} \lambda^{(k)} &= \lambda^{(k-1)} + \delta\lambda^{(k)} \\ \{c\}^{(k)} &= \{c\}^{(k-1)} + \{\delta \bar{c}\}^{(k-1)} + \delta\lambda^{(k)} \{\delta \bar{c}\}^{(k-1)} \end{aligned} \quad (3.9.13)$$

Note that both $\delta\lambda^{(k)}$ and $\delta\{c\}^{(k)}$ have to be determined simultaneously, requiring an additional function $f(\delta\lambda^{(k)}, \delta\{c\}^{(k)})$ for the additional unknown (λ). The spherical constant arc-length criterion has been adopted (see [102] and [103]), which can be written as:

$$(\lambda^{(k)})^2 + \frac{\{c\}^{T(k)} \{c\}^{(k)}}{\mathcal{G}} = \ell^2 \quad (3.9.14)$$

where ℓ is the arc-length for the current step and \mathcal{G} a normalizing factor, calculated in the current implementation [85] as:

$$\mathcal{G} = \{c_{init}\}^T \{c_{init}\} \quad (3.9.15)$$

with $\{c_{init}\}$ being the vector of the Ritz constants calculated linearly using the initial increment size (*initialInc*). Substituting Eq. (3.9.13) into Eq. (3.9.14) will create a second order equation that can be solved for $\delta\lambda^{(k)}$ as:

$$\delta\lambda^{(k)} = \frac{-b \pm \sqrt{d}}{2a} \quad (3.9.16)$$

such that:

$$\begin{aligned} a &= \mathcal{G} + \{\delta \bar{c}\}^T \{\delta \bar{c}\} \\ b &= 2(\mathcal{G}\lambda + \{c\}^T \{\delta \bar{c}\} + \{\delta \bar{c}\}^T \{\delta \bar{c}\}) \\ c &= \mathcal{G}(\lambda^2 - \ell^2) + \{c\}^T \{c\} + 2\{c\}^T \{\delta \bar{c}\} + \{\delta \bar{c}\}^T \{\delta \bar{c}\} \end{aligned} \quad (3.9.17)$$

with all quantities taken at increment $(k - 1)$.

Note in Eq. (3.9.16) that two directions are possible for $\delta\lambda$ due to the two possible signs for \sqrt{d} . If the wrong sign is taken the algorithm will go backwards. For the purpose of the present study only the buckling load is sought, such that λ should increase until the maximum load is reached, and therefore the positive sign “+” is always adopted. The choice of the right sign becomes more critical when the non-linear analysis has to be taken up to the post-buckling regime, and this would go beyond the scope of this thesis.

The initial arc-length value adopted is $\ell = 0.1$. The values for $\lambda^{(1)}$ and $\{c\}^{(1)}$ are calculated using the linear stiffness matrix $[K_0]$ instead of $[K_T]$. For each increment, Eqs. (3.9.11) and (3.9.12) are used to compute $\{\delta \bar{c}\}^{(k-1)}$ and $\{\delta \bar{c}\}^{(k-1)}$, then Eqs. (3.9.16) and (3.9.17) used to calculate $\delta\lambda^{(k)}$, and Eq. (3.9.13) used to calculate $\lambda^{(k)}$ and $\{c\}^{(k)}$. The convergence and divergence are checked as explained in Section 3.9.5. In case of convergence the arc-length is increased in 95% and the next increment started. If divergence occurs the arc-length is reduced to 30% of the current value

and the current increment is restarted. Note that $[K_T]$ can be updated at every iteration (full-Riks) or at the beginning of each load increment (modified-Riks), analogously to what can be done for the Newton-Raphson method, and both cases have been implemented by the author if Ref. [85].

3.9.5 Convergence and Divergence Criteria and Other Non-Linear Parameters

All the convergence and divergence criteria are applied to the third or higher iterations, i.e. for $k > 2$, meaning that at least 3 iterations are allowed. The convergence criterion adopted is:

$$R_{max}^{(k)} = \max(|\{R\}^{(k)}|) \leq 0.001 N \quad (3.9.18)$$

where $\{R\}^{(k)}$ is the residual force vector calculated at iteration k . The divergence criterion is:

$$R_{max}^{(k)} > R_{max}^{(k-1)} \quad (3.9.19)$$

meaning that the current load step is restarted with a smaller increment size when the maximum residue increases from the previous to the current iteration. The increment size is reduced down to a *minInc* parameter, below which the analysis is terminated. The maximum number of iterations *maxNumIter* used is 30, and if $k > \text{maxNumIter}$ the current load step is restarted with a smaller increment size. Another criterion that considerably accelerated the non-linear analyses in cases where the convergence was slow is the slow convergence criterion:

$$\frac{|R_{max}^{(k-1)} - R_{max}^{(k)}|}{R_{max}^{(k-1)}} < 0.05 \quad (3.9.20)$$

such that the load step is restarted with a smaller increment size when the maximum residual force decreases less than 5%.

4 Verification of the Proposed Models

This chapter presents numerous results using different possible models obtained with the content of Chapters 2 and 3, and at this point it is convenient to define a nomenclature that allows an easy identification of a given model. In Chapter 2 it was presented the kinematic equations obtained using the Classical Laminated Plate Theory (CLPT) and the First-order Shear Deformation Theory (FSDT), with both Donnell's and Sanders' non-linear equations. The kinematic and the non-linear theory chosen will be referred as CLPT-Donnell, FSDT-Donnell, CLPT-Sanders and so forth. Section 3.6 presents the approximation functions proposed in this thesis for the four boundary conditions discussed in Section 3.5, which will result in four different base functions identified as BC1, BC2, BC3 and BC4, as shown in Table 3.6.1, which are added to the proposed nomenclature resulting in: CLPT-Donnell-BC1, CLPT-Sanders-BC2 and so forth. In situations where simply supported (SS) or clamped (CC) boundary conditions are specifically evaluated, the models will be identified as CLPT-Donnell-SS3, for example, replacing in this case BC3 by SS3 to explicitly indicate simply supported conditions.

All the cylindrical and conical structures herein evaluated are summarized in Appendix A, which contains the material properties in Table A.1 and the geometric and laminate data in Table A.2.

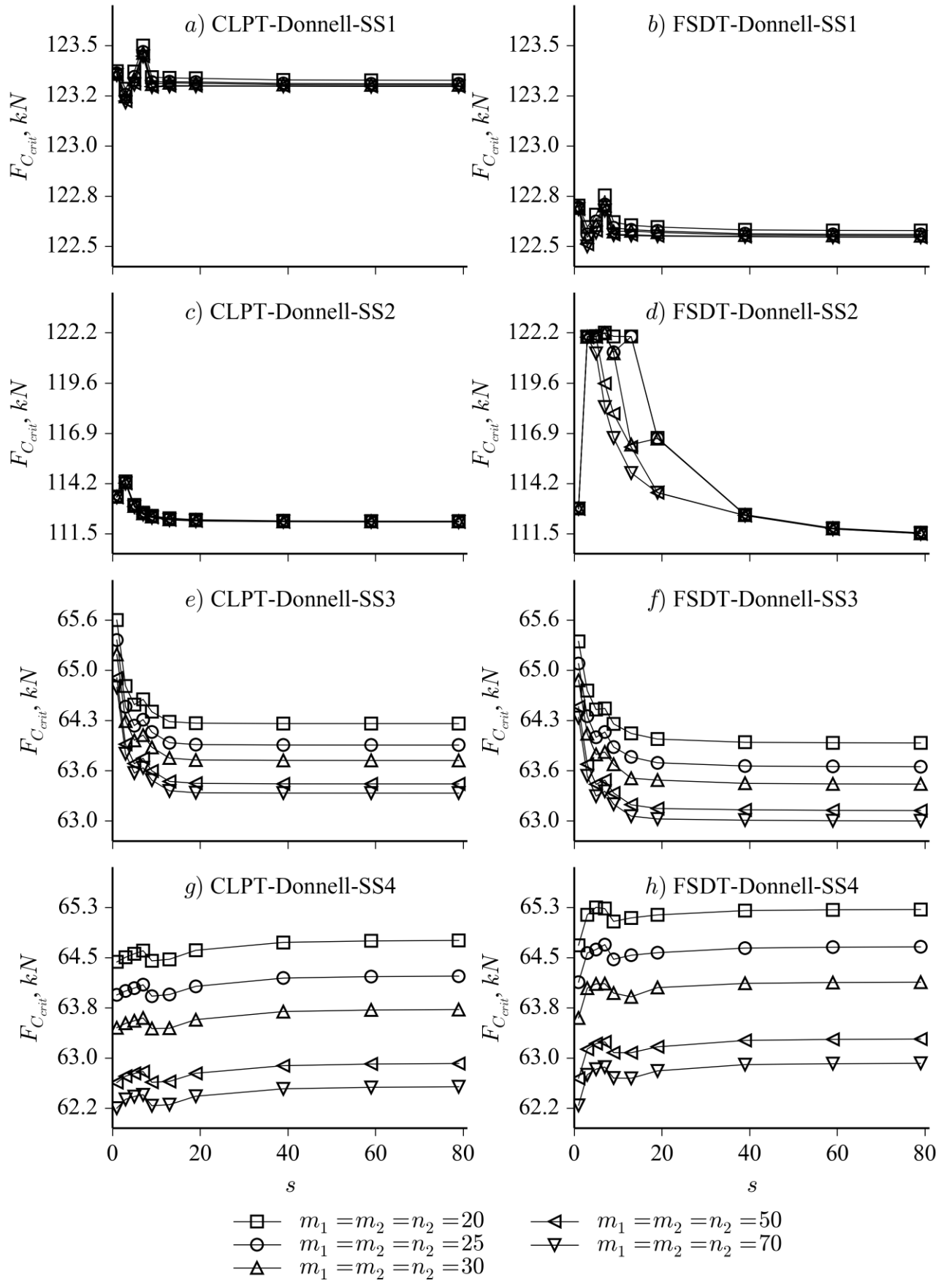
The first sections of this chapter are focused on convergence analyses, which is of extreme importance in order to identify how many approximation terms m_1, m_2, n_2 (cf. Eq. (3.6.3)) are required for different purposes, how many cross sections are required for the analytical integration of cones (cf. Section 3.8.3), how many terms should be used in the half-cosine function used to approximate the initial imperfection field (cf. Eq. (3.3.1)) and how many integration points n_x, n_θ should be used for the numerical integration of the non-linear stiffness matrices $[K_{0L}]$, $[K_{LL}]$, $[K_G]$ and the internal force vector $\{F_{int}\}$ (cf. Section 3.8.4).

The following sections will focus on the verification of the proposed models against finite element results, semi-analytical models proposed in the literature and experimental results available in the literature.

4.1 Convergence of the Analytical Integration for Cones

Section 3.8.3 proposes a new method to approximate the analytical integration of the linear stiffness matrix $[K_0]$ and the initial stress geometric stiffness matrix $[K_{G_0}]$ for cones, where the dependency of the radius with the meridional position x creates non-integrable terms. This section will investigate the convergence behavior when the number of integration cross-sections s is increased. Three cones: C01, C02 and C14; described in Table A.2 were selected and two responses were monitored for these convergence studies: the critical linear buckling load $F_{C_{crit}}$ and the normal displacement at the application point of a single perturbation load, called w_{PL} , obtained with linear static analysis. Numerous cases have been tested using approximation functions with different number of terms $20 \leq (m_1 = m_2 = n_2) \leq 70$ for the $F_{C_{crit}}$ responses and $20 \leq (m_1 = m_2 = n_2) \leq 80$ for the w_{PL} responses, using different number of sections $1 \leq s \leq 79$ and the eight types of boundary conditions shown in Table 3.5.1. Note that s is selected always to be an odd number (1, 3, 5, ..., 79), such that the middle section will have mid-radius equal the radius at the cone middle cross-section (radius at $x = L/2$).

Only the results for cones C02 and C14 for simply supported boundary conditions are shown since they lead to the slowest convergence rate of the s parameter. The convergence response of $F_{C_{crit}}$ is shown in Fig. 4.1.1 for C02 and Fig. 4.1.2 for C14, and the convergence response of w_{PL} is shown in Fig. 4.1.3 for C02 and Fig. 4.1.4 for C14. The first observation is that the convergence for the CLPT is usually faster than for the FSDT. The second is that for many cases the use of only one section ($s = 1$) already leads to a good approximation, where in average the buckling load can be estimated within an error of $1.11 \pm 0.78 \%$ and the displacement field within an error of $2.66 \pm 1.32 \%$. The approach using $s = 1$ considers the cone as an equivalent cylinder with the radius measured in the middle cross-section ($x = L/2$), and such simplification would be adequate for optimization procedures, some non-linear analyses or in another case where a very small pre-solver time is required. The figures also show that the convergence behavior does not depend on the number of terms used for the Ritz approximation, and that for the adopted range ($m_1 = m_2 = n_2$ from 20 to 80) a satisfactory convergence is achieved dividing the cone in 39 sections. In order to guarantee a good convergence of this parameter, the default value adopted for the subsequent studies is $s = 79$, if not otherwise specified. In all figures it can also be seen that increasing the number of terms for the approximation series m_1, m_2, n_2 will lead to a converged behavior, and the convergence analysis for the parameters m_1, m_2, n_2 will be covered in the next sections.

Fig. 4.1.1: Convergence of $F_{C_{crit}}$ with the number of sections, C02

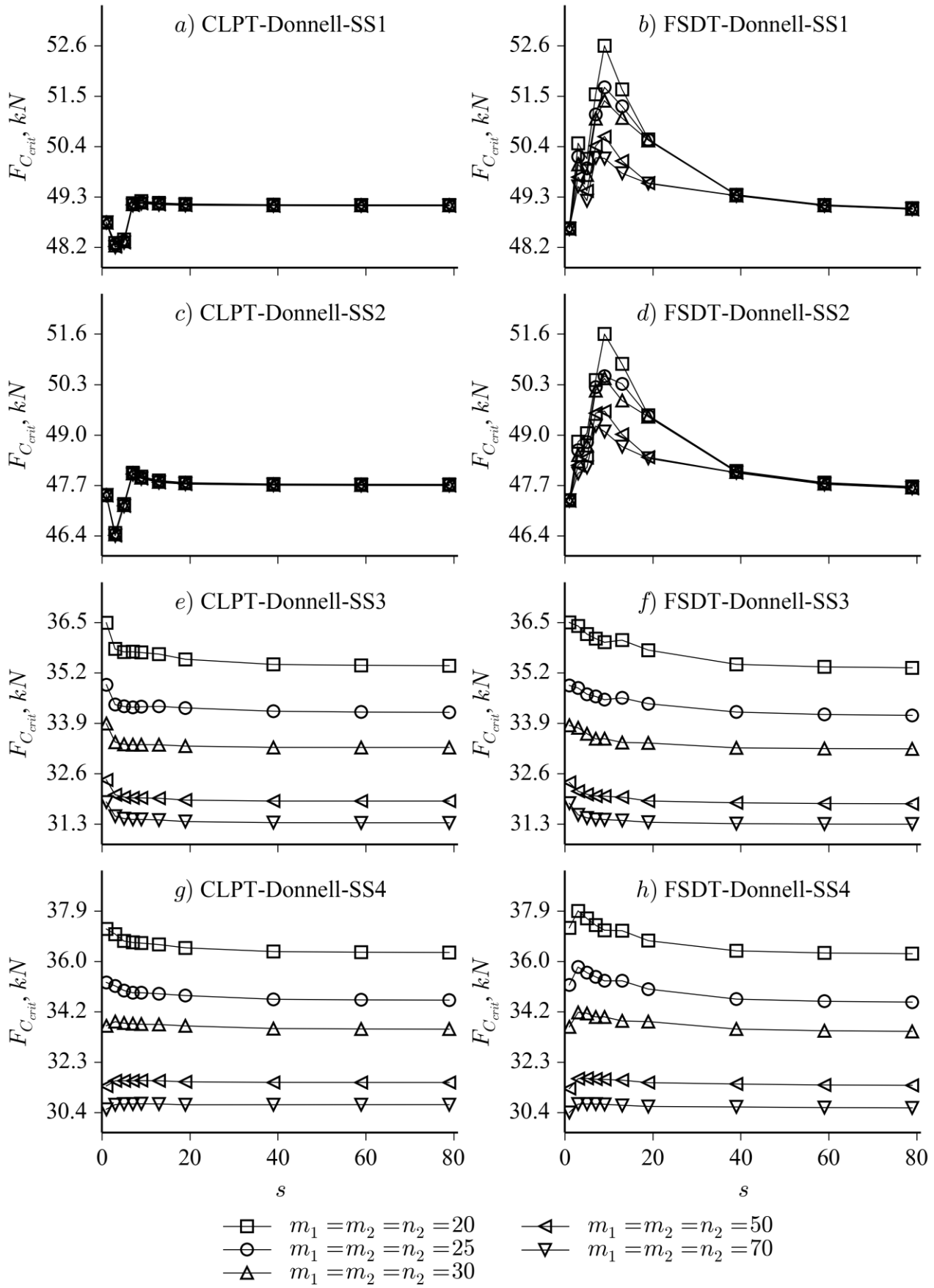
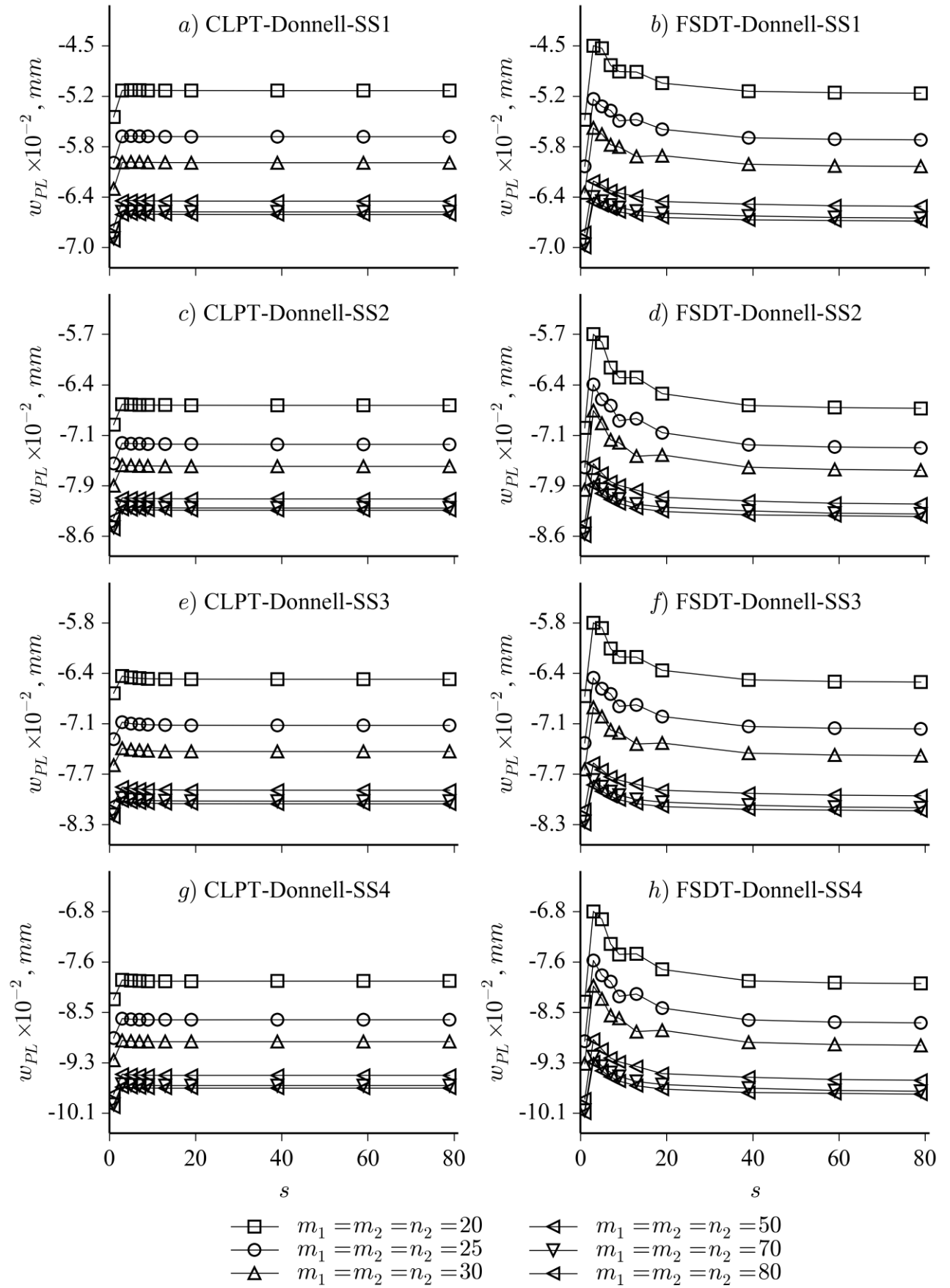
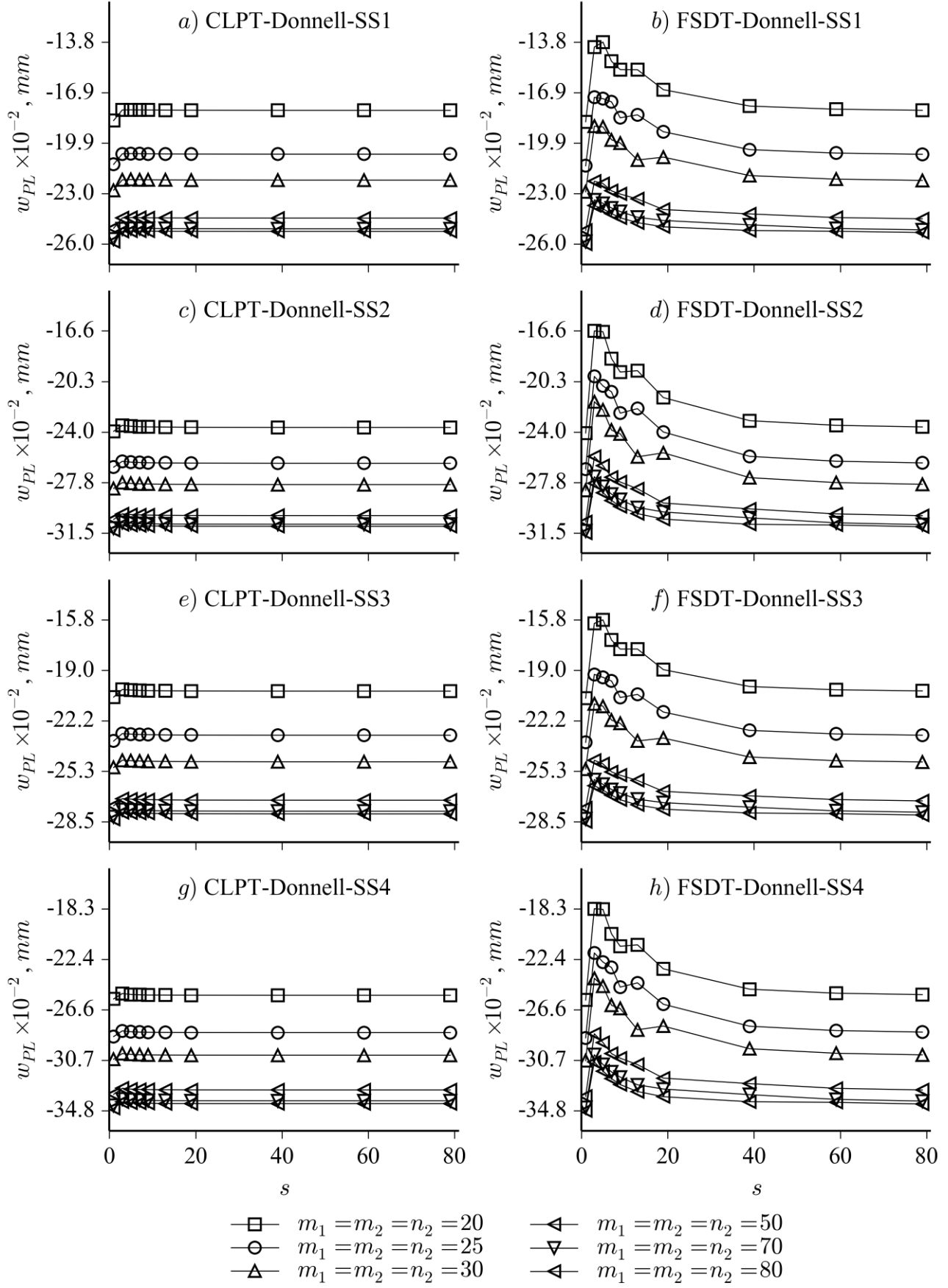


Fig. 4.1.2: Convergence of $F_{C_{crit}}$ with the number of sections, C14

Fig. 4.1.3: Convergence of w_{PL} with the number of sections, C02

Fig. 4.1.4: Convergence of w_{PL} with the number of sections, C14

4.2 Convergence of Linear Buckling Responses

From Fig. 4.1.1 and Fig. 4.1.2 it can be seen that the response using a higher value for the terms m_1, m_2, n_2 progressively reaches a converged behavior and this section is devoted to study the convergence behavior of the linear buckling response in more details, monitoring the linear buckling modes (eigenvectors) and the critical buckling loads (eigenvalues). Three cones: C02, C14 and C26; and one cylinder: Z33, all detailed in Table A.2; are evaluated for linear buckling under pure axial compression, pure torsion and pure pressurization (no combined load cases were selected). The first 50 buckling modes were evaluated and the most representative ones plotted. It has been observed that the even modes (2, 4, 6, ..., 50) have the same eigenvalue and eigenvector of the corresponding predecessor odd modes (1, 3, 5, ..., 49), and only the latter are shown. Only two types of boundary conditions are shown using the simply supported cases, the SS1 and SS4. It was verified that the clamped cases showed a higher convergence than the corresponding simply supported ones.

In Fig. 4.2.1 the linear buckling calculations using axial compression is shown. For the SS1 case the fastest convergence is achieved, and using $m_1 = m_2 = n_2 = 20$ already suffices. For the SS4 case a slowest convergence rate is obtained and $m_1 = m_2 = n_2 = 80$ may be required in some cases in order to get converged estimatives. In fact, it was observed that the SS4 boundary condition is the one with the slowest convergence rate among the eight presented in Table 3.5.1. All the buckling modes converge in a similar rate, but shifts between the buckling mode positions were observed increasing m_1, m_2, n_2 , as depicted in Fig. 4.2.2 and Fig. 4.2.3, mainly because the buckling modes are close to each other, which is a typical characteristic for the buckling modes of imperfection sensitive shells [104].

The linear buckling convergence using torsion load is shown Fig. 4.2.4, where it can also be seen a faster convergence of the SS1 boundary condition. With the SS4 boundary conditions the buckling load converges faster than in the cases of pure axial compression. The same conclusion can be obtained from the convergence studies using pressure loads, shown in Fig. 4.2.5, where only the higher modes seem to converge slower when compared to the corresponding torsion load cases.

Based on the convergence results for axial compression at least $m_1 = m_2 = n_2 = 50$ should be used and for torsion or pressure loads $m_1 = m_2 = n_2 = 30$ already gives a satisfactory convergence. For the next linear buckling results presented in this chapter the value $m_2 = n_2 = 50$ will be used by default when not otherwise specified. In Section 4.3.1 it will be discussed that the m_1 parameter will be determined by the axisymmetric component of the displacement field variables that appears in a cone or cylinder under axial compression, giving the so called “elephant foot” pattern.

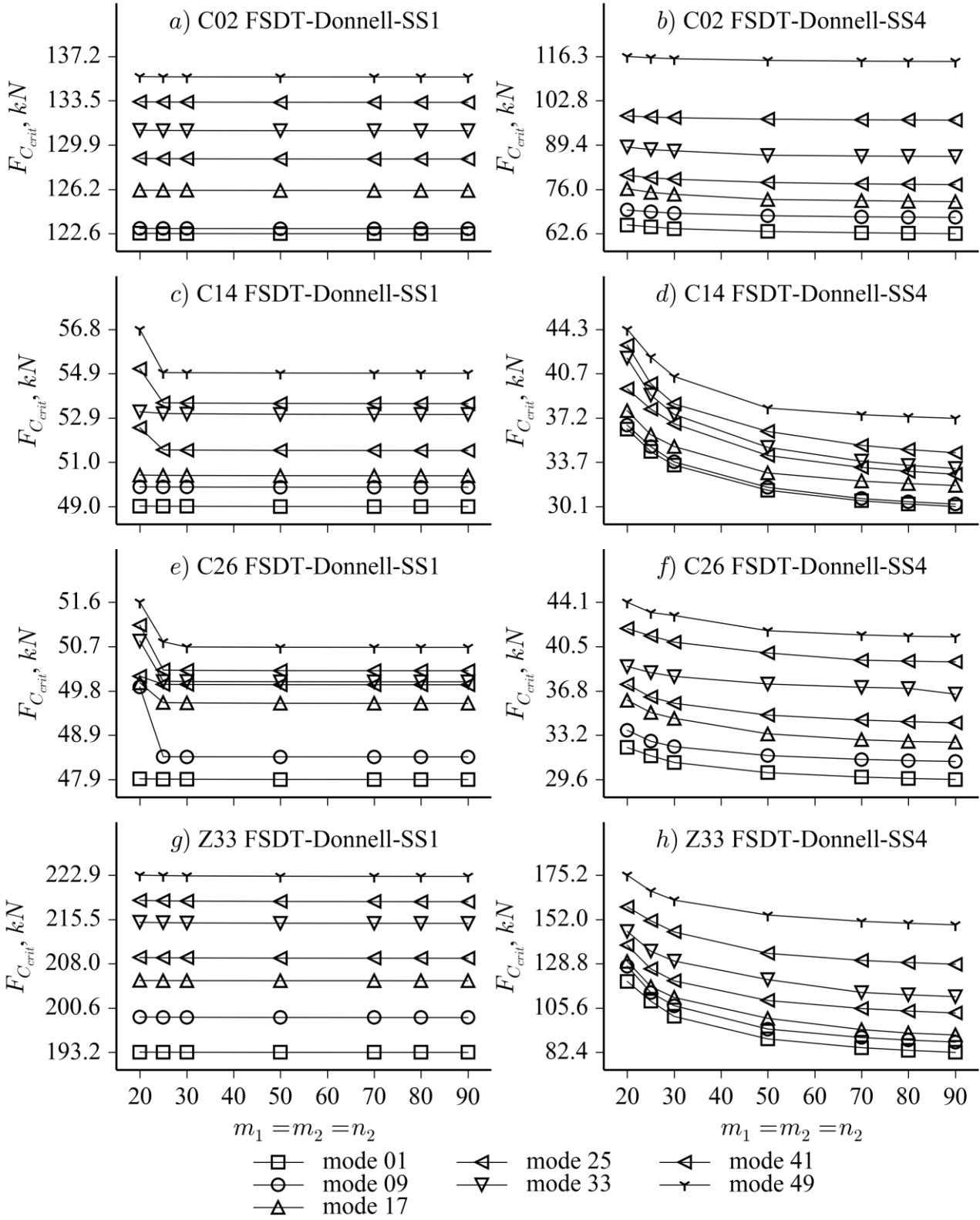


Fig. 4.2.1: Convergence of Linear Buckling under Axial Compression

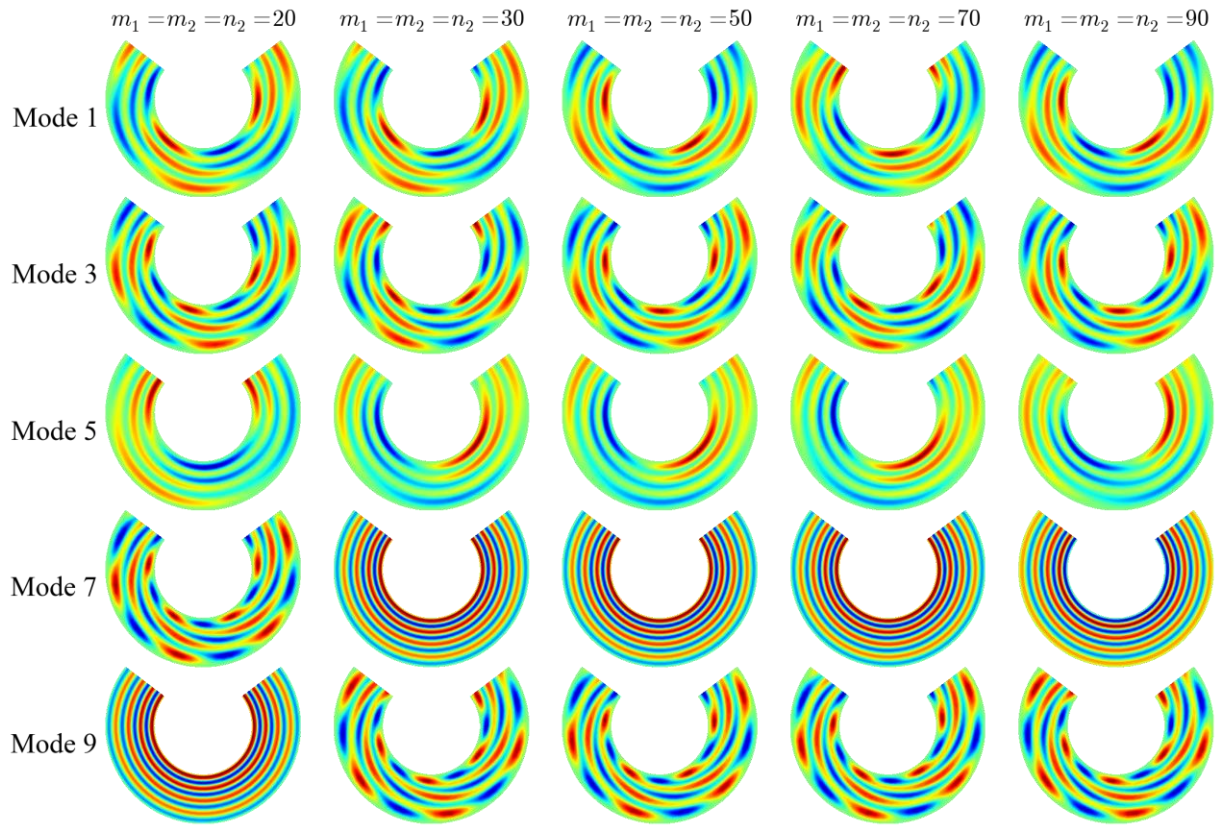


Fig. 4.2.2: Convergence of First Buckling Modes for Axial Compression, cone C02, FSDT-Donnell-SS1

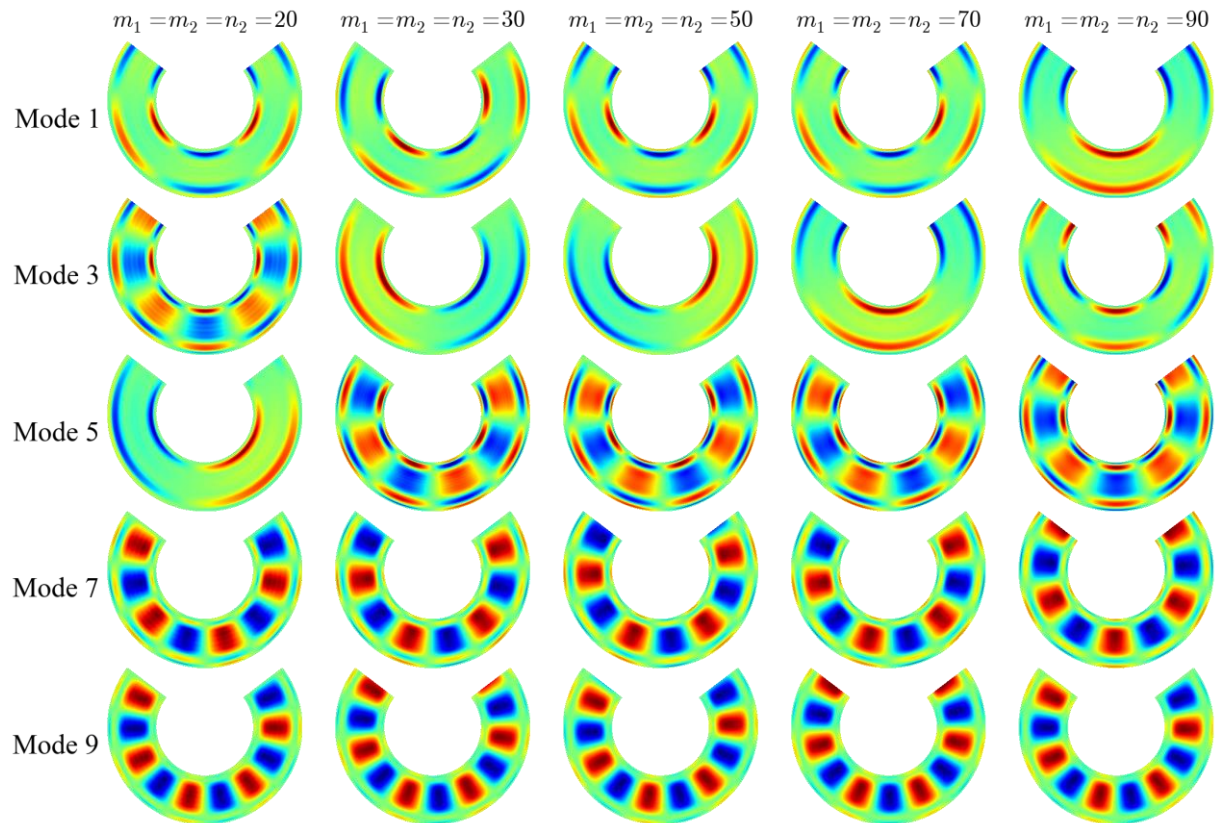


Fig. 4.2.3: Convergence of First Buckling Modes for Axial Compression, cone C02, FSDT-Donnell-SS4

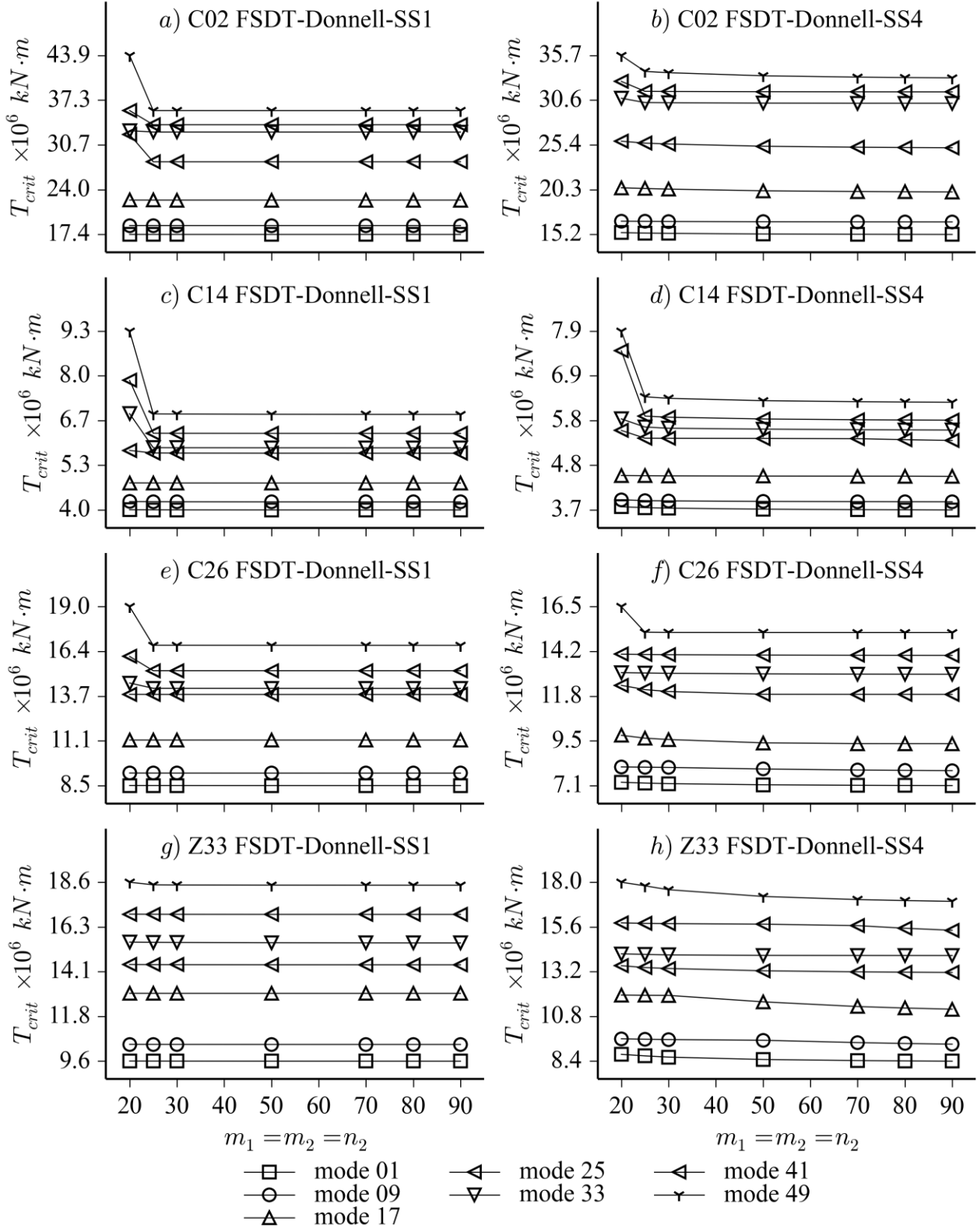


Fig. 4.2.4: Convergence of Linear Buckling under Torsion

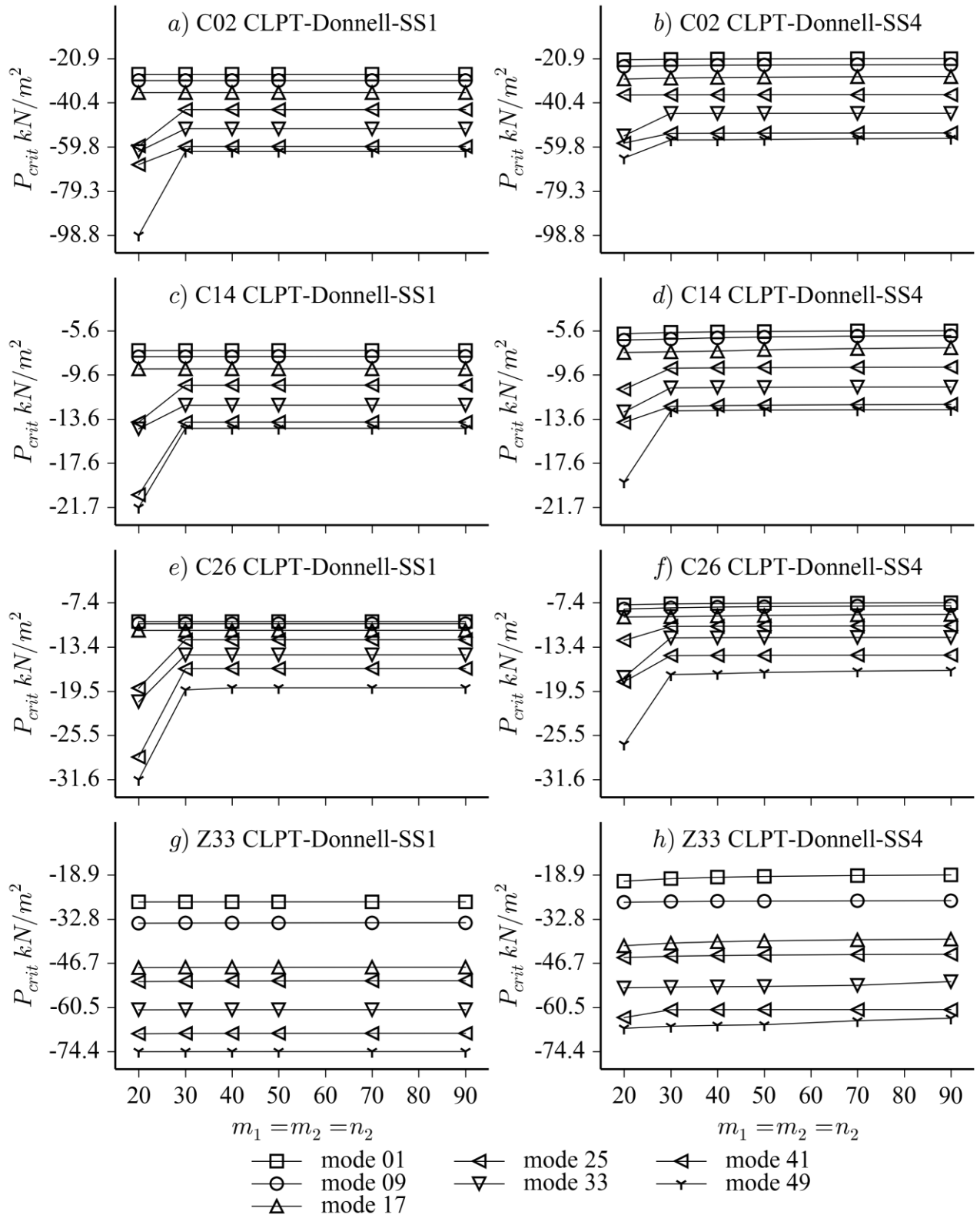


Fig. 4.2.5: Convergence of Linear Buckling under Pressure

4.3 Convergence of Linear Static Responses

4.3.1 Displacement Field

The convergence analysis using displacement field variables is presented in this section. The approximation functions of Eq. (3.6.3) show that the base functions that depend on an arbitrary number of terms are included in two matrices $[g_1]$ and $[g_2]$, where $[g_1]$ contains the functions homogeneous over θ (axisymmetric functions). In the investigation of axially compressed cones and cylinders with simply supported or fixed edges (actually, with any boundary conditions that restraint the w displacement at the edges) the “elephant foot” pattern can be observed, which consists of a high variation of the normal displacement pattern along the meridian (x axis) close to the edges. The elephant’s foot may cause a failure mode that governs the design of many practical structures [105] and a proper representation of its pattern is primarily required. Due to this and due to the fact that the elephant’s foot can be represented using only $[g_1]$, the convergence study carried out along this section will first determine the number of terms m_1 required for the base functions contained in $[g_1]$ and proceed with the determination of m_2 and n_2 that form the base functions $[g_2]$.

In Fig. 4.3.1 it is shown the w displacement along the meridian for cylinder Z33 under axial load using four different boundary conditions, where it can be seen a similar convergence behavior for all types of boundary conditions. A detailed convergence analysis is shown in Fig. 4.3.2, where it can be seen that with $m_1 = 120$ the mean relative difference about $m_1 = 110$ is less than 0.01%. A similar convergence behavior has been observed for other cylindrical and conical structures.

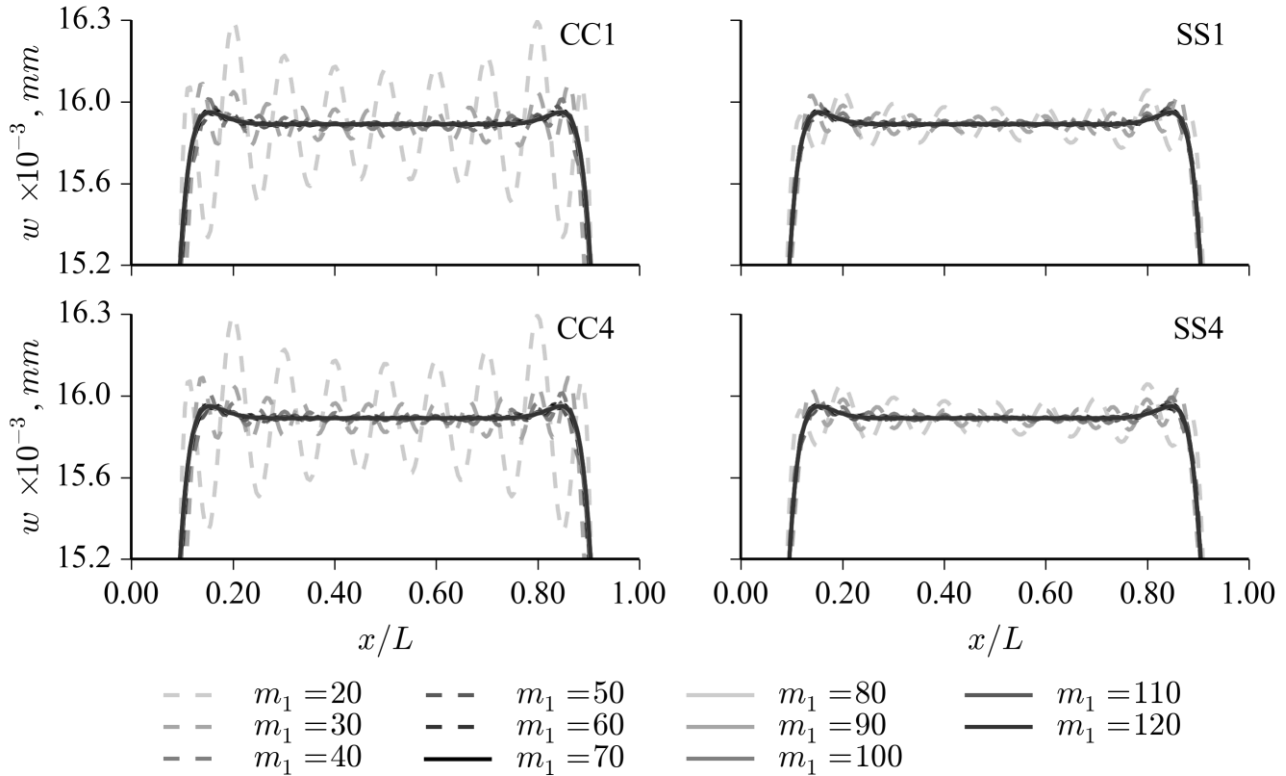


Fig. 4.3.1: Convergence of Cylinder Z33 using FSDT-Donnell, $m_2 = n_2 = 0$, $F_c = 10kN$

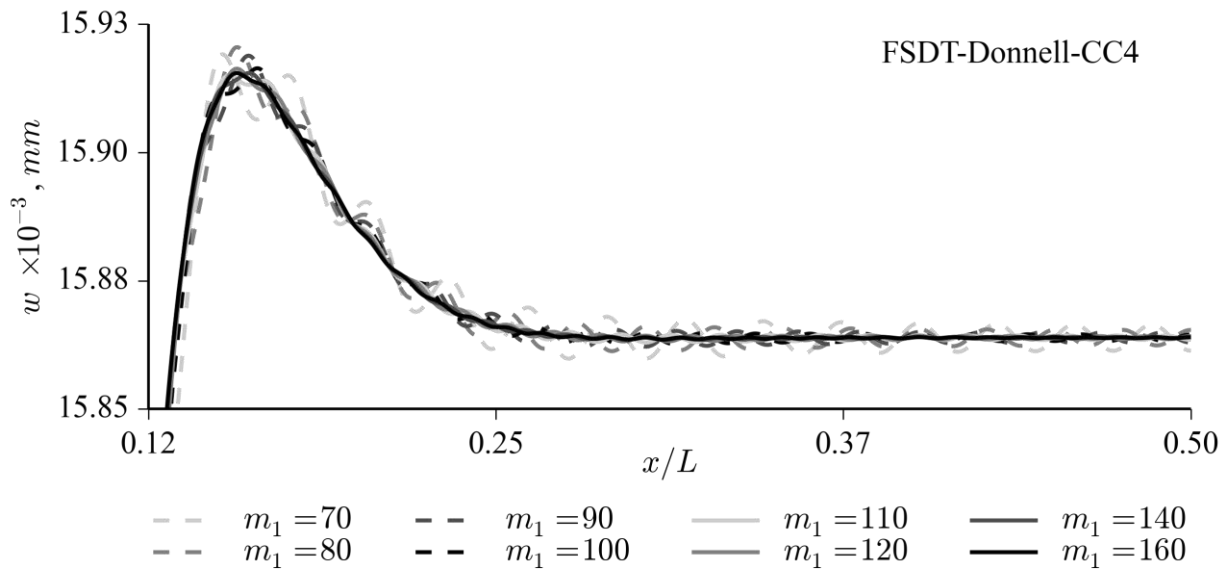


Fig. 4.3.2: Convergence of Cylinder Z33 detailed, with
 $m_2 = n_2 = 0$

In Fig. 4.3.3 and Fig. 4.3.4 it is assumed $m_1 = 120$ and it is shown how the number of terms m_2 and n_2 affect the v and w displacement fields. In these plots the cone is shown from $\theta = -\pi/2$ to $\theta = +\pi/2$, and it can be seen qualitatively that with $m_2 = n_2 = 30$ a good convergence is already achieved. A similar convergence behavior is observed for other conical and cylindrical shells using different boundary conditions other than the SS4 or using the CLPT.

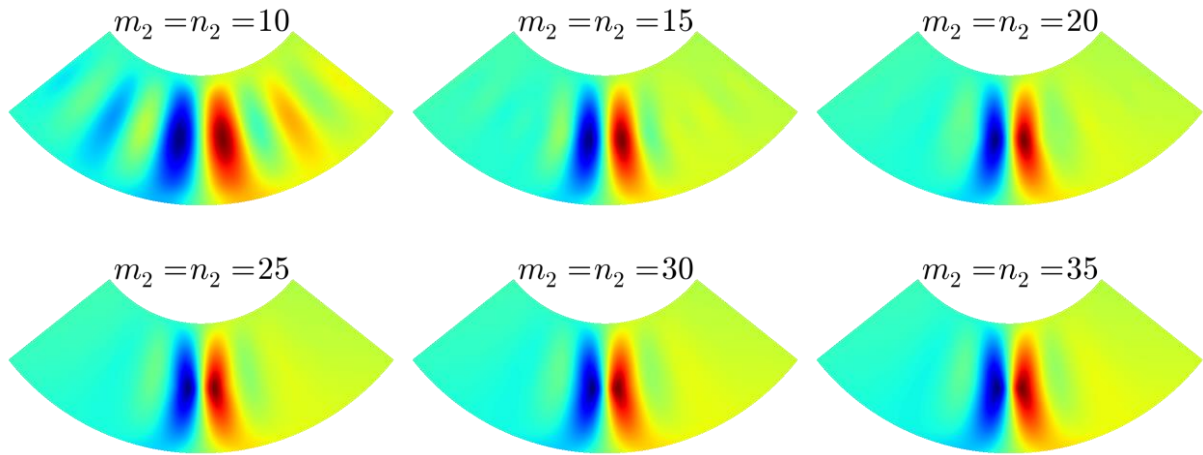


Fig. 4.3.3: Convergence of Cone C14, FSDT-Donnell-SS4,
 $m_1 = 120$, $F_C = 10kN$, $F_{PL} = 10N$, contour v

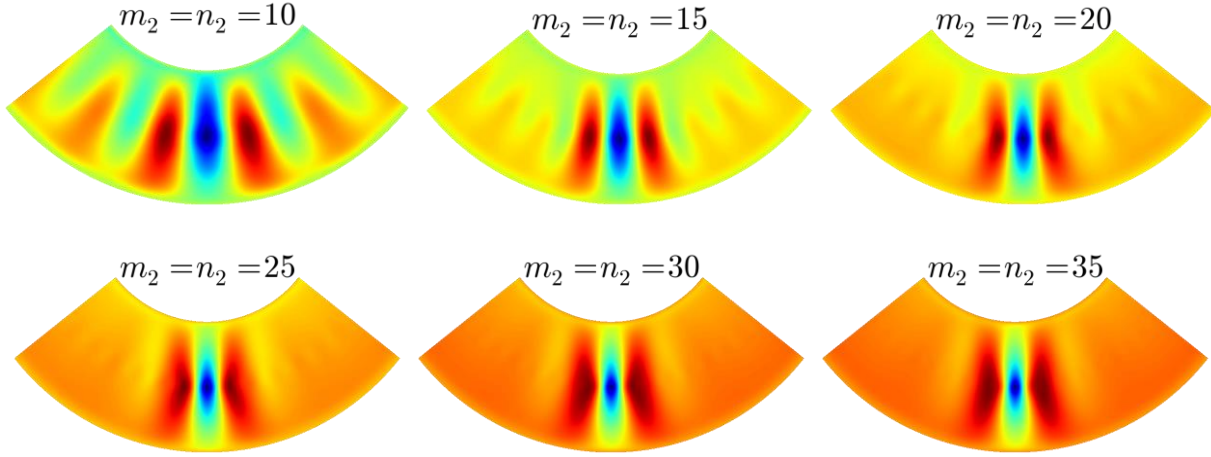


Fig. 4.3.4: Convergence of Cone C14, FSDT-Donnell-SS4,
 $m_1 = 120$, $F_C = 10kN$, $F_{PL} = 10N$, contour w

In Fig. 4.3.5 it is shown the convergence of the normal displacement at the perturbation load application point w_{PL} increasing the number of terms n_2 and using $m_1 = 120$ and $m_2 = n_2/2$. A compressive load of $75 kN$ and a perturbation load of $60 N$ are applied to cylinder Z33. The included finite element result used the model described in Fig. 4.6.1 with a lateral perturbation load applied. The computational efficiency of the proposed models for this case is about two orders of magnitude faster than Abaqus for $n_2 = 60$.

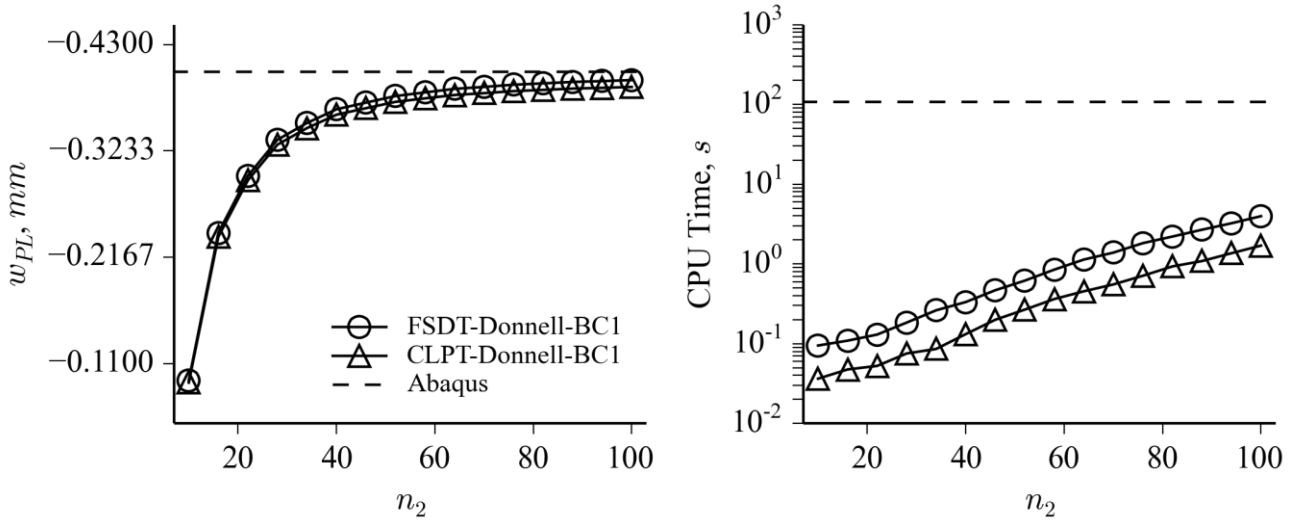


Fig. 4.3.5: Convergence of Cylinder Z33, w_{PL} , $m_1 = 120$, $m_2 = n_2/2$, $n_x = n_\theta = 120$, $F_C = 75kN$, $F_{PL} = 60N$

4.3.2 Stress Field

In Fig. 4.3.6 it is shown the N_{xx} stress component close to the top edge for cone C14 using boundary conditions SS1 and CC1. Note the variation of the minimum stress peak position when the number of approximation terms is increased, making it more difficult to take a point where the convergence analysis can be evaluated. The curves on the right show the convergence behavior of N_{xx} at the top edge at $\theta = 0$. It can be seen that a complete convergence is not achieved even with $m_1 = 200$. For the following stress convergence analyses the value $m_1 = 180$ was chosen.

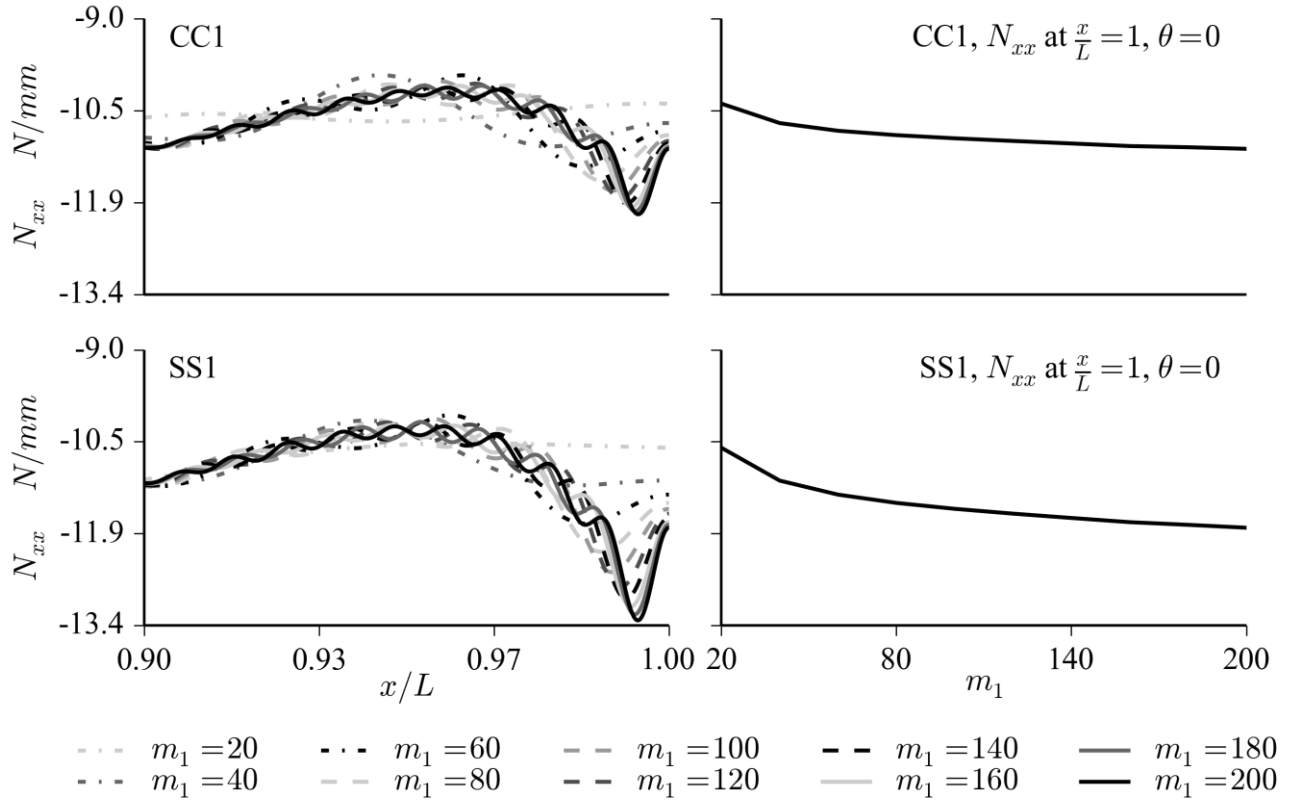


Fig. 4.3.6: Convergence of Cone C14, FSDT-Donnell-BC1,
 $m_2 = n_2 = 0, F_C = 20kN$

In Fig. 4.3.7 it is shown how m_2 and n_2 change the N_{xx} stress for an opened cone (C14) cut from $\theta = -\pi/4$ to $\theta = +\pi/4$. The displacements u, v, w and the stress components $N_{xx}, N_{\theta\theta}, N_{x\theta}$ where measured at the perturbation load application point to evaluate the convergence behavior, as shown in Fig. 4.3.8. It can be seen that the shear membrane stress $N_{x\theta}$ converges faster using the FSDT than the CLPT, which can be explained by the relaxed kinematic equations of the FSDT where the shell rotations ϕ_x and ϕ_θ are independent field variables.

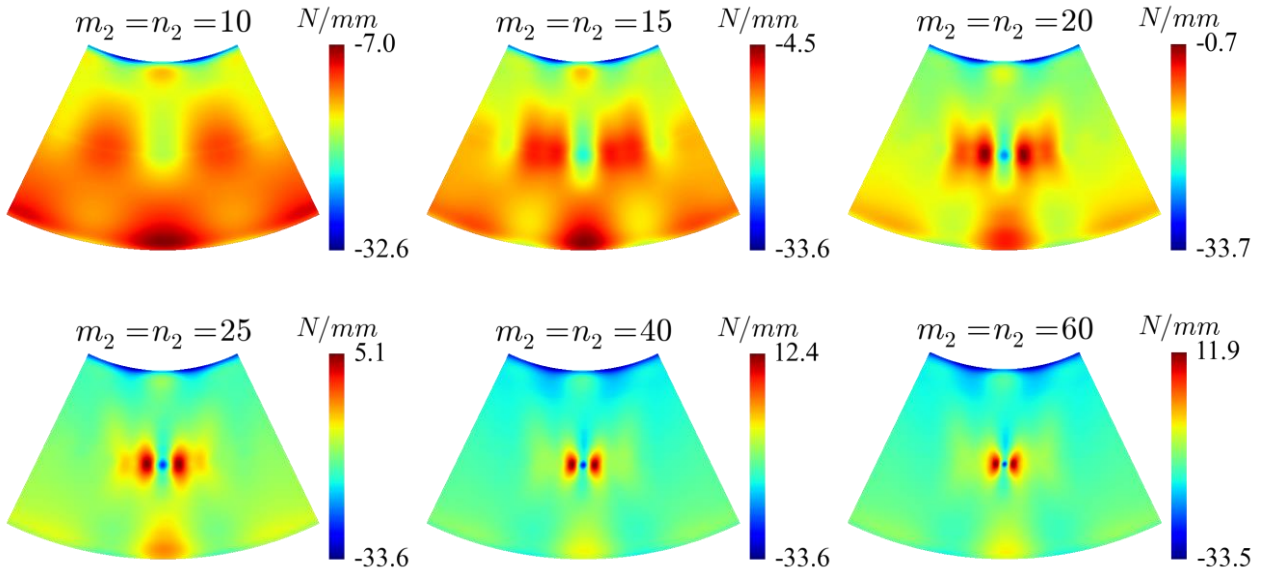


Fig. 4.3.7: Convergence of Cone C14, FSDT-Donnell-SS1,
 $m_1 = 180$, $F_C = 20kN$, $F_{PL} = 60N$, contour N_{xx}

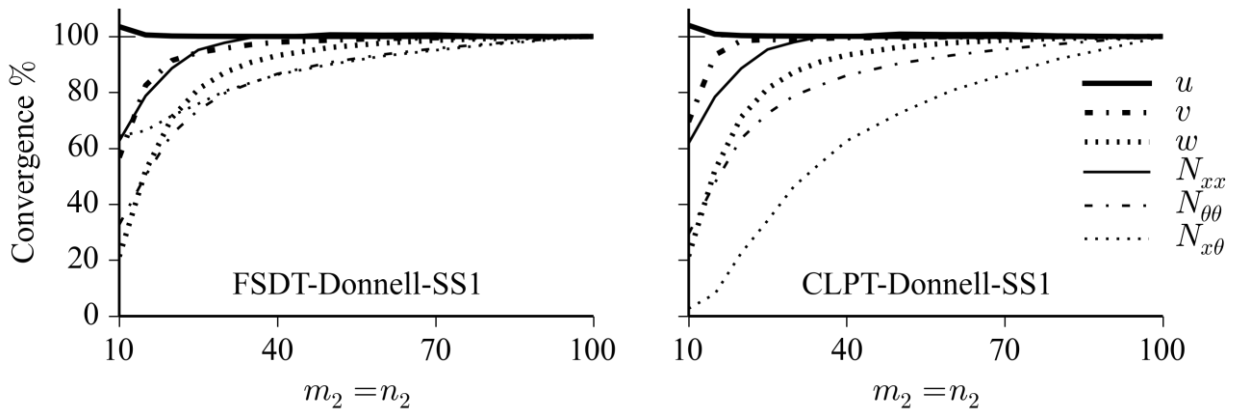


Fig. 4.3.8: Convergence of Cone C14, field variables,
 $m_1 = 180$, $F_C = 20kN$, $F_{PL} = 60N$

4.4 Convergence of the Numerical Integration

As discussed in Section 3.8.4, matrices $[K_{0L}]$, $[K_{LL}]$ and $[K_G]$ and the non-linear parts of the internal force vector $\{F_{int}\}$ are integrated numerically. The number of points required for the numerical integrations depends on the number of terms used in the approximation functions m_1, m_2, n_2 of Eq. (3.6.3), as illustrated in Fig. 4.4.1, where $n_x = 8$ could be used to integrate $\sin(x)$ but not to integrate $\sin(8x)$ or $\cos(8x)$. Based on the non-linear results presented in Sections 4.9, 4.11 and 4.12, the author found that adopting for n_x and n_θ the value of four times ($4 \times$) the maximum frequency for the approximation functions of x and θ , respectively, already gives converged results and further increase of n_x and n_θ leads to an increased computational cost without significantly changing the calculated non-linear buckling loads. When not otherwise specified, the non-linear studies presented in the thesis will use the above mentioned number of integration points. Along the numerical evaluations the author concluded that using fewer points than this reference value may lead to diverged results due to the large integration errors associated.

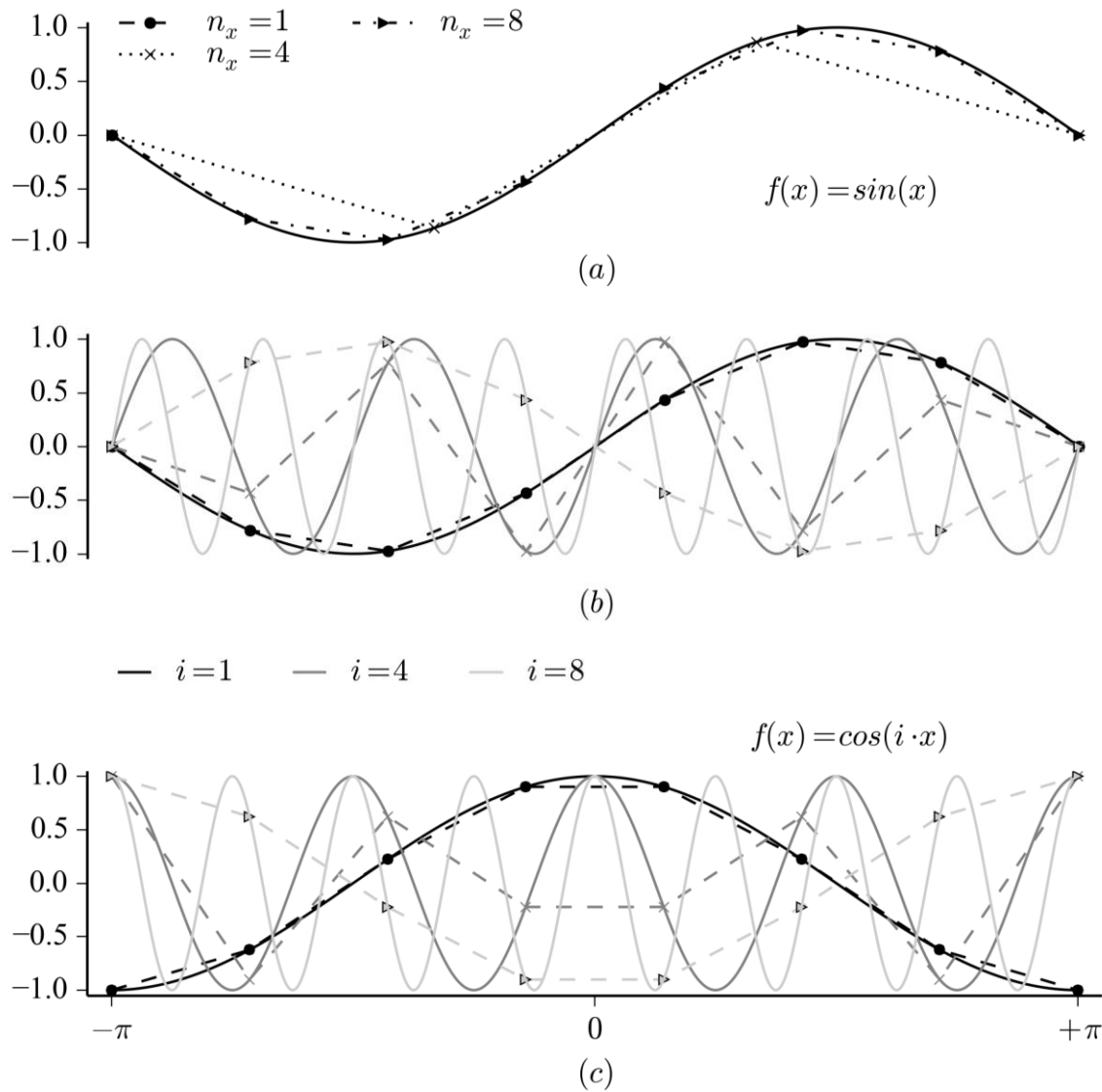


Fig. 4.4.1: Number of Integration Points for Different Frequencies

4.5 Convergence of Non-Linear Static Responses

The convergence behavior of non-linear responses have also been evaluated and compared with finite element results. In Fig. 4.5.1 it is shown the convergence of the normal displacement obtained using a perturbation load of 60 N at the middle cross section of cylinder Z33 and an axial compression of $F_C = 75\text{ kN}$, with model CLPT-Donnell-SS1. The result obtained with finite element using the model described in Fig. 4.6.1 was included for comparison, with its corresponding computational cost, where it can be seen that Abaqus is almost one order of magnitude faster for this case. Using the modified Newton-Raphson (NR) incremental method (cf. Section 3.9.2) reduces the computational cost by approximately its half in this case, with the tangent stiffness matrix $[K_T]$ updated at every 4th iteration. The author also tested Abaqus with the modified NR method updating $[K_T]$ at every 4th or every 8th and surprisingly the computational cost was slightly higher than using the full NR, showing a case where the increased number of iterations required by the modified NR is not compensated by the reduced computational cost of each iteration, giving a strong indication that Abaqus is very efficient to calculate the non-linear stiffness matrices, otherwise the slower convergence would be compensated by the reduced cost of each iteration, as in the Ritz method. Comparing the linear results of Fig. 4.3.5 with the non-linear results of Fig. 4.5.1 it can be seen that the semi-analytical models give accurate predictions in both cases, and that the numerical integration necessary to obtain $[K_T]$ creates a bottleneck that can significantly increase the computational cost.

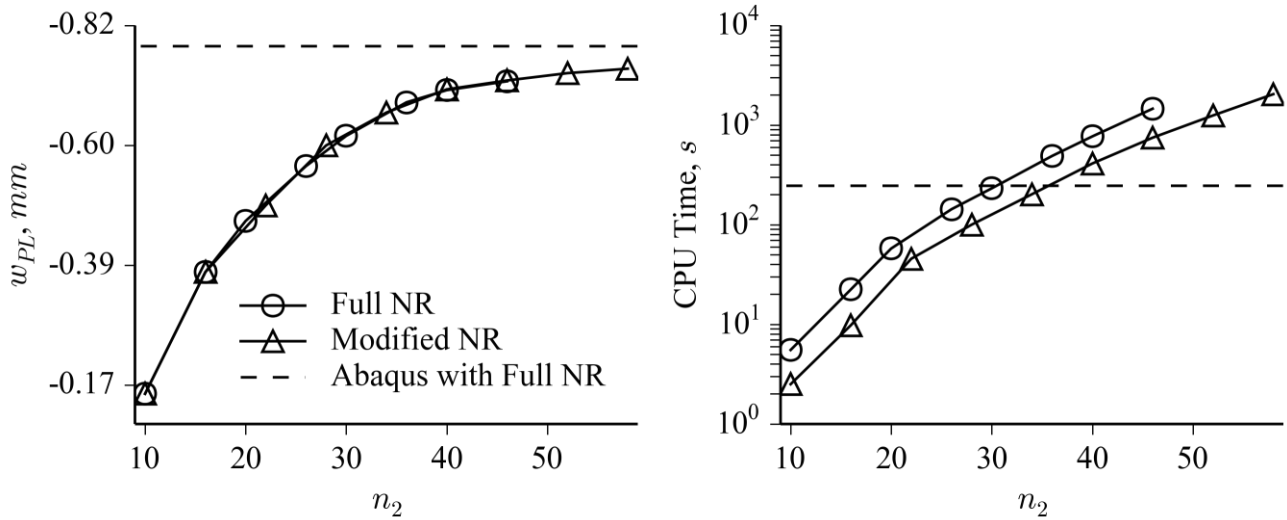


Fig. 4.5.1: Convergence of Cylinder Z33, w_{PL} , $m_1 = 120$, $m_2 = n_2/2$, $n_x = n_\theta = 120$, $F_C = 75\text{ kN}$, $F_{PL} = 60\text{ N}$

4.6 Studies with Linear Buckling Responses

The linear buckling results have been verified using converged finite element models with 420 elements around the circumference and 136 elements along the meridian, keeping the element aspect ratio close to 1:1. The shell element chosen is the linear squared with reduced integration, called S4R in Abaqus [83]. The 50 first buckling modes were compared for axial compression, torsion and pressure loads, for cylinder Z33 and cone C02, both structures described in Table A.2. For axial compression and pressure the SS1 type of boundary conditions was applied to both the bottom and the top edges while for the comparisons using torsion the SS1 type of boundary conditions was applied to the bottom edge and the SS3 type of boundary condition applied to the top edge, due to the difficulty of using the finite element model under torsion with $v = 0$ at the top edge. All the cases were simulated using $m_1 = m_2 = n_2 = 80$. A schematic view of the finite element model used for axial compression and pressure is illustrated in Fig. 4.6.1. The finite element used for torsion is different, as shown in Fig. 4.6.2. The transformation of the outputs from the rectangular coordinate system to the semi-analytical model coordinate system is performed using Eq. (4.6.1).

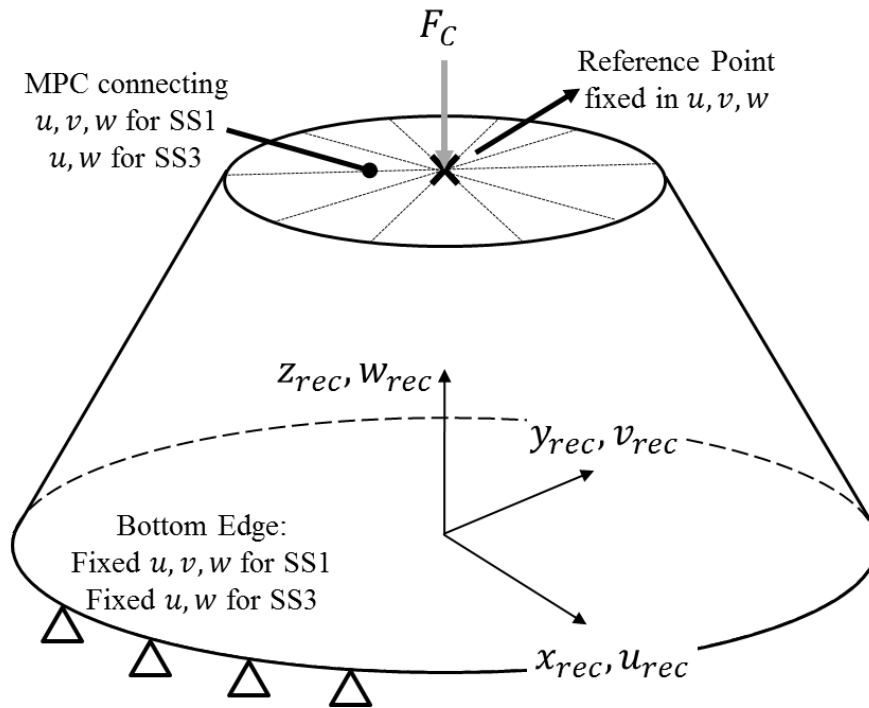


Fig. 4.6.1: Finite Element Model for Linear Buckling with Axial Compression and Pressure

$$\theta_{coord} = \arctan(y_{coord}/x_{coord})$$

$$\begin{aligned}
 u_{cyl} &= -w_{rec} & u_{cone} &= w_{cyl} \sin \alpha + u_{cyl} \cos \alpha \\
 v_{cyl} &= v_{rec} \cos \theta_{coord} - u_{rec} \sin \theta_{coord} & v_{cone} &= v_{cyl} \\
 w_{cyl} &= v_{rec} \sin \theta_{coord} + u_{rec} \cos \theta_{coord} & w_{cone} &= w_{cyl} \cos \alpha - u_{cyl} \sin \alpha
 \end{aligned} \tag{4.6.1}$$

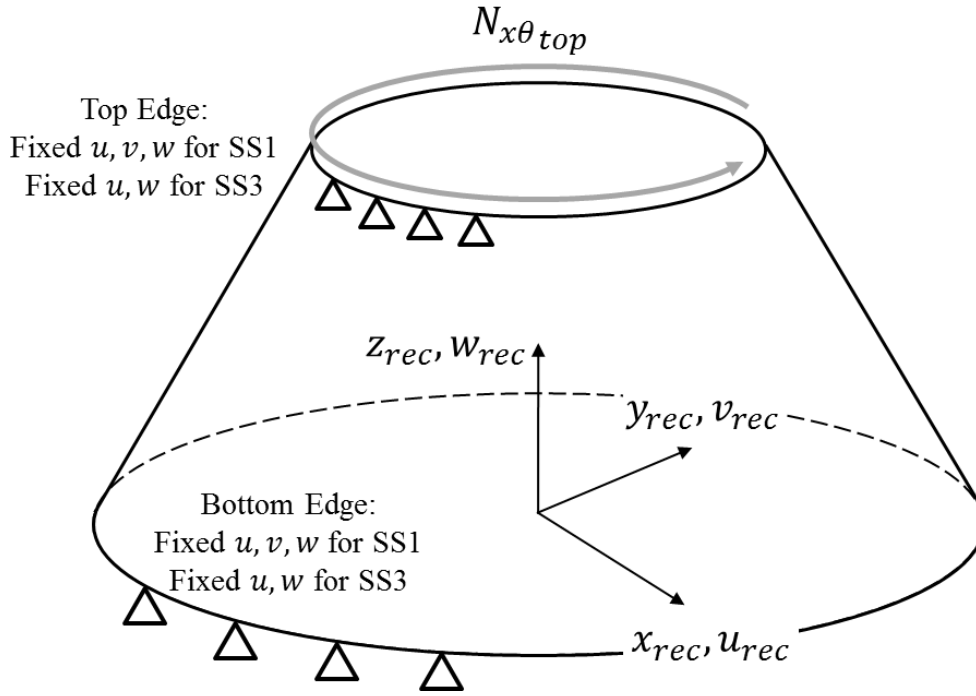


Fig. 4.6.2: Finite Element Model for Linear Buckling with Torsion

4.6.1 Axial Compression

Table 4.6.1 shows the linear buckling predictions for cylinder Z33 under axial compression using Abaqus, the CLPT model with Donnell's and Sanders's equations and the FSDT model with Donnell's equations. The percentage difference between the semi-analytical models and Abaqus, calculated using Eq. (4.6.2) is shown in Table 4.6.2, where it can be seen the maximum difference of 1.8% for the 37th mode. The buckling modes are compared in Fig. 4.6.3, showing that the first buckling modes are identical and that the higher buckling modes may be interchanged, due to the proximity of the eigenvalues, as shown in Table 4.6.1.

$$\%diff = 100 \times \frac{Ritz - Abaqus}{Abaqus} \quad (4.6.2)$$

Table 4.6.3 shows the predictions for cone C02, and the percentage difference is shown in Table 4.6.4, where it can be seen a maximum difference of -0.81% for the 43rd mode. From the buckling modes shown in Fig. 4.6.4 and Fig. 4.6.5 it can be seen that the first modes are identical and that there is an interchange of the higher modes due to the proximity of the eigenvalues. The FSDT model has the closest behavior when compared to the finite element, as expected since the finite elements are also formulated using the FSDT, though using a different shear correction factor than the value of 5/6 adopted for the FSDT semi-analytical models herein presented (cf. Section 2.3 about shear correction factors).

The author has recently published [106] a study about linear buckling predictions where the proposed models are compared to other models available in the literature, showing that in the available models the orthotropic laminate approximation is used, i.e. the terms $A_{16}, A_{26}, B_{16}, B_{26}, D_{16}, D_{26}, A_{45}$ of the laminate stiffness matrix are assumed to be zero, such that the torsion-like buckling shapes (found in Fig. 4.6.3, Fig. 4.6.4 and Fig. 4.6.5) cannot be obtained.

Table 4.6.1: Linear Buckling under Axial Compression, Cylinder Z33 (all in kN)

Mode	Abaqus	CLPT Donnell	CLPT Sanders	FSDT Donnell	Mode	Abaqus	CLPT Donnell	CLPT Sanders	FSDT Donnell
01	192.860	194.532	193.467	193.202	26	208.086	210.452	209.540	208.974
02	192.860	194.532	193.467	193.202	27	209.122	211.083	209.675	209.553
03	192.954	194.959	193.792	193.596	28	209.122	211.083	209.675	209.553
04	192.954	194.959	193.792	193.596	29	209.689	212.733	211.878	211.287
05	195.748	197.200	196.210	195.850	30	209.689	212.733	211.878	211.287
06	195.748	197.200	196.210	195.850	31	212.495	214.531	213.488	212.826
07	196.635	199.039	197.730	197.580	32	212.495	214.531	213.488	212.826
08	196.635	199.039	197.730	197.580	33	213.636	216.114	215.228	214.813
09	198.100	200.489	199.282	199.039	34	213.636	216.114	215.228	214.813
10	198.100	200.489	199.282	199.039	35	214.204	216.200	215.240	214.983
11	199.808	201.950	200.826	200.485	36	214.204	216.200	215.240	214.983
12	199.808	201.950	200.826	200.485	37	214.241	218.094	217.128	216.544
13	200.422	202.580	201.639	201.151	38	214.241	218.094	217.128	216.544
14	200.422	202.580	201.639	201.151	39	215.959	219.395	218.541	217.767
15	201.244	203.305	202.003	201.832	40	215.959	219.395	218.541	217.767
16	201.244	203.305	202.003	201.832	41	217.062	219.694	218.751	218.449
17	204.686	206.745	205.672	205.194	42	217.062	219.694	218.751	218.449
18	204.686	206.745	205.672	205.194	43	218.305	220.642	219.743	218.880
19	205.569	208.826	207.284	207.165	44	218.305	220.642	219.743	218.880
20	205.569	208.826	207.284	207.165	45	219.216	222.367	220.664	220.571
21	207.015	209.402	208.544	208.099	46	219.216	222.367	220.664	220.571
22	207.015	209.402	208.544	208.099	47	220.115	224.053	223.211	222.418
23	207.821	210.169	209.304	208.886	48	220.115	224.053	223.211	222.418
24	207.821	210.169	209.304	208.886	49	220.609	224.166	223.333	222.685
25	208.086	210.452	209.540	208.974	50	220.609	224.166	223.333	222.685

Table 4.6.2: Linear Buckling under Axial Compression, Cylinder Z33, Percentage Differences

Mode	CLPT Donnell	CLPT Sanders	FSDT Donnell	Mode	CLPT Donnell	CLPT Sanders	FSDT Donnell
01	0.87%	0.31%	0.18%	27	0.94%	0.26%	0.21%
03	1.04%	0.43%	0.33%	29	1.45%	1.04%	0.76%
05	0.74%	0.24%	0.05%	31	0.96%	0.47%	0.16%
07	1.22%	0.56%	0.48%	33	1.16%	0.75%	0.55%
09	1.21%	0.60%	0.47%	35	0.93%	0.48%	0.36%
11	1.07%	0.51%	0.34%	37	1.80%	1.35%	1.07%
13	1.08%	0.61%	0.36%	39	1.59%	1.20%	0.84%
15	1.02%	0.38%	0.29%	41	1.21%	0.78%	0.64%
17	1.01%	0.48%	0.25%	43	1.07%	0.66%	0.26%
19	1.58%	0.83%	0.78%	45	1.44%	0.66%	0.62%
21	1.15%	0.74%	0.52%	47	1.79%	1.41%	1.05%
23	1.13%	0.71%	0.51%	49	1.61%	1.23%	0.94%
25	1.14%	0.70%	0.43%				

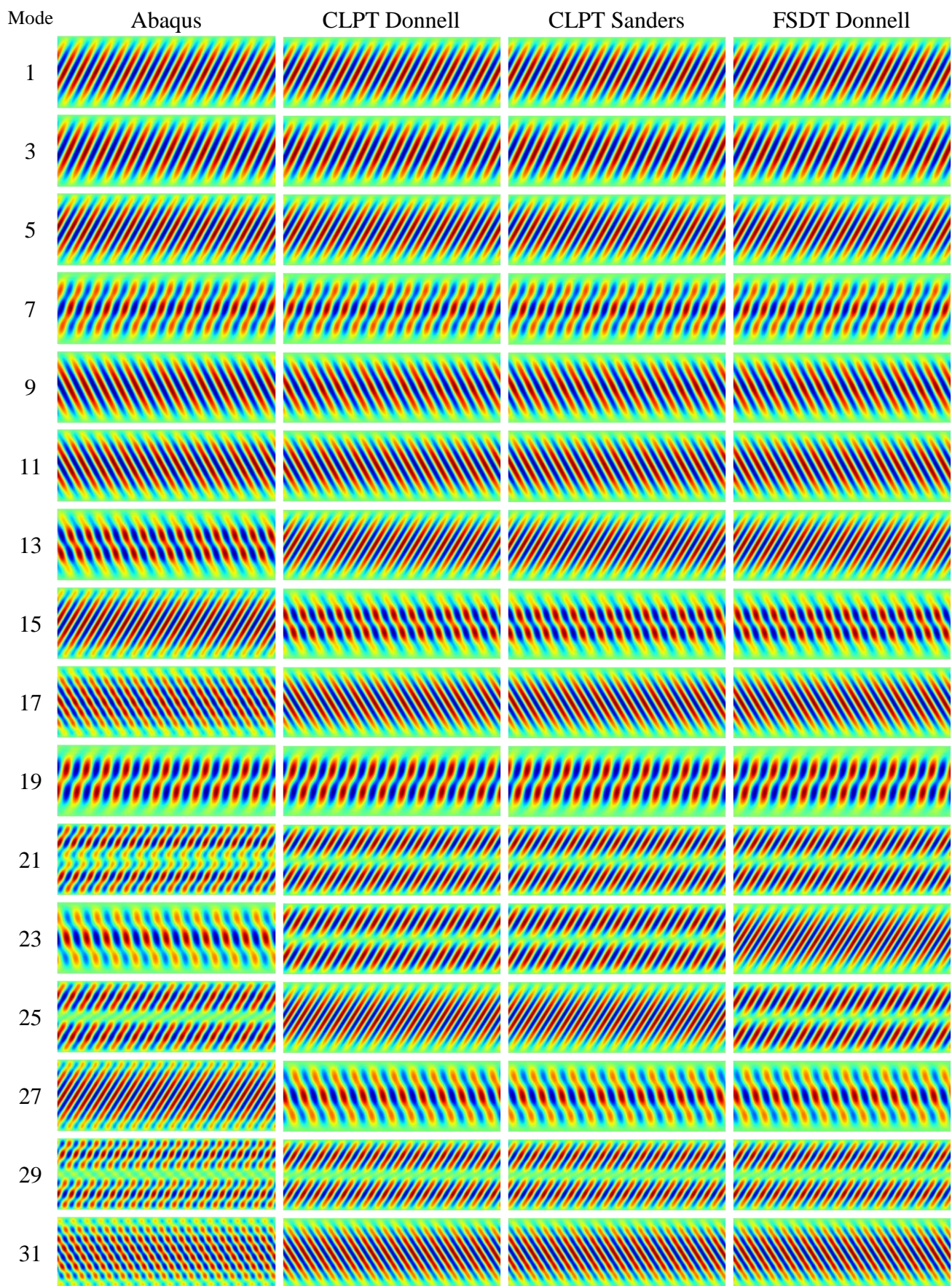


Fig. 4.6.3: Linear Buckling, Axial Compression, Cylinder Z33, modes 1-31

Table 4.6.3: Linear Buckling under Axial Compression, Cone C02 (all in kN)

Mode	Abaqus	CLPT Donnell	CLPT Sanders	FSDT Donnell	Mode	Abaqus	CLPT Donnell	CLPT Sanders	FSDT Donnell
01	122.626	123.285	123.285	122.590	26	128.695	129.469	129.462	128.727
02	122.626	123.285	123.285	122.590	27	130.186	130.592	130.565	129.888
03	122.676	123.311	123.309	122.637	28	130.186	130.592	130.565	129.888
04	122.676	123.311	123.309	122.637	29	130.214	130.980	130.970	130.166
05	122.871	123.541	123.541	122.791	30	130.214	130.980	130.970	130.166
06	122.871	123.541	123.541	122.791	31	131.742	132.109	132.109	130.757
07	122.972	123.669	123.665	122.977	32	131.742	132.408	132.408	131.053
08	123.064	123.669	123.665	123.003	33	131.902	132.408	132.408	131.053
09	123.064	123.800	123.800	123.003	34	132.193	132.587	132.573	131.715
10	123.805	124.375	124.368	123.708	35	132.193	132.587	132.573	131.715
11	123.805	124.375	124.368	123.708	36	132.570	132.893	132.857	131.941
12	124.259	125.067	125.067	124.650	37	132.570	132.893	132.857	131.941
13	124.836	125.432	125.422	124.759	38	133.059	133.304	133.302	132.178
14	124.836	125.432	125.422	124.759	39	133.059	133.304	133.302	132.178
15	124.901	125.622	125.621	125.120	40	133.358	134.291	134.271	133.382
16	124.901	125.622	125.621	125.120	41	133.358	134.291	134.271	133.382
17	125.953	126.730	126.727	126.141	42	134.503	134.793	134.790	133.419
18	125.953	126.730	126.727	126.141	43	134.503	134.793	134.790	133.419
19	126.346	126.833	126.818	126.151	44	135.046	135.391	135.346	134.678
20	126.346	126.833	126.818	126.151	45	135.046	135.391	135.346	134.678
21	127.273	128.045	128.041	127.380	46	135.118	136.100	136.070	135.173
22	127.273	128.045	128.041	127.380	47	135.118	136.100	136.070	135.173
23	128.126	128.562	128.542	127.869	48	136.517	136.860	136.854	135.467
24	128.126	128.562	128.542	127.869	49	136.517	136.860	136.854	135.467
25	128.695	129.469	129.462	128.727	50	136.910	137.817	137.746	137.136

Table 4.6.4: Linear Buckling under Axial Compression, Cone C02, Percentage Differences

Mode	CLPT Donnell	CLPT Sanders	FSDT Donnell	Mode	CLPT Donnell	CLPT Sanders	FSDT Donnell
01	0.54%	0.54%	-0.03%	27	0.31%	0.29%	-0.23%
03	0.52%	0.52%	-0.03%	29	0.59%	0.58%	-0.04%
05	0.55%	0.55%	-0.06%	31	0.28%	0.28%	-0.75%
07	0.57%	0.56%	0.00%	33	0.38%	0.38%	-0.64%
09	0.60%	0.60%	-0.05%	35	0.30%	0.29%	-0.36%
11	0.46%	0.46%	-0.08%	37	0.24%	0.22%	-0.47%
13	0.48%	0.47%	-0.06%	39	0.18%	0.18%	-0.66%
15	0.58%	0.58%	0.18%	41	0.70%	0.68%	0.02%
17	0.62%	0.61%	0.15%	43	0.22%	0.21%	-0.81%
19	0.39%	0.37%	-0.15%	45	0.26%	0.22%	-0.27%
21	0.61%	0.60%	0.08%	47	0.73%	0.70%	0.04%
23	0.34%	0.32%	-0.20%	49	0.25%	0.25%	-0.77%
25	0.60%	0.60%	0.02%				

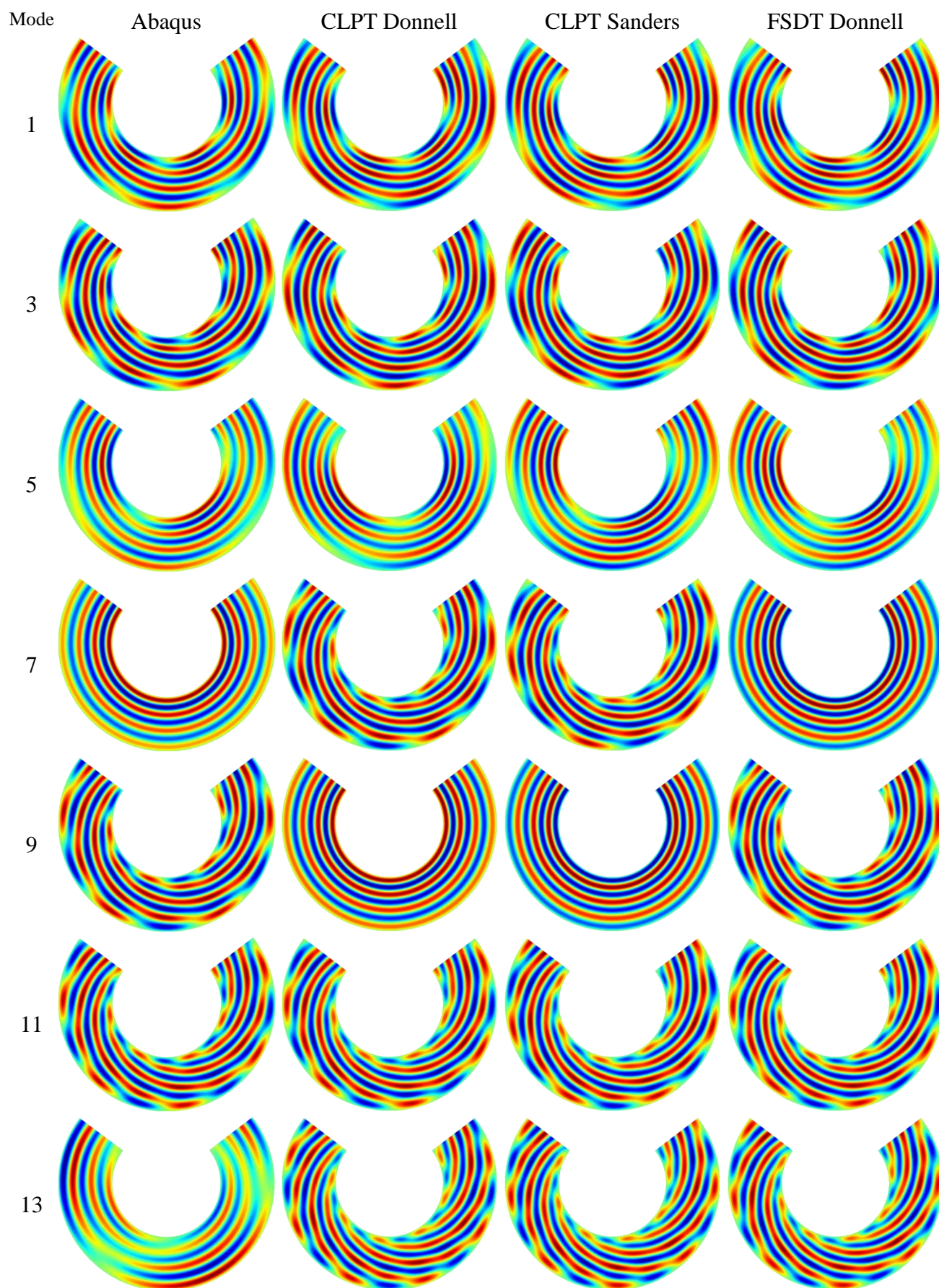


Fig. 4.6.4: Linear Buckling, Axial Compression, Cone C02, modes 1-13

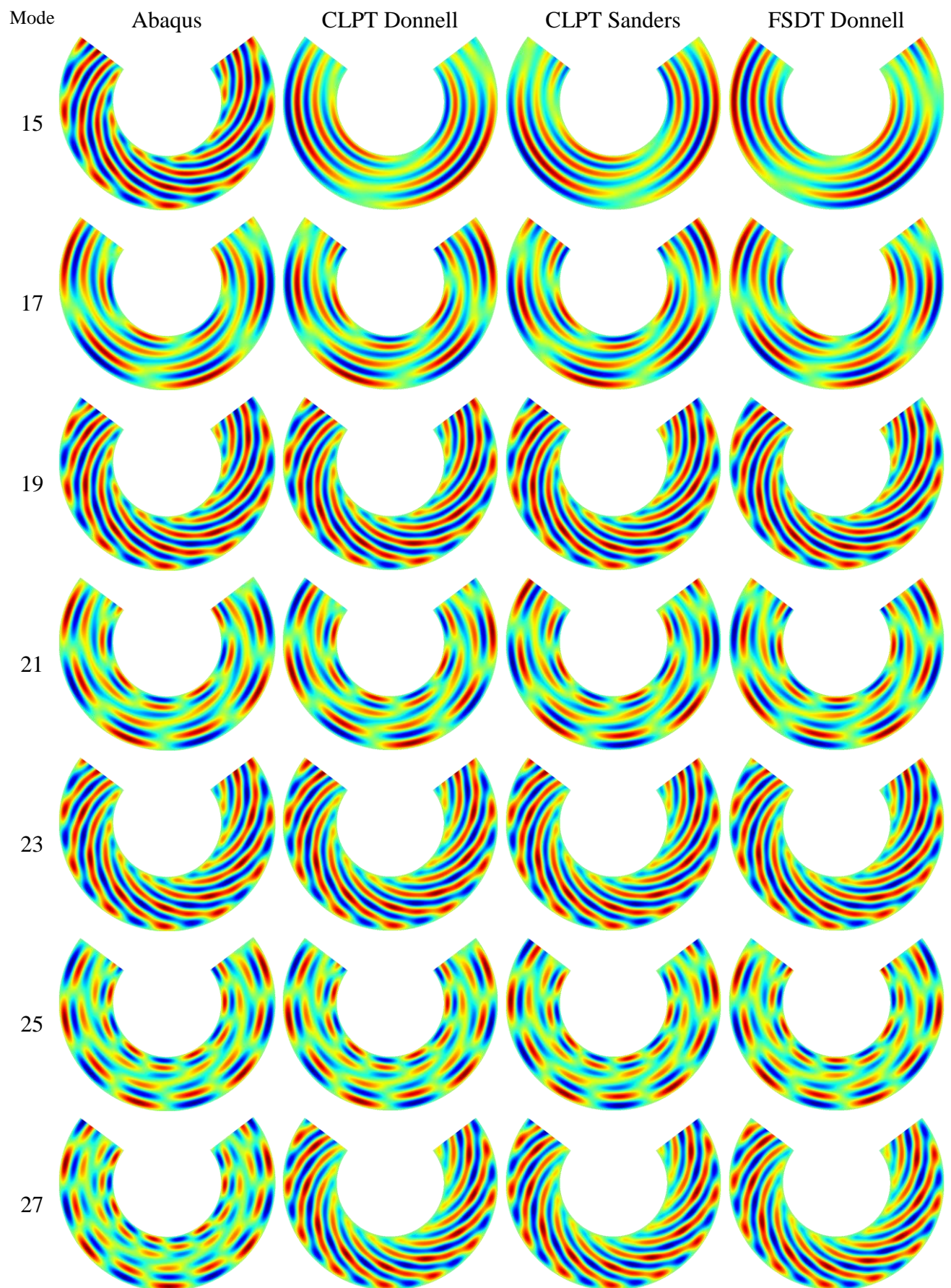


Fig. 4.6.5: Linear Buckling, Axial Compression, Cone C02, modes 15-27

4.6.2 Torsion

Table 4.6.5 shows the linear buckling predictions for cylinder Z33 under torsion using Abaqus, the CLPT-Donnell, CLPT-Sanders and the FSDT-Donnell models. The percentage difference between the semi-analytical models and Abaqus, calculated using Eq. (4.6.2) is shown in Table 4.6.6, where it can be seen the maximum difference of 8.81% for the 17th mode. Table 4.6.7 shows the predictions for cone C02, and the percentage difference is shown in Table 4.6.8, where it can be seen a maximum difference of 7.34% also for the 17th mode. Similarly to the axial compression cases, the FSDT model has the closest behavior when compared to the finite element, which was expected for the same reasons already mentioned.

4.6.3 Pressure

Table 4.6.9 shows the linear buckling predictions for cylinder Z33 under pressure using Abaqus, the CLPT-Donnell, CLPT-Sanders and the FSDT-Donnell models. The percentage difference between the semi-analytical models and Abaqus, calculated using Eq. (4.6.2) is shown in Table 4.6.10, where it can be seen the maximum difference of -7.88% for the 45th mode. Table 4.6.11 shows the predictions for cone C02, and the percentage difference is shown in Table 4.6.12, where it can be seen a maximum difference of 3.87% for the 29th mode. From the results it can be seen that for pressure loads the CLPT-Donnell better approaches the finite element predictions, contrasting with the axial compression and torsion cases where the FSDT-Donnell is the model that best approaches the finite element results. A reasonable explanation is that the shear correction factor of 5/6 adopted for the semi-analytical models using the FSDT is causing this larger difference between the FSDT and the finite element results, making it necessary to investigate more advanced shear correction factors for the proposed semi-analytical models using the FSDT.

Table 4.6.5: Linear Buckling under Torsion, Cylinder Z33 (all in $kN \times m$)

Mode	Abaqus	CLPT Donnell	CLPT Sanders	FSDT Donnell	Mode	Abaqus	CLPT Donnell	CLPT Sanders	FSDT Donnell
01	9.017	9.511	9.524	9.414	26	13.830	14.210	14.318	14.106
02	9.017	9.540	9.525	9.429	27	14.190	14.335	14.350	14.220
03	9.129	9.566	9.545	9.459	28	14.190	14.337	14.353	14.225
04	9.129	9.569	9.547	9.462	29	14.281	14.451	14.437	14.327
05	9.246	9.908	9.885	9.799	30	14.281	14.453	14.467	14.329
06	9.246	9.910	9.885	9.802	31	14.643	15.128	15.104	14.996
07	9.706	9.968	10.001	9.884	32	14.643	15.129	15.104	15.005
08	9.706	10.000	10.002	9.897	33	15.005	15.376	15.396	15.250
09	9.812	10.467	10.444	10.361	34	15.005	15.376	15.399	15.267
10	9.812	10.470	10.445	10.364	35	15.441	15.449	15.410	15.301
11	10.340	11.200	11.175	11.091	36	15.441	15.450	15.421	15.302
12	10.340	11.202	11.176	11.092	37	15.560	16.014	15.986	15.869
13	11.117	11.310	11.328	11.187	38	15.560	16.014	15.988	15.878
14	11.117	11.325	11.360	11.209	39	15.924	16.799	16.765	16.636
15	11.578	12.077	12.047	11.959	40	15.924	16.800	16.769	16.638
16	11.578	12.079	12.052	11.963	41	16.357	17.076	17.047	16.916
17	12.024	13.083	13.057	12.955	42	16.357	17.077	17.049	16.925
18	12.024	13.084	13.079	12.964	43	16.802	17.383	17.452	17.260
19	13.049	13.956	13.946	13.823	44	16.802	17.409	17.455	17.313
20	13.049	13.956	13.956	13.840	45	17.011	18.258	18.225	18.071
21	13.607	14.035	13.983	13.900	46	17.011	18.259	18.227	18.075
22	13.607	14.037	14.023	13.919	47	18.096	18.290	18.264	18.116
23	13.793	14.171	14.178	14.032	48	18.096	18.292	18.265	18.118
24	13.793	14.184	14.183	14.063	49	18.245	18.363	18.361	18.224
25	13.830	14.208	14.224	14.077	50	18.245	18.364	18.364	18.228

Table 4.6.6: Linear Buckling under Torsion, Cylinder Z33, Percentage Differences

Mode	CLPT Donnell	CLPT Sanders	FSDT Donnell	Mode	CLPT Donnell	CLPT Sanders	FSDT Donnell
01	5.48%	5.62%	4.41%	27	1.02%	1.13%	0.22%
03	4.79%	4.56%	3.62%	29	1.19%	1.09%	0.32%
05	7.16%	6.91%	5.98%	31	3.31%	3.15%	2.41%
07	2.70%	3.04%	1.83%	33	2.47%	2.60%	1.63%
09	6.67%	6.44%	5.59%	35	0.05%	-0.20%	-0.91%
11	8.32%	8.08%	7.26%	37	2.92%	2.73%	1.98%
13	1.73%	1.90%	0.63%	39	5.49%	5.28%	4.47%
15	4.31%	4.05%	3.29%	41	4.39%	4.22%	3.42%
17	8.81%	8.59%	7.75%	43	3.46%	3.87%	2.73%
19	6.94%	6.87%	5.92%	45	7.34%	7.14%	6.23%
21	3.15%	2.77%	2.15%	47	1.07%	0.93%	0.11%
23	2.74%	2.79%	1.74%	49	0.65%	0.64%	-0.11%
25	2.73%	2.85%	1.79%				

Table 4.6.7: Linear Buckling under Torsion, Cone C02 (all in $kN \times m$)

Mode	Abaqus	CLPT Donnell	CLPT Sanders	FSDT Donnell	Mode	Abaqus	CLPT Donnell	CLPT Sanders	FSDT Donnell
01	16.511	17.183	17.187	17.078	26	26.025	27.444	27.565	27.327
02	16.511	17.186	17.188	17.079	27	28.083	28.446	28.434	28.149
03	16.664	17.187	17.201	17.091	28	28.083	28.447	28.435	28.150
04	16.664	17.190	17.201	17.093	29	30.275	30.677	30.665	30.334
05	16.970	17.667	17.667	17.551	30	30.275	30.677	30.665	30.335
06	16.970	17.671	17.667	17.552	31	31.589	32.088	32.105	31.788
07	17.254	17.873	17.895	17.778	32	31.589	32.091	32.106	31.792
08	17.254	17.877	17.897	17.782	33	31.773	32.284	32.299	31.963
09	18.174	18.524	18.519	18.393	34	31.773	32.292	32.300	31.968
10	18.174	18.526	18.519	18.394	35	31.919	32.397	32.422	32.120
11	18.328	19.511	19.558	19.420	36	31.919	32.401	32.423	32.125
12	18.328	19.515	19.559	19.428	37	32.376	32.909	32.915	32.553
13	19.356	19.670	19.663	19.521	38	32.376	32.914	32.916	32.554
14	19.356	19.674	19.663	19.523	39	32.595	33.044	33.032	32.651
15	20.759	21.057	21.048	20.887	40	32.595	33.046	33.032	32.652
16	20.759	21.059	21.048	20.888	41	32.884	33.331	33.366	33.067
17	21.044	22.513	22.589	22.411	42	32.884	33.342	33.367	33.075
18	21.044	22.529	22.592	22.416	43	33.324	33.883	33.886	33.488
19	22.350	22.649	22.639	22.454	44	33.324	33.888	33.886	33.489
20	22.350	22.650	22.639	22.455	45	33.414	35.022	35.081	34.718
21	24.111	24.421	24.410	24.197	46	33.414	35.028	35.081	34.720
22	24.111	24.422	24.411	24.198	47	34.565	35.042	35.156	34.784
23	25.786	26.357	26.346	26.100	48	34.565	35.046	35.156	34.789
24	25.786	26.359	26.346	26.100	49	34.630	35.156	35.263	34.892
25	26.025	27.430	27.561	27.318	50	34.630	35.158	35.271	34.915

Table 4.6.8: Linear Buckling under Torsion, Cone C02, Percentage Differences

Mode	CLPT Donnell	CLPT Sanders	FSDT Donnell	Mode	CLPT Donnell	CLPT Sanders	FSDT Donnell
01	4.07%	4.09%	3.43%	27	1.29%	1.25%	0.23%
03	3.14%	3.22%	2.56%	29	1.33%	1.29%	0.20%
05	4.11%	4.11%	3.43%	31	1.58%	1.63%	0.63%
07	3.59%	3.72%	3.04%	33	1.61%	1.66%	0.60%
09	1.93%	1.90%	1.21%	35	1.50%	1.58%	0.63%
11	6.45%	6.71%	5.96%	37	1.65%	1.67%	0.55%
13	1.62%	1.58%	0.85%	39	1.38%	1.34%	0.17%
15	1.44%	1.40%	0.62%	41	1.36%	1.47%	0.56%
17	6.98%	7.34%	6.49%	43	1.68%	1.69%	0.49%
19	1.34%	1.29%	0.46%	45	4.81%	4.99%	3.90%
21	1.28%	1.24%	0.36%	47	1.38%	1.71%	0.63%
23	2.21%	2.17%	1.22%	49	1.52%	1.83%	0.75%
25	5.40%	5.90%	4.97%				

Table 4.6.9: Linear Buckling under Pressure, Cylinder Z33 (N/mm^2)

Mode	Abaqus	CLPT Donnell	CLPT Sanders	FSDT Donnell	Mode	Abaqus	CLPT Donnell	CLPT Sanders	FSDT Donnell
01	-0.0275	-0.0274	-0.0263	-0.0269	26	-0.0540	-0.0521	-0.0500	-0.0517
02	-0.0275	-0.0274	-0.0263	-0.0269	27	-0.0549	-0.0547	-0.0537	-0.0541
03	-0.0283	-0.0280	-0.0268	-0.0275	28	-0.0549	-0.0547	-0.0537	-0.0541
04	-0.0283	-0.0280	-0.0268	-0.0275	29	-0.0567	-0.0557	-0.0546	-0.0551
05	-0.0296	-0.0295	-0.0285	-0.0290	30	-0.0567	-0.0557	-0.0546	-0.0551
06	-0.0296	-0.0295	-0.0285	-0.0290	31	-0.0612	-0.0583	-0.0566	-0.0577
07	-0.0331	-0.0330	-0.0321	-0.0325	32	-0.0612	-0.0583	-0.0566	-0.0577
08	-0.0331	-0.0330	-0.0321	-0.0325	33	-0.0617	-0.0612	-0.0601	-0.0606
09	-0.0347	-0.0340	-0.0324	-0.0335	34	-0.0617	-0.0612	-0.0601	-0.0606
10	-0.0347	-0.0340	-0.0324	-0.0335	35	-0.0622	-0.0615	-0.0604	-0.0608
11	-0.0376	-0.0375	-0.0366	-0.0370	36	-0.0622	-0.0615	-0.0604	-0.0608
12	-0.0376	-0.0375	-0.0366	-0.0370	37	-0.0685	-0.0675	-0.0664	-0.0668
13	-0.0429	-0.0427	-0.0418	-0.0422	38	-0.0685	-0.0675	-0.0664	-0.0668
14	-0.0429	-0.0427	-0.0418	-0.0422	39	-0.0689	-0.0686	-0.0673	-0.0679
15	-0.0483	-0.0468	-0.0456	-0.0463	40	-0.0689	-0.0686	-0.0673	-0.0679
16	-0.0483	-0.0468	-0.0456	-0.0463	41	-0.0722	-0.0686	-0.0675	-0.0679
17	-0.0486	-0.0479	-0.0468	-0.0473	42	-0.0722	-0.0686	-0.0675	-0.0679
18	-0.0486	-0.0479	-0.0468	-0.0473	43	-0.0731	-0.0700	-0.0687	-0.0692
19	-0.0491	-0.0485	-0.0475	-0.0479	44	-0.0731	-0.0700	-0.0687	-0.0692
20	-0.0491	-0.0485	-0.0475	-0.0479	45	-0.0751	-0.0707	-0.0692	-0.0700
21	-0.0513	-0.0494	-0.0480	-0.0488	46	-0.0751	-0.0707	-0.0692	-0.0700
22	-0.0513	-0.0494	-0.0480	-0.0488	47	-0.0754	-0.0735	-0.0722	-0.0727
23	-0.0522	-0.0511	-0.0496	-0.0505	48	-0.0754	-0.0735	-0.0722	-0.0727
24	-0.0522	-0.0511	-0.0496	-0.0505	49	-0.0764	-0.0744	-0.0732	-0.0736
25	-0.0540	-0.0521	-0.0500	-0.0517	50	-0.0764	-0.0744	-0.0732	-0.0736

Table 4.6.10: Linear Buckling under Pressure, Cylinder Z33, Percentage Differences

Mode	CLPT Donnell	CLPT Sanders	FSDT Donnell	Mode	CLPT Donnell	CLPT Sanders	FSDT Donnell
01	-0.61%	-4.38%	-2.38%	27	-0.32%	-2.18%	-1.48%
03	-1.11%	-5.25%	-2.81%	29	-1.78%	-3.74%	-2.93%
05	-0.38%	-3.74%	-2.08%	31	-4.80%	-7.62%	-5.71%
07	-0.29%	-3.25%	-1.86%	33	-0.69%	-2.50%	-1.81%
09	-2.06%	-6.47%	-3.44%	35	-1.27%	-2.94%	-2.35%
11	-0.27%	-2.87%	-1.70%	37	-1.47%	-3.10%	-2.53%
13	-0.27%	-2.58%	-1.59%	39	-0.40%	-2.35%	-1.46%
15	-2.95%	-5.50%	-4.14%	41	-5.00%	-6.51%	-5.97%
17	-1.48%	-3.86%	-2.70%	43	-4.32%	-6.10%	-5.31%
19	-1.24%	-3.29%	-2.46%	45	-5.89%	-7.88%	-6.78%
21	-3.72%	-6.42%	-4.81%	47	-2.55%	-4.23%	-3.57%
23	-2.05%	-5.01%	-3.23%	49	-2.63%	-4.11%	-3.65%
25	-3.53%	-7.48%	-4.42%				

Table 4.6.11: Linear Buckling under Pressure, Cone C02 (N/mm^2)

Mode	Abaqus	CLPT Donnell	CLPT Sanders	FSDT Donnell	Mode	Abaqus	CLPT Donnell	CLPT Sanders	FSDT Donnell
01	-0.0280	-0.0278	-0.0276	-0.0277	26	-0.0430	-0.0434	-0.0433	-0.0432
02	-0.0280	-0.0278	-0.0276	-0.0277	27	-0.0456	-0.0461	-0.0459	-0.0458
03	-0.0283	-0.0282	-0.0280	-0.0281	28	-0.0456	-0.0461	-0.0459	-0.0458
04	-0.0283	-0.0282	-0.0280	-0.0281	29	-0.0478	-0.0466	-0.0459	-0.0464
05	-0.0286	-0.0284	-0.0281	-0.0283	30	-0.0478	-0.0466	-0.0459	-0.0464
06	-0.0286	-0.0284	-0.0281	-0.0283	31	-0.0484	-0.0489	-0.0487	-0.0486
07	-0.0292	-0.0292	-0.0290	-0.0291	32	-0.0484	-0.0489	-0.0487	-0.0486
08	-0.0292	-0.0292	-0.0290	-0.0291	33	-0.0512	-0.0518	-0.0517	-0.0515
09	-0.0305	-0.0306	-0.0303	-0.0304	34	-0.0512	-0.0518	-0.0517	-0.0515
10	-0.0305	-0.0306	-0.0303	-0.0304	35	-0.0542	-0.0549	-0.0547	-0.0545
11	-0.0310	-0.0307	-0.0304	-0.0305	36	-0.0542	-0.0549	-0.0547	-0.0545
12	-0.0310	-0.0307	-0.0304	-0.0305	37	-0.0572	-0.0580	-0.0579	-0.0576
13	-0.0321	-0.0322	-0.0320	-0.0321	38	-0.0572	-0.0580	-0.0579	-0.0576
14	-0.0321	-0.0322	-0.0320	-0.0321	39	-0.0604	-0.0594	-0.0590	-0.0590
15	-0.0340	-0.0341	-0.0339	-0.0340	40	-0.0604	-0.0594	-0.0590	-0.0590
16	-0.0340	-0.0341	-0.0339	-0.0340	41	-0.0607	-0.0596	-0.0592	-0.0593
17	-0.0360	-0.0359	-0.0354	-0.0358	42	-0.0607	-0.0596	-0.0592	-0.0593
18	-0.0360	-0.0359	-0.0354	-0.0358	43	-0.0612	-0.0602	-0.0599	-0.0599
19	-0.0365	-0.0362	-0.0360	-0.0360	44	-0.0612	-0.0602	-0.0599	-0.0599
20	-0.0365	-0.0362	-0.0360	-0.0360	45	-0.0614	-0.0613	-0.0611	-0.0608
21	-0.0382	-0.0385	-0.0383	-0.0383	46	-0.0614	-0.0613	-0.0611	-0.0608
22	-0.0382	-0.0385	-0.0383	-0.0383	47	-0.0629	-0.0615	-0.0611	-0.0612
23	-0.0405	-0.0409	-0.0407	-0.0407	48	-0.0629	-0.0615	-0.0611	-0.0612
24	-0.0405	-0.0409	-0.0407	-0.0407	49	-0.0634	-0.0618	-0.0615	-0.0614
25	-0.0430	-0.0434	-0.0433	-0.0432	50	-0.0634	-0.0618	-0.0615	-0.0614

Table 4.6.12: Linear Buckling under Pressure, Cone C02, Percentage Differences

Mode	CLPT Donnell	CLPT Sanders	FSDT Donnell	Mode	CLPT Donnell	CLPT Sanders	FSDT Donnell
01	-0.41%	-1.36%	-0.88%	27	1.04%	0.62%	0.45%
03	-0.18%	-1.02%	-0.65%	29	-2.56%	-3.87%	-2.84%
05	-0.73%	-1.78%	-1.18%	31	1.12%	0.80%	0.51%
07	0.02%	-0.74%	-0.46%	33	1.20%	0.91%	0.56%
09	0.19%	-0.68%	-0.29%	35	1.27%	1.00%	0.60%
11	-1.16%	-2.14%	-1.58%	37	1.34%	1.08%	0.63%
13	0.34%	-0.27%	-0.14%	39	-1.74%	-2.31%	-2.27%
15	0.48%	-0.07%	-0.01%	41	-1.76%	-2.38%	-2.26%
17	-0.27%	-1.56%	-0.64%	43	-1.60%	-2.13%	-2.17%
19	-0.89%	-1.38%	-1.39%	45	-0.21%	-0.55%	-0.93%
21	0.73%	0.28%	0.21%	47	-2.29%	-2.86%	-2.75%
23	0.84%	0.43%	0.30%	49	-2.53%	-3.01%	-3.12%
25	0.95%	0.57%	0.38%				

4.7 Comparison with Shadmehri

Among the recent studies carried out by the author in Ref. [106] a comparison between the models proposed in this thesis and the model of Shadmehri et al. [70] was performed. Shadmehri's publication seems to be the most recent (prior to Ref. [106]) dealing with semi-analytical linear buckling predictions for cones, and Shadmehri's model is originally designed to fulfill the boundary conditions SS3, but in the reproduced model herein implemented the CC3 can also be achieved using the elastic constraints described in Section 3.5.

Cone ShadC04 described in Table A.2 with a R/h ratio of 100 was used along the comparisons, with the ply angle γ varying between 0 and 90°. Two different heights H were studied and the details about the finite element models for each height are given in Table 4.7.1. The FSDT-Donnell-BC3 model was used for the comparisons. The finite element model, similar to the one shown in Fig. 4.6.1, was run using two shear correction factors: the one calculated using Abaqus' procedure as detailed in Section 2.3; and a constant shear correction factor of $K = 5/6$. The results are shown in Fig. 4.7.1, where it can be seen that Shadmehri's model is limited to short cones. The reason for this limitation can be perceived from the eigenvector corresponding to the critical buckling mode, shown in Fig. 4.7.2, where it can be seen that the torsion-like pattern of the buckling mode cannot be represented by Shadmehri's model.

Additional comparisons with finite elements were performed by the author [106] using cones ShadC02 and ShadC04 described in Table A.2; and the boundary conditions SS1 and CC1. The FSDT-Donnell-BC1 model was selected for these comparisons and the results are shown in Fig. 4.7.3 and Fig. 4.7.4, where it can be seen a good correlation between the finite element results and the proposed models. For the cone with two plies, ShadC02, the differences that appear when Abaqus is run with $K = 5/6$ can be clearly noticed. This difference would be expected for the shorter cone with $H = 25.4 \text{ mm}$ where the shear strains should have a stronger effect, but surprisingly the difference also occurs for $H = 254 \text{ mm}$. Recalling that this cone has a $R/h = 200$, this case is a remarkable case where a thin-walled structure has its linear buckling behavior strongly depending on the shear correction factor.

Table 4.7.1: Finite Element Parameters for the Comparisons with Shadmehri's Models

Model	Elements Around θ	Element Size (mm)
$H = 254 \text{ mm}$	178	6.35
$H = 25.4 \text{ mm}$	420	3.75

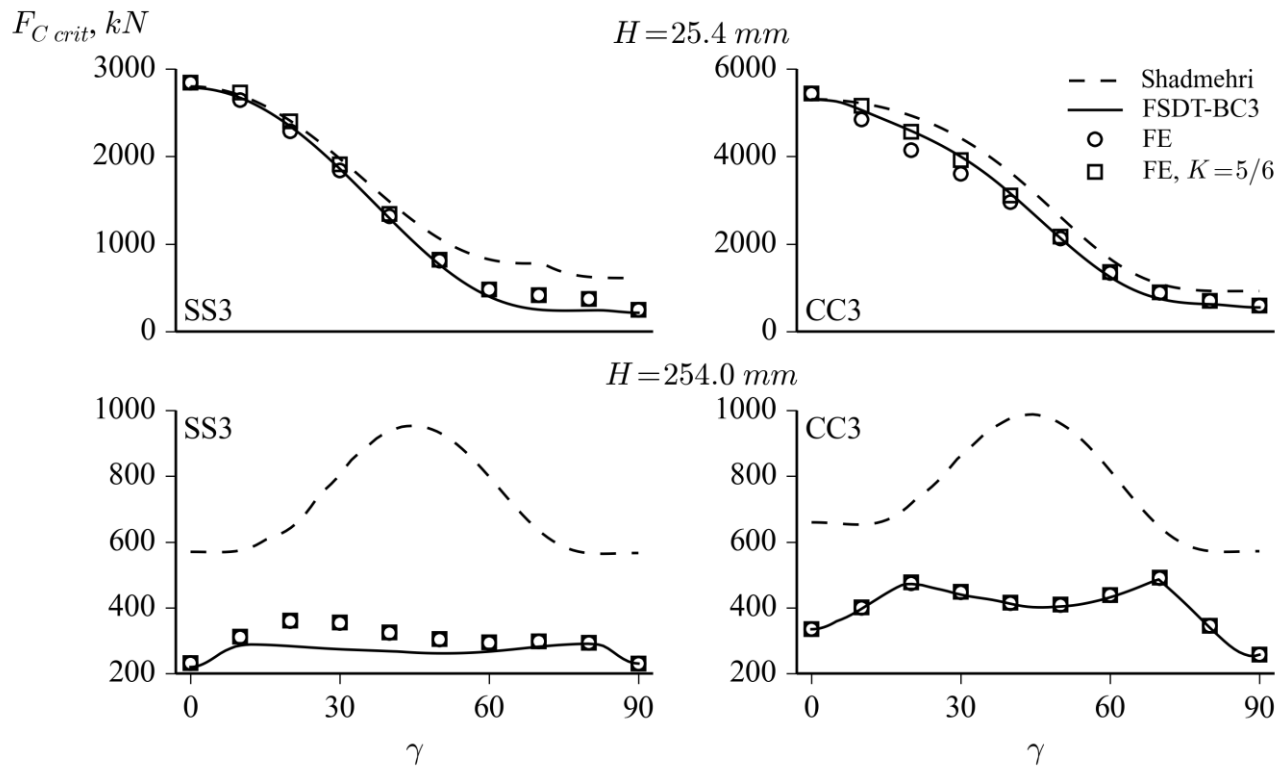


Fig. 4.7.1: FEM compared to Shadmehri and the FSDT-Donnell-BC3 model,
Cone ShadC04,
Ref. [106]

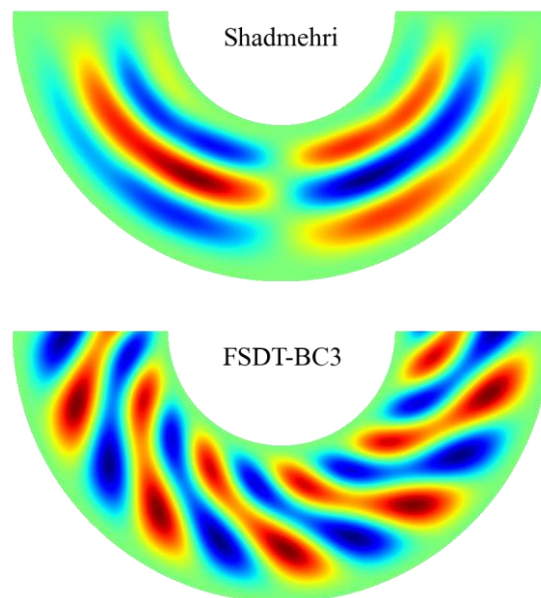


Fig. 4.7.2: Critical Buckling Mode for Cone ShadC04 with:
 $H = 254\ mm$, $\gamma = 20^\circ$, CC3,
Ref. [106]

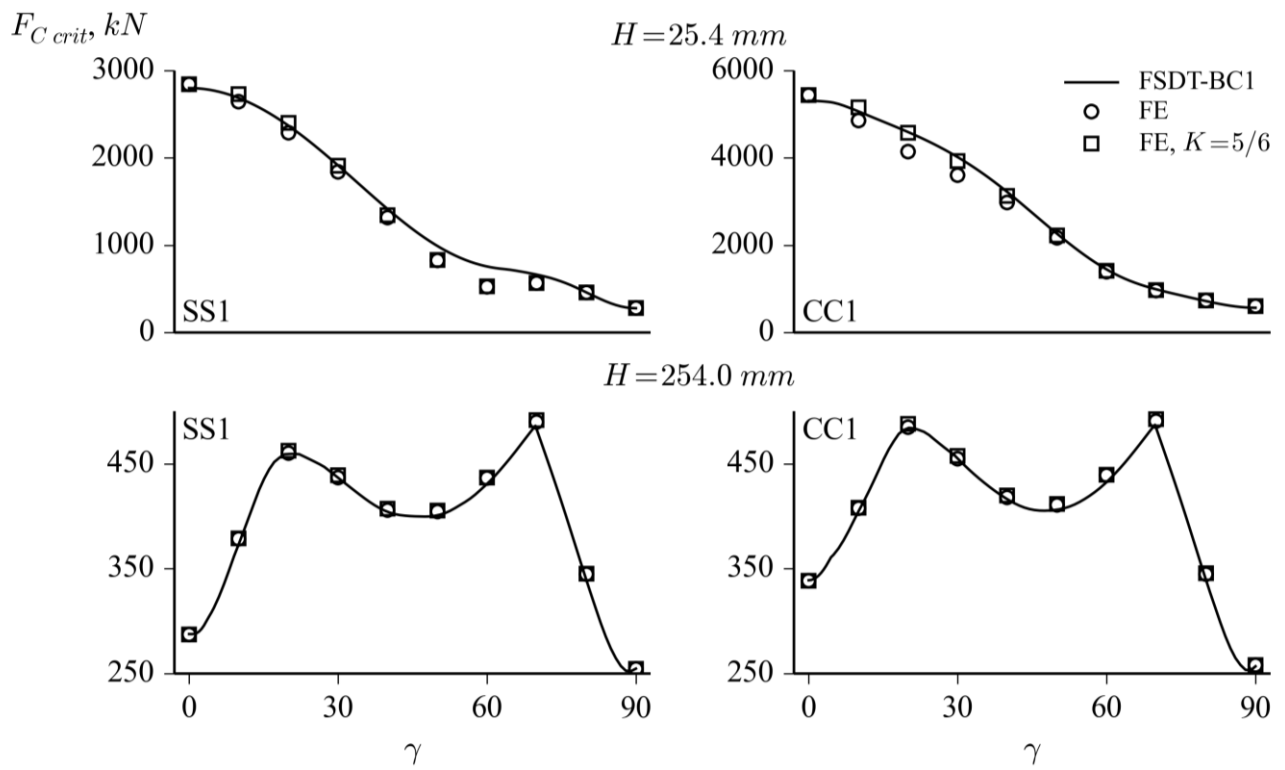


Fig. 4.7.3: FEM compared to Shadmehri and the FSDT-Donnell-BC1 model, Cone ShadC04, Ref. [106]

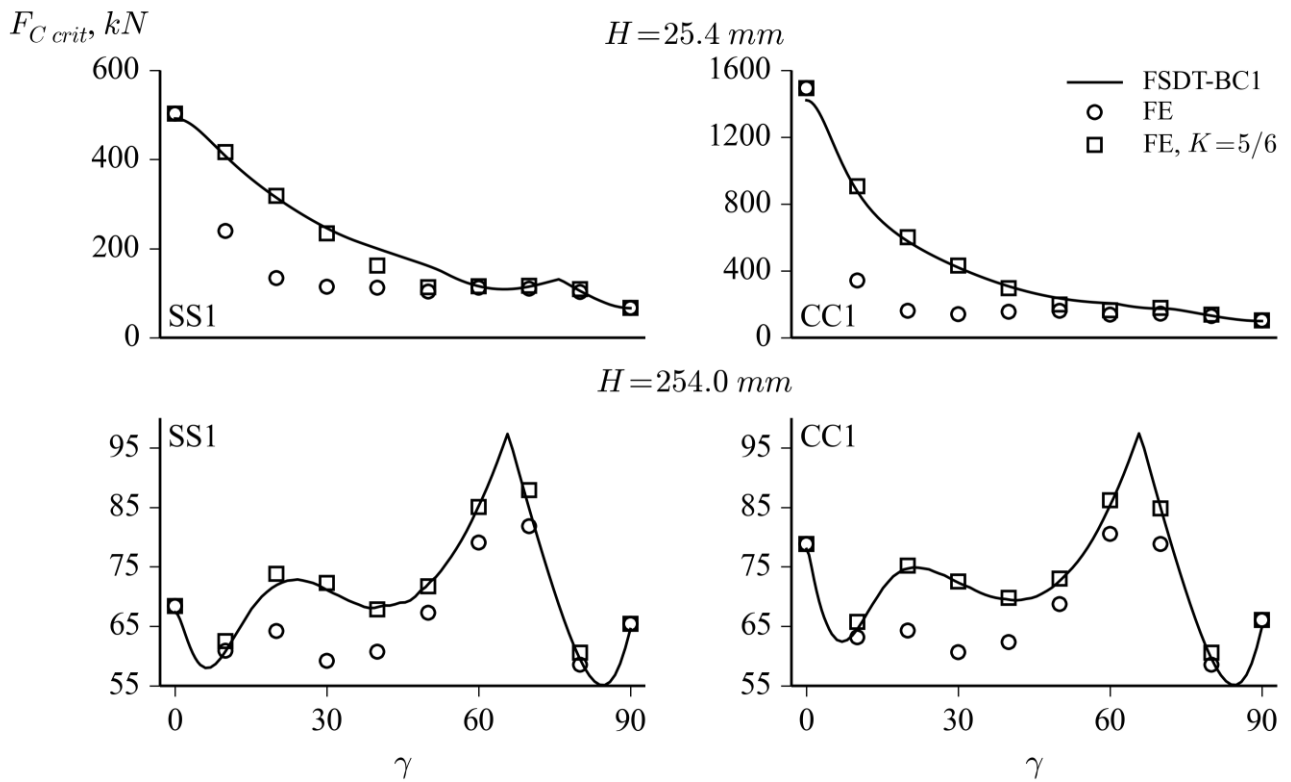


Fig. 4.7.4: FEM compared to Shadmehri and the FSDT-Donnell-BC1 model, Cone ShadC02, Ref. [106]

4.8 Test Results from Meyer-Piening

Experimental results obtained with combined load cases using axial and torsion loads are presented by Meyer-Piening [107] for many cylinders. The experimental results for four cylinders Z11, Z12, Z28 and Z33, described in Table A.2, were used to verify the semi-analytical models FSDT-Donnell-BC1 and FSDT-Donnell-BC2. The linear buckling problem was solved using Eq. (3.4.11) where the critical axial compression load is obtained for a fixed and initially applied torsion load. In the actual experiments Meyer-Piening et al. fixed the axial load and found the critical torsion load, but the author found that fixing the torsion load and finding the critical axial load gives the same result and leads to an easier approach for building the desired curves. The author has published these results in Ref. [106].

Considering first the results of Fig. 4.8.1, it can be seen that for the combined load cases closer to pure axial compression the linear buckling predictions overestimates the load carrying capacity of the cylinders since in these analyses no geometric or load imperfections are taken into account. However, when the torsion component increases the structural sensitivity to these imperfections is reduced leading to a good correlation between the test results and the linear buckling predictions. Taking a closer look into the boundary conditions, Meyer-Piening et al. reported that a cushion of epoxy resin was placed between the test specimen and the rigid plates of the testing machine, creating a condition $u|_{x=0} \neq 0$ and $u|_{x=L} \neq 0$, which corresponds to something in between the first and the second type of boundary conditions (cf. Table 3.5.1). Therefore, a simulation using CC2 boundary conditions was performed and the results are shown in Fig. 4.8.2, where a better correlation with the test results can be observed.

Another important consideration regarding the boundary conditions is that the perfect clamped conditions may not be achieved and that the test conditions will most probably fall between the SS2 and the CC2 boundary conditions, and Fig. 4.8.3 shows the results for SS2. It can be seen that for higher torsion loads the test results can be predicted by the semi-analytical models using boundary conditions between CC1, CC2 and the SS2. The actual test conditions can be determined using vibration correlation techniques [108] and once the actual stiffnesses are known the semi-analytical models can be evaluated using measured values for $K_{bot}^{u,v,w,\phi_x,\phi_\theta}$ and $K_{top}^{u,v,w,\phi_x,\phi_\theta}$, as discussed in Section 3.5.

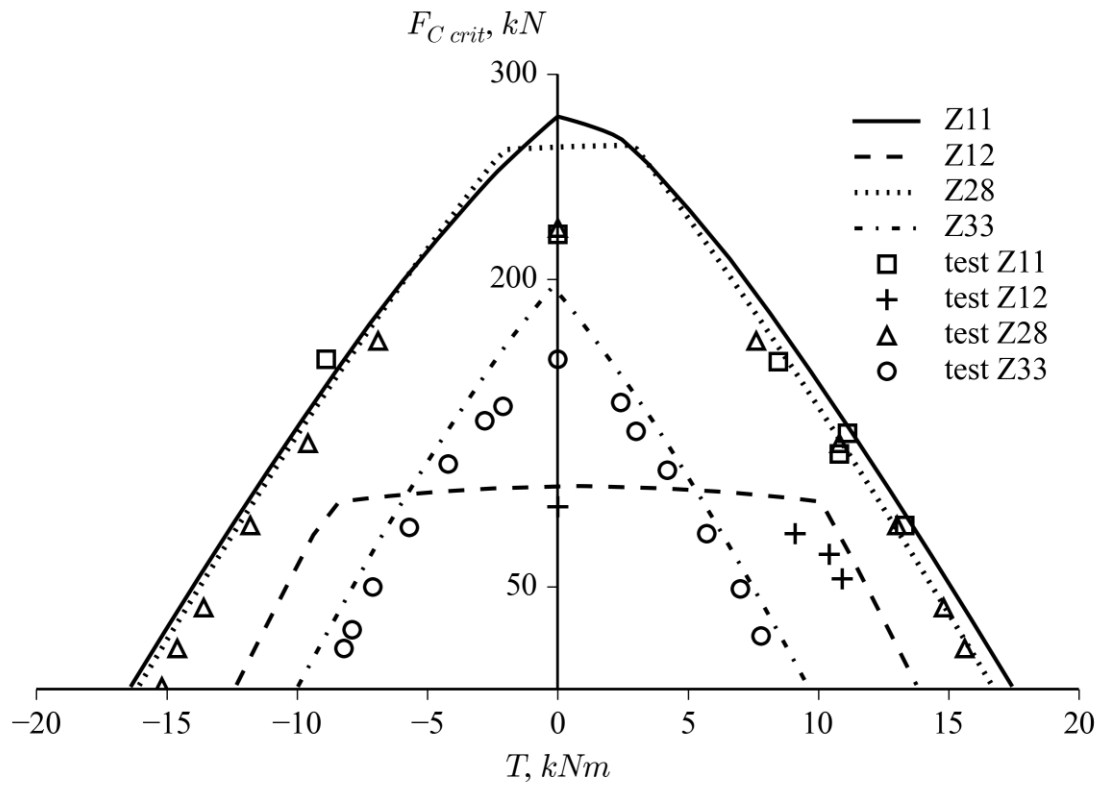


Fig. 4.8.1: Combined Torsion-Axial Compression, FSDT-Donnell-CC1, modified from Ref. [106]

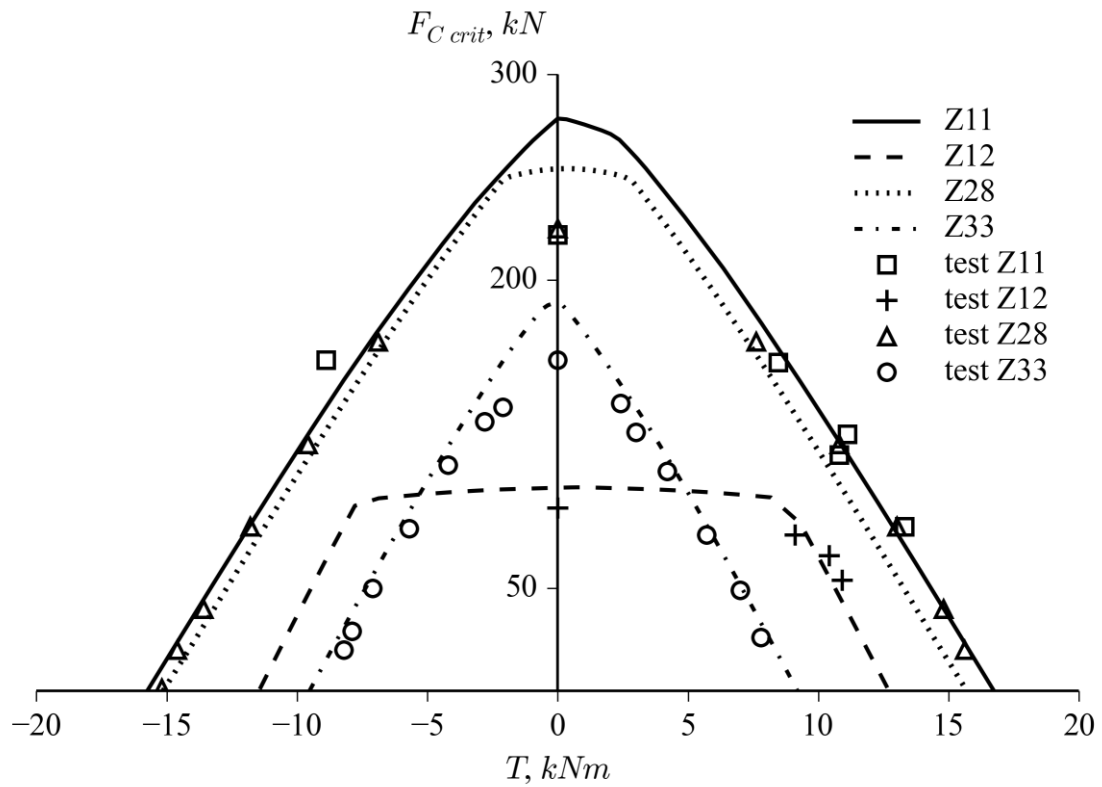


Fig. 4.8.2: Combined Torsion-Axial Compression, FSDT-Donnell-CC2, modified from Ref. [106]

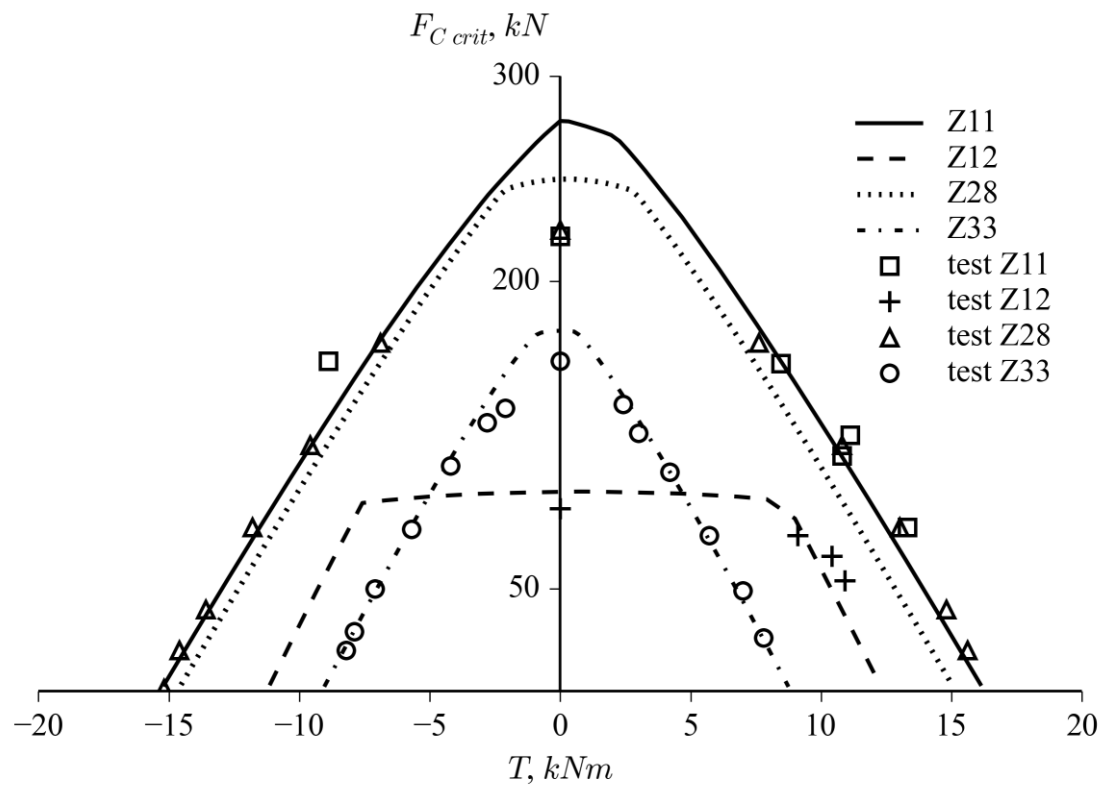


Fig. 4.8.3: Combined Torsion-Axial Compression, FSDT-Donnell-SS2, modified from Ref. [106]

4.9 Non-Linear Analysis using the SPLA

The Single Perturbation Load Approach (SPLA) is introduced in Section 1.2 as a potential method to calculate the knock-down factor of imperfection sensitive shells. The full Newton-Raphson non-linear algorithm, presented in Section 3.9, has been used to calculate the knock-down curve and the results are compared to Castro et al. [2] for cylinder Z33 and with Abaqus for cone C02, as shown in Fig. 4.9.1 and Fig. 4.9.2, respectively. The first observation is that the correct imperfection sensitivity was obtained using the semi-analytical models. From Fig. 4.9.1 it can be seen that the difference between Sanders' model about Donnell's model is -4.57% for a perturbation load $SPL < 45\text{ N}$; and -15.57% for $SPL \geq 45\text{ N}$, in average. In Fig. 4.9.2 a small convergence analysis using different sets of integration points n_x and n_θ is presented, where it can be seen a higher influence of n_x and n_θ for small imperfection amplitudes, and that the results are converged for these parameters for $SPL > 5\text{ N}$.

A third observation is that the full Newton-Raphson method stops in the local snap-through, i.e. the first instability, while the finite element results go further up to the global buckling. Both the local snap-through and the global buckling are explained in Section 1.2. In order to verify if the local snap-through is a limit point (where all the eigenvalues of the tangent stiffness matrix $[K_T]$ tend to zero) or a bifurcation point (where at least two eigenvalues of $[K_T]$ tend to zero), the eigenvalue analysis of Eq. (3.4.6) has been performed to verify if the eigenvalues are approaching 1 as the non-linear analyses approach the critical loads shown in Fig. 4.9.2. The value "1" means that multiplying the current geometric stiffness matrix $[K_G]$ by $\lambda = 1$ will lead to the instability condition: $\det([K_L] + \lambda[K_G]) = 0$. Three single perturbation load (SPL) values were chosen 24, 30 and 40 N, with the first two falling below $P1$ and the third above $P1$. The $F_{C_{crit}}$ values for the three cases are 97.52 kN, 88.52 kN and 75.55 kN, respectively. As shown in Fig. 4.9.4, the first four eigenvalues approach 1 when F_C approaches $F_{C_{crit}}$, and this behavior is the same for all the three cases. Recalling from Fig. 4.9.2 that for $SPL = 24\text{ N}$ and $SPL = 30\text{ N}$, the $F_{C_{crit}}$ corresponds to a global buckling, and that for $SPL = 40\text{ N}$, the $F_{C_{crit}}$ corresponds to a local snap-through, one concludes that the local snap-through can also be interpreted as a limit point, and therefore the full Newton-Raphson method is not capable of going beyond this point to find the global buckling load represented by the filled lines of Fig. 4.9.1 and Fig. 4.9.2 in the region $SPL > P1$. In Fig. 4.9.3, modified from Castro et al. (2013) [2], it is indicated in the load-shortening curves where the local snap-through and the global buckling appear, and how these curves change for different perturbation loads.

The current implementation of the Riks method described in Section 3.9.4 has the potential to go beyond the limit points indicated in the discussion above, where the major difficulty will appear when finding the correct sign for \sqrt{d} in Eq. (3.9.16) in order to track the load-displacement curve along the correct direction.

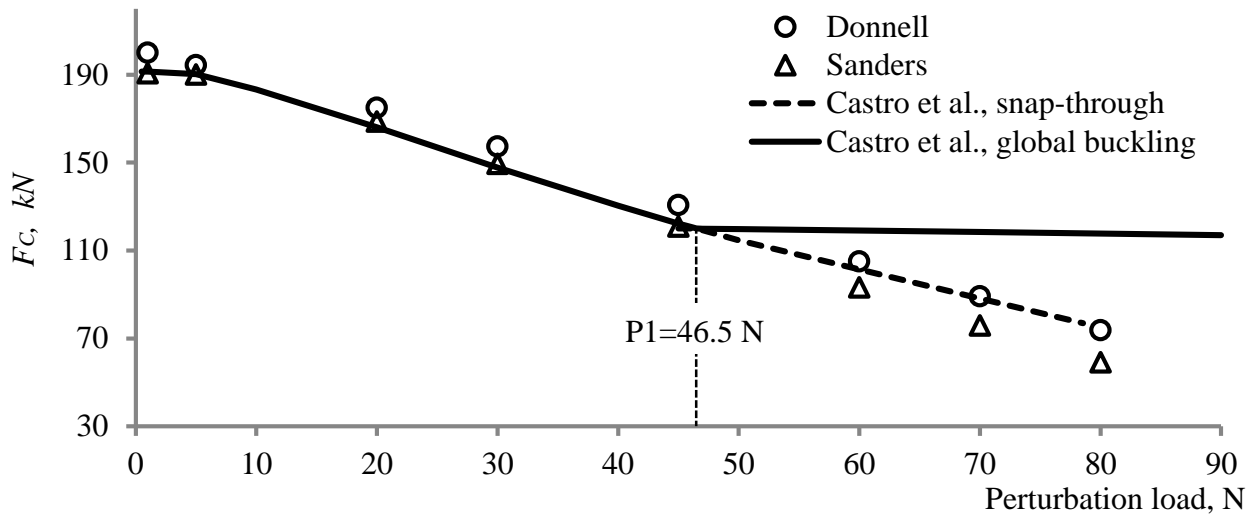


Fig. 4.9.1: Knock-Down Curve, Cylinder Z33

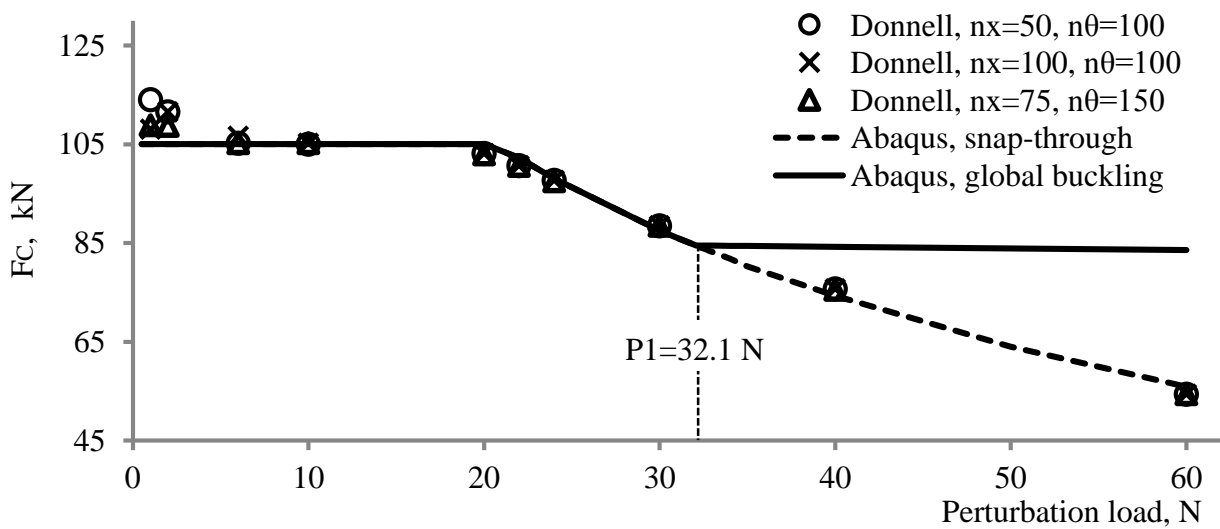


Fig. 4.9.2: Knock-Down Curve, Cone C02

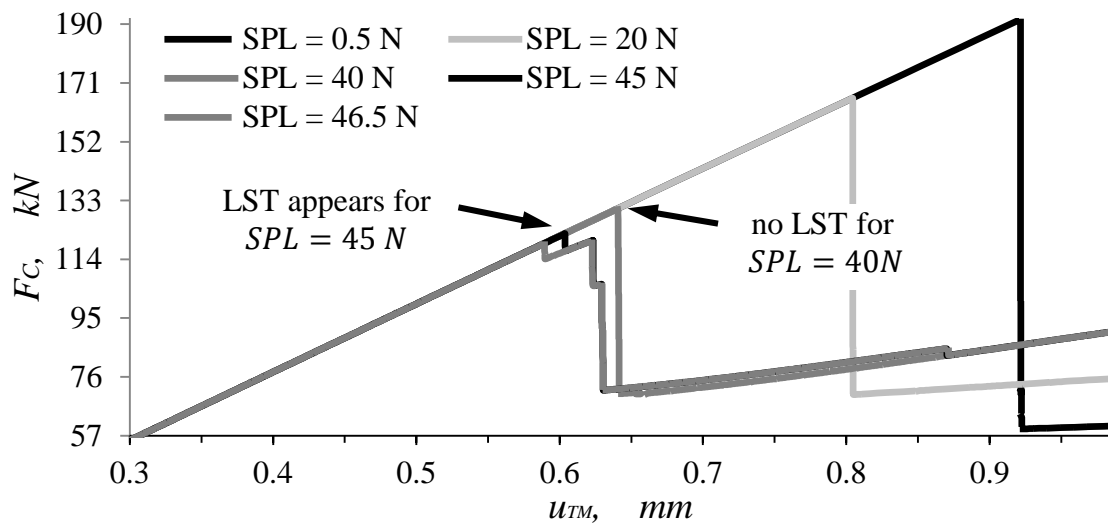


Fig. 4.9.3: Load Shortening Curves for Cylinder Z33, modified from Castro et al. (2013) [2]

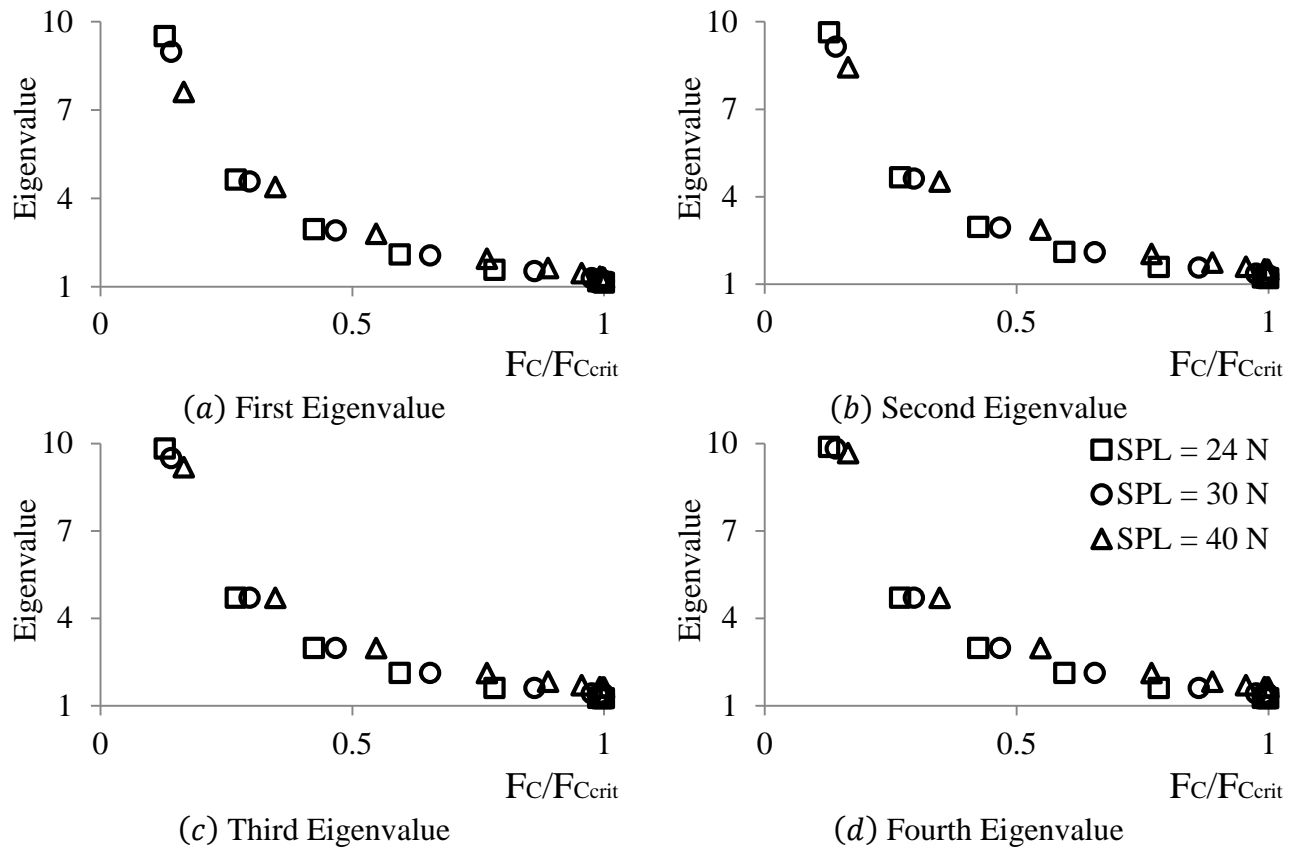


Fig. 4.9.4: Eigenvalue Analysis for C02

4.10 Representation of Measured Imperfection Fields

As discussed in Section 3.3 the half-cosine function of Arbocz [91] can be used to approximate geometric imperfection data using Eq. (3.3.1), where the approximation accuracy is dictated by m_0 and n_0 . In Fig. 4.10.1–Fig. 4.10.3 it is shown the measured imperfection field for cylinders Z23, Z25 and Z26 [31], and the approximated imperfection field using Eq. (3.3.1) with different values for m_0 and n_0 . All the contours are plotted with the same color scale of the corresponding measured imperfections.

From Fig. 4.10.1–Fig. 4.10.3 one clearly sees how the approximated pattern approaches the measured pattern by increasing m_0 and n_0 , and in theory one could choose m_0 and n_0 as high as necessary in order to obtain a given accuracy, but in practice the least squares algorithms applied to obtain the A_{ij} and B_{ij} coefficients of Eq. (3.3.1) will usually require a high amount of RAM memory that limits the maximum m_0 and n_0 that can be chosen.

The author adopted two strategies to increase the maximum values for m_0 and n_0 in order to achieve a better accuracy for the approximated imperfection field, given the amount of RAM memory of the computer used in the calculations, detailed in Appendix D. The first strategy is based on the geometry of the structures under evaluation. For cylinders Z23, Z25 and Z26, described in Table A.2, it can be seen that $2\pi R_1/H \approx 3$ and that the first approximation functions over x has the half the frequency of the approximation function over θ , such that at the convergence it is expected that $n_0 \approx 1.5 \times m_0$, assuming a similar imperfection pattern along x and θ . This relation allows one to use less terms over x and more terms over θ without losing the accuracy.

The second strategy is to avoid using the full sample of measured points when building the coefficient matrix used for the least squares fit. For example, in the case of cylinder Z23 the geometric imperfection is represented in a text file with 341099 lines, having one measured point per line, for cylinder Z25 there are 340357 points and for cylinder Z26 331307 points. A coefficient matrix built with these points using double precision (64 bits for each entry) will have approximately $m_0 \times n_0 \times 5.4 \text{ MB}$, which would limit the maximum number of terms to $m_0 = 30$ and $n_0 = 45$ (6.86 GB), considering that in the applied least squares routine [6] this amount will be doubled and that the computer used for the calculations is the one presented in Appendix D. The author suggests a number of randomly chosen measured points according to the formula:

$$n_{points} = n_{sample} (2 m_0 n_0) \quad n_{sample} = 10 \quad (4.10.1)$$

which allowed to achieve successful approximations up to $m_0 = 60$ and $n_0 = 90$ terms with the computer used in the course of this thesis, described in Appendix D. If the reader identifies that the approximated field does not correspond to the measured imperfection pattern when the reduced sample is used, it is likely that a higher value other than $n_{sample} = 10$ in the formula of Eq. (4.10.1) has to be adopted. Highly discrepant results were verified for $n_{sample} = 1$, i.e. when the number of measured points is equal the number of rows of the coefficient matrix used in the least squares routine, and therefore it is recommended to keep $n_{sample} \geq 2$.

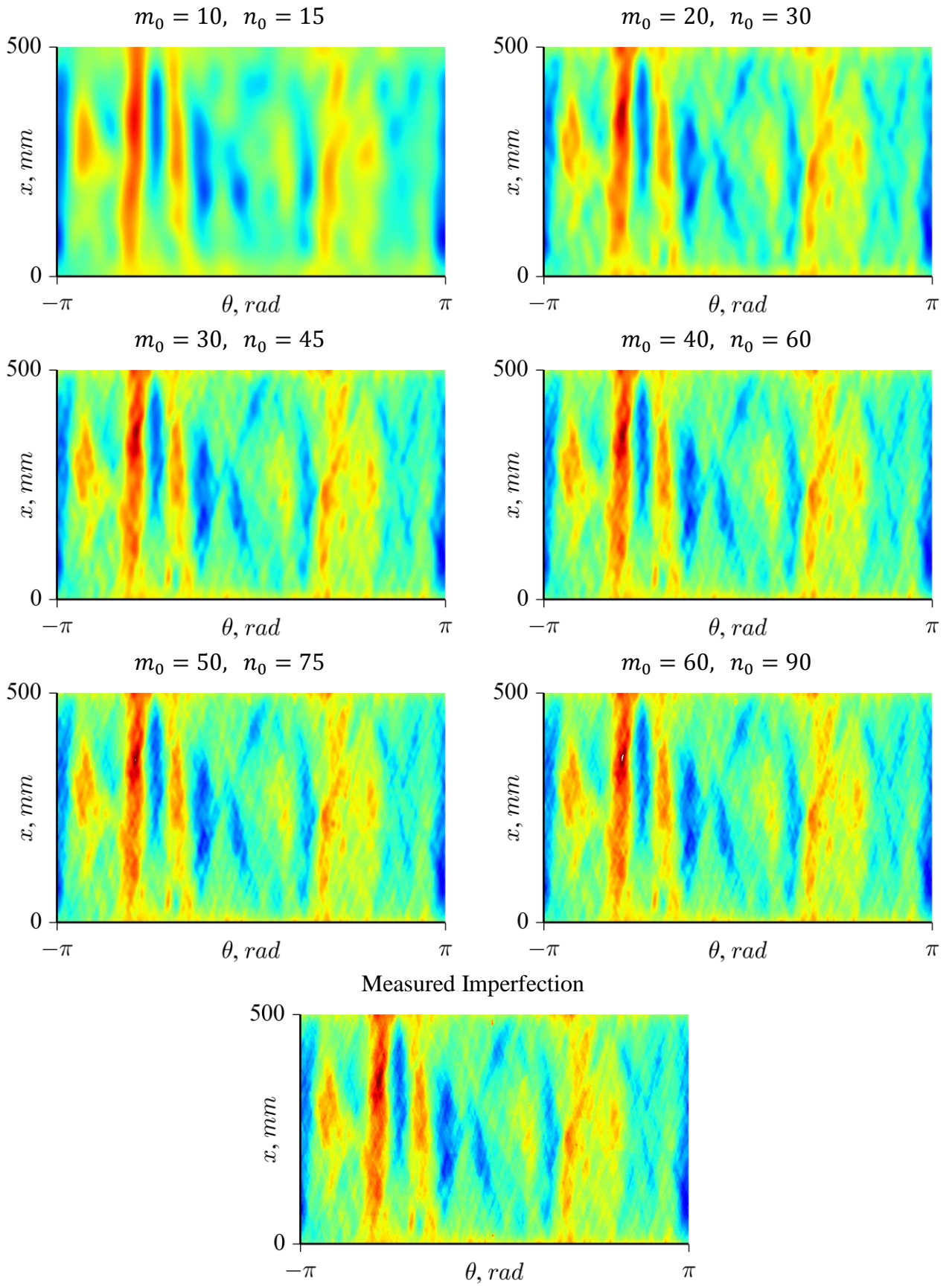


Fig. 4.10.1: Number of terms to Approximate Measured Imperfection Data, Cylinder Z23

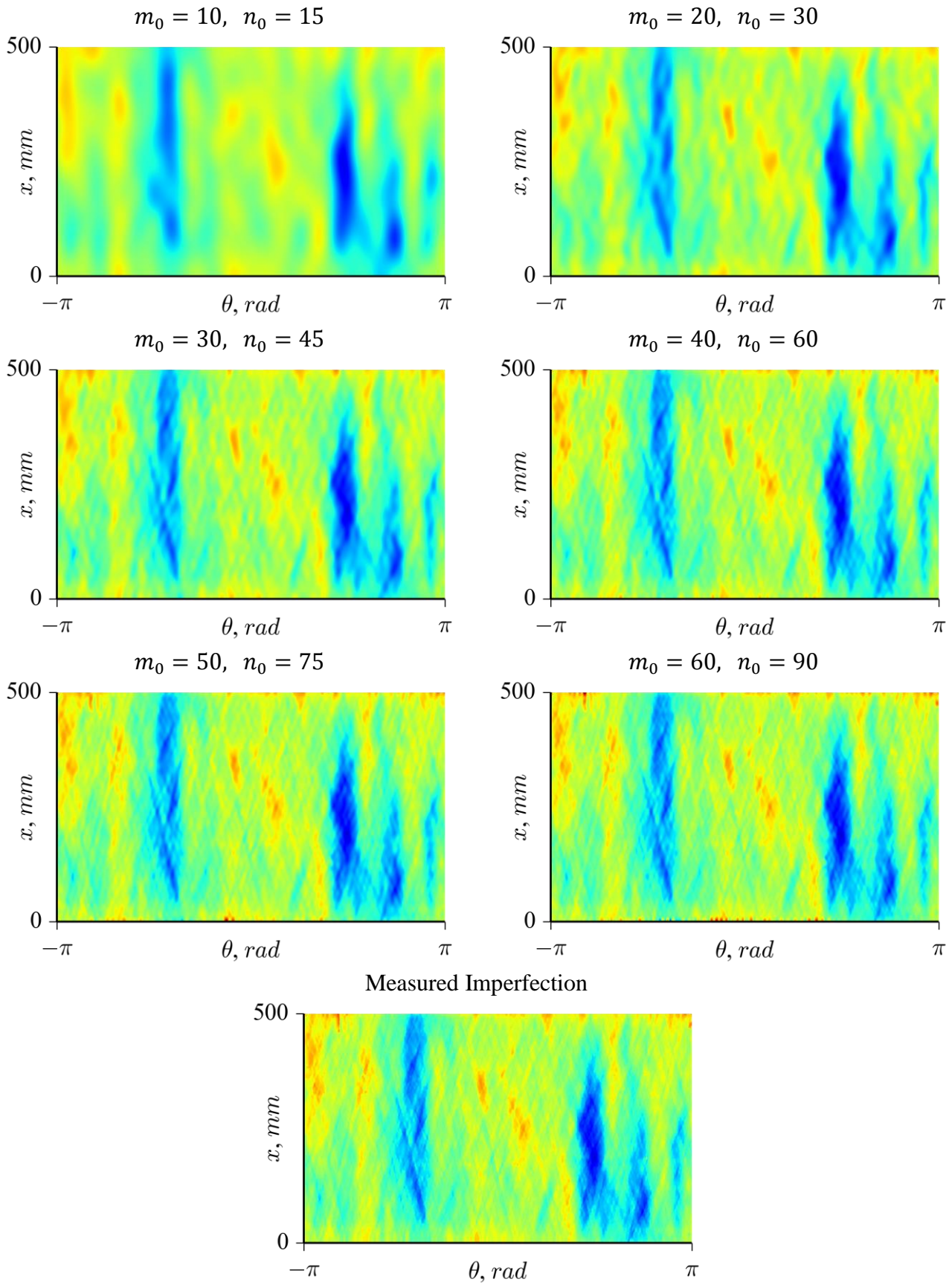


Fig. 4.10.2: Number of terms to Approximate Measured Imperfection Data, Cylinder Z25

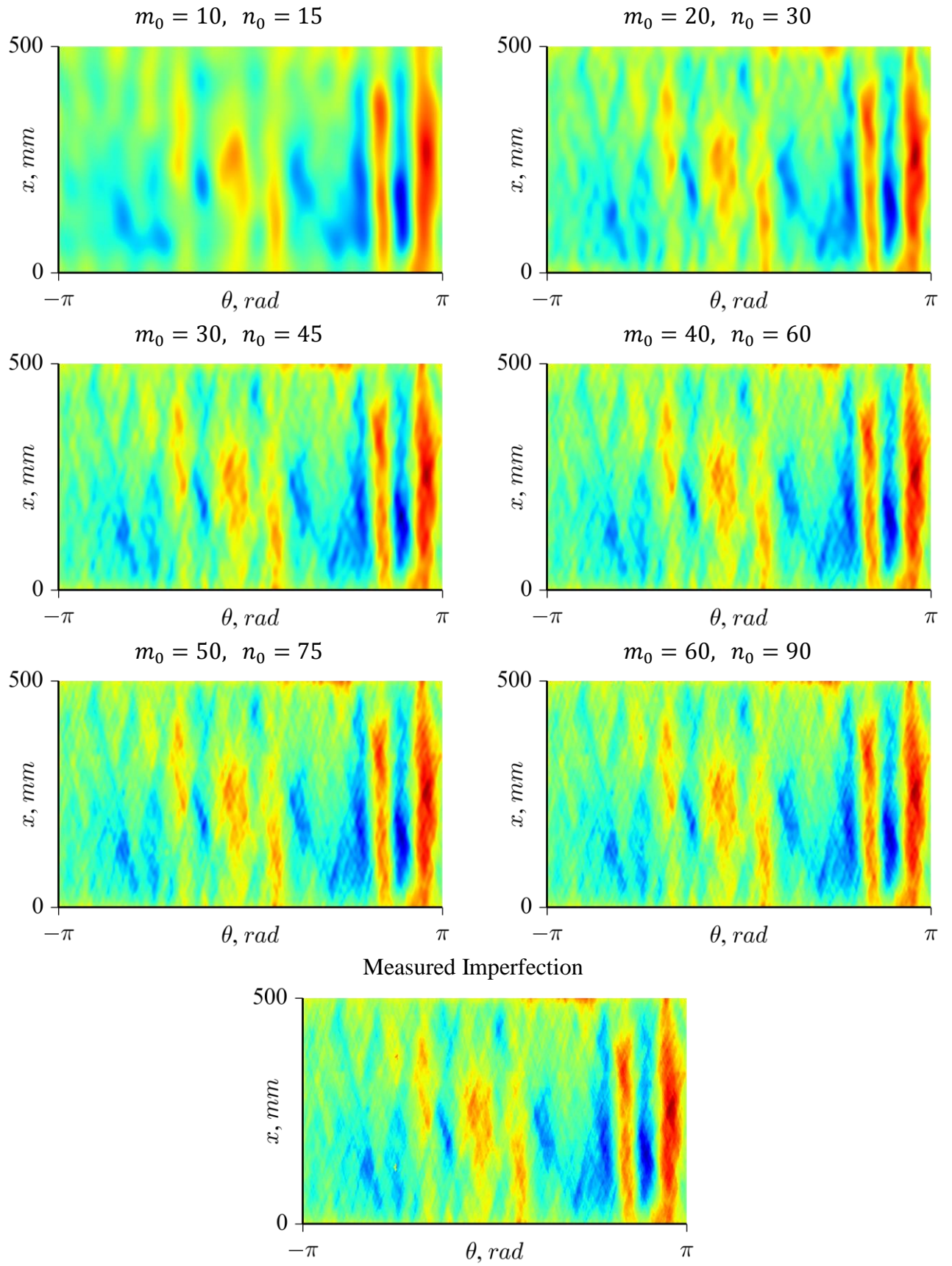


Fig. 4.10.3: Number of terms to Approximate Measured Imperfection Data, Cylinder Z26

Since the database for conical shells is limited and a higher amount of data is available for cylinders, it becomes convenient to define a methodology to map imperfection from cylindrical shells to cones. The approach herein suggested consists on simply mapping the imperfection amplitudes in a 2-D space, where the two coordinates are the normalized meridional position x/L and the angular circumferential position θ . In Fig. 4.10.4 it is shown the conical surface opened at $\theta = \pi$ with the imperfections from cylinders Z23, Z25 and Z26 mapped to cone C02, whose properties are presented in Table A.2.

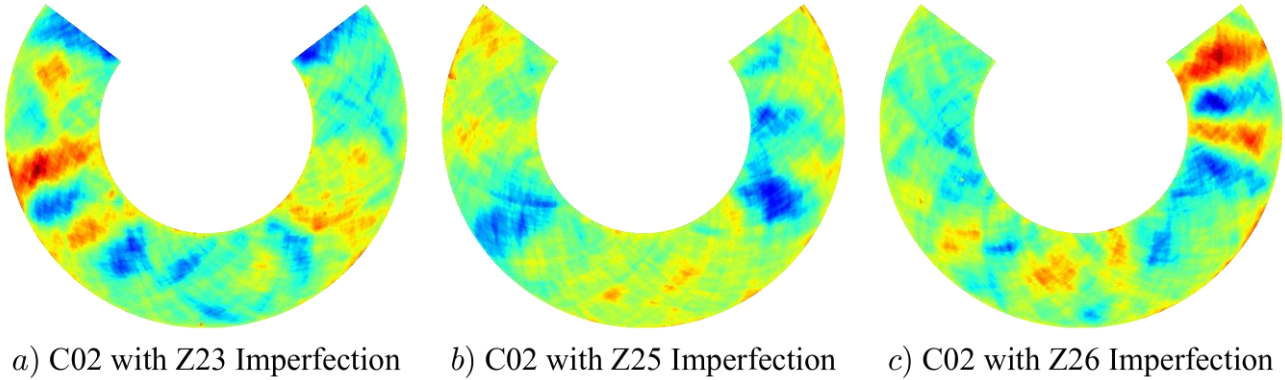


Fig. 4.10.4: Measured Imperfections Mapped to Cone C02

For the cases of Fig. 4.10.4 one can expect the same convergence behavior shown in Fig. 4.10.1–Fig. 4.10.3 when the measured imperfections are approximated using different values of m_0 and n_0 . The effect of using different values for m_0 and n_0 on the non-linear buckling behavior is investigated in Section 4.11, where the results from the semi-analytical models are also compared to finite element analyses.

4.11 Non-Linear Analyses using Initial Imperfections

From the convergence analysis presented in Section 4.10 it was shown how the measured imperfection pattern is progressively better approximated using higher values of m_0 and n_0 in the half-cosine function of Eq. (3.3.1). In this section it is investigated the effect of m_0 and n_0 on the non-linear buckling response for axially compressed structures. Cylinders Z23, Z25 and Z26, detailed in Table A.2, are evaluated using their respective geometric imperfection measurements obtained by Degenhardt et al. (2010) [31], given in Fig. 4.10.1, Fig. 4.10.2 and Fig. 4.10.3. Scaling factors in the range between 0.1 and 4.0 are applied to the imperfection amplitudes by directly multiplying vector $\{c_0\}$, this allowed to obtain a range of imperfection amplitudes up to $2h$, where h is the laminate thickness (cf. Fig. 3.2.1).

Finite element simulations were used to verify the semi-analytical predictions and in the following discussion all the semi-analytical results are obtained using model CLPT-Donnell-BC1 and all the simulations using the SS1 type of boundary conditions. Two methods for applying the measured imperfections to the finite element models have been investigated: an inverse-weighted (IW) interpolation and the half-cosine function of Eq. (3.3.1), for which the imperfection at each node w_{0node} is directly obtained when the nodal coordinates are inputted using the cylindrical coordinate system of Fig. 3.2.1. In both methods the initial nodal positions are changed according to the translations Δx_{node} , Δy_{node} and Δz_{node} calculated with the relations:

$$\begin{aligned}\theta &= \arctan\left(\frac{y_{node}}{x_{node}}\right) \\ \Delta x_{node} &= SF \cdot w_{0node} \cdot \cos \alpha \cdot \cos \theta \\ \Delta y_{node} &= SF \cdot w_{0node} \cdot \cos \alpha \cdot \sin \theta \\ \Delta z_{node} &= SF \cdot w_{0node} \sin \alpha\end{aligned}\tag{4.11.1}$$

where w_{0node} is the nodal imperfection computed using one of the two methods, α is the cone semi-vertex angle, defined in Fig. 3.2.1; x_{node} and y_{node} are the coordinates of the node in the rectangular coordinate system of Fig. 4.6.1.

In the inverse-weighted interpolation algorithm for each node in the finite element model a set of n closest points belonging to the measured data is selected and used to compute the imperfection value of the node. Equation (4.11.2) is used for this purpose and this approach has been presented by the author in Ref. [3].

$$\begin{aligned}w_{0node} &= \left(\sum_i^n w_{0i} \frac{1}{w_i}\right) / \sum_i^n \frac{1}{w_i} \\ w_i &= [(x_{node} - x_i)^2 + (y_{node} - y_i)^2 + (z_{node} - y_i)^2]^p\end{aligned}\tag{4.11.2}$$

with w_i is the weight of one closest point w_i , w_{0i} is the measured imperfection corresponding to point i and p is the power parameter, set to 2 in the current study. Increasing the power parameter will increase the relative weight of the closest points.

The results plotted in Fig. 4.11.1 present how the number of terms m_2 and n_2 affect the buckling response using $m_1 = 120$. The imperfection amplitude is normalized by the shell thickness, giving the abscissa parameter ξ/h . The approximation field is described using $m_0 = 20$, $n_0 = 30$. A good balance between computational cost and accuracy is achieved using $m_2 = 25$, $n_2 = 45$, and this set of parameters is used to further investigate the effect of an imperfection field described with a different number of terms m_0, n_0 .

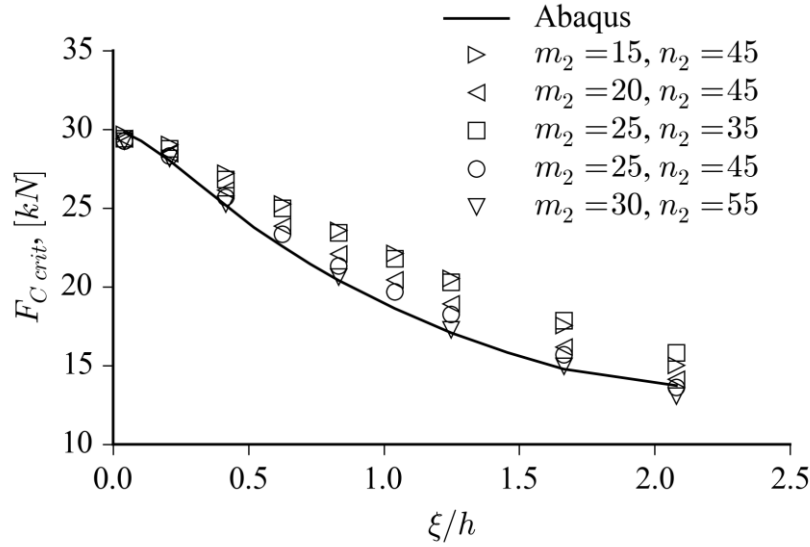


Fig. 4.11.1: Cylinder Z23 with Geometric Imperfections convergence for m_2 and n_2

Table 4.11.1 shows the non-linear buckling loads obtained with finite elements and the proposed Ritz model CLPT-Donnell-SS1 for the three imperfect cylinders Z23, Z25 and Z26 using six different approximation levels. From the relative errors it can be seen that the proposed models achieve a high accuracy for all cases, with the maximum error of 3.74% and an average error of 1.43%.

Table 4.11.1: Critical axial buckling loads (kN) for the imperfect cylinders Z23, Z25 and Z26 using the measured imperfection amplitude ($m_1 = 120$, $m_2 = 30$, $n_2 = 55$)

	Z23			Z25			Z26		
	Abaqus	Ritz	Error	Abaqus	Ritz	Error	Abaqus	Ritz	Error
$m_0 = 10, n_0 = 15$	28.2662	28.0928	-0.61%	27.5364	27.4670	-0.25%	28.4355	28.1704	-0.93%
$m_0 = 20, n_0 = 30$	25.1809	25.2666	0.34%	24.2768	24.8645	2.42%	24.4703	24.4893	0.08%
$m_0 = 30, n_0 = 45$	24.6906	25.0311	1.38%	24.3387	24.9011	2.31%	25.2465	25.5161	1.07%
$m_0 = 40, n_0 = 60$	24.8207	25.0319	0.85%	24.5905	25.1889	2.43%	25.0483	25.2667	0.87%
$m_0 = 50, n_0 = 75$	24.5939	24.9160	1.31%	24.1308	25.0336	3.74%	25.1253	25.5419	1.66%
$m_0 = 60, n_0 = 90$	24.6139	24.9890	1.52%	25.4377	25.2263	-0.83%	24.9266	25.7106	3.15%

In Fig. 4.11.2 cone C02 was simulated using the imperfections from cylinders Z23 and Z25 mapped as illustrated in Fig. 4.10.4. An approximated imperfection field using $m_0 = 20$, $n_0 = 30$ was selected and the difference between the Ritz method and the finite element predictions is small up to $\xi/h = 2$.

The studies with non-linear analysis of geometrically imperfect shells here in presented were published in Ref. [109].

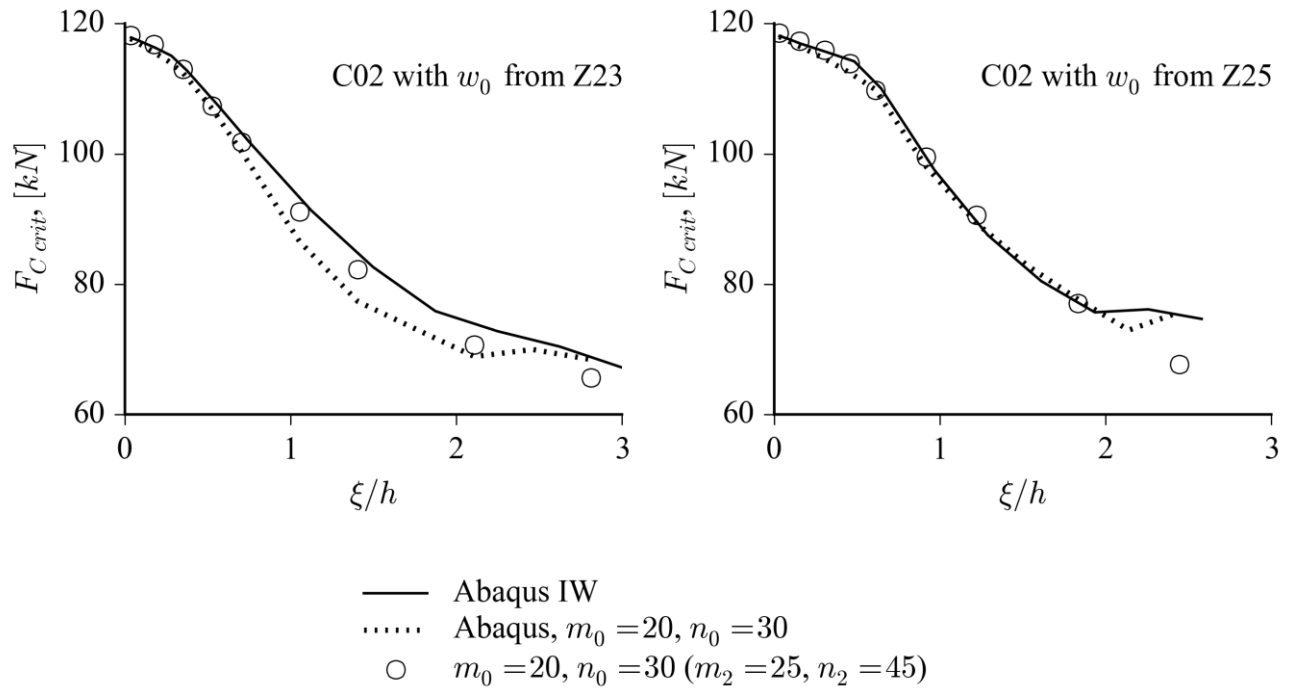


Fig. 4.11.2: Cone C02 using imperfection of Z23 and Z25

4.12 Non-Uniform Axial Load

The simplest case of load asymmetry is obtained when only N_{xx0} and N_{xx1b} are non-zero in Eq. (3.2.1), leading to a load case which is the equivalent of having an axial load F_C and a bending moment M_{LA} applied, as demonstrated in Section 3.2.1. In Fig. 4.12.1 the results using model CLPT-Donnell-BC2 with $m_1 = 120$ and $m_2 = n_2 = 35$ are verified against finite elements. The loads are $F_C = 100 \text{ kN}$ and $M_{LA} = 10^4 \text{ kN} \cdot \text{mm}$, and the boundary conditions are SS1 at the bottom and SS2 at the top edge, and therefore only models BC2 and BC4 could have been selected for this analysis (cf. Section 3.5). Note that obtained approximation is very satisfactory and a higher accuracy could be achieved increasing m_1 , m_2 and n_2 .

Performing a similar analysis for cone C02 will lead to the results presented in Fig. 4.12.2 using SS1-SS2, and to the results of Fig. 4.12.3 using SS1-SS4. The applied moment in this case was $M_{LA} = 1.25 \times 10^3 \text{ kN} \cdot \text{mm}$ and the axial load $F_C = 25 \text{ kN}$. Note that for the w field the results are different because the finite element model does not had its top edge constrained in w , which is relatively harder to achieve for cones and would significantly increase the complexity of the model for the purpose of this verification.

The non-linear analysis of Fig. 4.12.4 was run with the same parameters used for the linear analysis presented in Fig. 4.12.1. Similarly, the non-linear result of Fig. 4.12.5 used the same parameters of the analysis shown in Fig. 4.12.2. The results demonstrate that the semi-analytical predictions for non-uniform axial loads have a high correlation with the finite element models.

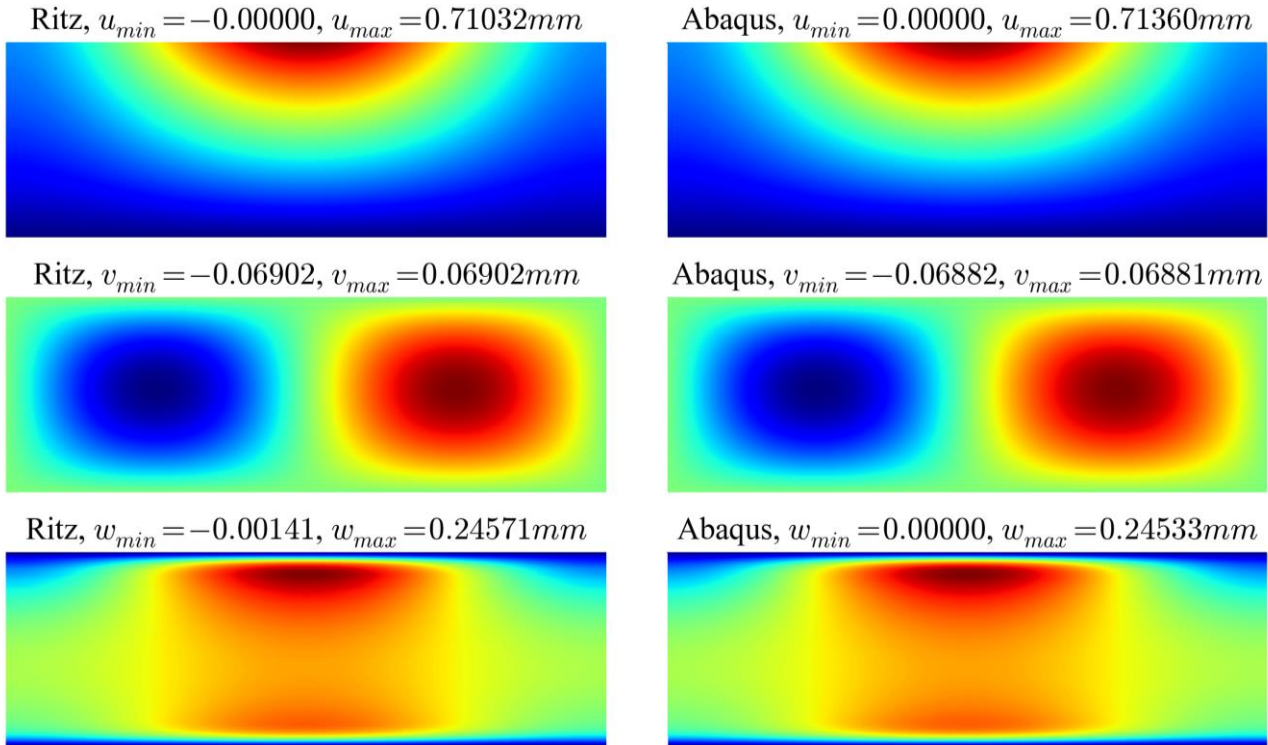


Fig. 4.12.1: Cylinder Z33, Linear Static with axial and bending loads, obtained with CLPT-Donnell-BC2

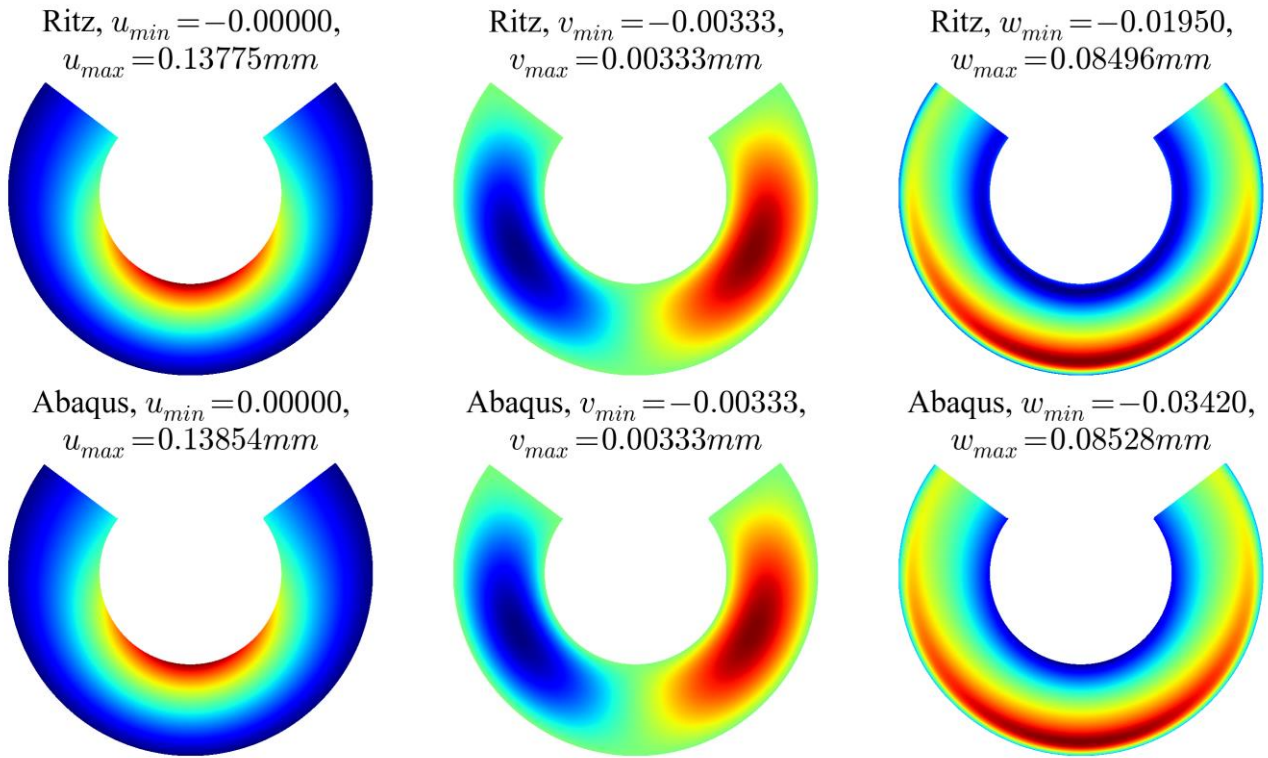


Fig. 4.12.2: Cone C02, Linear Static with axial and bending loads, with SS1-SS2 boundary conditions

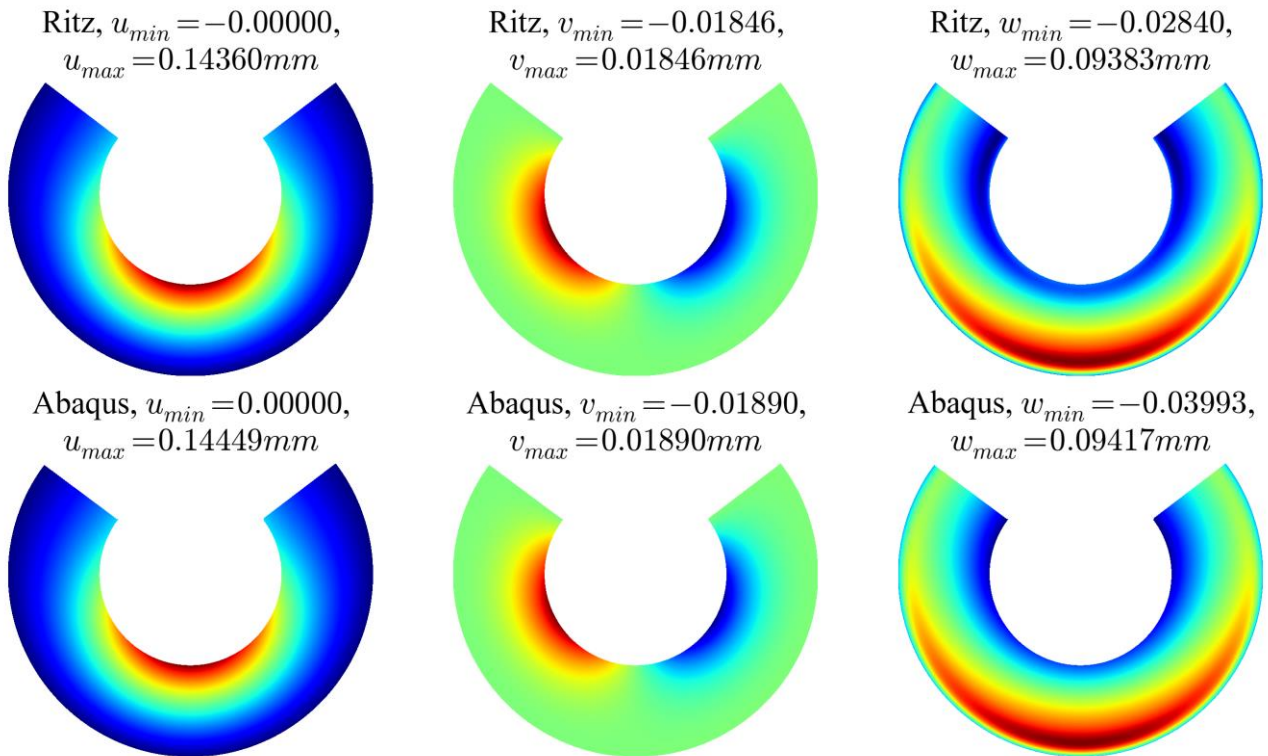


Fig. 4.12.3: Cone C02, Linear Static with axial and bending loads, with SS1-SS4 boundary conditions

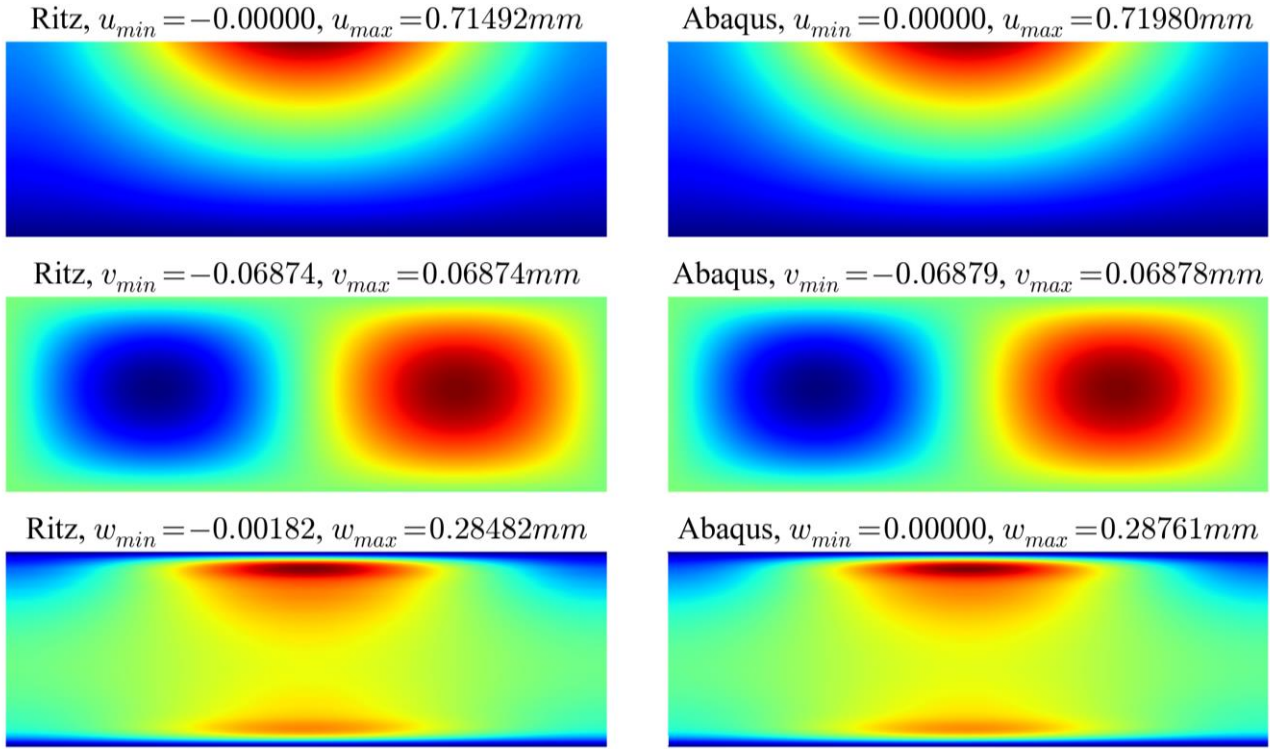


Fig. 4.12.4: Cylinder Z33, Non-Linear Static with axial and bending loads, obtained with CLPT-Donnell-BC2

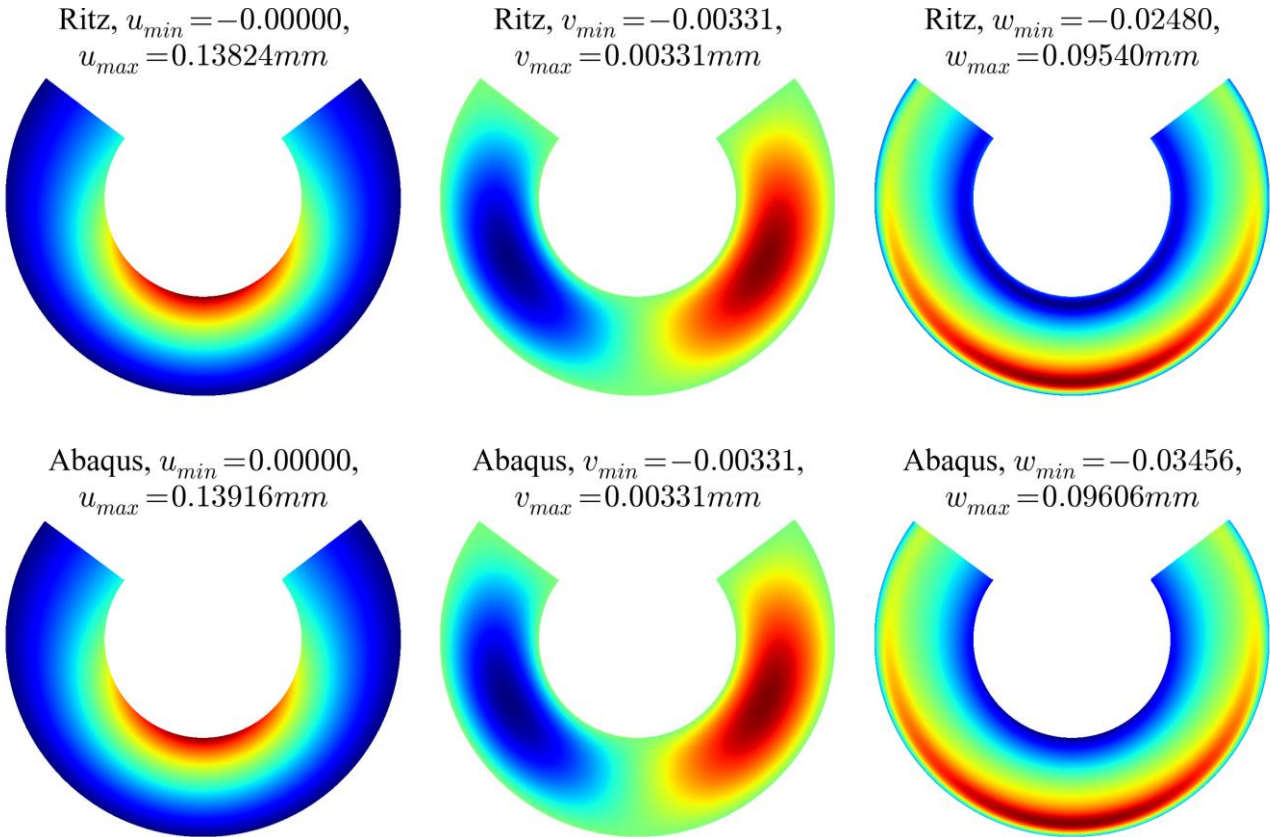


Fig. 4.12.5: Cone C02, Non-Linear Static with axial and bending loads, with SS1-SS2 boundary conditions

5 Conclusion

The general formulation herein presented can be used for any semi-analytical model based on the Ritz method given that the correct approximation functions and the kinematic equations are used, building a robust framework for future developments. The implemented subroutines were made available as part of the CompMech package [85] developed and maintained by the author with the aim to spread the use of semi-analytical tools applied in computational mechanics. The models developed for the design of unstiffened conical and cylindrical shells successfully achieved the purpose of performing accurately for the prediction of displacement, strain and stress fields, as well as for the prediction of critical buckling loads. These models can be used as alternative options to finite elements and can be easily integrated in design processes. The main motivation behind this development is the current need for fast tools capable of calculating the knock-down factors of imperfection sensitive structures, as discussed in Chapter 1.

Chapter 2 presented a matrix notation for the kinematic equations and Chapter 3 a general non-linear formulation using the Ritz method, which was applied to the kinematic equations developed in Chapter 2 in order to obtain the system of equations for the conical and cylindrical shells discussed in the thesis. Chapter 3 also details how to take geometric and load imperfections into account, and the main aspects concerning a successful implementation of the proposed semi-analytical tools.

In Chapter 4 verifications of the proposed formulation have been performed using data from the literature and finite element simulations. Among the investigated cases, the worst agreement (8.81%) was found for the linear buckling analyses of cylinder Z33 under pure torsion. Most of the cases showed a very good agreement between the proposed models and the finite element results, for linear and non-linear analyses.

For linear static analysis the proposed semi-analytical models in the current implementation [85] perform more than two orders of magnitude faster than the counterpart finite element models and for linear buckling analysis the gain is between one and two orders of magnitude. However, for non-linear analysis the computational efficiency of the proposed semi-analytical models in the current implementation [85] is significantly smaller than the commercial finite element solver (Abaqus), between one and even two orders of magnitude slower in some cases. This can be mainly attributed to the fact that a numerical integration scheme is currently being used, requiring the computation of the whole stiffness matrix for each integration point, while in a finite element scheme only the element's stiffness matrix is evaluated at each integration point.

Future improvements should focus on new algorithms and methods for obtaining the non-linear matrices $[K_{OL}]$, $[K_{LL}]$ and $[K_G]$. As mentioned in Section 3.8.4, many attempts aiming the analytical integration of the non-linear matrices were carried out by the author and they all failed due to the highly complicated handling of the hundreds of integration conditions that appear. Another approach that also deserves investigation is to describe the stiffness matrices in a frequency domain based on the fact that the approximation functions are trigonometric functions, allowing one to use integration frequencies instead of integration points. New approximation functions based on polynomials could

also be investigated, where the number of integration points could be drastically reduced if quadrature rules could be employed.

The author observed that the bisection method applied to reduce the load increments until a minimum increment size is inefficient to find the bucking loads. Future studies should take advantage of the known condition of the tangent stiffness matrix $[K_T]$ at the limit point, by estimating how much load can still be incremented using for example the result of the eigenvalue analysis of Eq. (3.4.6).

Appendix A Material and Geometric Data for Cones and Cylinders

This appendix is dedicated to summarize in one place all the material and geometric data for all conical and cylindrical shells used along the thesis.

Table A.1: Material properties (modulus in GPa)

Material name	Reference	E_{11}	E_{22}	ν_{12}	G_{12}	G_{13}	G_{23}
Geier 1997	[65], [51]	123.550	8.708	0.319	5.695	5.695	5.695
Deg Cocomat	[31]	142.500	8.700	0.28	5.100	5.100	5.100
Shadmehri	[70]	210.290	5.257	0.25	3.154	3.154	2.764

Table A.2: Geometric and laminate data

Cone / cylinder name	Reference	Material	R_1 (mm)	H (mm)	α (degrees)	Ply thickness (mm)	Stacking sequence Inwards – Outwards
Z07	[35]	Deg Cocomat	250	510	0	0.125	$[\pm 24 / \pm 41]$
Z11	[65], [107]	Geier 1997	250	510	0	0.125	$[\pm 60 / 0_2 / \pm 68 / \pm 52 / \pm 37]$
Z12	[65], [107]	Geier 1997	250	510	0	0.125	$[\pm 51 / \pm 45 / \pm 37 / \pm 19 / 0_2]$
Z28	[107]	Geier 1997	250	510	0	0.125	$[\pm 38 / \pm 68 / 90_2 / \pm 8 / \pm 53]$
Z23	[31]	Deg Cocomat	250	500	0	0.1195	$[\pm 24 / \pm 41]$
Z25	[31]	Deg Cocomat	250	500	0	0.117	$[\pm 24 / \pm 41]$
Z26	[31]	Deg Cocomat	250	500	0	0.1195	$[\pm 24 / \pm 41]$
Z32	[54], [51]	Geier 1997	250	510	0	0.125	$[\mp 51 / \mp 45 / \mp 37 / \mp 19 / 0_2]$
Z33	[54], [51]	Geier 1997	250	510	0	0.125	$[0_2 / \pm 19 / \pm 37 / \pm 45 / \pm 51]$
Zsym	[2]	Geier 1997	250	510	0	0.125	$[\pm 45 / 0]_{\text{sym}}$
C01	None	Geier 1997	400	200	30	0.125	$[+60 / -60]$
C02	[110]	Deg Cocomat	400	200	45	0.125	$[30/-30/-60/60/\bar{0}]_{\text{sym}}$
C14	None	Deg Cocomat	400	300	35	0.125	$[0/0/60/-60/45/-45]$
C26	None	Deg Cocomat	400	300	35	0.125	$[45/0/-45/-45/0/45]$
ShadC02	[70]	Shadmehri	254	H	30	0.635	$[+\gamma / -\gamma]$
ShadC04	[70]	Shadmehri	254	H	30	0.635	$[+\gamma / -\gamma / -\gamma / +\gamma]$

Appendix B Implementing Differential Operators

The matrix notation used along this thesis allows an easy interchange among the different kinematic theories (CLPT, FSDT), non-linear assumptions (Donnell, Sanders) and approximation functions (BC1, BC2, BC3 and BC4). A seemingly complicated part of such matrix notation is handling the matrices of differential operators, which are the matrices $[d_0]$ of Eq. (2.2.36) and matrices $[G_d]$ of Eqs. (2.2.38) and (2.2.40). This appendix has the aim to clarify to the reader how such operators can be implemented using two programming languages: Mathematica and Python.

Starting with Mathematica, the approximation functions are stored in “Tables” as shown in Eq. (B.1) for the CLPT-Donnell-BC1 model. Considering the integrand of $[K_{0ab}]$ given in Eq. (3.8.2) the multiplication $[g_a]^T [d_0]^T [F] [d_0] [g_b]$ is carried out as $[B_{0a}]^T [F] [B_{0b}]$, with $[B_{0a}] = [d_0] [g_a]$ and $[B_{0b}] = [d_0] [g_b]$, recalling that $[g_a]$ and $[g_b]$ will be $[g_0]$, $[g_1]$ or $[g_2]$, depending on the sub-matrix being evaluated (cf. Section 3.8.1 for more details about how to subdivide the stiffness matrices). Since the indices are different for $[g_a]$ and $[g_b]$, being i_1, i_2, k_2 and k_1, j_2, ℓ_2 , respectively, two variables for $[g_1]$ are needed, called $[g_{1a}]$ and $[g_{1b}]$; and two variables for $[g_2]$ are needed, called $[g_{2a}]$ and $[g_{2b}]$. The calculation of $[B_{0a}]$ and $[B_{0b}]$ is shown in Eq. (B.2).

Similarly, the integrand $[g_a]^T [G_d]^T [N_{K_G}] [G_d] [g_b]$ of $[K_{G0ab}]$ given in Eq. (3.8.2) is evaluated as $[G_a]^T [N_{K_G}] [G_b]$, with $[G_a] = [G_d] [g_a]$ and $[G_b] = [G_d] [g_b]$, and the calculation of $[G_a]$ and $[G_b]$ is shown in Eq. (B.3).

The reader can find all the “.nb” files in the implemented package [85] under “compmech/theory/conecyl”, where the suffixes “Left” and “Right” are used instead of “a” and “b”.

In Python, the SymPy [5] library contains the basic classes needed to implement a differential operator properly. Initially the author was using SymPy to obtain all the integrands and then sending it to Mathematica for the analytical integrations, since this integration step in SymPy (version 0.7.3) was orders of magnitude slower. The motivation to move the differentiation part to Mathematica was the high input-output management cost, not justifying keeping both. Nevertheless, a successful implementation of a differential operator has been achieved and the author thinks it is reasonable to share the implemented differential operator with the reader, especially if SymPy goes faster in the future.

The differential operator implementation is based on the principle illustrated in Eq. (B.4), where the differential operator is applied to every expression that falls on the right-hand side of the operator. Note that the order of the product in this case determines the result, forcing the condition that the expression and all its symbols must be non-commutative. Equation (B.4) also shows how the differential operator is interpreted in terms of partial derivatives. Equation (B.7) shows the differential operator class D and the most needed function “evaluateExpr()”, which goes recursively in the expression, from the right to the left, applying the differential operator to every sub-expression. Equation (B.5) shows how the implemented differential operator is used for the example of Eq. (B.4), assuming that the reader has the “sympy” and the “compmech” modules installed. Equation (B.6) shows how matrices $[d_0]$ and $[G_d]$ can be defined using the proposed

implementation. Based on the differential operator implemented in SymPy the “compmech” module has a function that readily returns the integrands of Eq. (3.8.2), and one example of how to use such a function to create the integrands corresponding to the CLPT-Donnell-BC1 model is given in Eq. (B.8).

```

num0 = 3;
num1 = 3;
num2 = 6;

g0 = Table[0, {3}, {num0}];
g1a = Table[0, {3}, {num1}];
g1b = Table[0, {3}, {num1}];
g2a = Table[0, {3}, {num2}];
g2b = Table[0, {3}, {num2}];

g0[[1, 1]] = (L - x)/(L*cosa);
g0[[2, 2]] = (L - x) r2/L;
g0[[1, 3]] = (L - x)/(L*cosa)*(1 - Cos[t - tLA]);

g1a[[1, 1]] = Sin[i1*Pi*x/L];
g1a[[2, 2]] = Sin[i1*Pi*x/L];
g1a[[3, 3]] = Sin[i1*Pi*x/L];

g1b[[1, 1]] = Sin[k1*Pi*x/L];
g1b[[2, 2]] = Sin[k1*Pi*x/L];
g1b[[3, 3]] = Sin[k1*Pi*x/L];

```

(B.1)

```

g2a[[1, 1]] = Sin[i2*Pi*x/L]*Sin[j2*t];
g2a[[1, 2]] = Sin[i2*Pi*x/L]*Cos[j2*t];
g2a[[2, 3]] = Sin[i2*Pi*x/L]*Sin[j2*t];
g2a[[2, 4]] = Sin[i2*Pi*x/L]*Cos[j2*t];
g2a[[3, 5]] = Sin[i2*Pi*x/L]*Sin[j2*t];
g2a[[3, 6]] = Sin[i2*Pi*x/L]*Cos[j2*t];

g2b[[1, 1]] = Sin[k2*Pi*x/L]*Sin[l2*t];
g2b[[1, 2]] = Sin[k2*Pi*x/L]*Cos[l2*t];
g2b[[2, 3]] = Sin[k2*Pi*x/L]*Sin[l2*t];
g2b[[2, 4]] = Sin[k2*Pi*x/L]*Cos[l2*t];
g2b[[3, 5]] = Sin[k2*Pi*x/L]*Sin[l2*t];
g2b[[3, 6]] = Sin[k2*Pi*x/L]*Cos[l2*t];

gu = ga[[1, All]];
gv = ga[[2, All]];
gw = ga[[3, All]];
B0a = {D[gu, x],
  1/r*sina*gu + 1/r*D[gv, t] + 1/r*cosa*gw,
  1/r*D[gu, t] + D[gv, x] - sina*1/r*gv,
  -D[gw, x, x],
  -1/r*(sina*D[gw, x] + 1/r*D[gw, t, t]),
  -1/r*(2*D[gw, x, t] - 1/r*sina*D[gw, t])};

```

(B.2)

```

gu = gb[[1, All]];
gv = gb[[2, All]];
gw = gb[[3, All]];
B0b = {D[gu, x],
  1/r*sina*gu + 1/r*D[gv, t] + 1/r*cosa*gw,
  1/r*D[gu, t] + D[gv, x] - sina*1/r*gv,
  -D[gw, x, x],
  -1/r*(sina*D[gw, x] + 1/r*D[gw, t, t]),
  -1/r*(2*D[gw, x, t] - 1/r*sina*D[gw, t])};

```

```

gu = gLeft[[1, All]];
gv = gLeft[[2, All]];
gw = gLeft[[3, All]];
gwx = D[gw, x];
gwt = D[gw, t];
Ga = {gwx, 1/r*gwt};

gu = gRight[[1, All]];
gv = gRight[[2, All]];
gw = gRight[[3, All]];
gwx = D[gw, x];
gwt = D[gw, t];
Gb = {gwx, 1/r*gwt};

```

(B.3)

$$\begin{aligned}
 D(x) \cdot x^3 \cdot y + x &= 3x^2y + x & \frac{\partial}{\partial x}(x^3 \cdot y) + x &= 3x^2y + x \\
 x^3 \cdot D(x) \cdot y + x &= x & x^3 \cdot \frac{\partial}{\partial x}(y) + x &= x
 \end{aligned}$$

(B.4)

```

from sympy import var

from compmech.symbolic.doperator import D, evaluateExpr

var('x, y', commutative=False)
print(evaluateExpr(D(x)*x**3*y + x))
print(evaluateExpr(x**3*D(x)*y + x))

```

(B.5)

```

import sympy
from sympy import sin, cos, pi, Matrix

from compmech.symbolic.doperator import D

sympy.var('x, t, sina, cosa, r, L', commutative=False)

d0 = Matrix([[
    D(x), 0, 0],
    [1/r*sina, 1/r*D(t), 1/r*cosa],
    [1/r*D(t), D(x)-sina*1/r, 0],
    [0, 0, -D(x,x)],
    [0, 0, 0, -1/r*(sina*D(x) + 1/r*D(t,t))],
    [0, 0, 0, -1/r*(2*D(x,t)-1/r*sina*D(t))]])

Gd = Matrix([[0, 0, D(x)],
             [0, 0, 1/r*D(t)]])

```

(B.6)

```

import subprocess

import sympy
from sympy.core.decorators import call_highest_priority
from sympy import Expr, Matrix, Mul, Add, diff
from sympy.core.numbers import Zero

class D(Expr):
    __op_priority__ = 11.
    is_commutative = False
    def __init__(self, *variables, **assumptions):
        super(D, self).__init__()
        self.evaluate = False
        self.variables = variables

    def __repr__(self):
        return 'D%s' % str(self.variables)

    def __str__(self):
        return self.__repr__()

    @call_highest_priority('__mul__')
    def __rmul__(self, other):
        return Mul(other, self)

    @call_highest_priority('__rmul__')
    def __mul__(self, other):
        if isinstance(other, D):
            variables = self.variables + other.variables
            return D(*variables)
        if isinstance(other, Matrix):
            other_copy = other.copy()
            for i, elem in enumerate(other):
                other_copy[i] = self * elem
            return other_copy

        if self.evaluate:
            return diff(other, *self.variables)
        else:
            return Mul(self, other)

    def __pow__(self, other):
        variables = self.variables
        for i in range(other-1):
            variables += self.variables
        return D(*variables)

def mydiff(expr, *variables):
    if isinstance(expr, D):
        expr.variables += variables
        return D(*expr.variables)
    if isinstance(expr, Matrix):
        expr_copy = expr.copy()
        for i, elem in enumerate(expr):
            expr_copy[i] = diff(elem, *variables)
        return expr_copy
    return diff(expr, *variables)

def evaluateMul(expr):
    end = 0
    if expr.args <> ():
        if isinstance(expr.args[-1], D):
            return Zero()
    for i in range(len(expr.args)-1+end, -1, -1):
        arg = expr.args[i]
        if isinstance(arg, Add):
            arg = evaluateAdd(arg)
        elif isinstance(arg, Mul):
            arg = evaluateMul(arg)
        elif isinstance(arg, D):
            left = Mul(*expr.args[:i])
            right = Mul(*expr.args[i+1:])
            right = mydiff(right, *arg.variables)
            ans = left * right
            return evaluateMul(ans)
        else:
            pass
    return expr

def evaluateAdd(expr):
    newargs = []
    for arg in expr.args:
        if isinstance(arg, Mul):
            arg = evaluateMul(arg)
        elif isinstance(arg, Add):
            arg = evaluateAdd(arg)
        elif isinstance(arg, D):
            arg = Zero()
        else:
            pass
    newargs.append(arg)
    return Add(*newargs)

def evaluateExpr(expr):
    if isinstance(expr, Matrix):
        for i, elem in enumerate(expr):
            elem = elem.expand()
            expr[i] = evaluateExpr(elem)
        return expr
    expr = expr.expand()
    if isinstance(expr, Mul):
        expr = evaluateMul(expr)
    elif isinstance(expr, Add):
        expr = evaluateAdd(expr)
    elif isinstance(expr, D):
        expr = Zero()
    return expr

def symList(string, imin, imax):
    outlist = []
    for i in range(imin, imax+1):
        string2 = (string+'%d' % i)
        sympy.var(string2)
        outlist.append(eval(string2))
    return outlist

def print_to_latex(expr):
    import matplotlib.pyplot as pyplot
    text = sympy.latex(expr, mode='inline')
    pyplot.plot()
    pyplot.text(0.5, 0.5, '{0}'.format(text))
    pyplot.show()
    return text

def print_to_file(guy, append=False,
                  software=r"C:\Program Files\
(x86)\Notepad++\notepad++.exe"):
    flag = 'w'
    if append: flag = 'a'
    outfile = open(r'print.txt', flag)
    outfile.write('\n')
    outfile.write(sympy.pretty(guy, wrap_line=False))
    outfile.write('\n')
    outfile.close()
    subprocess.Popen(software + ' print.txt')

```

(B.7)

```

import sympy
from sympy import sin, cos, pi, Matrix

from compmech.conecyl.sympytools.clpt.matrices import calc_matrices

sympy.var('i1, i2, j2, k1, k2, l2', commutative=False)
sympy.var('x, t, sina, cosa, r2, L, tLA', commutative=False)
sympy.var('c00, c01, c02', commutative=False)
sympy.var('c0i, cli, c2i', commutative=False)
sympy.var('c0ij, clij, c2ij, c3ij, c4ij, c5ij', commutative=False)
bi1 = i1*pi*x/L
bi2 = i2*pi*x/L
bj2 = j2*t
bk1 = k1*pi*x/L
bk2 = k2*pi*x/L
bl2 = l2*t
g0 = Matrix([[ (L-x)/(L*cosa), 0, (L-x)/(L*cosa)*(1-cos(t-tLA)) ],
              [ 0, (L-x)*r2/L, 0 ],
              [ 0, 0, 0 ]])
g1a = Matrix([[sin(bi1), 0, 0],
              [0, sin(bi1), 0],
              [0, 0, sin(bi1)]])
g1b = Matrix([[sin(bk1), 0, 0],
              [0, sin(bk1), 0],
              [0, 0, sin(bk1)]])
g2a = Matrix([[sin(bi2)*sin(bj2), sin(bi2)*cos(bj2), 0, 0, 0, 0],
              [0, 0, sin(bi2)*sin(bj2), sin(bi2)*cos(bj2), 0, 0],
              [0, 0, 0, 0, sin(bi2)*sin(bj2), sin(bi2)*cos(bj2)]])
g2b = Matrix([[sin(bk2)*sin(bl2), sin(bk2)*cos(bl2), 0, 0, 0, 0],
              [0, 0, sin(bk2)*sin(bl2), sin(bk2)*cos(bl2), 0, 0],
              [0, 0, 0, 0, sin(bk2)*sin(bl2), sin(bk2)*cos(bl2)]])
c0 = Matrix([[c00, c01, c02]]).T
ci = Matrix([[c0i, cli, c2i]]).T
cij = Matrix([[c0ij, clij, c2ij, c3ij, c4ij, c5ij]]).T
cs_left = [c0, ci, cij]
cs_right = cs_left
gs_left = [g0, g1a, g2a]
gs_right = [g0, g1b, g2b]

matrices = calc_matrices(cs_left, gs_left, cs_right, gs_right, NL='Donnell')

```

(B.8)

Appendix C Some Routines Used in the Studies

This appendix contains some subroutines used along the studies.

```
import os
import numpy

from desicos.abaqus import study
from desicos import conecylDB

cname_loads = {
    'huehne_2002_z14': [1, 2, 3, 5, 10, 20, 30],
    'huehne_2002_z22': [1, 2, 3, 5, 10, 20, 30],
    'huehne_2002_z23': [1, 5, 10, 30, 50, 70, 90, 110, 130],
    'huehne_2002_z24': [1, 5, 10, 30, 50, 70, 90, 110, 130],
    'huehne_2002_z26': [1, 2, 3, 4, 5, 6, 10],
    'huehne_2002_z27': [1, 2, 3, 4, 5, 6, 10],
}

omegadegs = [0, 45, 90, 135, 180]
studies = study.Studies()
studies.name = 'wp3_t02_02_la_spla'
betadegs_dict = {}
for omegadeg in omegadegs:
    for cname, loads in cname_loads.iteritems():
        cylDB = conecylDB.ccs[cname]
        d = 2 * cylDB['r']
        if omegadeg == 0:
            ts = [0.00, 0.05, 0.10, 0.20, 0.30, 0.40, 0.50]
        else:
            ts = [0.05, 0.10, 0.20, 0.30, 0.40, 0.50]
            betadegs = [numpy.rad2deg(numpy.arctan(t/d)) for t in ts]
            betadegs_dict[cname] = betadegs
        for i, betadeg in enumerate(betadegs):
            t = ts[i]
            study_name = studies.name + '_' + cname.split('_2002_')[1]
            study_name += '_o_%03d_t_%03d' % (int(omegadeg), int(100*t))
            ##### FILE MANAGEMENT SECTION #####
            study_dir = os.path.join(r'C:\Temp', 'abaqus', study_name)
            if not os.path.isdir(study_dir):
                os.makedirs(study_dir)
            output_dir = os.path.join(study_dir, 'outputs')
            print 'configuring folders...'
            print '\t' + output_dir
            if not os.path.isdir(output_dir):
                os.makedirs(output_dir)
            #####
            std = study.Study()
            std.name = study_name
            std.rebuild()
            count = 0
            for pltotal in loads:
                count += 1
                cc = std.add_cc_fromDB(cname)
                cc.separate_load_steps = True
                cc.betadeg = betadeg
                cc.omegadeg = omegadeg
                cc.impconf.loads = []
                cc.impconf.add_load(pltotal = pltotal,
                                    pt = 0.5,
                                    theta = 0.)
                cc.damping_factor2 = 1.e-7
                cc.initialInc2 = 1.e-2
                cc.minInc2 = 1.e-6
                cc.maxInc2 = 1.e-2
                cc.maxNumInc2 = 100000
                cc.axial_displ = 2.5
                cc.rename = False
                cc.jobname = study_name + '_model_%02d' % count
            std.create_models()
            std.write_inputs()
            studies.studies.append(std)
```

(C.1)

Run using the “job stopper” [13] with:

```
SET TMP_DIR=C:\Temp
cd TMP_DIR
for %i /r in (run*.py) do python %i use_stopper
```

The least squares algorithm of NumPy [6] was used to calculate the fitting coefficients $\{c_0\}$ from measured imperfection data, as described in Section 3.3. Equation (C.2) shows an efficient implementation using pure Python (the implementation of Ref. [85] recurs to Cython for this task). In this function “xs, thetas, w0measured” are arrays containing the measured imperfection for each x, θ position, which can be obtained from a comma separated value text file as exemplified in Eq. (C.3).

```
import numpy as np
from numpy import sin, cos, pi

def calc_c0(xs, thetas, w0measured):
    assert xs.shape[0]==thetas.shape[0]==w0measured.shape[0]
    n = xs.shape[0]
    a = np.array([[cos(i*pi*xs)*sin(j*thetas), cos(i*pi*xs)*cos(j*thetas)]
                  for j in range(n0) for i in range(m0)])
    a = a.swapaxes(0,2).swapaxes(1,2).reshape(n,-1)
    c0, residues, rank, s = np.linalg.lstsq(a, w0measured)

    return c0
```

(C.2)

```
import numpy as np

xs, thetas, w0measured = np.genfromtxt('data.txt', delimiter=',', unpack=True)
```

(C.3)

Appendix D Hardware and Software Configuration Used Along this Thesis

The machine used to perform all the studies herein presented has the hardware:

- Intel® Core™ i7-2869QM CPU @ 2.50 GHz 1.50 GHz
- 64 Bit
- 16 GB of RAM
- 500 GB of Hard Disk

And the Software (only those relevant for the studies are listed):

- Windows 7 64 Bit
- Python 2.7.5 64 bit
- Numpy 1.8.0
- Scipy 0.12.0
- SymPy 0.7.3
- Matplotlib 1.3.1
- Cython 0.20.1
- Microsoft ® C/C++ Optimizing Compiler Version 15.00.30729.01 for x64 which comes with the Microsoft Windows SDK for Windows 7 and .NET Framework 3.5 SP1 (ISO), required to compile Cython for Windows 7 64 bit. As detailed in this thread available in Cython's GitHub: <https://github.com/cython/cython/wiki/64BitCythonExtensionsOnWindows>;

For the interested reader who has only a short experience with compilers, the author recommends to use scientific package managers for Python such as the Anaconda, available at: <https://store.continuum.io/cshop/anaconda/>; or to download pre-compiled packages, such as the ones available at <http://www.lfd.uci.edu/~gohlke/pythonlibs/>; by Christoph Gohlke of the University of California. The author experience is that using Linux distributions such as Ubuntu would make the life easier for scientific development using freely distributed and high quality tools.

References

- [1] "DESICOS - New Robust DESign Guideline for Imperfection Sensitive COMposite Launcher Structures," 2012. [Online]. Available: <http://www.desicos.eu>.
- [2] S. G. P. Castro, M. A. Arbelo, R. Zimmermann and R. Degenhardt, "Exploring the constancy of the global buckling load after a critical geometric imperfection level in thin-walled cylindrical shells for less conservative knock-down factors," *Thin-Walled Structures*, vol. 72, pp. 76-87, 2013.
- [3] S. G. P. Castro, R. Zimmermann, M. A. Arbelo, R. Khakimova, M. W. Hilburger and R. Degenhardt, "Geometric imperfections and lower-bound methods used to calculate knock-down factors for axially compressed composite cylindrical shells," *Thin-Walled Structures*, vol. 74, pp. 118-132, 2014.
- [4] "Python Language Reference, version 2.7.5.," Python Software Foundation, [Online]. Available: <http://www.python.org>.
- [5] SymPy Development Team, "SymPy: Python library for symbolic mathematics," 2013. [Online]. Available: <http://www.sympy.org>.
- [6] T. E. Oliphant, "Python for scientific computing," *Computing in Science & Engineering*, vol. 9, no. 3, pp. 10-20, 2007.
- [7] E. Jones, T. Oliphant, P. Peterson and others, "Scipy: open source scientific tools for Python," 2001. [Online]. Available: <http://www.scipy.org/>.
- [8] G. Ewing, R. W. Bradshaw, S. Behnel and D. S. S. e. al., "The Cython compiler," [Online]. Available: <http://cython.org/>.
- [9] J. D. Hunter, "Matplotlib: A 2D graphics environment," *Computing In Science & Engineering*, vol. 9, no. 3, pp. 90-95, 2007.
- [10] S. G. Johnson, "Cubature (Multi-dimensional integration)," MIT - Massachusetts Institute of Technology, 21 05 2014. [Online].
- [11] S. G. P. Castro, "Cubature (Cython/Python wrapper)," 21 05 2014. [Online]. Available: <https://github.com/saullocaastro/cubature/blob/master/README.rst>.
- [12] "StackOverflow," 01 03 2013. [Online]. Available: <http://stackoverflow.com/>.
- [13] S. G. P. Castro and P. Schor, "DESICOS Improved Software," 1 March 2014. [Online]. Available: <http://desicos.github.io/desicos/>.
- [14] R. V. Southwell, "On the general theory of elastic stability," *Philosophical Transactions of the Royal Society A, London*, vol. 213, pp. 187-244, January 1914.
- [15] W. Flügge, "Die Stabilität der Kreiszyinderschale," *Ingenieure Architektur*, vol. 3, p. 463, 1932.
- [16] L. H. Donnell, "A new theory for the buckling of thin cylinders under axial compression and bending," *ASME Transactions*, vol. 56, pp. 795-806, 1934.
- [17] W. T. Koiter, "A translation of the stability of elastic equilibrium," *Technische Hooge School at Delft, Department of Mechanics, Shipbuilding and Airplane Building. 14th November.*, 1945.
- [18] L. H. Donnell and C. Wan, "Effect of imperfections on buckling of thin cylinders and columns under axial compression," *Journal of Applied Mechanics*, vol. 17, no. 1, p. 73, 1950.
- [19] N. S. Khot, "On the influence of initial geometric imperfections on the buckling and postbuckling behavior of fiber-reinforced cylindrical shells under uniform axial compression," Air Force Flight Dynamics Laboratory, Air Force Systems Command, Wright-Patterson Air Force Base, Ohio, 1968.
- [20] J. Arbocz, "The effect of initial imperfections on shell stability - an updated review," *TU Delft Report LR-695, Faculty of Aerospace Engineering, The Netherlands*, 1992.
- [21] C. D. Babcock and E. E. Sechler, "The effect of initial imperfections on the buckling stress of cylindrical shells," *NASA D-1510 Collected papers on instability of shell structures. California Institute of Technology.*, 1962.
- [22] H. Xu, Buckling, postbuckling and imperfection sensitivity analysis of different type of cylindrical shells by Hui's postbuckling method, New Orleans: University of New Orleans Theses and Dissertations, 2013.
- [23] J. Arbocz and J. H. Starnes Jr., "Future directions and challenges in shell stability analysis," *Thin-Walled Structures*, vol. 40, pp. 729-754, 2002.

- [24] P. Seide, V. I. Weingarten and E. J. Morgan, "The development of design criteria for elastic stability of thin shell structures," Space Technology Laboratory, Inc. (now TRW Systems). STL/TR-60-0000-19425 (AFBMD/TR-61-7), 1960.
- [25] V. I. Weingarten, E. J. Morgan and P. Seide, "Elastic stability of thin-walled cylindrical and conical shells under axial compression," *AIAA Journal*, vol. 3, pp. 500-505, 1965.
- [26] V. I. Weingarten, P. Seide and J. P. Peterson, "NASA SP-8007 - buckling of thin-walled circular cylinders," *NASA Space Vehicle Design Criteria - Structures*, 1965 (revised 1968).
- [27] J. Arbocz, B. Jr. and C. D., "The effect of general imperfections on the buckling of cylindrical shells," *Journal of Applied Mechanics*, vol. 36, no. 1, pp. 28-38, 1969.
- [28] J. Singer, J. Arbocz and C. D. Babcock Jr., "Buckling of imperfect stiffened cylindrical shells under axial compression," *AIAA Journal*, vol. 9, no. 1, pp. 68-75, 1971.
- [29] J. Singer, H. Abramovich and R. Yaffe, "Initial imperfection measurements of integrally stringer-stiffened shells," TAE report No. 220, Technion, Haifa, Israel, 1978.
- [30] A. C. Walker and S. Stridharan, "Buckling of compressed, longitudinally stiffened cylindrical shells," in *BOSS 79, Proceedings 2nd International Conference on the Behaviour of Off-shore Structures*, vol. 2, p. 341-356, London: Imperial College, 1979.
- [31] R. Degenhardt, A. Kling, A. Bethge, J. Orf, L. Kärger, R. Zimmermann, K. Rohwer and A. Calvi, "Investigations on imperfection sensitivity and deduction of improved knock-down factors for unstiffened CFRP cylindrical shells," *Composite Structures*, vol. 92, no. 8, pp. 1939-1946, 2010.
- [32] R. Rolfes, B. Kriegesmann and C. Hühne, "A probabilistic based design load for composite shells with non-traditional imperfections," in *2nd ECCOMAS thematic conference on the mechanical response of composites*, London, UK, 2009.
- [33] B. Kriegesmann, R. Rolfes, C. Hühne and A. Kling, "Fast probabilistic design procedure for axially compressed composite cylinders," *Composite Structures*, vol. 93, pp. 3140-3149, 2011.
- [34] C. Hühne, R. Rolfes and J. Tessmer, "A new approach for robust design of composite cylindrical shells under axial compression," in *Proceedings of the international ESA conference, Noordwijk*, 2005.
- [35] C. Hühne, R. Rolfes, E. Breitbach and J. Teßmer, "Robust design of composite cylindrical shells under axial compression - simulation and validation," *Thin-Walled Structures*, vol. 46, pp. 947-962, 2008.
- [36] S. P. Timoshenko and J. M. Gere, *Theory of elastic stability*. Second edition, New York: McGraw-Hill, 1985.
- [37] W. T. Haynie and M. W. Hilburger, "Comparison of methods to predict lower bound buckling loads of cylinders under axial compression," in *51st AIAA/ASME/ASCE/AHS/ASC, 12-15 Apr.*, Orlando, FL, United States, 2010.
- [38] T. A. Winterstetter and H. Schmidt, "Stability of circular cylindrical shells under combined loading," *Thin-Walled Structures*, vol. 40, no. 10, pp. 893-909, 2002.
- [39] M. Deml and W. Wunderlich, "Direct evaluation of the "worst" imperfection shape in shell buckling," *Computer Methods in Applied Mechanics and Engineering*, vol. 149, pp. 201-222, 1997.
- [40] M. Esslinger, "Hochgeschwindigkeitsaufnahmen vom Beulvorgang dünnwandiger, axialbelasteter Zylinder," *Der Stahlbau*, vol. 3, 1970.
- [41] B. Geier, H. Klein and R. Zimmermann, "Experiments on buckling of CFRP cylindrical shells under non-uniform axial load," *Proceedings, Int. Conference on Composite Engineering, ICCE71*, pp. 28-31, August 1994.
- [42] C. Hühne, R. Zimmermann, R. Rolfes and B. Geier, "Sensitivities to geometrical and loading imperfections on buckling of composite cylindrical shells," in *proceeding of: European Conference on Spacecraft*, 2002.
- [43] R. Wagner and C. Hühne, "Single perturbation load approach (SPLA) to determine buckling loads of composite shells under axial compression," in *European Conference on Spacecraft Structures, Materials & Environmental Testing*, Braunschweig, Germany, 2014.
- [44] J. G. A. Croll, "Towards simple estimates of shell buckling loads," Thin Walled Structures Study Group, Cranfield Institute of Technology, March, 1972.
- [45] R. Batista and C. J. G. A., "A design approach for unstiffened cylindrical shells under external pressure,," in *In: Proceedings of the international conference on thin-walled structures*, University of Strathclyde, Crosby Lockwood, Glasgow, 1979.
- [46] J. G. A. Croll and R. Batista, "Explicit lower bounds for the buckling of axially loaded cylinders," *International Journal of Mechanical Sciences*, vol. 23, pp. 333-343, 1981.
- [47] J. G. A. Croll, "Towards simple estimates of shell buckling loads," *Der Stahlbau*, Vols. Part I, Heft, August, 1975; Part II, Heft, September, 1975.
- [48] J. G. A. Croll, "Towards a rationally based elastic-plastic shell buckling design methodology," *Thin-Walled Structures*, vol. 23, pp. 67-84, 1995.

- [49] E. M. Sosa, L. A. Godoy and J. G. A. Croll, "Computation of lower-bound elastic buckling loads using general-purpose finite element codes," *Computers and Structures*, vol. 84, pp. 1934-1945, 2006.
- [50] E. M. Sosa and L. A. Godoy, "Challenges in the computation of lower-bound buckling loads for tanks under wind pressures," *Thin-Walled Structures*, vol. 48, pp. 935-945, 2010.
- [51] B. Geier, H. Meyer-Piening and R. Zimmermann, "On the influence of laminate stacking on buckling of composite cylindrical shells subjected to axial compression," *Composite Structures*, vol. 55, pp. 467-474, 2002.
- [52] M. W. Hilburger, M. P. Nemeth and J. H. Starnes Jr., "Shell buckling design criteria based on manufacturing imperfection signatures," *NASA Report TM-2004-212659*, 2004.
- [53] R. Degenhardt, A. Bethge, A. King, R. Zimmermann, K. Rohwer, J. Teßmer and A. Calvi, "Probabilistic approach for improved buckling knock-down factors of CFRP cylindrical shells," *In proceeding of: First CEAS European Air and Space Conference*, 2008.
- [54] R. Zimmermann, "Optimierung axial gedrückter CFK-Zylinderschalen," *Fortschrittsberichte VDI-Reihe 1, Nr.207, Düsseldorf VDI Verlag*, 1992.
- [55] H. Wang, A. P. Bueschel, R. Degenhardt, K. Rohwer, X. Sun and W. Wagner, "An empirical formula for the critical perturbation load," *German Aerospace Institute - DLR, Braunschweig*, 2008.
- [56] M. A. Arbelo, R. Degenhardt, S. G. P. Castro and R. Zimmermann, "Numerical characterization of imperfection sensitive composite structures," *Composite Structures*, vol. 108, pp. 295-303, 2014.
- [57] B. Kriegesmann, R. Rolfes, C. Hühne, J. Teßmer and J. Arbocz, "Probabilistic design of axially compressed composite cylinders with geometric and loading imperfections," *International Journal of Structural Stability and Dynamics*, vol. 10, no. 4, pp. 623-644, 2010.
- [58] L. Wulschleger and H. R. Meyer-Piening, "Buckling of geometrically imperfect cylindrical shells - definition of a buckling load," *International Journal of Non-Linear Mechanics*, vol. 37, pp. 645-657, 2002.
- [59] J. N. Reddy, *Mechanics of laminated composite plates and shells, theory and analysis*. Second Edition, Boca Raton: CRC Press, 2004.
- [60] R. M. Jones, *Mechanics of composite materials*, United States of America: Taylor & Francis, 1999.
- [61] S. Timoshenko and J. N. Goodier, *Theory of elasticity*. Second Edition, McGraw-Hill, 1951.
- [62] G. J. Simitses, I. Sheinman and D. Shaw, "The accuracy of the Donnell's equations for axially-loaded, imperfect orthotropic cylinders," *Computers & Structures*, vol. 20, no. 6, pp. 939-945, 1985.
- [63] J. L. Sanders, "Nonlinear theories of thin shells," *Quarterly of Applied Mathematics*, vol. 21, pp. 21-36, 1963.
- [64] Y. Goldfeld, I. Sheinman and M. Baruch, "Imperfection sensitivity of conical shells," *AIAA Journal*, vol. 4, no. 3, pp. 517-524, 2003.
- [65] B. Geier and G. Singh, "Some simple solutions for buckling loads of thin and moderate thick cylindrical shells and panels made of laminated composite material," *Aerospace Science and Technology*, vol. 1, pp. 47-63, 1997.
- [66] Y. Goldfeld, "Imperfection sensitivity of laminated conical shells," *International Journal of Solids and Structures*, vol. 44, pp. 1221-1241, 2007.
- [67] G.-Q. Zhang, *Stability analysis of anisotropic conical shells*, Technical University Delft - Faculty of Aerospace Engineering, 1993.
- [68] N. H. Hadi and K. A. Ameen, "Nonlinear free vibration of cylindrical shells with delamination using high order shear deformation theory: a finite element approach," *American journal of scientific and industrial research*, vol. 2, no. 2, pp. 251-277, 2011.
- [69] V. V. Novozhilov, *Foundations of the nonlinear theory of elasticity*, Rochester: Graylock Press, 1953.
- [70] F. Shadmehri, S. V. Hoa and M. Hojjati, "Buckling of conical composite shells," *Composite Structures*, vol. 94, pp. 787-792, 2012.
- [71] F. Shadmehri, *Buckling of laminated composite conical shells; theory and experiment*, Montreal, Quebec, Canada: PhD thesis, Concordia University, 2012.
- [72] E. J. Barbero, J. N. Reddy and J. L. Teply, "General two-dimensional theory of laminated cylindrical shells," *AIAA Journal*, vol. 28, no. 3, pp. 544-553, 1990.
- [73] L. Tong and T. K. Wang, "Simple solutions for buckling of laminated conical shells," *International Journal of Mechanical Sciences*, vol. 34, no. 2, pp. 93-111, 1992.
- [74] S. Timoshenko, *Strength of Materials, Part I*, Lancaster, PA.: D. Van Nostrand Company, Inc., 1948.
- [75] J. N. Reddy, "A general non-linear third-order theory of plates with moderate thickness," *International Journal of Non-Linear Mechanics*, vol. 25, no. 6, pp. 677-686, 1990.
- [76] J. N. Reddy, "A simple higher-order theory of plates with moderate thickness," *Journal of Applied Mechanics*, vol. 51, pp. 745-752, 1984.

- [77] G. J. Simitses, D. Shaw, I. Sheinman and J. Giri, "Imperfection sensitivity of fiber-reinforced, composite, thin cylinders," *Composite Science and Technology*, vol. 22, pp. 259-276, 1985.
- [78] K. Y. Yeh, B. H. Sun and F. P. J. Rimrott, "Buckling of imperfect sandwich cones under axial compression - equivalent-cylinder approach. Part I," *Technische Mechanik*, vol. 14, no. 3/4, pp. 239-248, 1994.
- [79] B. O. Almroth, "Influence of imperfections and edge restraint on the buckling of axially compressed cylinders," NASA CR-432. Lockheed Missiles and Space Company, Sunnyvale, California, 1966.
- [80] S. Yamada, J. G. A. Croll and N. Yamamoto, "Nonlinear buckling of compressed FRP cylindrical shells and their imperfection sensitivity," *Journal of Applied Mechanics*, vol. 75, no. July, pp. 41005-1 to 41005-10, 2008.
- [81] A. J. M. Ferreira and J. T. Barbosa, "Buckling behaviour of composite shells," *Composite Structures*, vol. 50, no. 1, pp. 93-98, 2000.
- [82] K.-J. Bathe, *Finite element procedures*, New Jersey: Prentice Hall, 1996.
- [83] Abaqus-6.11, *Analysis user's manual. Volume II: analysis*, Dassault Systemes, 2011.
- [84] R. G. Cowper, "The shear coefficient in Timoshenko's Beam Theory," *Journal of Applied Mechanics*, vol. 33, pp. 335-340, 1966.
- [85] S. G. P. Castro, "Computational Mechanics Tools, Version 0.2.0," 8 October 2014. [Online]. Available: <http://compmech.github.io/compmech/>.
- [86] S. Timoshenko, *Strength of Materials, Part II*, Lancaster, PA: D. Van Nostrand Company, Inc., 1948.
- [87] S. Timoshenko and S. Woinowsky-Krieger, *Theory of plates and shells*. Second Edition, McGraw-Hill, 1959.
- [88] J. N. Reddy, *Energy Principles and Variational Methods in Applied Mechanics*, Second Edition, New Jersey: John Wiley & Sons, 2002.
- [89] O. C. Zienkiewicz and R. L. Taylor, *The Finite Element Method, Volume 2: Solid Mechanics*, Fifth Edition, Oxford: Butterworth-Heinemann, 2000.
- [90] M. A. Crisfield, *Non-linear finite element analysis of solids and structures - Volume 1*, London, UK: John Wiley & Sons, 2000.
- [91] J. Arbocz, "The imperfection data bank, a mean to obtain realistic buckling loads," *Journal of Applied Mechanics*, pp. 535-567, 1968.
- [92] R. Degenhardt, A. Kling, H. Klein, W. Hillger, H. C. Goetting, R. Zimmermann and K. Rohwer, "Experiments on buckling and postbuckling of thin-walled CFRP structures using advanced measurement systems," *International Journal of Structural Stability and Dynamics*, vol. 7, no. 2, pp. 337-358, 2007.
- [93] R. M. Jones, *Buckling of bars, plates and shells*, Blacksburg, Virginia, USA: Bull Ridge Publishing, 2006.
- [94] A. Jennings, J. Halliday and M. J. Cole, "Solution of linear generalized eigenvalue problems containing singular matrices," *Journal of the Institute of Mathematics and its Applications*, vol. 22, pp. 401-410, 1978.
- [95] P. Som and A. Deb, "A generalized Ritz-based method for nonlinear buckling of thin cylindrical shells," *Thin-Walled Structures*, vol. 76, pp. 14-27, 2014.
- [96] E. W. Weisstein, "Generalized Fourier Series," From MathWorld--A Wolfram Web Resource, 2013. [Online]. Available: <http://mathworld.wolfram.com/GeneralizedFourierSeries.html>.
- [97] P. Buermann, R. Rolfes, J. Tessmer and M. Schagerl, "A semi-analytical model for local post-buckling analysis of stringer- and frame-stiffened cylindrical panels," *Thin-Walled Structures*, vol. 44, pp. 102-114, 2006.
- [98] Wolfram Research, Inc., *Mathematica*, Version 9.0, Champaign, IL (2013)..
- [99] A. D. Polyanin and A. V. Manzhirov, *Handbook of integral equations*, CRC Press LLC, 1998.
- [100] E. W. Weisstein, "Cubature," From MathWorld--A Wolfram Web Resource, 21 05 2014. [Online]. Available: <http://mathworld.wolfram.com/Cubature.html>.
- [101] J. H. Mathews, "2D Integration using the Trapezoidal and Simpson Rules," California State University Fullerton, 2003. [Online]. Available: <http://mathfaculty.fullerton.edu/mathews/n2003/SimpsonsRule2DMod.html>. [Accessed 21 05 2013].
- [102] M. A. Crisfield, "A fast incremental/iterative solution procedure that handles snap-through," *Computers & Structures*, vol. 13, pp. 55-62, 1981.
- [103] J. K. Ramm, "Strategies for tracing nonlinear responses near limit points," *Nonlinear finite element analysis in structural mechanics*, Vols. Springer-Verlag, pp. 63-89, 1981.
- [104] D. Ho, "The influence of imperfections on systems with coincident buckling loads," *International Journal of Non-linear Mechanics*, vol. 7, pp. 311-321, 1972.
- [105] J. M. Rotter, "Elephant's foot buckling in pressurized cylindrical shells," *Stahlbau*, vol. 75, no. 9, pp. 742-747, 2006.

- [106] S. G. P. Castro, C. Mittelstedt, F. A. C. Monteiro, M. A. Arbelo, G. Ziegmann and R. Degenhardt, "Linear buckling predictions of unstiffened laminated composite cylinders and cones under various loading and boundary conditions using semi-analytical models," *Composite Structures*, vol. 10.1016/j.compstruct.2014.07.037, 2014.
- [107] H.-R. Meyer-Piening, M. Farshad, B. Geier and R. Zimmermann, "Buckling loads of CFRP composite cylinders under combined axial and torsion loading - experiment and computations," *Composite Structures*, vol. 53, pp. 427-435, 2001.
- [108] M. A. Arbelo, S. F. M. d. Almeida, M. V. Donadon, S. R. Rett, R. Degenhardt, S. G. P. Castro, K. Kalnins and O. Ozoliņš, "Vibration correlation technique for the estimation of real boundary conditions and buckling load of unstiffened plates and cylindrical shells," *Thin-Walled Structures*, vol. 79, no. June, pp. 119-128, 2014.
- [109] S. G. P. Castro, C. Mittelstedt, F. A. C. Monteiro, R. Degenhardt and G. Ziegmann, "Evaluation of non-linear buckling loads of geometrically imperfect composite cylinders and cones with the RItz method," *Composite Structures*, vol. 122, no. April, pp. 284-299, 2015.
- [110] S. G. P. Castro, C. Mittelstedt, F. A. C. Monteiro, M. A. Arbelo and R. Degenhardt, "A semi-analytical approach for the linear and non-linear buckling analysis of imperfect unstiffened laminated composite cylinders and cones under axial, torsion and pressure loads," *Thin-Walled Structures*, 2014 (submitted).

List of Symbols

x	The coordinate along the meridian (cf. Fig. 3.2.1)
θ	The coordinate along the circumference (cf. Fig. 3.2.1)
z	The coordinate along the shell normal (cf. Fig. 3.2.1)
u	Displacement along x (cf. Fig. 3.2.1)
v	Displacement along θ (cf. Fig. 3.2.1)
w	Displacement along z (cf. Fig. 3.2.1)
ϕ_x	Rotation along the xz plane
ϕ_θ	Rotation along the θz plane
r	Radius as a function of z only (cf. Fig. 3.2.1)
$R(x, z)$	Radius as a function of x and z
R_2	Radius at the top edge of a cone / cylinder (cf. Fig. 3.2.1)
R_1	Radius at the bottom edge of a cone / cylinder (cf. Fig. 3.2.1)
h	Total thickness of the shell (cf. Fig. 3.2.1)
H	Height of the cone / cylinder (cf. Fig. 3.2.1)
α	Cone semi-vertex angle (cf. Fig. 3.2.1)
L	Length of the cone / cylinder meridian (cf. Fig. 3.2.1)
u_{TM}	Displacement of the testing machine upper plate along the axial direction (cf. Fig. 3.2.1)
F_C	Compressive force applied along the axial direction (cf. Fig. 3.2.1)
θ_T	Torsion angle at the top edge of the cone / cylinder (cf. Fig. 3.2.1)
T	Torque applied at the top edge of the cone / cylinder (cf. Fig. 3.2.1)
P	Pressure load applied uniformly in the z direction (cf. Fig. 3.2.1)
F_{PLi}	Perturbation load applied normally to the shell surface (cf. Fig. 3.2.1)
β	Load asymmetry angle
ξ_{LA}	Misalignment of the axial load F_C about the cone / cylinder axis (cf. Fig. 3.2.1)
M_{LA}	Moment due to the misalignment ξ_{LA} (cf. Fig. 3.2.1)
ω	Azimuth angle of the load asymmetry (cf. Fig. 3.2.1)
$U, \delta U$	Strain or internal energy and its variation
$V, \delta V$	Work due to the applied forces and its variation
$\Pi, \delta \Pi$	Total potential energy and its variation
$\gamma_{x\theta}$	In-plane shear strain
$\gamma_{x\theta}^{(0)}$	Mid-surface in-plane shear strain
$\gamma_{x\theta}^{(1)}$	Mid-surface torsional strain
$\gamma_{\theta z}$	Transverse shear strain θz
$\gamma_{\theta z}^{(0)}$	Mid-surface transverse shear strain θz
γ_{xz}	Transverse shear strain xz
$\gamma_{xz}^{(0)}$	Mid-surface transverse shear strain xz
ϵ_{xx}	Extensional strain xx

$\varepsilon_{xx}^{(0)}$	Mid-surface extensional strain xx
$\varepsilon_{xx}^{(1)}$	Mid-surface rotational strain xx
$\varepsilon_{\theta\theta}$	Extensional strain $\theta\theta$
$\varepsilon_{\theta\theta}^{(0)}$	Mid-surface extensional strain $\theta\theta$
$\varepsilon_{\theta\theta}^{(1)}$	Mid-surface rotational strain $\theta\theta$
N_{xx}	Distributed membrane force xx
$N_{\theta\theta}$	Distributed membrane force $\theta\theta$
$N_{x\theta}$	Distributed membrane shear force
M_{xx}	Distributed bending moment xx
$M_{\theta\theta}$	Distributed bending moment $\theta\theta$
Q_{θ}	Distributed transverse force in the θz plane
Q_x	Distributed transverse force in the xz plane
$\{R\}, \{\delta R\}$	Residual force vector and its variation
$\{F_{int}\}, \{\delta F_{int}\}$	Internal force vector and its variation
$\lambda, \delta\lambda$	Load multiplier and its variation
$\{F_{ext0}\}$	External force vector that are not multiplied by λ
$\{F_{ext\lambda}\}$	External force vector that are multiplied by λ
$\{\varepsilon\}, \{\delta\varepsilon\}$	Strain vector and its variation
$\{\varepsilon_0\}$	Strain vector containing the linear components
$\{\varepsilon_L\}$	Strain vector containing the non-linear components due to large displacements
$\{\varepsilon_{L0}\}$	Strain vector containing the non-linear components due to initial imperfections
$[d_0]$	Matrix containing the differential operators for the linear kinematic equations
$[B_0]$	Matrix containing the linear kinematic relations
$[B_L]$	Matrix containing the non-linear kinematic relations due to large displacements
$[B_{L0}]$	Matrix containing the non-linear kinematic relations due to initial imperfections
$[\bar{B}], [\delta\bar{B}]$	Defined matrix and its variation such that: $[\bar{B}] = [B_0] + [B_L] + [B_{L0}]$; and: $[\delta\bar{B}] = [\delta B_L]$
$[A], [\delta A]$	Matrix containing part of the non-linear terms due to large displacements and its variation. Also used to represent a sub-matrix of the laminate constitutive matrix $[F]$
$[A_0]$	Matrix containing part of the non-linear terms due to initial imperfections
$\{c\}, \{\delta c\}$	Vector containing the Ritz constants and its variation (amplitudes of the approximation functions)
$[g]$	Matrix containing the base functions (the shapes of the approximation functions)
$[g^{u,v,w,\phi_x,\phi_\theta}]$	Base functions for a specific displacement u, v, w or rotation ϕ_x, ϕ_θ
$[g_0]$	Matrix containing the non-homogeneous base functions
$[g_1]$	Matrix containing the base functions depending only of x
$[g_2]$	Matrix containing the base functions depending on x and θ
m_1	The number of terms for x in the approximation functions corresponding to $[g_1]$
m_2	The number of terms for x in the approximation functions corresponding to $[g_2]$
n_2	The number of terms for θ in the approximation functions corresponding to $[g_2]$
i_1, k_1	Indices for the base functions corresponding to $[g_1]$
i_2, k_2, j_2, ℓ_2	Indices for the base functions corresponding to $[g_2]$

$\{c_0\}, \{c_1\}, \{c_2\}$	Vectors containing the Ritz constants corresponding to $[g_0], [g_1], [g_2]$, respectively
$[G_d]$	Matrix containing the differential operators to be applied to the base functions to give $[G]$
$[G]$	Matrix containing the result after applying $[G_d]$ to the base functions
u_0	Axial displacement of the mid-surface (at $z = 0$)
v_0	Circumferential displacement of the mid-surface (at $z = 0$)
w_0	Initial imperfection field represented only by normal displacements. In Chapter 2 symbol w_0 is used for the normal displacement of the mid-surface (at $z = 0$)
$w_{0,x}$	Partial derivative of the initial imperfection field for x
$w_{0,\theta}$	Partial derivative of the initial imperfection field for θ
$w_{,x}, \delta w_{,x}$	Partial derivative of the normal displacement for x and its variation
$w_{,\theta}, \delta w_{,\theta}$	Partial derivative of the normal displacement for θ and its variation
K	Shear correction factor
$[K_0]$	Linear constitutive stiffness matrix
$[K_L]$	Non-linear constitutive stiffness matrix due to large displacements
$[K_{0L}]$	Component $0L$ of the non-linear constitutive matrix
$[K_{LL}]$	Component LL of the non-linear constitutive matrix
$[K_G]$	Geometric stiffness matrix
$[K_{G_0}]$	Linear geometric stiffness matrix calculated using the initial stress state
$[K_{G_0}]_{F_C}$	Term of $[K_{G_0}]$ considering only the axial force F_C
$[K_{G_0}]_T$	Term of $[K_{G_0}]$ considering only the torsion load T
$[K_{G_0}]_P$	Term of $[K_{G_0}]$ considering only the pressure load P
$[K_T]$	Tangent stiffness matrix
N_{xx0}	Initial stress state for the distributed membrane force N_{xx}
$N_{\theta\theta0}$	Initial stress state for the distributed membrane force $N_{\theta\theta}$
$N_{x\theta0}$	Initial stress state for the distributed membrane shear force $N_{x\theta}$
$\{\Phi\}$	Eigenvector obtained in an eigenvalue analysis
$[F]$	The laminate constitutive matrix composed by the sub matrices $[A]$, $[B]$ and $[D]$
A_{ij}	Terms of the $[A]$ constitutive sub-matrix or the coefficients of half-cosine imperfection function
B_{ij}	Terms of the $[B]$ constitutive sub-matrix or the coefficients of half-cosine imperfection function
$\{c_0\}$	Coefficients of the half-cosine imperfection function in matrix form (formed by A_{ij} and B_{ij})
$K_{Bot}^{u,v,w,\phi_x,\phi_\theta}$	Elastic constants at the bottom edge for displacements u, v, w or rotations ϕ_x, ϕ_θ
$K_{Top}^{u,v,w,\phi_x,\phi_\theta}$	Elastic constants at the top edge for displacements u, v, w or rotations ϕ_x, ϕ_θ
$[K_{Bot}]$	Matrix grouping the elastic constants at the bottom edge
$[K_{Top}]$	Matrix grouping the elastic constants at the top edge
$[K_e]$	Stiffness matrix contribution due to the elastic constraints at the edges
$[K_{0e}]$	Linear constitutive stiffness matrix with the elastic constraints contribution added
$[K_{ab}]$	Smallest repeatable sub-matrices ($[K_{0ab}]$, $[K_{0Lab}]$, $[K_{LLab}]$, $[K_{Gab}]$ and $[K_{eab}]$)
$\{N\}, \{\delta N\}$	Distributed membrane force vector (usually called stress vector) and its variation
$\{N_0\}$	Linear component of the distributed membrane force vector

$\{N_L\}$	Non-linear component of the distributed membrane force vector due to large displacements
$N_{xx_{top}}$	Distributed axial load at the top edge
$\{F_{int_{00}}\}$	Linear component of the internal force vector
$\{F_{int_{0L}}\}$	Component $0L$ of the internal force vector
$\{F_{int_{L0}}\}$	Component $L0$ of the internal force vector
$\{F_{int_{LL}}\}$	Component LL of the internal force vector
η	Scalar multiplier used in the update of $\{c\}$ in the line search algorithm applied to non-linear analysis
ℓ	The arc-length used in the Riks method with the constant arc-length criterion
ϕ	A normalizing factor used in the Riks method with the constant arc-length criterion

List of Figures

Fig. 1.1.1: The Single Perturbation Load Approach (SPLA)	3
Fig. 1.1.1: Test Data for Isotropic Cylinders under Axial Compression (modified from Arbocz and Starnes Jr. [23])	5
Fig. 1.1.2: Membrane Forces, Moments, Extensional and Rotation Strains acting in a Shell Element	6
Fig. 1.1.3: Coupling Stiffness Matrices for Cylinders Z32 and Z33	6
Fig. 1.2.1: Four Regions in the SPLA Knock-Down Curve, modified from Castro et al. [2]	8
Fig. 1.2.2: Displacement Patterns for the Local Snap-Through and the Global Buckling, modified from Castro et al. [2] ..	8
Fig. 1.2.3: LS curves for different perturbation load levels, cylinder Z33, copied from Castro et al. [2]	9
Fig. 1.2.4: Detailed Evaluation of the LS curves and KD curves close to P1, Cylinder Z33	9
Fig. 1.2.5: Load cases used in the MPLA, copied from Arbelo et al. [56]	11
Fig. 1.2.6: MPLA curves for cylinder Z33, copied from Arbelo et al. [56]	11
Fig. 1.2.7: Bending angle β in terms of the axial displacement, modified from Wagner and Hühne [43]	12
Fig. 1.3.1: KDFs using the Reduced Energy Method (REM), copied from Castro et al. [3]	14
Fig. 1.3.2: First 50 th Buckling Modes for Cylinder Z07	14
Fig. 1.3.3: First 50 th Buckling Modes for Cylinder Z33	15
Fig. 1.4.1: Geometric Dimple Imperfection (GDI), modified from Wullschleger [58]	16
Fig. 1.4.2: Knock-down curves for the MSI, SPLI, and GDIs, for Z07, modified from Castro et al. [3]	17
Fig. 1.4.3: Knock-down curves for SPLA, REM, NASA SP-8007 and LBMI, modified from Castro et al. [3]	18
Fig. 1.5.1: Load Asymmetry Created with Shims, copied from Hühne et al. [42]	19
Fig. 1.5.2: Imperfection amplitude effect for different shims thicknesses	21
Fig. 1.5.3: Imperfection amplitude effect for different ω values	22
Fig. 2.1.1: Notation used for the stress components in Cartesian rectangular coordinates	27
Fig. 2.1.2: Ply and laminate coordinate systems	31
Fig. 2.1.3: Force and moment resultants on a plate element	34
Fig. 2.2.1: Coordinate system used for the derivation of the shell equations	39
Fig. 2.2.2: Scheme to show the shallow shell assumption $r \gg h$	41
Fig. 2.2.3: Kinematics of a Shell Plate for the CLPT and the FSDT	44
Fig. 3.2.1: Cone / Cylinder Model	64
Fig. 3.2.2: Load Distribution at the Top Edge	65
Fig. 3.2.3: Load Distribution due to Axial Load + Bending Moment	65
Fig. 3.5.1: Elastic Boundary Conditions	74
Fig. 3.8.1: Cross-sectional slices of a conical structure for analytical integration.	89
Fig. 4.1.1: Convergence of F_{crit} with the number of sections, C02	101
Fig. 4.1.2: Convergence of F_{crit} with the number of sections, C14	102
Fig. 4.1.3: Convergence of w_{PL} with the number of sections, C02	103
Fig. 4.1.4: Convergence of w_{PL} with the number of sections, C14	104
Fig. 4.2.1: Convergence of Linear Buckling under Axial Compression	106
Fig. 4.2.2: Convergence of First Buckling Modes for Axial Compression, cone C02, FSDT-Donnell-SS1	107
Fig. 4.2.3: Convergence of First Buckling Modes for Axial Compression, cone C02, FSDT-Donnell-SS4	107
Fig. 4.2.4: Convergence of Linear Buckling under Torsion	108
Fig. 4.2.5: Convergence of Linear Buckling under Pressure	109
Fig. 4.3.1: Convergence of Cylinder Z33 using FSDT-Donnell, $m_2 = n_2 = 0$, $F_C = 10kN$	110
Fig. 4.3.2: Convergence of Cylinder Z33 detailed, with $m_2 = n_2 = 0$	111
Fig. 4.3.3: Convergence of Cone C14, FSDT-Donnell-SS4, $m_1 = 120$, $F_C = 10kN$, $F_{PL} = 10N$, contour v	111
Fig. 4.3.4: Convergence of Cone C14, FSDT-Donnell-SS4, $m_1 = 120$, $F_C = 10kN$, $F_{PL} = 10N$, contour w	112
Fig. 4.3.5: Convergence of Cylinder Z33, w_{PL} , $m_1 = 120$, $m_2 = n_2/2$, $n_x = n_\theta = 120$, $F_C = 75kN$, $F_{PL} = 60N$	112
Fig. 4.3.6: Convergence of Cone C14, FSDT-Donnell-BC1, $m_2 = n_2 = 0$, $F_C = 20kN$	113
Fig. 4.3.7: Convergence of Cone C14, FSDT-Donnell-SS1, $m_1 = 180$, $F_C = 20kN$, $F_{PL} = 60N$, contour N_{xx}	114
Fig. 4.3.8: Convergence of Cone C14, field variables, $m_1 = 180$, $F_C = 20kN$, $F_{PL} = 60N$	114
Fig. 4.4.1: Number of Integration Points for Different Frequencies	115
Fig. 4.5.1: Convergence of Cylinder Z33, w_{PL} , $m_1 = 120$, $m_2 = n_2/2$, $n_x = n_\theta = 120$, $F_C = 75kN$, $F_{PL} = 60N$	116
Fig. 4.6.1: Finite Element Model for Linear Buckling with Axial Compression and Pressure	117
Fig. 4.6.2: Finite Element Model for Linear Buckling with Torsion	118
Fig. 4.6.3: Linear Buckling, Axial Compression, Cylinder Z33, modes 1-31	120
Fig. 4.6.4: Linear Buckling, Axial Compression, Cone C02, modes 1-13	122
Fig. 4.6.5: Linear Buckling, Axial Compression, Cone C02, modes 15-27	123
Fig. 4.7.1: FEM compared to Shadmehri and the FSDT-Donnell-BC3 model, Cone ShadC04, Ref. [106]	130

Fig. 4.7.2: Critical Buckling Mode for Cone ShadC04 with: $H = 254\text{ mm}$, $\gamma = 20^\circ$, CC3, Ref. [106]	130
Fig. 4.7.3: FEM compared to Shadmehri and the FSDT-Donnell-BC1 model, Cone ShadC04, Ref. [106]	131
Fig. 4.7.4: FEM compared to Shadmehri and the FSDT-Donnell-BC1 model, Cone ShadC02, Ref. [106]	131
Fig. 4.8.1: Combined Torsion-Axial Compression, FSDT-Donnell-CC1, modified from Ref. [106]	133
Fig. 4.8.2: Combined Torsion-Axial Compression, FSDT-Donnell-CC2, modified from Ref. [106]	133
Fig. 4.8.3: Combined Torsion-Axial Compression, FSDT-Donnell-SS2, modified from Ref. [106]	134
Fig. 4.9.1: Knock-Down Curve, Cylinder Z33	136
Fig. 4.9.2: Knock-Down Curve, Cone C02	136
Fig. 4.9.3: Load Shortening Curves for Cylinder Z33, modified from Castro et al. (2013) [2]	136
Fig. 4.9.4: Eigenvalue Analysis for C02	137
Fig. 4.10.1: Number of terms to Approximate Measured Imperfection Data, Cylinder Z23	139
Fig. 4.10.2: Number of terms to Approximate Measured Imperfection Data, Cylinder Z25	140
Fig. 4.10.3: Number of terms to Approximate Measured Imperfection Data, Cylinder Z26	141
Fig. 4.10.4: Measured Imperfections Mapped to Cone C02	142
Fig. 4.11.1: Cylinder Z23 with Geometric Imperfections convergence for m_2 and n_2	144
Fig. 4.11.2: Cone C02 using imperfection of Z23 and Z25	145
Fig. 4.12.1: Cylinder Z33, Linear Static with axial and bending loads, obtained with CLPT-Donnell-BC2	146
Fig. 4.12.2: Cone C02, Linear Static with axial and bending loads, with SS1-SS2 boundary conditions	147
Fig. 4.12.3: Cone C02, Linear Static with axial and bending loads, with SS1-SS4 boundary conditions	147
Fig. 4.12.4: Cylinder Z33, Non-Linear Static with axial and bending loads, obtained with CLPT-Donnell-BC2	148
Fig. 4.12.5: Cone C02, Non-Linear Static with axial and bending loads, with SS1-SS2 boundary conditions	148

List of Equations

(1.1.1).....	4
(1.1.2).....	5
(1.1.3).....	6
(1.2.1).....	12
(1.3.1).....	13
(1.3.2).....	13
(1.3.3).....	13
(2.1.1).....	26
(2.1.2).....	27
(2.1.3).....	28
(2.1.4).....	28
(2.1.5).....	29
(2.1.6).....	29
(2.1.7).....	29
(2.1.8).....	29
(2.1.9).....	29
(2.1.10).....	29
(2.1.11).....	30
(2.1.12).....	30
(2.1.13).....	30
(2.1.14).....	30
(2.1.15).....	31
(2.1.16).....	32
(2.1.17).....	32
(2.1.18).....	32
(2.1.19).....	32
(2.1.20).....	33
(2.1.21).....	33
(2.1.22).....	34
(2.1.23).....	34
(2.1.24).....	35
(2.1.25).....	35
(2.1.26).....	35
(2.2.1).....	36
(2.2.2).....	36
(2.2.3).....	36
(2.2.4).....	37
(2.2.5).....	37
(2.2.6).....	38
(2.2.7).....	38
(2.2.8).....	39
(2.2.9).....	39
(2.2.10).....	40
(2.2.11).....	40
(2.2.12).....	40
(2.2.13).....	42
(2.2.14).....	42
(2.2.15).....	42
(2.2.16).....	42
(2.2.17).....	42
(2.2.18).....	42
(2.2.19).....	43
(2.2.20).....	43
(2.2.21).....	43
(2.2.22).....	43
(2.2.23).....	44
(2.2.24).....	45

(2.2.25)	46
(2.2.26)	46
(2.2.27)	47
(2.2.28)	47
(2.2.29)	48
(2.2.30)	48
(2.2.31)	49
(2.2.32)	49
(2.2.33)	49
(2.2.34)	49
(2.2.35)	50
(2.2.36)	50
(2.2.37)	51
(2.2.38)	51
(2.2.39)	51
(2.2.40)	52
(2.2.41)	52
(2.2.42)	53
(2.2.43)	53
(2.3.1)	54
(2.3.2)	54
(2.3.3)	54
(2.3.4)	55
(2.3.5)	55
(2.4.1)	56
(2.4.2)	56
(2.4.3)	56
(2.4.4)	56
(2.4.5)	57
(2.4.6)	57
(2.4.7)	57
(2.4.8)	57
(2.4.9)	57
(2.4.10)	58
(2.4.11)	58
(3.1.1)	60
(3.1.2)	60
(3.1.3)	60
(3.1.4)	60
(3.1.5)	60
(3.1.6)	60
(3.1.7)	60
(3.1.8)	61
(3.1.9)	61
(3.1.10)	61
(3.1.11)	61
(3.1.12)	61
(3.1.13)	61
(3.1.14)	61
(3.1.15)	61
(3.1.16)	62
(3.1.17)	62
(3.1.18)	62
(3.1.19)	62
(3.1.20)	62
(3.1.21)	62
(3.1.22)	62
(3.1.23)	62
(3.1.24)	63
(3.1.25)	63
(3.1.26)	63
(3.1.27)	63

(3.2.1).....	64
(3.2.2).....	65
(3.2.3).....	65
(3.2.4).....	65
(3.2.5).....	66
(3.2.6).....	66
(3.2.7).....	66
(3.2.8).....	66
(3.2.9).....	66
(3.2.10).....	67
(3.2.11).....	67
(3.2.12).....	67
(3.2.13).....	67
(3.2.14).....	67
(3.2.15).....	67
(3.2.16).....	67
(3.2.17).....	67
(3.2.18).....	68
(3.2.19).....	68
(3.2.20).....	68
(3.2.21).....	68
(3.2.22).....	68
(3.2.23).....	68
(3.2.24).....	69
(3.2.25).....	69
(3.2.26).....	69
(3.2.27).....	69
(3.2.28).....	69
(3.3.1).....	70
(3.3.2).....	70
(3.3.3).....	70
(3.3.4).....	70
(3.4.1).....	71
(3.4.2).....	71
(3.4.3).....	71
(3.4.4).....	71
(3.4.5).....	71
(3.4.6).....	71
(3.4.7).....	71
(3.4.8).....	72
(3.4.9).....	72
(3.4.10).....	73
(3.4.11).....	73
(3.4.12).....	73
(3.4.13).....	73
(3.4.14).....	73
(3.5.1).....	74
(3.5.2).....	74
(3.5.3).....	74
(3.5.4).....	75
(3.5.5).....	75
(3.5.6).....	75
(3.5.7).....	75
(3.6.1).....	76
(3.6.2).....	76
(3.6.3).....	77
(3.6.4).....	77
(3.6.5).....	77
(3.6.6).....	77
(3.6.7).....	78
(3.6.8).....	78
(3.6.9).....	78

(3.6.10)	78
(3.6.11)	79
(3.6.12)	79
(3.6.13)	80
(3.6.14)	80
(3.6.15)	80
(3.7.1)	81
(3.7.2)	81
(3.7.3)	81
(3.7.4)	81
(3.7.5)	81
(3.7.6)	82
(3.7.7)	82
(3.7.8)	82
(3.7.9)	82
(3.7.10)	82
(3.7.11)	83
(3.7.12)	83
(3.7.13)	83
(3.7.14)	83
(3.7.15)	83
(3.7.16)	83
(3.7.17)	84
(3.7.18)	84
(3.7.19)	84
(3.7.20)	84
(3.7.21)	84
(3.8.1)	85
(3.8.2)	86
(3.8.3)	86
(3.8.4)	86
(3.8.5)	86
(3.8.6)	86
(3.8.7)	87
(3.8.8)	89
(3.8.9)	89
(3.8.10)	90
(3.8.11)	91
(3.8.12)	92
(3.8.13)	92
(3.8.14)	92
(3.9.1)	94
(3.9.2)	94
(3.9.3)	94
(3.9.4)	94
(3.9.5)	94
(3.9.6)	95
(3.9.7)	95
(3.9.8)	95
(3.9.9)	95
(3.9.10)	95
(3.9.11)	95
(3.9.12)	96
(3.9.13)	96
(3.9.14)	96
(3.9.15)	96
(3.9.16)	96
(3.9.17)	96
(3.9.18)	97
(3.9.19)	97
(3.9.20)	97
(4.6.1)	117

(4.6.2).....	118
(4.10.1).....	138
(4.11.1).....	143
(4.11.2).....	143
(B.1).....	154
(B.2).....	154
(B.3).....	155
(B.4).....	155
(B.5).....	155
(B.6).....	155
(B.7).....	156
(B.8).....	157
(C.1).....	159
(C.2).....	160
(C.3).....	160